

THÈSE

PRÉSENTÉE A

L'UNIVERSITÉ BORDEAUX 1

ÉCOLE DOCTORALE DES SCIENCES CHIMIQUES

Par Zahra Ali Fattah

POUR OBTENIR LE GRADE DE

DOCTEUR

SPÉCIALITÉ : Chimie-Physique

Applications of Bipolar Electrochemistry: From Materials Science to Biological Systems

Directeur de thèse : Prof. Alexander KUHN

Soutenue le : 22.11.2013

Devant la commission d'examen formée de:

Prof. Marken, Frank
Dr. Björefors, Fredrik
Prof. Zakri, Cécile
Dr. Mavré, François
Prof. Kuhn, Alexander
Dr. Bouffier, Laurent

Professor, University of Bath, UK
Associate Professor, Uppsala University, Sweden
Professeur, Université Bordeaux I, CRPP, France
Maitre de Conférence, Université Paris 7 - Denis Diderot, France
Professeur, Institut Polytechnique de Bordeaux, France
Chargé de Recherche, CNRS, France

Rapporteur
Rapporteur
Président
Examineur
Directeur de thèse
Co-directeur de thèse

“When the reality we are facing is inconsistent with the dominating theory, then the reality must be accepted, even if everybody believes in the dominating theories in order to agree with famous scientists.”

Abu Bakr Al-Razi

854 – 925 CE

Abstract

Bipolar electrochemistry deals with the exposure of an isolated conducting substrate that has no direct connection with a power supply except via an electric field. Therefore it can be considered as a “wireless technique”. The polarization of the substrate with respect to the surrounding medium generates a potential difference between its opposite ends which can support localized electrochemical oxidation reduction reactions and break the surface symmetry of the substrate. The method was applied in the present thesis to materials science and biological systems.

In the frame of designing asymmetric particles, also called “Janus” particles, bipolar electrochemistry was adapted for the bulk preparation of these objects. Conductive substrates with different nature, sizes and shapes have been modified with various materials such as metals, ionic and inorganic compounds using this approach. Moreover, a control over the deposit topology could be achieved for substrates at different length scales. Bipolar electrodeposition is also a good tool for investigating the generation of different metal morphologies. Further developments in the bipolar setup allowed us to use the technology for microstructuration of conductive objects.

Furthermore the concept has shown to be very useful in the field of the induced motion of particles. The asymmetric objects that have been prepared by bipolar electrodeposition were employed as microswimmers which could show both translational and rotational motion. The application of electric fields in the bipolar setup can be used for the direct generation of motion of isotropic objects through bubble generation. A levitation motion of objects combined with light emission was possible using this concept.

Finally, bipolar electrochemistry was also used for studying the intrinsic conductivity of biological molecules (DNA), which is of great importance in the nanotechnology.

Keywords:

Bipolar Electrochemistry, Electrodeposition, Asymmetric particles, Janus particles, Electrocrystallization, Microswimmers, DNA Conductivity.

Résumé

L'électrochimie bipolaire est possible quand un substrat conducteur qui n'est pas directement connecté à un générateur est exposé à un champ électrique. Il s'agit donc d'une technique « sans fil ». La polarisation du substrat par rapport à la solution génère une différence de potentiel entre les extrémités du substrat qui peuvent devenir le siège de réactions rédox et briser ainsi la symétrie à la surface du substrat. Dans cette thèse, cette méthode a été appliquée à l'élaboration de matériaux ainsi qu'à l'étude de systèmes biologiques.

L'électrochimie bipolaire a été adaptée pour la préparation « bulk » de particules asymétriques également appelées particules « Janus ». Des substrats conducteurs de différentes natures, tailles et formes ont été modifiées avec des dépôts métalliques, ioniques ou inorganiques. De plus, un contrôle de la morphologie du dépôt a été possible sur des substrats d'échelle variée. L'électrodéposition bipolaire permet d'étudier la génération de différentes morphologies métalliques, ainsi que la micro-structuration sur des objets conducteurs grâce au développement de nouveaux setups expérimentaux.

Le concept s'est également montré très utile dans le domaine de la mise en mouvement de particules. D'une part, les objets asymétriques qui ont été préparés par électrodéposition bipolaire peuvent agir comme des micro-nageurs capables de mouvement de translation ou de rotation. D'autre part, l'application d'un champ électrique peut directement induire le déplacement d'objets isotropes par génération localisée de bulles. Un mouvement de lévitation combinée à l'émission de lumière est également possible.

Finalement, l'électrochimie bipolaire a été utilisée pour étudier la conductivité de biomolécules (ADN), ce qui est d'une grande importance dans le domaine de la nanotechnologie.

Mots Clés:

Electrochimie Bipolaire, Electrodéposition, Particules Asymétriques, Particules Janus, Electrocrystallisation, Micro-nageurs, Conductivité de l'ADN

Acknowledgments

I would like to express my sincere gratitude to my supervisor Prof. Alexander Kuhn for the continuous support of my PhD research and beyond, for his patience, motivation, enthusiasm, and wide scientific knowledge. The confidence that he gave motivated me during all the time of research and writing. I could not have imagined having a better supervisor and mentor for my PhD study. “Schönen dank”.

My sincere thanks also go to my co-supervisor Dr. Laurent Bouffier for his encouragement, broad scientific interest, guidance and patience. I am grateful for the confidence, all the support and suggestions that he gave me during my study which provided significant inputs to my work. “Merci”.

I strongly acknowledge erasmus mundus (ECW) program including Bordeaux-1 University for the financial support.

I also thank Duhok University for giving me the opportunity to apply for a scholarship provided by ECW program.

I would like to thank all the committee members of my PhD defense, in particular Prof. Frank Marken and Dr. Fredrik Björefors for having accepted to be the referees of the thesis, and also Prof. Cécile Zakri and Dr. François Mavré, for evaluating my work.

I acknowledge all the collaborators for their contributions that have been described in details in appendix 4, especially Dr. Christine Labrugère and Dr. Brice Kauffmann for XPS and XRD characterization of the crystal samples.

Acknowledgement is also for the working staff at Bordeaux imaging center: Etienne, Sabrina, Melina and Isabelle, and also at CREMEM center: Martineau, for their kindness and help.

My deep thanks for Dr Dodzi Zigah for his support and honesty during all my study.

Also a big thanks go for the bipolar team including Dr. Gabriel Loget (specially for his help), Dr. Jérôme Roche, Chawanwit Kumsapaya for the exciting scientific discussions, advices,

Acknowledgments

and jointly with Julie Gillion, for all the work we did together as well as the impressive electric arcs we had sometimes with our experiments.

I acknowledge all NSysA members for the great family atmosphere: Aline, Dr. Valérie, Prof. Neso, Dr. Isabelle, Dr. Stéphane, Dr. Sandra, Dr. Matthias, Dr. Yémima, Dr. Milena, Dr. Hélène, Dr. Léa, Dr. Laurent, Dr. Churalat, Dr. Nina, Dr. Michael, Lorenzo, Dr. María, Dr. Emeline (thanks dear), Dr. Emmanuel, Suresh, Salem, Catherine, Florent, Eugenio, Aleksandar and Sudarat. Thank you so much Milica Sentic for the nice friendship and also the work we did together (хвала драга). A great appreciation for Dr. Lisa Peyrard for everything she did for me “Merci ma chère”. Véronique, Patrick and Bertrand are also acknowledged for their technical supports.

A special word of thanks goes to my family, in particular my parents, my brothers and sisters for their continuous love and encouragement. Finally, I am grateful for the support, confidence and cordiality of my husband “Radhwan”, the man who, without his patience, I could not have completed this thesis. “Shukran”.

Zahra Ali Fattah

November, 2013

Table of Contents

Symbols	IX
Abbreviations	XI
Preface	XIII
Chapter 1. Bipolar electrochemistry	1
1.1. Introduction to Bipolar Electrochemistry	1
1.2. The Open Configuration of Bipolar Electrochemistry	3
1.3. The Closed Configuration of Bipolar Electrochemistry	11
1.4. Traditional and Macroscopic Applications of Bipolar Electrochemistry	12
1.4.1. Bipolar Plate Electrodes	12
1.4.2. Study of Corrosion	13
1.5. Recent Micro- and Nano Applications of Bipolar Electrochemistry	14
1.5.1. Fabrication of Electronic Devices	14
1.5.2. Electroanalytical Purposes	16
1.5.2.1. Concentration and Separation of Analytes in Microfluidic Systems	16
1.5.2.2. Electrochemical Detection	18
1.5.2.3. Optical Detection Based on Electrodissolution of a Bipolar Electrode	19
1.5.2.4. Optical Detection Based on Electrochemiluminescence	21
1.5.2.5. Optical Detection Based on Fluorescence	24
1.5.3. Generation of Molecular and Material Gradients	26
1.5.4. Functionalization of a Single Micro- and Nanopore	28
1.5.5. Asymmetric Modification of Micro- and Nanoparticles	29
1.5.5.1. The Closed Configuration for Preparation of Asymmetric Particles	29
1.5.5.2. Two-Dimensional Modification	30
1.5.5.3. Capillary Electrophoresis for Bipolar Electrochemistry	32
1.5.5.4. Bipolar Cell for Up-scaling the Asymmetric Product	33

1.5.6. Electric Fields Generated Motion	34
References	36
Chapter 2. Bipolar Electrochemistry with Materials Science: Asymmetric Particles, Applications and Design	41
2.1. Asymmetric Particles	41
2.2. Physical Properties and Applications	43
2.2.1. Adsorption at Interfaces	43
2.2.2. Self-Assembly of Asymmetric Particles	45
2.2.3. Applications of Janus Particles	48
2.3. Synthetic Strategies for the Preparation of Asymmetric Particles	51
2.4. Capillary-Assisted Bipolar Electrodeposition	55
2.4.1. Instrument Description	56
2.4.2. Metal Deposition on Carbon Microtubes	58
2.5. Up-Scaling the Production Using the Bipolar Cell	67
2.5.1. Cell Description	67
2.5.2. Metal Electrodeposition on Anisotropic Substrates	70
2.5.3. Toposelectivity of the Metal Cluster	76
2.5.3.1. Control of the Topology of the Metal on Carbon Fibers	76
2.5.3.2. Control of the Topology of the Metal on Carbon Microtubes	80
2.5.4. Electrodeposition of an Inorganic Functional Layer on Graphite Rods	88
2.5.5. Bipolar Electrogeneration of Single Crystals	98
2.5.6. Generation of Different Metal Morphologies on a Single Substrate	108
2.6. Technology Development and Surface Microstructuration	110
References	115
Chapter 3 Bipolar Electrochemistry and Swimmers	123
3.1. Microswimmers: Principles, Synthesis and Applications	123
3.1.1. Biocatalytic Swimmers	123
3.1.2. Chemically Powered Swimmers	125
3.1.3. Externally Stimulated Swimmers	129
3.2. Asymmetric Swimmers Designed by Bipolar Electrochemistry	132
3.2.1. Magnetically Driven Motion	132
3.2.2. Chemically Induced Motion	134

3.3. Bubble Induced Motion of the Lighting Up Bipolar Swimmers Under External Electric Field	138
References	145
Chapter 4 Bipolar Electrochemistry with Soft Material: Deoxyribonucleic acid (DNA)	149
4.1. Introduction to DNA: Structure, Charge Transport and Conductivity	149
4.1.1. DNA Structure	149
4.1.2. DNA Charge Transport (CT) and Conductivity	151
4.2. Bipolar electrochemistry for Asymmetric Metal deposition on DNA	155
References	162
Chapter 5 Conclusion and Perspectives	165
5.1. Conclusion	165
5.2. Perspectives	168
References	173
Appendix	175
1. Preparation of Ethyl Cellulose Gel, and Recovery of the Modified Carbon Beads	175
2. The Electrochemical Measurement of H_2O_2 and luminol in NaOH Solution, Combined with a Simultaneous Monitoring of the ECL Intensity	175
3. Fabrication of the PDMS Bipolar Electrochemical Cell	176
4. Collaborations	177
5. List of Publications That Came out of This Thesis	178
Résumé	179

Symbols

Symbol	Meaning	Usual units
Abs	absorbance	none
d	distance between the feeder electrodes	cm
\mathcal{E}	applied electric field	V/cm
E	potential	V
E°	standard potential for the redox couple	V
E_a	anode potential	V
E_{appl}	applied potential between the feeder electrodes	V
E_c	cathode potential	V
F	Faraday constant	C/mol
i	current	A
i_{bpe}	faradaic current through the bipolar electrode	A
i_{bs}	by-pass current	A
i_t	total current flowing in the cell	A
j	current density	A/cm ²
j_0	apparent exchange current density	A/cm ²
l	length of a bipolar electrode	cm
l_{dep}	deposit length	cm
l_{eff}	effective length of a bipolar electrode	cm
n	stoichiometric number of electrons involved in an electrochemical reaction	none
pK_a	acid dissociation constant	none
R	gas constant	J mol ⁻¹ K ⁻¹
r	reaction rate	none
R_{bpe}	resistance of the bipolar electrode	Ω
R_{bs}	solution resistance close to the bipolar electrode	Ω
R_t	total cell resistance ($R_{bs} + R_{bpe}$)	Ω
T	temperature	K
V	polarization potential at the solution/substrate interface	V
ΔV	maximum polarization potential	V
V_a	solution potential at the anodic pole of a bipolar electrode	V
V_c	solution potential at the cathodic pole of a bipolar electrode	V
ΔV_{min}	minimum potential value to trigger electrochemical reactions at a bipolar electrode	V
V_{sub}	equilibrium potential	V
x	position on the bipolar electrode	cm
x_o	position on the bipolar electrode where $V = V_{sub}$	cm

Symbols

Symbol	Meaning	Usual units
Θ	angular position	rad
λ	wavelength	nm

Abbreviations

Abbreviation	Meaning
A	acceptor orbital
AC	alternating current
AFM	atomic force microscopy
AP	asymmetric particle
APP	asymmetric patchy particle
BEF	bipolar electrode focusing
BODIPY	boron-dipyrromethene
bp	base pair
BP _e	bipolar electrode
CABED	capillary assisted bipolar electrochemistry
CE	capillary electrophoresis
CF	carbon fiber
CF _e	carbon fiber microelectrodes
CL	chemiluminescence
CMT	carbon microtube
CNF	carbon nanofiber
CNP	carbon nanope
CNT	carbon nanotube
CT	charge transport
CV	cyclic voltammetry
D	donor orbital
DA	dopamine
DBAE	2-(dibutylamino)ethanol
DC	direct current
DCM	dichloromethane
DDT	dodecanethiol
DMSO	dimethylsulfoxide
DNA	deoxyribonucleic acid
dsDNA	double-stranded DNA
ECL	electrogenerated chemiluminescence
EDOT	3,4-ethylenedioxythiophene
EDP	electrophoretic deposition paint
EDX	energy dispersive X-ray spectroscopy
EM	electromagnetic
EOF	electroosmotic flow
e-papers	electronic papers
EPF	electrophoretic flow
ESEM	environmental scanning electron microscope
ET	electron transfer
FEEM	fluorescence-enabled electrochemical microscopy

Abbreviations

Abbreviation	Meaning
GC	glassy carbon
GDH	glucose dehydrogenase
GOx	glucose oxidase
IBED	indirect bipolar electrodeposition
ICEP	induced charge electrophoresis
JP	Janus particle
MCP	microchannel plate
MOON	modulated optical nanoprobe
MPTS ³⁻	8-methoxypyrene-1,3,6-trisulfonic acid
MRI	magnetic resonance imaging
MWCNT	multi-walled carbon nanotube
NAD ⁺	nicotinamide adenine dinucleotide
NP	nanoparticle
ODN	oligonucleotide conjugate
ODT	octadecanethiol
PANI	polyaniline
PB	Prussian Blue
PBD	polybutadiene
PDMS	polydimethylsiloxane
PE	polyethylene
PEDOT	poly(3,4-ethylenedioxythiophene)
PEG	poly(ethylene glycol)
PMAA	poly(methacrylic acid)
PMMA	poly(methyl methacrylate)
PMT	poly(3-methylthiophene)
PP	polypropylene
PPy	polypyrrole
PS	polystyrene
PTFE	polytetrafluoroethylene
PTS ⁴⁻	1,3,6,8-pyrene tetrasulfonic acid
SA	self-assembly
SAM	self- assembled monolayer
SCBE	spatially coupled bipolar electrochemistry
SEM	scanning electron microscopy
STM	scanning tunneling microscopy
SWCNT	single walled carbon nanotube
TEM	transmission electron microscopy
TPrA	tripropylamine
XPS	X-ray photoelectron spectroscopy
XRD	X-ray diffraction

Preface

Bipolar electrochemistry is a “wireless” technique that deals with the application of electric fields on isolated conducting substrates to break their surface symmetry. The concept itself is not new, however, it has recently emerged as a novel and easy method for different purposes. The aim of the present thesis is to further develop the concept of bipolar electrochemistry and its applications especially for materials science and biological systems.

Chapter one is dedicated to an introduction to bipolar electrochemistry, its principles and the traditional and recent applications of the technique in different fields like electronics, electroanalysis and electrodeposition processes.

The experimental part and the obtained results of the thesis will be presented in the following chapters. Application of bipolar electrochemistry in materials science will be demonstrated in chapter two with the bulk preparation of asymmetric particles. These objects are of great potential in many fields, and usually require interfaces during their fabrication process as we will briefly discuss. Various materials and substrates will be employed for bipolar electrodeposition using new bulk techniques, allowing a site-selectivity of the resulting deposit. The development of a setup will be presented which can be used for surface microstructuration of objects.

Chapter three addresses the progress in the frame of autonomous microswimmers. All the motors that have been reported in the literature need the generation of asymmetry as a key for the motion as we are going to discuss. Bipolar electrochemistry will be adapted to produce motion in two different ways. In the first one, the asymmetric particles that have been prepared in chapter two will be used as swimmers in the presence of a certain fuel. In other words bipolar electrochemistry plays an indirect role in this case. The second method depends on the direct use of the electric fields to drive isotropic objects. Levitation motion coupled with light emission will be generated using this method.

Bipolar electrochemistry can also be employed for studying biological systems as we will demonstrate in chapter four. DNA conductivity and charge transport which is of a great importance in various applications will be briefly discussed based on the work that has been described previously in this field. We will use different metal ions, playing the role of precursors for DNA mediated metal deposition, mixed together with DNA in a bipolar setup in order to investigate the electrical properties of DNA.

Chapter five includes a general summary and conclusion of what has been reported in this thesis, in addition to different possible perspectives in the fields of materials science, microswimmers and biological systems.

Chapter 1

Bipolar Electrochemistry

1.1. Introduction to Bipolar Electrochemistry

Bipolar electrochemistry is a technique based on the polarization of an isolated substrate, also called “bipolar electrode” (BP_e), under an external electric field.¹⁻³ Similar to conventional electrochemical systems, a BP_e can be any kind of material with sufficient conductivity regardless of the size and shape, however in bipolar electrochemistry no physical connection between the substrate and the power supply is required.⁴ In bipolar electrochemistry, the BP_e acts as an anode and a cathode that allows simultaneously oxidation and reduction reactions on the same substrate,⁵⁻⁶ contrary to conventional electrochemistry, where the cathode and the anode are physically separated. The BP_e behavior can be originated from the hybrid chemical composition of the object that promotes redox reactions such as in the case of self propelled bioelectrochemical motors.⁷ On the other hand (that is of interest to the present thesis) the bipolar behavior arises from the effect of an applied electric field on an object, in general chemically isotropic, which might induce electrochemical reactions in the presence of reactive species. This case of bipolar electrochemistry can be listed under either an open or a closed bipolar configuration⁴ that will be described in the two following sections.

For better understanding of the electrochemistry in bipolar configurations, let's first have a view on the redox reactions in a classic electrochemical cell with a three-electrode setup, which consists of a working, auxiliary and reference electrodes. The potential of the working electrode is controlled against a reference electrode using a potentiostat, this means controlling the energy of the electrons within the working electrode.⁸ The potential of the solution is at a floating value that depends on the composition of the solution in the absence of externally applied electric field.⁵ By driving the working electrode to more negative potentials (raising the energy of the electrons) than that of electroactive molecules in the solution, electrons may transfer from the electrode to reduce species in the solution (Figure 1.1a) inducing a cathodic current.⁸ Similarly, oxidation reactions occur when electrons transfer from the solutes in the solution to the electrode when the later has a significant lower potential than the solution (Figure 1.1b).⁸ Thus, in conventional electrochemistry the driving force of the redox reactions is directly controlled by tuning the potential of the working electrode that is connected to a power supply.

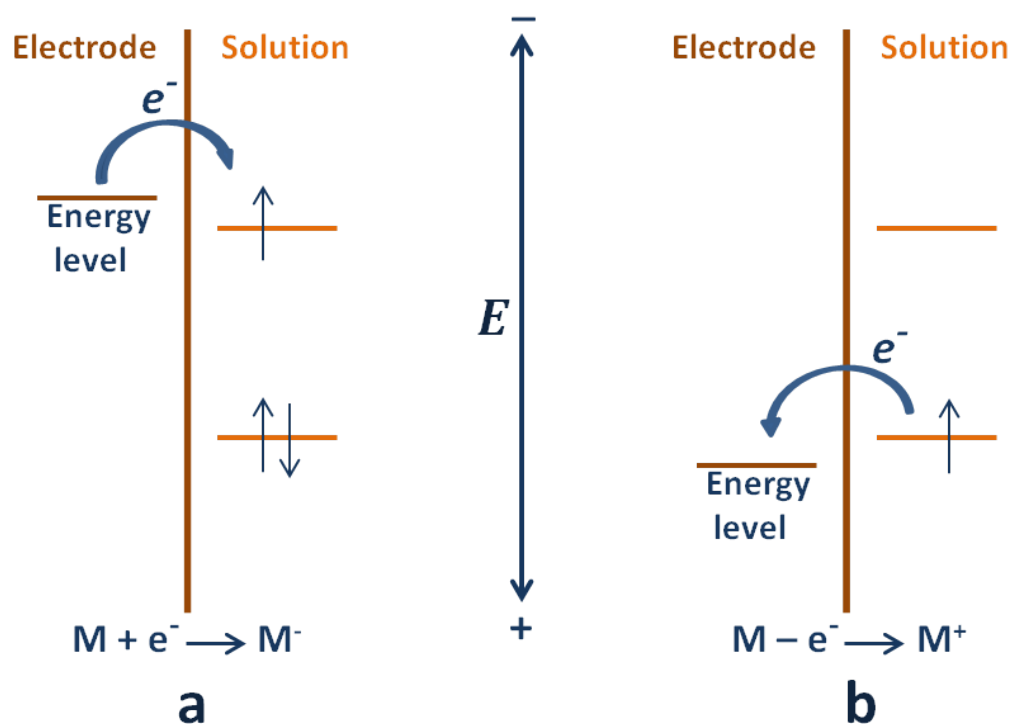


Figure 1.1 Representation of electron transfer for (a) reduction and (b) oxidation of a species (M) in solution. E , indicates the potential of the working electrode vs. a reference electrode. Inspired from Ref. (8).

1.2. The Open Configuration of Bipolar Electrochemistry

In the open bipolar configuration, the conductive substrate is suspended in an electrolytic solution between two feeder electrodes without direct physical connection between the substrate and the power supply (wireless manner), as illustrated in Figure 1.2.

In bipolar electrochemistry, the roles of the electrode and solution are different somehow from the conventional electrochemistry. A potential difference $E_{\text{appl}} = E_a - E_c$ (where E_a , E_c represents the potential of the anode and the cathode, respectively) is applied in the bipolar setup between the feeder electrodes that are spaced by a distance d . If we assume that the potential drop at the feeder electrode/solution interface and the distortion of the electric field by faradaic current at the feeder electrodes are negligible, then the applied potential E_{appl} drops linearly through the electrolytic solution. Therefore, the interfacial difference of potential between the substrate (an equipotential conductor) and the solution becomes the driving force for the bipolar electrochemical reactions. Then, the potential difference between the substrate and the solution is determined by the value of the electric field \mathcal{E} in the solution that is given by:

$$\mathcal{E} = \frac{E_a - E_c}{d} \quad (1.1)$$

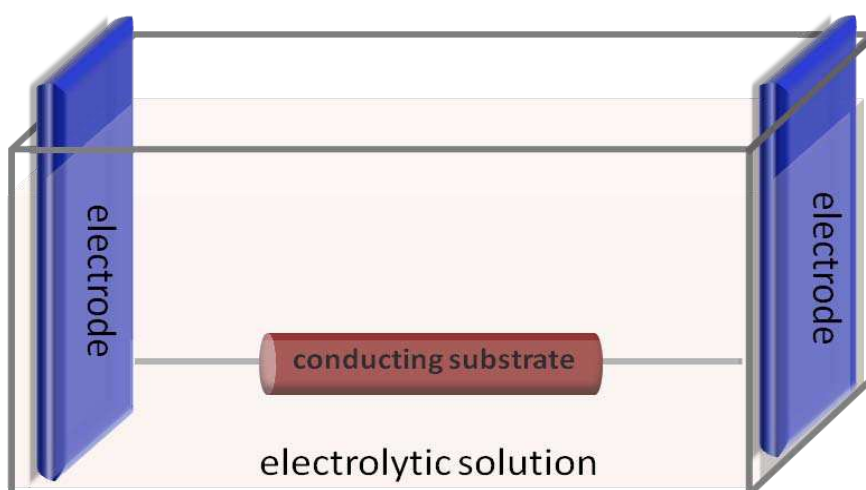


Figure1.2 Scheme of a conductive substrate positioned between two feeder electrodes in an electrolytic solution in the bipolar open configuration.

Figure 1.3 illustrates the potential distribution of the solution along a tubular (a), and a spherical (b) conductive substrate. As the electric field is applied, a polarization potential V is induced at the solution/substrate interface due to the potential difference between them. The surface of the substrate experiences a continuum of solution potentials ranging from V_c to V_a . Hence, the potential of the substrate floats, which means it is not controlled against a reference value, but rather will adjust to an equilibrium value (V_{sub}) situated between the solution potential over the first end (V_c), and the solution potential under the second end (V_a) of the substrate.⁹ At the position x_0 , the potential of the solution is equal to V_{sub} (so the driving force for the electrochemical reactions is equal to zero), thus dividing the electrode into a cathodic pole (δ^-) and an anodic pole (δ^+), where the $x < x_0$ or $x > x_0$, respectively.

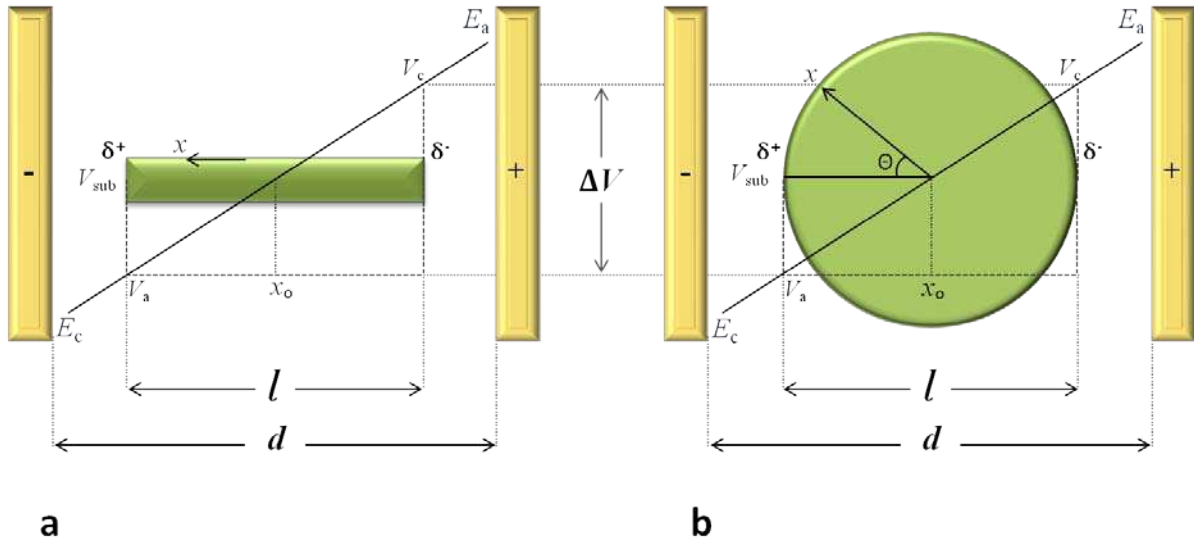


Figure 1.3 Illustrations for the polarization of a linear (a), and spherical (b) conductive substrates within the electric field in the open bipolar configuration.

Considering the electric field to be constant, the value of V varies linearly as a function of the position x along the solution/substrate interface, and can be calculated as:

$$V_{(x)} = \mathcal{E}(x - x_0) \quad (1.2)$$

for a tubular substrate (Figure 1.3a) and:

$$V_{(x)} = \mathcal{E}(x - x_0) \cos \Theta \quad (1.3)$$

for a spherical substrate (Figure 1.3b). Accordingly, V increases from the x_0 location towards both ends of the substrate as shown in Figure 1.3a and b, and the maximum polarization

potential difference (ΔV) occurs at the extremities of the substrate. With l being the length (or diameter) of the substrate, ΔV is:

$$\Delta V = \mathcal{E}l \quad (1.4)$$

The value of ΔV indicates the overall polarization at the ends of the substrate. Now, let us assume the presence of electroactive species, R_{ed} and O_x' in the described system, which can undergo the following reactions:



and



n and n' represent the number of electrons involved in each half-reactions with E_1° and E_2° being the standard potential for the redox couples R_{ed}/O_x and R_{ed}'/O_x' , respectively. The minimum potential value ΔV_{min} , required to provoke reactions (1.5) and (1.6) at both extremities of the polarized substrate has to be, in first approximation, at least equal to the difference between the standard potentials of the two involved redox couples:

$$\Delta V_{min} = E_1^\circ - E_2^\circ \quad (1.7)$$

Obviously, if the applied electric field induced a sufficient polarization over a given size of a conductive substrate (eq. 1.4), the case $\Delta V > \Delta V_{min}$, then the electrochemical reactions (1.5) and (1.6) will occur at both ends of the substrate at the same time (Figure 1.4). The oxidation reaction (1.5) happens at the anodic pole coupled with the reduction reaction (1.6) at the cathodic pole to ensure that electroneutrality is maintained within the substrate.

Thus, ΔV_{min} can be considered as the polarization potential threshold value that should be overcome before the conductive substrate behaves as a BP_e , promoting oxidation/reduction reactions on its interface. As ΔV_{min} is a constant value for two given half-reactions (eq. 1.7), then the first two important parameters that influence the efficiency of the bipolar reaction are, the length l of the BP_e and the applied electric field value \mathcal{E} .

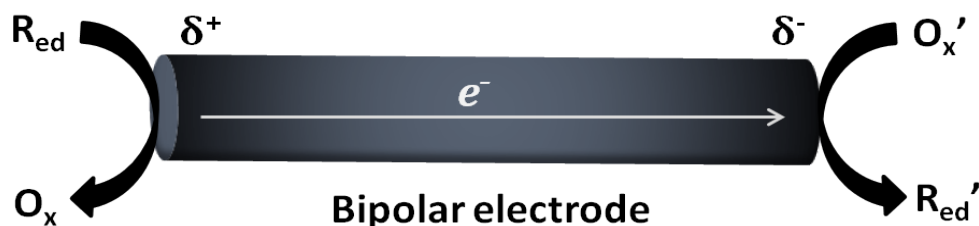


Figure 1.4 Scheme of a tubular conductive substrate acting as a bipolar electrode for redox reactions when exposed to a sufficient external electric field in the electrolytic solution.

The effect of these variables has been recently reported by our group in a bipolar setup applied to the modification of a graphite bar with a silver deposition in a 1 mM AgNO_3 aqueous solution.¹⁰ First the effect of different \mathcal{E} values on the bipolar electrodeposition of silver on several graphite rods, having the same length l , was investigated. At a relatively low \mathcal{E} value, when the polarization potential difference is inferior to the thermodynamic threshold ΔV_{\min} for silver reduction, no deposition was observed.¹⁰ Above this threshold, silver deposits were formed at the cathodic pole of the rods, and the deposit length increased linearly with the applied field up to a certain value, where the cathodic and anodic areas reach their maximum at the position x_0 .¹⁰ For the second set of experiments, the \mathcal{E} value was fixed, and graphite rods with different lengths were employed for the bipolar electrodeposition. Again, when the rod was too short to induce the sufficient polarization ($\Delta V < \Delta V_{\min}$), no silver was observed on the rod, but after this threshold was reached, the length of the deposit increased linearly with the length of the rod.¹⁰

For studying the potential gradient at the BP_e , hence, the reactivity at the extremities of the polarized interface, a theoretical model has been reported by Duval *et al.*¹⁴ The bipolar behavior of metallic surfaces in a flow-cell setup used for electrokinetic measurements was computed and simulations for the potential and current density distribution along the BP_e were performed in various model conditions. As a result, this work has shown that the current density peaks at the edges and the slope of the potential profile decreases at the middle of BP_e .¹¹ Ulrich *et al.* have reported a measure of the potential and current distribution at the electrolyte/ BP_e interface.¹² The authors presented an experimental method for measuring potential and current density on a gold BP_e for different \mathcal{E} values.¹² The approach involved estimating the potential difference between the BP_e and a reference electrode in the solution placed at different positions above the gold surface. The current density was also evaluated

being proportional to the voltage measured between two closely positioned reference electrodes in the vicinity of the BP_e.¹² Plotting the calculated current densities and solution potentials for different positions along the BP_e, displayed a good agreement of the results with the simulation obtained from the conductivity model, a longer gold surface exhibiting a higher global polarization.¹²

From eq. 1.4 and the presented works, one can conclude that a longer BP_e will require a less important \mathcal{E} value than a smaller one to exhibit a sufficient reactivity towards the electrochemical reactions at the poles of the BP_e. For a better estimation of the \mathcal{E} value required to achieve a certain bipolar reaction, the difference of standard potentials of the two involved redox couples (ΔV_{\min}) can be evaluated by recording a cyclic voltammetry (CV) using the same material than the BP_e as a working electrode. As the bipolar experiment is far from standard conditions that have been used to calculate ΔV_{\min} , CV leads to a more realistic value.

The composition of the electrolytic solution is another essential parameter that affects the electrochemistry on the isolated BP_e. In the bipolar experiment, the total current flowing in the cell i_t (Fig. 1.5a) can be carried either through the solution via the migration of ions; this one called by-pass current i_{bs} , or through the BP_e via the electrons generated by faradaic processes (Fig. 1.4), called faradaic current i_{bpe} , then,

$$i_t = i_{bpe} + i_{bs} \quad (1.8)$$

Comparing the case with an equivalent circuit (Fig. 1.5b), it is clear that the relative resistance of the solution R_{bs} , and also the one from the BP_e, R_{bpe} , have a high impact on the relative current distribution between them, and they are correlated as following:⁵

$$\frac{i_{bpe}}{i_t} = 1 - \frac{i_{bs}}{i_t} = \frac{R_{bs}}{R_{bpe} + R_{bs}} \quad (1.9)$$

Eq. 1.9 predicts that using a solution with a higher resistance results in increasing the current passing through the BP_e, a point that we have shown previously,¹⁰ thus reducing the value of the by-pass current i_{bs} .

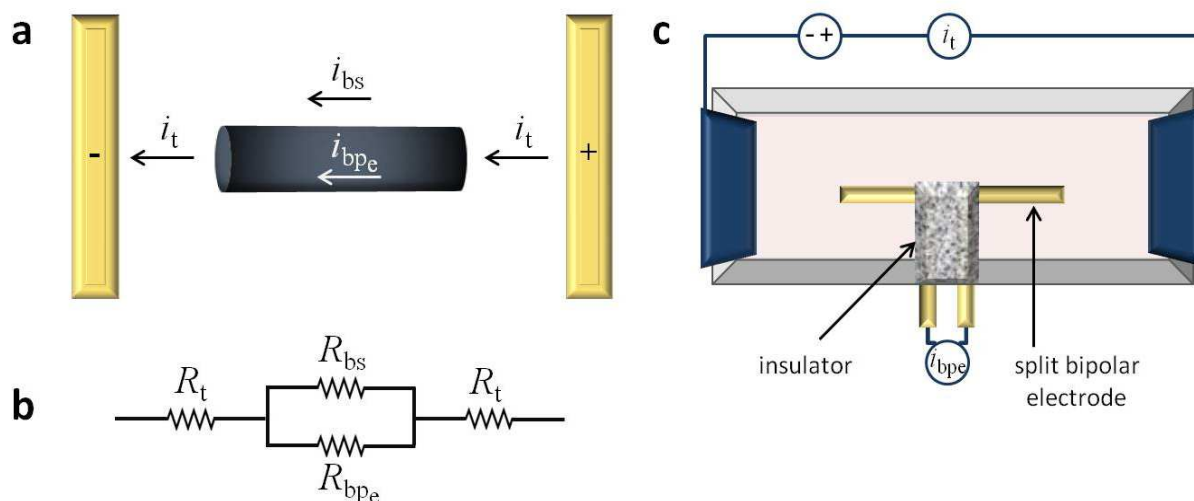


Figure 1.5 Illustration of the current flowing through the bipolar cell during the experiment (a), and the equivalent circuit (b); R_t : the total resistance includes R_{bs} and R_{bpe} , c) Scheme of a split bipolar electrode usually used to measure the faradaic current i_{bpe} through the BP_e (top view).

The presence of the by-pass current i_{bs} is the main disadvantage of the bipolar systems, especially in the case of bipolar electrochemical reactors,¹³⁻¹⁴ which leads to a faradaic efficiency loss and nonhomogenous potential and current distributions. Therefore many efforts have been devoted for providing theoretical and experimental models depending on different strategies for estimating and minimizing the value of i_{bs} .^{13, 15-18} Kuhn *et al.* briefly reviewed the origins, means of measurement and the importance of reducing the i_{bs} .¹⁹ By using a split BP_e for direct determination of i_{bpe} , it was possible to calculate i_{bs} .^{10, 20} Fig. 1.5c shows a simple scheme of this electrode which consists of two conductive separated wires folded by 90° with one part inside and the other outside of the cell. The split BP_e will experience the same polarization than a continuous wire having a length equal to the distance between the immersed ends in the solution.¹⁰ The i_{bpe} , and consequently i_{bs} (eq. 1.8), was directly detected by connecting the outer parts of the wires with an ammeter, and this allowed the measurements in different experimental conditions which is useful for investigating the optimum conditions for the bipolar process.¹⁰ In this setup, the effect of \mathcal{E} on i_t and i_{bpe} was observed, i_{bpe} increased linearly with \mathcal{E} . The total current i_t displayed a linear response with the applied \mathcal{E} as it is controlled by the cell resistance in the absence of the split BP_e,¹⁰ however the response was more important in the present of the BP_e when a sufficient \mathcal{E} was applied, as the BP_e provides an easier current pathway.^{10, 21} Finally the BP_e with a smaller

diameter showed a lower i_{bpe} , as its resistance R_{bpe} increased.¹⁰ Inagi *et al.* measured the current passing through a split ITO bipolar plate in a U-type cell.²² The two parts of the BP_e were separated by an insulating material and an ammeter was connected between them, after applying a constant field between the driving electrodes, the current was then monitored for 30 s.²²

Another point which needs to be considered is the local decrease of the electric field above the BP_e ‘faradaic depolarization’ as defined by Duval and coworkers.²³ As a fraction of the i_t passes through the BP_e, a nonuniform distribution of the electric field will be generated due to concentration gradients along the BP_e. This results in a deviation of the solution potential drop from linearity for which a theoretical model was provided.²⁴

The last important aspect is the kinetics of the faradaic current over the BP_e. As we mentioned in the beginning of this section, the BP_e is usually divided into a cathodic and an anodic pole through the x_0 position, thus this location is of interest because it provides kinetics information about the involved electrochemical reactions. Several models have been proposed for the investigation of the current profile along the BP_e. In 1985, Fleischman *et al.* treated the case of bipolar electrolysis of suspensions of spherical ultramicroelectrodes.²⁵ Current distribution on a single sphere in an electrolytic cell was investigated in 1991 by Yen *et al.*²⁶ A semiempirical prediction of current flow through a BP_e,⁹ and an analytical study of a metallic BP_e double-layer in the presence of a reversible redox couple²⁷ was proposed in the domain of streaming potential as well.

Duval *et al.* proposed a delicate mathematical model to describe the current profile over a macroscopic planar surface, the model was confirmed experimentally by following the bipolar dissolution of aluminum wafers.²⁸ The concept is based on mixed potential and Butler-Volmer kinetics to calculate the current density along the Al wafer, assuming irreversible electrochemical reactions that are electron-transfer limited and a homogeneous electric field around BP_e.²⁸ This model, in some cases, is far from real experimental situation, especially when dealing with strong electric fields and/or big BP_e, however, it provides a straightforward method for qualitative understanding of the faradaic current along the BP_e.¹⁰ Depending on this model we can clarify the x_0 position by proposing a BP_e immersed in a solution of electroactive species R_{ed} and O_x, which can undergo the oxidation (1.5) and reduction (1.6) reactions, with a rate of r ($r = n(1-\alpha)$), r' ($r' = n'\alpha'$) respectively, (n : the number of exchanged electrons, α : the charge transfer coefficient). Considering the reactions

to be electron-transfer limited, Butler-Volmer relation should be applied, and the current densities at the anodic pole j and cathodic pole j' can be described respectively as:

$$j_{(V)} = j_0 \exp \left[r \frac{F}{RT} (V - E_1^\circ) \right] \quad (1.10)$$

$$j'_{(V)} = j_0' \exp \left[-r' \frac{F}{RT} (V - E_2^\circ) \right] \quad (1.11)$$

j_0 and j_0' being the apparent exchange current densities of reaction (1.5) and (1.6), respectively, F Faraday constant, R the ideal gas constant, T the temperature, then x_0 is the position on the BP_e for which the net faradaic current is zero.

Since there is no accumulation of charge in the BP_e, the total anodic and cathodic current, i and i' , respectively, have to obey:

$$i = -i' = i_{\text{bpe}} \quad (1.12)$$

From these equations we can conclude that the x_0 position (the frontier between the anodic and cathodic domains of the BP_e) depends among others on r , r' , j_0 and j_0' .²⁸ When $r = r'$ and $j_0 = j_0'$ the position of x_0 will be at the middle of the BP_e, but for all other cases it will shift to another location.

1.3. The Closed Configuration of Bipolar Electrochemistry

Unlike the open setup, the closed bipolar configuration requires the BP_e to be constructed within the structure of the cell and between the feeder electrodes in such a way that separates the electrolytic solution in two different compartments³ (Figure 1.6).²⁹ In this case the electrochemical current would pass through the BP_e and can be directly measured due to the absence of the ionic current path, providing information on the rates of the faradaic processes.²⁹ Another important aspect is the potential across the substrate being equal to the applied potential via the feeder electrodes, thus the voltage is dropped almost entirely at the solution interface adjacent to both ends of the substrate.³⁰ This feature increases the probability to use variety of substrates as a BP_e, no matter the material³¹ and the geometry,²⁹ as the bipolar reactions require a relatively low electric fields within this cell design. This represents another difference compared to the open configuration because it is size-independent.

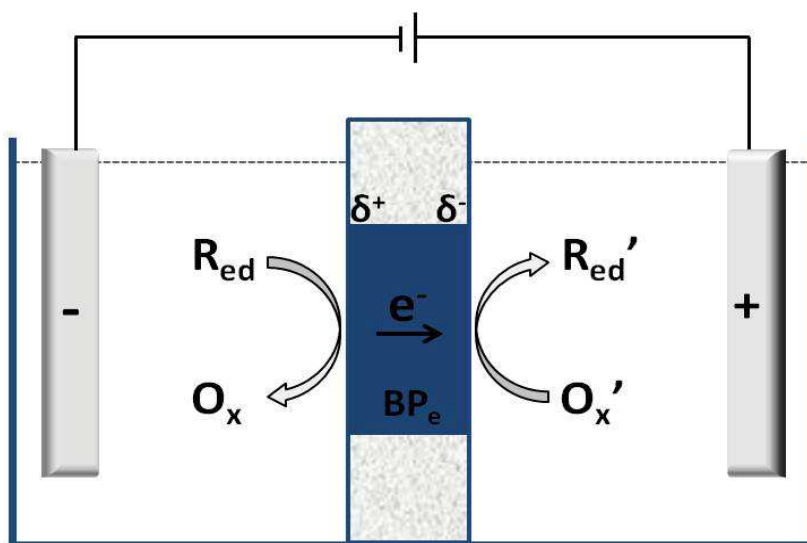


Figure 1.6 Scheme of a closed bipolar electrochemical cell inspired from Ref. (29).

The closed bipolar system was adapted recently by Cox *et al.* to quantitatively describe the steady-state voltammetry of closed bipolar microelectrodes. In this study, they fabricated metal microelectrodes by encapsulating a wire in a glass capillary,²⁹ as well as carbon fiber microelectrodes (CF_e).²⁹⁻³⁰ The bipolar response had the same, but slower, limiting current comparing to its voltammetric response in a conventional two-electrode setup. The slower response in the bipolar setup was attributed to the additional voltage/energy requirement to

drive the faradaic reactions at the coupling poles.²⁹ The improvement in the voltammetric response of such closed microelectrodes might be of great interest, especially the CF_e which are routinely used for the quantitative analysis in biological systems.³² The closed bipolar cell was employed by Plana *et al.* in order to investigate electroless deposition,³³ as well as bimolecular electron transfer (ET) under the potential control.³⁴

1.4. Traditional and Macroscopic Applications of Bipolar Electrochemistry

1.4.1. Bipolar Plate Electrodes

Bipolar plate electrodes are conductive materials inserted between two feeder electrodes in the presence of a suitable electrolyte. The bipolar plates have been used widely in electrolysis cells and batteries technology.

The electrolytic cells with bipolar plates have the advantage of a compact structure, due to the fact that the unit cells are connected in series, thus saving space and facilitating the electricity supply.³⁵⁻³⁶ In this area, the bipolar plate electrodes have been used for fused salt electrolysis for light metal production,³⁷⁻³⁸ water electrolysis,³⁹ metal electroplating,⁴⁰ dissolution of iron in water,⁴¹ and to analyze the mass transfer during Cu (II) electrodeposition,⁴²

The bipolar plates are stacked together in bipolar batteries, as a negative electrode; a positive electrode and a separator disposed between them. The separator is electrically insulating the electrodes from one another, and an electrolyte is filled within at least one of the negative electrode, positive electrode and the separator.⁴³ Because of a much shorter electrical bath by comparison with monopolar batteries, the power loss due to ohmic drop in the circuit is minimized, and the volume of the battery is also reduced through elimination of the outer circuit materials, such as straps, posts and tabs.⁴⁴⁻⁴⁵ The bipolar plates have been adapted for a great diversity of bipolar batteries such as nickel-metal hybrid,⁴⁶⁻⁴⁸ vanadium redox flow,⁴⁹⁻⁵⁰ lithium/composite polymer⁵¹⁻⁵² and lead-acid batteries,⁵³⁻⁵⁵ with several designs of construction.⁵⁶⁻⁵⁸

1.4.2. Study of Corrosion

The anodic dissolution of a metallic BP_e by an oxidation reaction has been adapted for several applications. The dissolution of centimeter-sized aluminum wafers under the influence of an external electric field was followed visually by Duval *et al.* in order to study the current distribution along the Al surface.²⁸ At a relatively low \mathcal{E} values, the current increased linearly with the applied field, showing the ohmic contribution of the cell. Beyond a certain threshold value of \mathcal{E} , the current increased exponentially through the cell due to the faradaic processes occurring at the BP_e interfaces, water reduction at the cathodic pole coupled with aluminum oxidation at the anodic pole. The wafer continued to dissolve until a limit where the ΔV_{\max} became insufficient as it depends on the wafer length (eq. 1.4), then the process stopped.²⁸ The dissolution of metals by bipolar electrochemistry has been proposed for industrial applications for the removal of fluoride from water using aluminum BP_e,⁵⁹⁻⁶⁰ and more recently for analytical applications.⁶¹

On the other hand, the polarization of metals in the electric field can give suitable information about the resistivity of the metals towards corrosion. The measurement of polarization resistance is a useful and widely used technique for the evaluation of corrosion rate, but requires a direct physical contact with the BP_e. A contact-less electrochemical measurement of the corrosion of a metallic BP_e immersed in an electrolytic medium was reported by Keddam *et al.*⁶² The investigation was done by numerical computation of the alternating current (AC) and potential fields and the feature has been later compared to the experimental data obtained with impedance spectroscopy with a four-electrode setup.⁶² The technique was employed to assess the polarization resistance of carbon steel in various electrolytes including mortar,⁶²⁻⁶³ and gave results very close to those obtained using the traditional 3-electrode method, where the BP_e was physically connected. Andrade *et al.* studied the phenomenon as well on a BP_e under DC conditions.⁶⁴ Very recently, Björefors and coworkers adapted the concept for high-throughput corrosion screening on single stainless steel samples which was combined with a rapid image analysis.⁶⁵ This new contact-less technique might promote new sensors for corrosion rate assessment.

1.5. Recent Micro- and Nano Applications of Bipolar Electrochemistry

1.5.1. Fabrication of Electronic Devices

The construction of electric paths is a key element in the fabrication of electronic devices, and one important application of bipolar electrochemistry that has been reported by Bradley *et al.* in 1997 and later.⁶⁶⁻⁷³ Indeed, bipolar electrochemistry is an appealing alternative to other industrial techniques such as photolithography for making electrical contacts especially in three-dimensional microcircuits. The process consists of applying an electric field in a parallel way with respect to the alignment of two millimeter-sized copper particles immersed in pure water.⁶⁷ Each copper particle acts as a BP_e where reduction of water occurs at the cathodic pole and oxidation of copper occurs at the anodic pole, leading to a local increase of copper ions concentration in the solution between the particles. These ions migrate to the cathodic pole of the neighboring particle where they experience a reduction into metallic copper (Figure 1.7a). The result is the formation of a dendritic electric wire which grows towards the nearest point on the second particle's surface. When the contact is made, there is no anymore a potential difference between both particles and the electrochemical processes stop (Figure 1.7b).⁶⁷ This method was called spatially coupled bipolar electrochemistry (SCBE),⁶⁸ and was followed by electroless deposition in order to increase the solidity of the wire.⁶⁹ The technique was also downscaled, using organic solvents that allowed the application of higher electric fields, to micro-and sub-micrometer scale of copper particles⁷⁰ and silver substrates,⁷¹ respectively. The later showed the practical limitation of SCBE for Ag to be in the range of few hundreds of nanometer; the limitation being related to the width of the growing wire, which reached a lower limit of about 200 nm.⁷¹ The programmed SCBE on commercial circuit boards allowed illumination of light-emitting diodes,⁷² and in the same field, fabricating of diodes using copper rings with doped silicon in between was equally possible by SCBE.⁷³

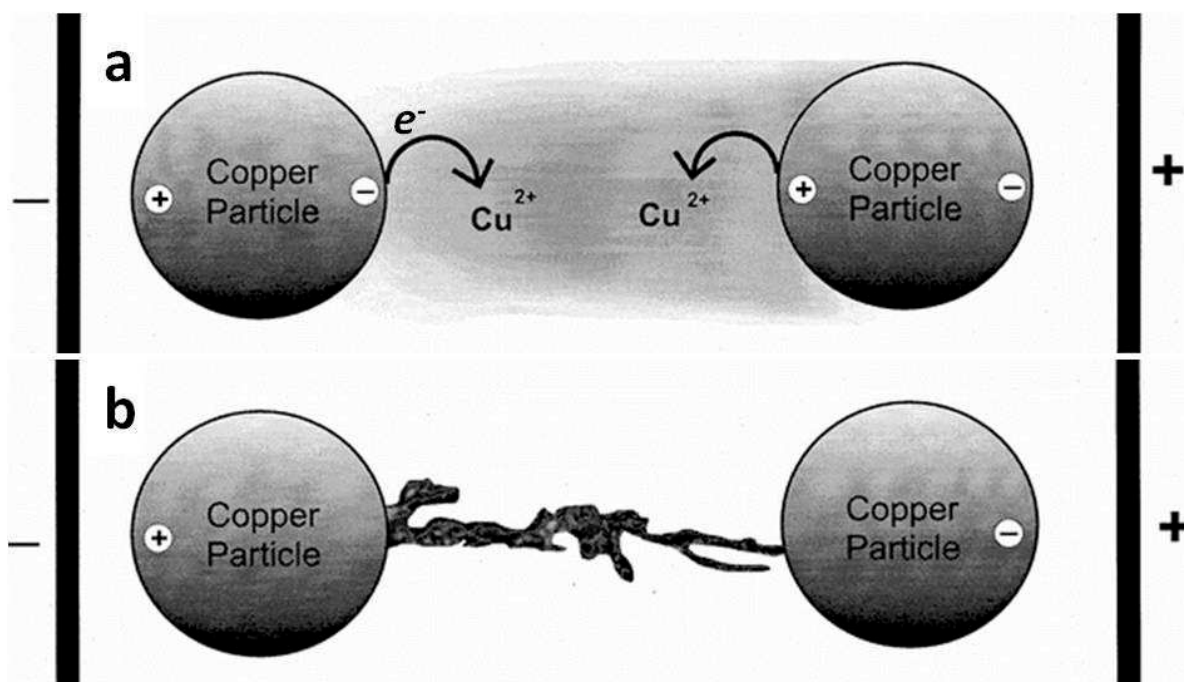


Figure 1.7 Schematic illustrations for wire formation between two copper particles under bipolar conditions. a) Illustration of SCBE mechanism on copper particles. b) When the wire reaches the particle on the right, electrical contact is made. Both adapted from Ref. (67).

In the frame of miniaturization of electronics, the manufacturing of microelectrochemical devices that mimic some functions of solid-state circuit components such as diodes is attracting attention.⁷⁴ The principles of bipolar electrochemistry were exploited by Chang *et al.* for the operation of individual and multiple microelectrochemical logic gates and circuits, respectively.⁷⁵ The integrated circuits into a single microfluidic channel, enabled the design of AND, OR, NOR, and NAND logic gates that can perform parallel functions. The inputs for these systems are simple voltage sources, and the output is an optical signal arising from electrogenerated chemiluminescence (ECL). These systems could provide on-chip data processing functions for lab-on-a-chip devices.⁷⁵

1.5.2. Electroanalytical Purposes

1.5.2.1. Concentration and Separation of Analytes in Microfluidic Systems

Concentration enrichment or preconcentration is often required prior to separation and detection in order to increase the sensitivity of the techniques. Capillary electrophoresis (CE) represents one of the widely used separation technique that depends on applying high electric fields, thus provides suitable conditions for bipolar electrochemistry experiments. In traditional electrophoresis, electrically charged analytes move in a conductive liquid medium under the influence of an electric field. This movement is directed by the action of two forces; electroosmotic flow (EOF) that drives positive and negative ions in the same direction, and electrophoretic flow (EPF) which control the direction of ions through the migration. A development in concentration enrichment by CE in the presence of BP_e has been explored recently.

Yeung and coworkers reported for the first time the use of BP_e in a CE setup for the enrichment of analyte.⁷⁶ In this experiment, they inserted a Pt wire into a fused-silica capillary together with the analytes (fluorescent derivatives) and the CE experiment was run using fluorescence detection. They attributed the enrichment to the pH gradient generated by electrolysis of water at the Pt wire extremities, thus leading to an acid gradient at the anodic pole coupled with a basic gradient at the cathodic pole.⁷⁶ The pH gradient instantaneously changed the local EOF but more importantly the charge on the analytes and consequently, its electrophoretic mobility; resulting in their accumulation close to the ends of the BP_e.⁷⁶ Thus the mechanism is limited to a tracer molecule that is a weak acid and has a pK_a close to the pH of the buffer.⁷⁷

Recently, Crooks and coworkers reported a new concentration and separation mechanism that have been developed intensively by them later.^{5, 77-86} The method is called bipolar electrode focusing (BEF) and it takes advantage of the extended electric field gradient formed at the edge of a BP_e in a buffer solution.⁷⁷ In this setup, a continuous or split gold BP_e is placed into a polydimethylsiloxane (PDMS)/glass microfluidic channel filled with the analyte in a low ionic strength buffer. In the first experiments, an anionic fluorescent tracer, boron-dipyrromethenedisulfonate (BODIPY disulfonate) in Tris-HCl buffer, was put in the

microchannel and a potential was applied between two platinum electrodes in the external compartments to generate an electric field within the channel. Electrokinetic transport of the tracer was captured with a microscope, showing its accumulation near to the cathodic pole of the gold BP_e.⁷⁷ This data could not be attributed to the pH-gradient mechanism proposed by Yeung and coworkers,⁷⁶ as the tracer (BODIPY disulfonate) is strongly acidic with a pK_a far from the pH of the Tris buffer. In fact, water electrolysis at the ends of the BP_e leads to the neutralization of the buffer cation (TrisH⁺) by OH⁻ generated at the cathodic pole of the BP_e. This reaction results in a region of low conductivity and hence a local increase of the electric field at the cathodic pole, as demonstrated by simulation⁷⁷⁻⁷⁸ and revealed experimentally.⁷⁹ The tracer flow through the channel, which is dominated by EOF (from the anodic to the cathodic part of the channel), will slow down when getting closer to the cathodic pole of the BP_e due to the opposite EPF. Enrichment occurs in this particular segment at a unique position where BODIPY molecules tend to focus as the bulk EOF is offset by the increase in EPF (Figure 1.8a).⁷⁸ Depending on the difference in the electrophoretic mobility of the analytes, it was possible by this technique to separate BODIPY disulfonate (BODIPY²⁻), 8-methoxypyrene-1,3,6-trisulfonic acid (MPTS³⁻) and 1,3,6,8-pyrene tetrasulfonic acid (PTS⁴⁻) anionic dyes from their mixture at different axial locations in the microchannel (Figure 1.8b).⁸⁰ In addition, the use of BP_e was demonstrated for depletion and membraneless filtration.⁸³

The fundamental parameters that affect the focusing process such as buffer concentration, flow rate, applied field strength, and the effect of a neutral, polymeric coating on the microchannel walls were investigated in details.⁸¹ When enrichment was initiated by a split BP_e, it was possible to simultaneously monitor the location of the anionic enriched band using both fluorescence microscopy and faradaic current i_{bpe} measurement by connecting the two poles to an ammeter,⁸² and to quantitatively measure the electric field gradient at the vicinity of the BP_e.⁷⁹ This provides insight into the underlying principles of electrochemical detection. The dual-channel design which decouples the potential drop across the BP_e from the applied voltage, allows a higher driving potential and a more rapid enrichment (71-fold/s) of anions.⁸⁴ By adjusting the direction⁸⁵ and magnitude of the EOF within the channel device and the type of buffer,⁸⁶ enrichment of cations⁸⁵ as well as separation of cations and anions was successfully achieved.⁸⁶

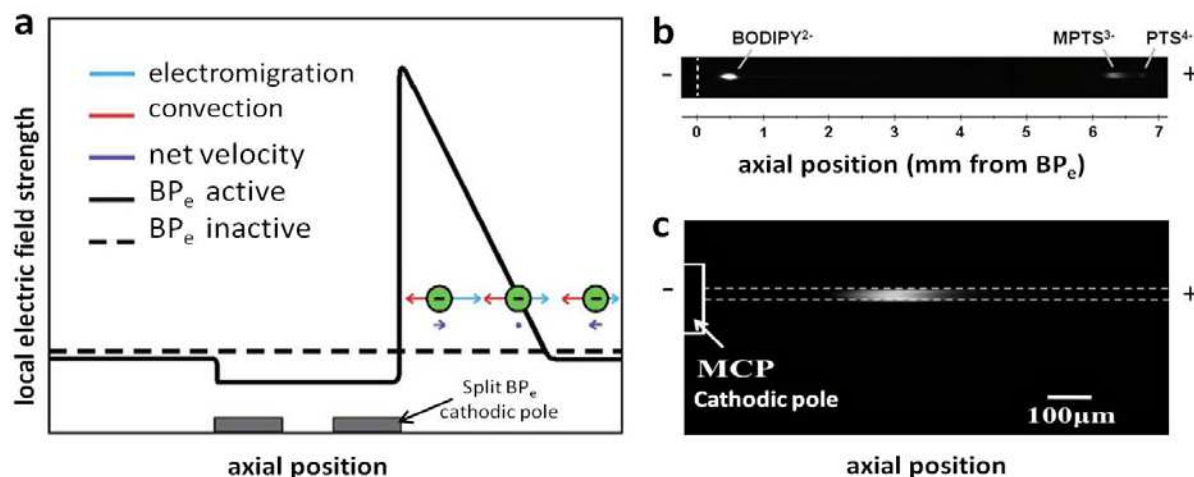


Figure 1.8 a) Schematic representation of the local axial electric field adjacent to the cathodic pole of a split BP_e when the BP_e is active (black solid line) and inactive (dashed line). The net velocity vectors are shown at three locations for an anionic species under the combined forces of convection and electromigration; adapted from Ref. (84). b) Fluorescence micrograph (top view) showing separation of BODIPY²⁻, MPTS³⁻ and PTS⁴⁻ in 5 mM TRIS in a Pluronic-modified channel; reprinted from Ref. (80). c) Fluorescent micrograph of a typical band enrichment of FI²⁻ in a buffer of 1 mM Tris-HCl using the MCP as a BP_e; adapted from Ref. (87).

Cao *et al.* very recently adapted a microchannel plate (MCP), a high-porosity semiconductor glass membrane used as an electron multiplier in analytical/scientific instruments, as a highly effective 3D BP_e for electrokinetic focusing of anions in an electrolyte buffer. A remarkable rate of up to 175-fold/s, exceeding those reported for planar BP_e has been shown for the concentration of fluorescein (FI²⁻) in Tris-HCl buffer (Figure 1.8c).⁸⁷ The high-performance characteristics of MCP could be beneficial for the rapid enrichment and detection of charged biomarkers including DNA and proteins in bioanalytical microdevices.⁸⁷

1.5.2.2. Electrochemical Detection

The BP_e provide a suitable platform for detecting electroactive analytes in micro-devices such as capillary electrophoresis, where high electric fields are required. Klett and Nyholm established a potentiostat-less detection scheme for amperometric detection of electroactive species in CE.⁸⁸ In this study, the potential difference and current between two gold microbands positioned 10 μm apart, as a split BP_e connected externally to an ammeter, in the CE outlet was investigated. Different electric fields and concentrations of a redox couple

($\text{Fe}(\text{CN})_6^{4-}/\text{Fe}(\text{CN})_6^{3-}$) was employed. At a sufficient electric field, the oxidation/reduction reactions of this couple occurred at the microband extremities, and the current was proportional to the concentration of the redox couple, with a detection limit of 100 μM of the analytes.⁸⁸

The previous technique was adapted to a microfluidic channel by Nyholm group.⁸⁹ They used a micro-fabricated flow system containing an array of 20 gold microband electrodes. The applied potential difference between two gold microbands in a PDMS microchannel enabled the electrochemical detection of electroactive species such as ascorbic acid and $\text{Fe}(\text{CN})_6^{4-}$. The effect of the flow rate on the current was characterized and the obtained results were compared with simulations. As a result, the potential difference between the two microband electrodes was dependent on the external electric field strength and the distance between the electrodes in the electric field.⁸⁹ This means that the potential difference between two microband electrodes can be adjusted to enable the detection of different electroactive species merely by selecting the appropriate electrode pair in an array of microband electrodes. The obtained currents found to be proportional to the concentrations of the electroactive species in the flowing solution, and the detection of at least 50 μM of ascorbic acid for example was performed. As the analysis was possible to carry out anywhere within the channel without interference of the external electric field,⁸⁹ this electrochemical detection approach holds great promises for the future development of new inexpensive analytical portable devices, for example, chip-based CE.

1.5.2.3. Optical Detection Based on Electrodissolution of Bipolar Electrode

A new type of sensing platform based on bipolar electrochemistry has been reported by Crooks' group.^{61, 90-91} The method relies on the anodic electrodissolution of a metallic BP_e as an indicator of a cathodic electrochemical reaction, and due to the charge neutrality, the amount of the oxidized pole must correspond to the number of electrons transferred at the cathodic pole of the BP_e .^{61, 90-91} The first experiment was performed with a continuous and a split BP_e that have been coated with a silver layer at the anodic pole and then put in a microchannel. When the electric field was applied, the reduction of p-benzoquinone at the cathodic pole led to the Ag dissolution as shown in Figure 1.9a and b.⁹⁰ The degree of

shortening of the BP_e was found to be directly related to the amount of the charge passed through it, as monitored via an ammeter connected to the split BP_e.⁹⁰ Afterwards, the authors used the same general approach to construct enzyme based biosensors for detecting DNA. When the target DNA binds to the capture probe at the cathodic pole of the BP_e, it triggers the oxidation and dissolution of Ag metal present at the anodic pole,⁹⁰ and the sensitivity of the method can be controlled through the Ag layer thickness.

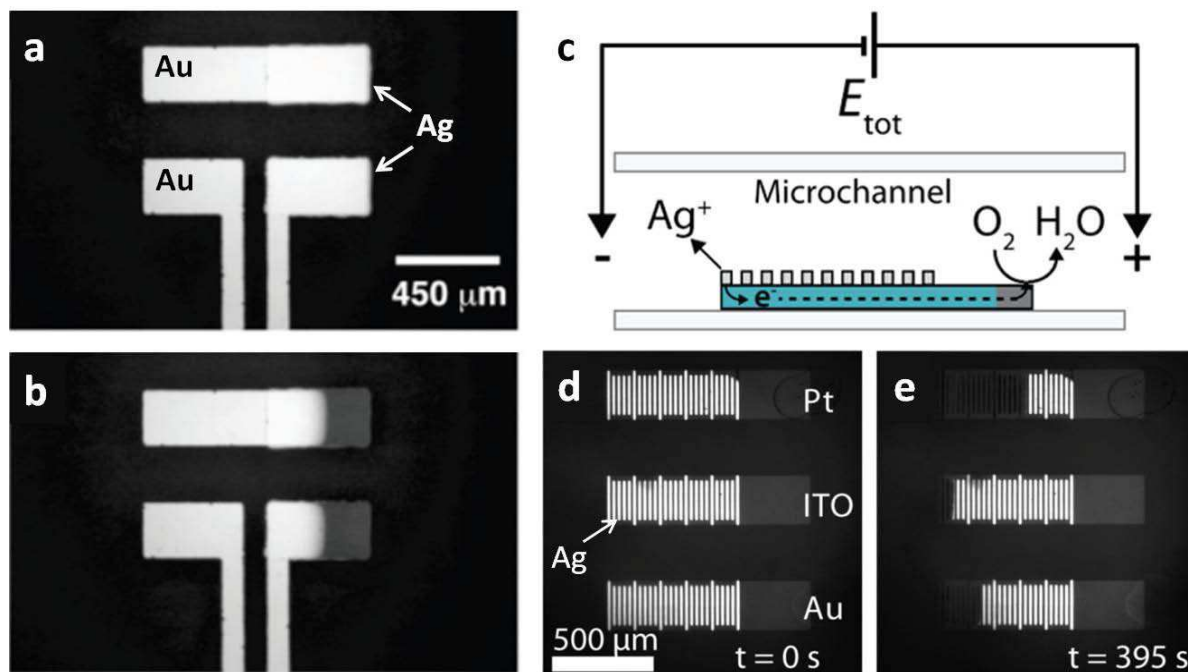


Figure 1.9 a, b) Optical micrographs of Ag-coated continuous and split BP_e in the microchannel (a) before and (b) after application of the electric field for 290 s in a solution of 1 mM p-benzoquinone in 0.1 M acetate buffer at pH 5.5. The dark regions of the electrodes in (b) correspond to dissolution of Ag, adapted from Ref. (90). c) Scheme of the sensing platform used for screening electrocatalysts of oxygen reduction reaction, adapted from Ref. (61). d, e) Optical micrographs of three BP_e that have been spotted at the cathodic pole with different electrocatalysts: the top with (Pt), the middle was naked (ITO), and the bottom with (Au) before (d) and after (e) 395 s exposure to the electric field, adapted from Ref. (61).

This technique was adapted as well for the rapid screening of electrocatalyst for oxygen reduction reaction as depicted in Figure 1.9c.⁶¹ The setup consisted of three microfabricated indium tin oxide (ITO) bipolar electrodes with parallel Ag microbands deposited at the anodic poles. The Ag microbands of each electrode were in electrical contact with one another via the underlying doped ITO contact. At the cathodic pole, the catalytic activity of dendrimer-encapsulated Pt, Au nanoparticles as well as bulk ITO (Figure 1.9d and e) was

investigated after applying a sufficient potential through the feeder electrodes for a certain time.⁶¹ The efficiency of the oxygen reduction reaction catalyst was then determined by counting the number of dissolved Ag microband electrodes; the more bands that dissolve, the better the catalyst.⁶¹

Further development of the previous setup has been achieved very recently by introducing a larger array of electrodes per sensing platform, and simultaneous screening of bimetallic electrocatalysts for the oxygen reduction reaction, which means more materials can be screened in each experiment.⁹¹ The metallic reporter was changed as well from Ag to chromium metal (Cr), as the later requires a more positive potential to oxidize, meaning that materials requiring low overpotentials for the oxygen reduction can be reliably evaluated.⁹¹ Among the three Pd-Au, Pd-Co, and Pd-W bimetallic electrocatalysts candidates, the Pd-Co was proved to be the most effective, and the dissolution of Cr microbands at the anodic pole was monitored by simple optical microscopy.⁹¹ Thus the method has the potential to provide quantitative information about electrocatalysts activity.

1.5.2.4. Optical Detection Based on Electrochemiluminescence

Electrogenerated chemiluminescence (also called Electrochemiluminescence, ECL) is the emission of light as a result of an electrochemical reaction, and proved to be very useful in analytical applications as a highly sensitive and selective method.⁹²⁻⁹³ ECL is usually generated by applying a potential on the electrode in the presence of both the luminophore and co-reactant. One of the best popular ECL system uses ruthenium tris bipyridyl $\text{Ru}(\text{bpy})_3^{2+}$ as the light-emitting species and an amine, such as tri-*n*-propylamine (TPrA) as a co-reactant. As a powerful analytical technique, ECL has been widely applied in the sensing devices based on BP_e .

Manz and co-workers first coupled ECL to bipolar electrochemistry as a signal reporting method.⁹⁴ It consists of a microfabricated U-shape platinum BP_e placed across the separation channel of electrokinetic chromatography. When the electric field was applied through the channel, one leg of the Pt electrode acted as a cathodic pole for the reduction of O_2 or H_2O , and the other leg acted as the anode where the oxidation of ruthenium complexes occurred.⁹⁴ ECL provoked at the anodic pole was detected for 10^{-6} M of ruthenium complexes. The indirect detection of three amino acids, that are ECL co-reactants, separated from a mixture

was also possible using this technique.⁹⁴ Similar protocol was adapted by Chen and coworkers to follow the decrease in ECL intensity for biosensing in cell analysis.⁹⁵⁻⁹⁶ Detection of the folate receptors level on a cell membrane was reported based on its high affinity to folic acid, the later had a quenching effect on the ECL intensity of the $\text{Ru}(\text{bpy})_3^{2+}/\text{TPrA}$ system which inhibited ECL signal at the anodic pole of the BP_e .⁹⁵ More recently, Jusková *et al.* presented a generation of ECL signal, based on square shaped gold BP_e with a size of 50 μm positioned inside a transparent fused silica capillary.⁹⁷ ECL reaction of the $\text{Ru}(\text{bpy})_3^{2+}$ with 2-(dibutylamino)ethanol (DBAE) as a co-reactant was selected as an indicator of the electrochemical reaction on freely moving and thus disposable BP_e ; the ECL signal being recorded using a photomultiplier tube as depicted in Figure 1.10a.⁹⁷

The described approach only took advantage of the anodic pole of the BP_e , thus limiting the detection to analytes that can actively interact with the ECL process. However, Crook's group demonstrated later that the presence of any electroactive analyte could be detected by taking advantage of both anodic and cathodic poles. In this setup, the analyte of interest is reduced at the cathodic pole of a single or arrays of BP_e located in microfluidic devices, and this faradaic reaction trigger light emission at the anodic pole by the corresponding oxidation of $\text{Ru}(\text{bpy})_3^{2+}$ and TPrA.⁹⁸ They also showed the effect of changing the shape of the anode and cathode relative to one another, on sensitivity enhancement of the method. Benzyl viologen was easily detected in the range of nM at an indium tin oxide (ITO) BP_e using this method.⁹⁸ A theoretical and experimental framework was reported for better understanding of ECL emission at bipolar electrodes.⁹ This concept has been utilized for microelectrochemical integrated circuits⁷⁵ (see section 1.4.3.), electric field mapping in the vicinity of a 2D- BP_e ,⁹⁹ and extracting kinetic information of the two redox couples at BP_e extremities.¹⁰⁰

The process was employed later to a large-scale microarray where 1000 individual BP_e could generate ECL at their anodic poles.¹⁰¹ Figure 1.10b shows a DNA sensing platform, it consists of 1 mm long Au microarray with the cathodic pole modified with DNA capture probes.¹⁰² The oxygen reduction at the cathodic pole was triggered by hybridization of target DNA labeled with Pt nanoparticles to immobilized capture DNA, accordingly, light was emitted from the anode, while a control experiment displayed no ECL signal without hybridization.¹⁰² Chang *et al.* demonstrated the use of a two channel sensor configuration that communicates between separated sensing and reporting microchannels via one or more BP_e (Figure 1.10c).¹⁰³ The sensing channel was filled with a conventional electroactive species, such as $\text{Fe}(\text{CN})_6^{3-}$, while the reporting channel with an ECL mixture, and the intensity of

ECL was found to be increased with $\text{Fe}(\text{CN})_6^{3-}$ concentration (Figure 1.10d and e) with a detection limit of 0.32 mM. This type of sensor allows to detect glycated hemoglobin and report its presence by ECL.¹⁰³ The key advantage of this configuration is the physical separation of the ECL reporting mixture and the solution containing the target, thus preventing chemical interference between the two channels.

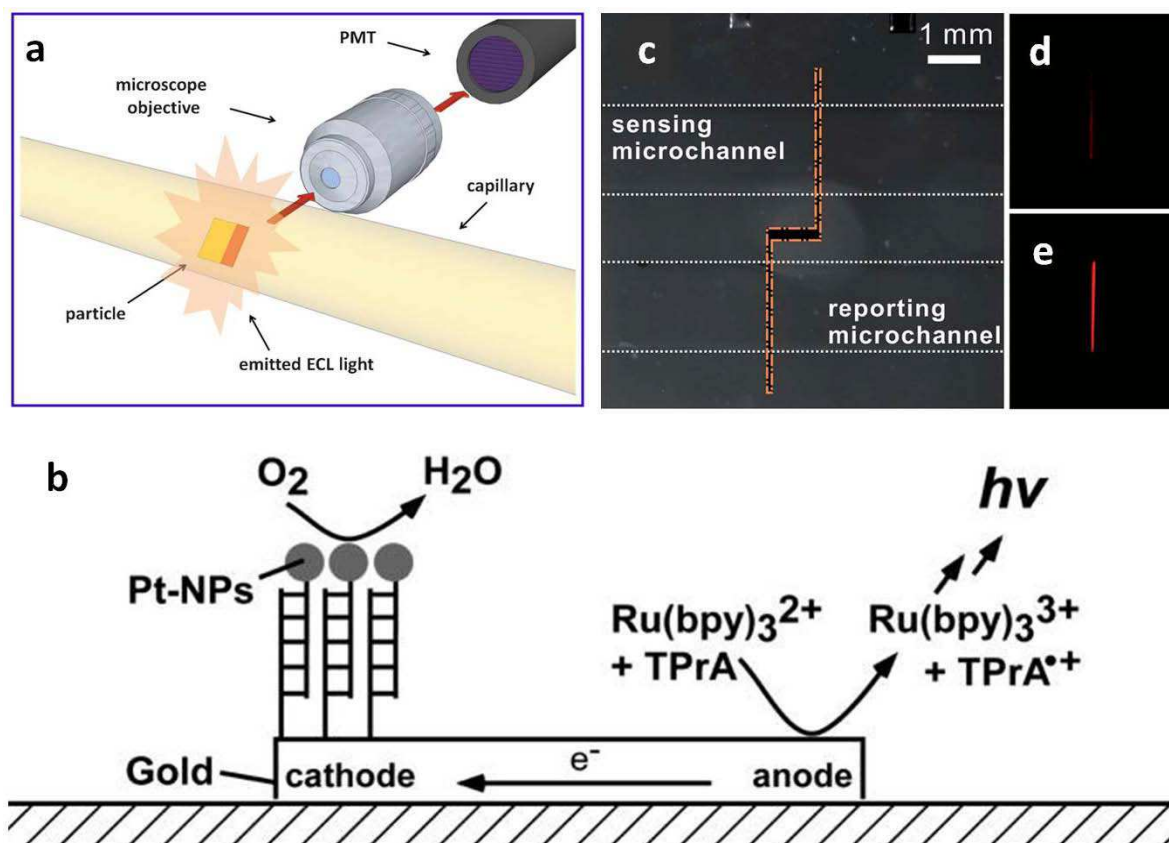


Figure 1.10 a) Schematic diagram of the detection system used by Jusková *et al.*, reprinted from Ref. (97). b) Scheme of a DNA sensing platform, adapted from Ref. (102). c) Micrograph of an interchannel BP_e spanning a two-channel configuration, the dashed white lines outline the two microchannels, and the burnt orange line emphasizes the location of the BP_e , the sensing microchannel was filled with the target molecule $\text{Fe}(\text{CN})_6^{3-}$ and the reporting microchannel was filled with the ECL mixture. Luminescence micrographs obtained with (d) 0.1 mM and (e) 5 mM $\text{Fe}(\text{CN})_6^{3-}$ present in the reporting channel, adapted from Ref. (103).

Finally, Wang's team reported a novel style of dual-channel ECL based bipolar configuration by using two-direction driving electrodes (only one kind of driving electrode such as driving anode or driving cathode was inserted into both ends of an individual channel as shown in Fig. 1.11), which could reach 100% current efficiency in theory.¹⁰⁴ More importantly, the

background signal from the integrated driving electrodes was completely eliminated, when this unique design was used to construct an ECL sensing platform. The mechanism, ECL behavior and potential distribution of this design have been investigated in details.¹⁰⁴ The applicability of the device was demonstrated by detecting, TPrA (co-reactant), dopamine (DA, quencher), H_2O_2 and $\text{K}_3\text{Fe}(\text{CN})_6$ (electroactive analytes), with a detection limit of 0.1 μM , 0.2 nM, 2.5 μM and 0.04 mM respectively.¹⁰⁴ The proposed sensing platform holds promising potential for designing electrochemical or ECL devices with high integration, high automation and high throughput.

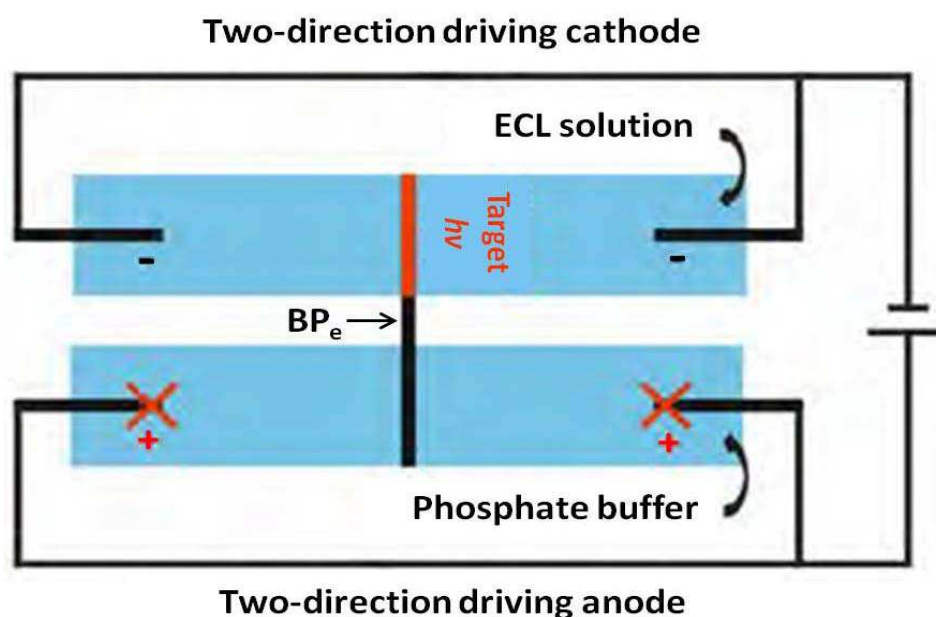


Figure 1.11 Scheme of the dual-channel ECL based bipolar configuration with two-direction driving electrodes, adapted from Ref. (104).

1.5.2.5. Optical Detection Based on Fluorescence

Fluorescence is the process of emitting light by a substance that has absorbed light, during a relatively short time delay between photon absorption and emission. In most cases, the emitted light has a longer wavelength, and therefore lower energy, than the absorbed radiation.

Guerrette *et al.* demonstrated recently the use of fluorescence microscopy and closed BP_e to reveal electrochemical and electrocatalytic activity on large electrochemical arrays.¹⁰⁵ Their approach, which was called fluorescence-enabled electrochemical microscopy (FEEM), differs from the conventional fluorescence-based electrochemical detection in that FEEM relies on the fluorogenic reaction only to report the rate of electrochemical processes

involving non-fluorescent redox species.¹⁰⁵ This makes possible the broad application of FEEM to study nearly any redox active species. Figure 1.12a illustrates the basic principles of FEEM; at the core of the setup is a closed BP_e, which along with its surrounding insulating material completely separates the two solution compartments.¹⁰⁵ One solution compartment contains an oxidizable redox analyte (R), while the other contains a buffered solution of resazurin (S), and the voltage was applied between the two Ag/AgCl feeder electrodes. The oxidation of R to O at the anodic pole was coupled to the two-electron, two-proton fluorogenic reduction of resazurin (Figure 1.12b).¹⁰⁵ Optical monitoring of the fluorescent product of this reaction, resorufin (P), provided a convenient and sensitive way to measure the electrochemical signal of the analyte.

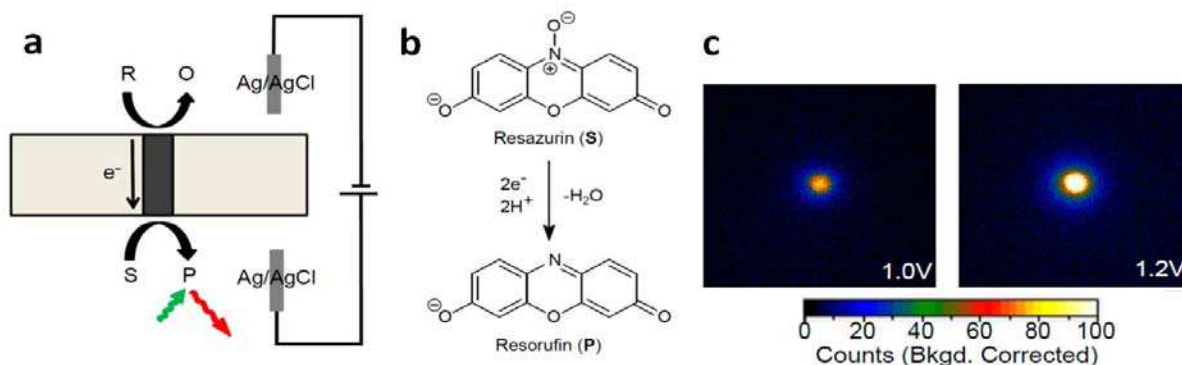


Figure 1.12 a) A schematic representation of the basic principle of FEEM and (b) the fluorogenic reduction of resazurin, reprinted from Ref. (105). c) Fluorescence images recorded at 1.0 and 1.2 V respectively, for detecting 2.5 μM ferrocene using 50 μM resazurin in a 50 mM phosphate buffer pH= 7.4, adapted from Ref. (105).

In the first experiment, 2.5 μM ferrocene in acetonitrile solution was oxidized at the anodic side of the BP_e by applying a potential sweep (0 – 1.4 V).¹⁰⁵ This corresponded to the resazurin reduction at the cathodic pole into resorufin which was illuminated with a lamp to excite its fluorescence. Figure 1.12c shows two background corrected fluorescence images recorded at 1.0 and 1.2 V respectively, this signal was produced from the coupling of the two electrochemical reactions, the oxidation of ferrocene and the fluorogenic reduction of resazurin, through the closed BP_e.¹⁰⁵

Next, electrochemical arrays containing thousands of ultramicroelectrodes were used to image redox species discharged from a glass micropipette. And finally they demonstrated the use of FEEM to map catalytically active hotspots on a carbon fiber electrode array, which

was selectively patterned and modified with Pt.¹⁰⁵ The later method can be adapted to multicomponent screening of electrocatalysts.

1.5.3. Generation of Molecular and Material Gradients

Surface gradient materials in which molecular functionalities or chemical properties change continuously along the materials, are highly attractive because of their potential sensor and biomimetic applications. Bipolar electrochemistry provides the suitable environment for generating such gradient based on the potential gradient alongside the BP_e.

The BP_e behavior was employed by Björefors and co-workers to create a surface gradient of molecular functionality, as the adsorption or desorption of a specific molecule can be controlled through the bipolar-electrode reactions.^{12, 106} A gold surface covered with a thiolated self-assembled monolayer (SAM) of methoxy poly(ethylene glycol) (mPEG) was employed as the BP_e.¹⁰⁶ Under the effect of the applied field, the SAM was selectively desorbed from the cathodic pole, and a carboxyl PEG was backfilled to generate a chemical gradient on the gold surface, which was characterized by ellipsometry.¹⁰⁶

Later, Shannon's group introduced the concept of generating solid-state material libraries along a BP_e.¹⁰⁷⁻¹⁰⁸ The deposition of Cd, CdS and S gradients on a gold wire immersed in a solution containing S₂O₃²⁻ and Cd²⁺ ions was done by applying a sufficient field.¹⁰⁷ The deposition potentials of Cd, CdS and S are very different; hence, the deposition of each one occurred at a different position along the wire. The resulted film was screened using resonance Raman spectroscopy and Auger electron spectroscopy.¹⁰⁷ As expected from the thermodynamic considerations, the reduction of Cd²⁺ into Cd⁰ started at the cathodic pole, followed by a stoichiometric CdS, and ended with S deposition, when moving from the cathodic pole toward the center of the BP_e.¹⁰⁷ In a second similar approach, they reported the synthesis of Ag-Au alloy gradients on stainless steel substrates.¹⁰⁸ The surface morphology of the electrodeposits was characterized using scanning electron microscopy (SEM), and their chemical composition was determined using energy dispersive X-ray spectroscopy (EDX), which displayed the Ag atomic percentage at the cathodic pole to be approximately 55 to 100, with a nearly linear variation of this percentage as a function of lateral position.¹⁰⁸

Bipolar doping of conducting polymers was also used to generate gradient materials. Conducting polymers generally have a high conductivity and show significant color changes when reduced or oxidized due to the modification in the polymer band gap. Ishigurao *et al.* successfully demonstrated the bipolar gradient patterning of poly(3-methylthiophene) (PMT) film that have been used as a BP_e.¹⁰⁹ This work was then extended to gradient doping of other conducting polymers such as poly(3,4-ethylenedioxythiophene) (PEDOT) and poly(aniline) (PANI).¹¹⁰ Optical micrographs of the three doped polymer films are shown in Figure 1.13a. The UV – vis absorption and EDX analyses supported the distribution of dopants in the polymer films reflecting the potential gradient on the BP_e.¹⁰⁹⁻¹¹⁰ Furthermore, the reversibility of the bipolar doping of the PMT film was demonstrated by a spectroelectrochemical investigation.¹¹⁰

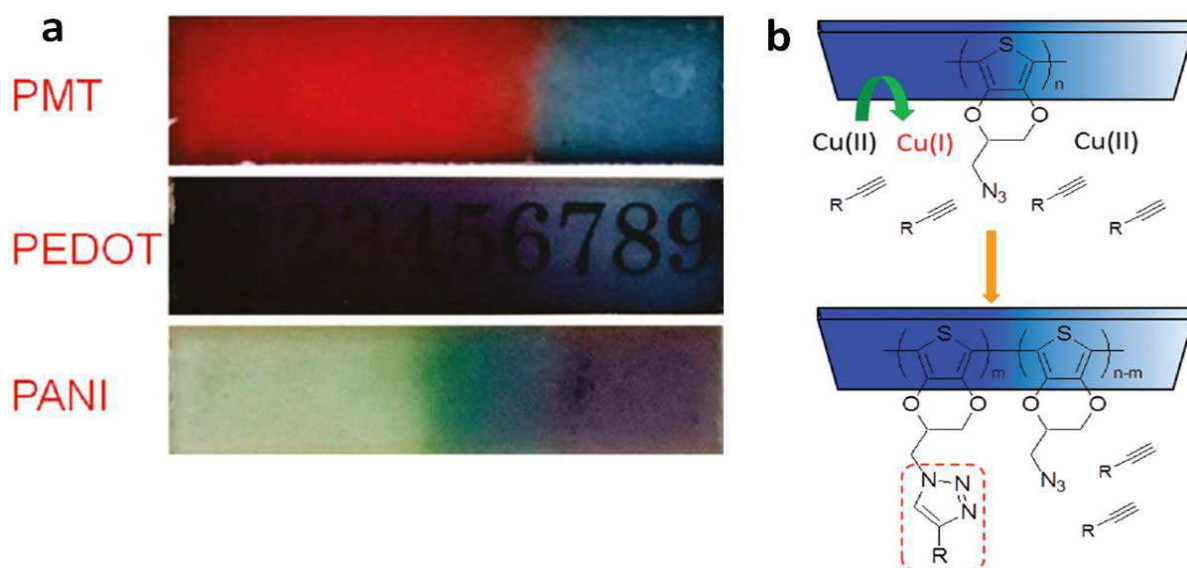


Figure 1.13 a) Photographs of three different conducting polymers that have been doped in a gradient manner using bipolar electrochemistry, adapted from Ref. (110). b) Schematic illustration of the electro-click reaction of PEDOT-N₃ film and terminal alkyne using cathodically generated Cu(I) species, adapted from Ref. (112).

The local potential distribution on the BP_e, which was confirmed by measuring the potential difference, enabled pattern spot modification of conducting polymer films.¹¹¹ By extending the bipolar spot patterning, the authors have also demonstrated a drawing application and array-type patterning in a site-controlled manner.¹¹¹ A recent report from the same group investigated the gradient modification of an azide-functionalized conducting polymer (PEDOT-N₃) via an electro-click reaction in the presence of a terminal alkyne and Cu(I).¹¹²

The later is a catalyst that has been generated at the cathodic side of the BP_e with a concentration gradient, which affected the density of the modifier introduced, as shown in Figure 1.13b. A variety of gradient functionalities such as gradient hydrophobicity/hydrophilicity and a visible marker could be introduced onto the PEDOT film.¹¹² Thus, the method looks quite promising to create versatile functionality-gradient surfaces.

1.5.4. Functionalization of a Single Micro- and Nanopore

The detection, identification, and purification of molecules and macromolecules such as DNA are of great importance for analytical applications, and customized pores have the potential to contribute significantly to this issue. Therefore, many efforts have been focused on synthesizing such customized micro- and nanopores.

In this frame, Bouchet and Liu *et al.* developed a contactless one-step technique allowing highly localized coating of the pore inner wall.¹¹³⁻¹¹⁵ The method depends on applying an electric field perpendicularly to a pore in a Si/SiO₂ membrane located between two compartments containing a solution of electroactive entities, leading to the deposition of material onto the pore wall. The procedure was employed to modify an 18 μm-wide inner pore wall with oligonucleotidic probes consisting of a polypyrrole (PPy), copolymer of pyrrole and pyrrole-oligonucleotide conjugate (py-ODN) as shown in Figure 1.14a.¹¹³ The effectiveness of the functionalization was investigated by hybridization with a complementary ODN. Fluorescence revelation was performed by adding streptavidin/phycoerythrin conjugate, which highlighted a fluorescent circle, corresponding to the presence of a deposit on the inner wall of the pore.¹¹³ The technique was also used to deposit other materials like gold, copper¹¹⁴ and iridium oxide.¹¹³ The mechanism has been demonstrated according to a set of experimental and simulation results obtained using a micropore.¹¹⁵ Under an adapted external electric field, electroactive species in the electrolyte can exchange electrons with the pore-wall surface, and electrodeposition occurs locally on the pore wall as a result of the silica layer defects that behave as a BP_e. In order to investigate the capacity of the process, a 200 nm nanopore was modified with a PPy-NH₂ followed by a functionalization with gold nanoparticles (Fig. 1.14b).¹¹⁵

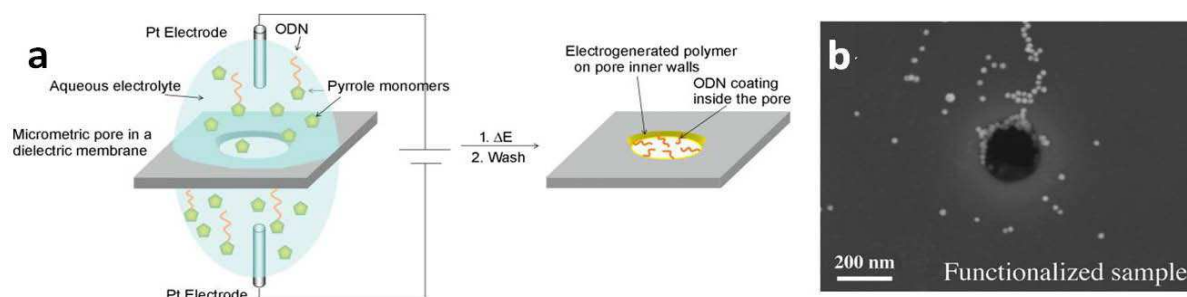


Figure 1.14 a) Illustration of the contactless modification process of a micrometric pore by applying an electric field between two platinum electrodes, and the resulted inner deposit (right image), reprinted from Ref. (113). b) SEM image of a 200 nm nanopore modified with PPy-NH₂ after incubation with 20 nm Au colloids, adapted from Ref. (115).

Furthermore, through proof-of-concept experiments using ODN-modified nanopores, the authors show that functionalized nanopores were suitable for translocation-based biosensing.¹¹⁵ The versatility of this process indicates a strong potential for diverse applications involving porous materials and biosensors.

1.5.5. Asymmetric Modification of Micro- and Nanoparticles

Fabrication of micro- and nanoparticles in an asymmetric fashion using the bipolar electrochemistry is one of the major parts of this thesis that will be presented in the next chapter. The asymmetric reactivity of the BP_e makes bipolar electrochemistry an appealing technique for the simple and wireless generation of asymmetric particles.¹¹⁶ An overview of the previous works in this frame will be given below.

1.5.5.1. The Closed Configuration for Preparation of Asymmetric Particles

Recently and in a proof-of-principle experiment, the closed bipolar configuration was adapted to prepare asymmetric particles.¹¹⁷ Kumsapaya *et al.* presented for the first time the use of bipolar electrochemistry to generate a grafted organic layer on one half sphere of glassy carbon (GC) beads, leading to asymmetric particles bearing organic functional groups.¹¹⁷ In this work, a single carbon bead was introduced into a capillary with the same diameter of the

bead, thus the bead was physically blocked in order to avoid any movement when submitted to an electric field. Aryl-diazonium molecules were grafted on one end of a GC bead by the formation of a covalent carbon–carbon bond via a wireless bipolar reduction.¹¹⁷ For visualization of the organic layer, subsequent adsorption of charged gold nanoparticles has been done which allowed the characterization by scanning electron microscopy (Figure 1.15a). Another possibility of direct visualization of the grafted layers has been explored by the grafting of 5-aminofluorescein that was observed under a fluorescent microscope (Figure 1.15b).¹¹⁷ The authors anticipated the process to be valid for a suspension of many particles as well, after immobilization of the particles by using a gel.

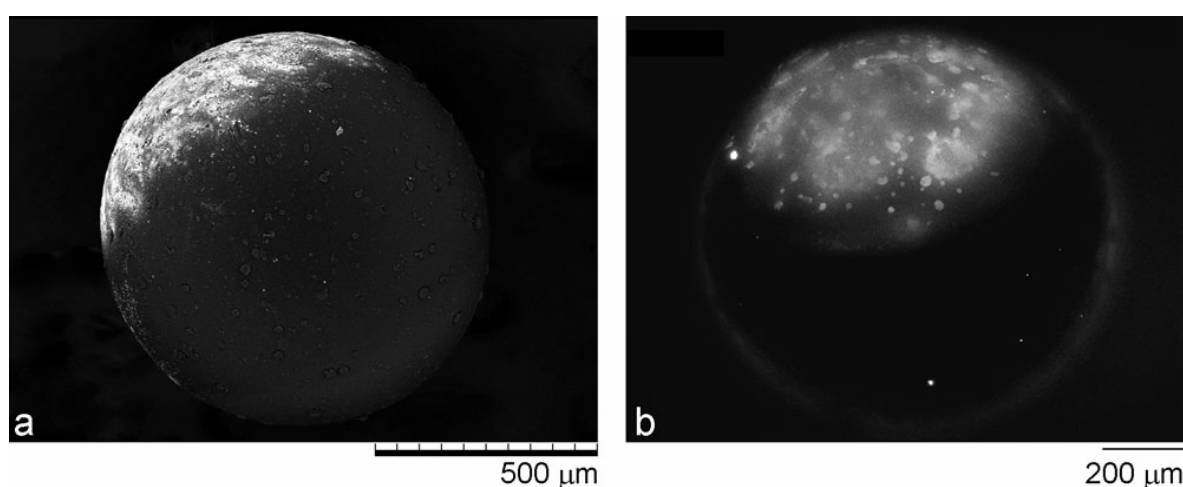


Figure 1.15 a) SEM image of a GC bead modified with aryl-diazonium molecules that interacted further with gold nanoparticles. b) Fluorescent microscope image of a GC bead modified with fluorescein-amine. Both reprinted from Ref. (117).

1.5.5.2. Two-Dimensional Modification

Bradley's group reported the first work about modifying microparticles by bipolar electrochemistry in 1999.¹¹⁸ The process includes the dispersion and immobilization of conductive particles onto a cellulose paper or track-etched membrane, this followed by applying a perpendicular electric field with respect to the sheet surface. The electrodeposition of Pd onto the cathodic pole was coupled with the oxidation of solvent (toluene/acetonitrile) at the anodic pole of micrometer-sized graphite particles as shown in Figure 1.16a.¹¹⁸ A strong correlation between the electric field intensity during the catalyst preparation and the catalytic activity was demonstrated. By exposing the resulted palladium-graphite particles to a solution of gold and reversing the field direction, Pd-C-Au hybrid micro-objects were

equally prepared.¹¹⁸ Pulsed bipolar electrodeposition of palladium onto graphite powder was also investigated.¹¹⁹ The amount of the deposited palladium increased with the field intensity, but it was independent of the frequency used. Fields of 0.5 to 3 kV/cm with frequencies of 0.5 to 20 kHz were used, and characterization of the hybrids by transmission electron microscopy (TEM) revealed different types of growth.¹¹⁹

On the other hand, the modification of isotropic carbon substrates was performed by the same group using a similar setup. In this case, the sheet supporting the immobilized particles was localized parallel to the applied field. DC and pulsed electric fields of 3 and 10 kV/cm were used to deposit Pd metal onto one tip of commercial carbon nanofibers (CNFs) and carbon nanotubes (CNTs) exhibiting a length of several micrometers, respectively.¹²⁰ Finally, they reported the modification of carbon nanopipes (CNPs) with PPy on specific ends.¹²¹ Figures 1.16b and c show environmental scanning electron microscope (ESEM) micrographs of two different CNPs that have been modified with PPy on either one or both ends, respectively. The later was obtained by reversing the direction of the applied field after the first deposition.¹²¹

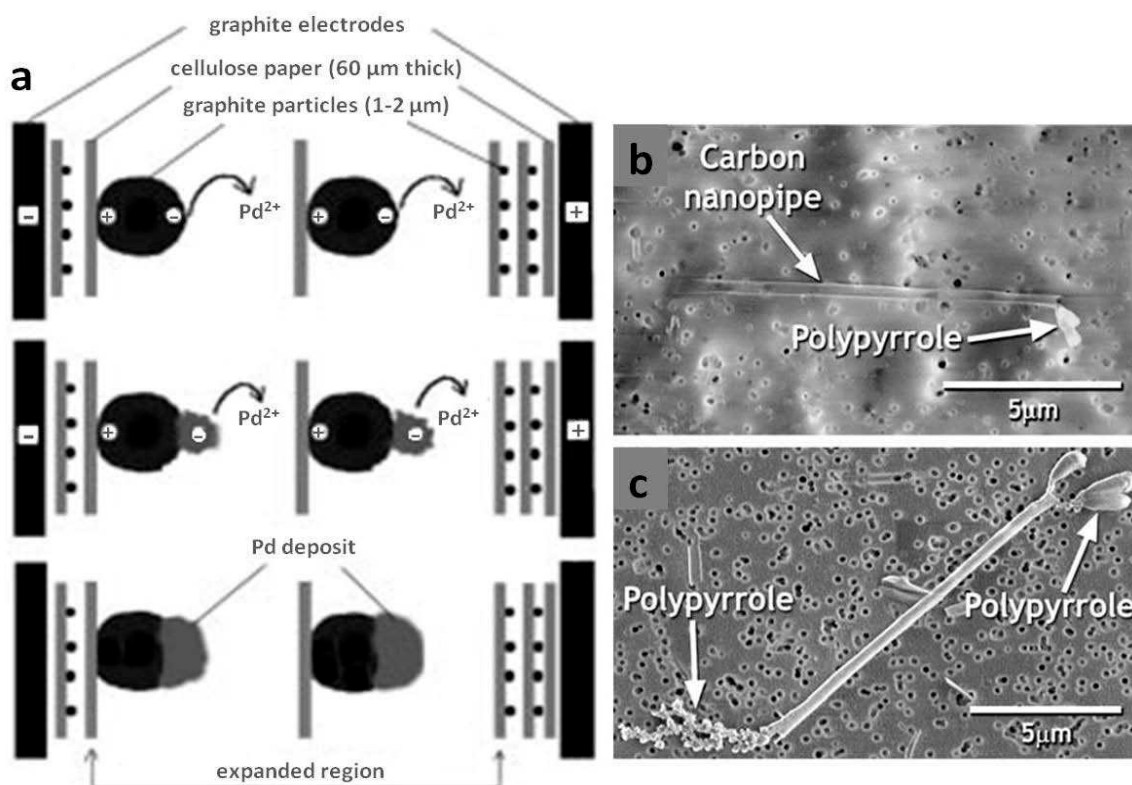


Figure 1.16 a) Schematic representation of the preparation of the bipolar setup used for Pd electrodeposited onto graphite particles, adapted from Ref. (118). b, c) ESEM micrographs of CNPs modified at one and both ends with PPy, respectively, adapted from Ref. (121).

1.5.5.3. Capillary Electrophoresis for Bipolar Electrochemistry

Bradley's group performed the pioneer work for the development of bipolar electrodeposition technology. However, it was only adapted for organic solvents, and the need to immobilize the particles on a sheet before the electrodeposition lead to produce just a monolayer of asymmetric particles. Therefore, the industrial applications of the process were limited because a high yield of production is required. These two issues have been overcome in our group in 2008 by introducing another technique for bipolar electrodeposition.¹²²⁻¹²³ This method which is based on a capillary electrophoresis is called capillary assisted bipolar electrodeposition (CABED) and it will be described in details in the next chapter as it has been used in the frame of this thesis. Using this setup, the selective modification of millimeter-sized carbon fiber with gold deposit at one extremity was possible as shown in Figure 1.17a.¹²³ Analogue experiments with multi-walled carbon nanotubes (MWCNTs) were successfully done (Fig.1.17b) as revealed under TEM imaging and EDX spectroscopy.¹²³

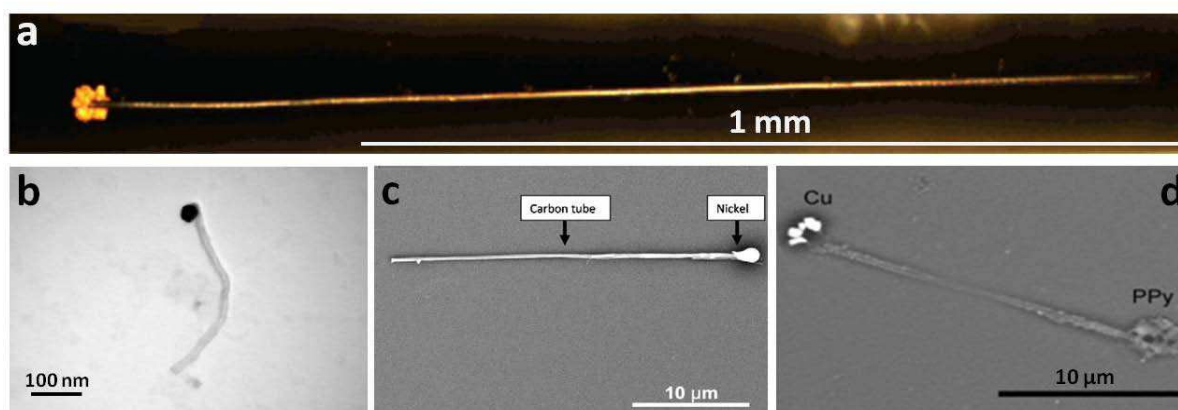


Figure 1.17 a) Optical micrograph of a carbon fiber inside a glass capillary during asymmetric bipolar gold deposition, adapted from Ref. (123). b) TEM image of a MWCNT modified with gold, adapted from Ref. (123). c) SEM picture of a CMT modified at one end with nickel, adapted from Ref. (124). d) SEM image of a dumbbell-like CMT with one copper end and one PPy end, adapted from Ref. (125).

More recently, the process was employed for the bulk modification of carbon microtubes (CMTs) with nickel at one extremity,¹²⁴ and for the preparation of dumbbell-like particles that are modified with copper at one end and PPy at the other end (using pulsed potential),¹²⁵ as shown in Figure 1.17c and d, respectively. The chemical composition of the deposits was confirmed for the case of the dumbbell-like CMT by the EDX analysis.¹²⁵ Thus, the CABED

represents the first bulk procedure allowing the modification of micro- and nanoparticles in aqueous and organic mediums.

1.5.5.4. Bipolar Cell for Up-Scaling the Asymmetric Product

CABED is considered as a bulk technique which allows producing a higher yield than 2D interfacial approaches. However, the scale of production is still insufficient for industrial applications as the modification volume is limited by the capillary dimensions. Therefore, a new cell design has been introduced in order to scale-up the production and prepare larger amounts of materials that might be interesting for industrial applications.¹²⁶⁻¹²⁷ The new cell was used for synthesizing asymmetric objects in the present thesis; hence, a complete description of the setup will be developed later. The design was adapted for the bulk modification of both anisotropic and isotropic objects.¹²⁷ Glassy carbon micro-beads were modified under different experimental conditions either with gold or silver, generating asymmetric spheres with a hemispherical metal coating or a single point electrodeposition as illustrated in Figures 1.18a and b, respectively.¹²⁷ The indirect electrodeposition of silver chloride at one extremity of a silver nanowire,¹²⁷ and insulating materials such as electrophoretic deposition paints (EDPs) or titanate on a GC bead (Fig. 1.18c) was also possible using this technology.¹²⁸

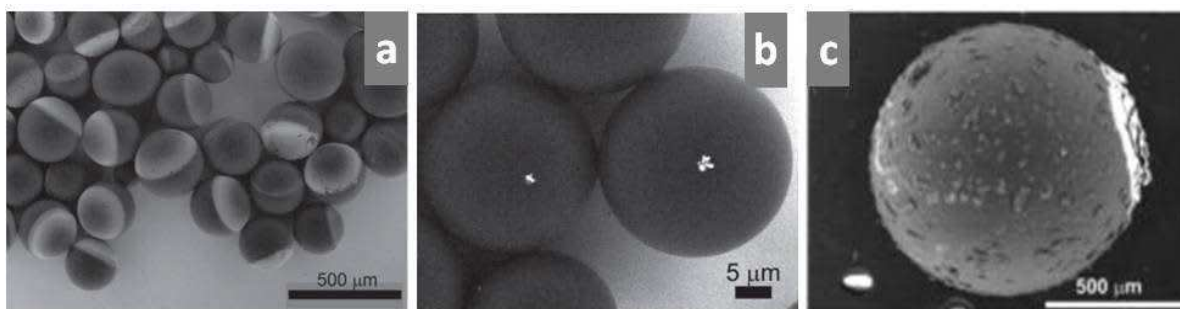


Figure 1.18 SEM images of glassy carbon beads modified asymmetrically with a) Gold, b) Silver, both adapted from Ref. (127), and c) Titanate, adapted from Ref. (128).

Thus, the process presents a true bulk procedure for the preparation of variety of asymmetric objects that might have different applications in the frame of nanotechnology.

1.5.6. Electric Fields Generated Motion

The asymmetric structure of particles is the key point for generating swimmers with controlled motion as we will see in chapter 3. However, bipolar electrochemistry can provide an intrinsic asymmetry for isotropic conductive particles, which triggers their motion in the electric field. Different mechanisms, ranging from translation, rotation to levitation have been reported by Kuhn's group for the propulsion of objects under the influence of applied electric fields.^{116, 129-133} First example of the translational motion was based on self-regeneration of metallic objects.¹²⁹ In this experiment, a Zn dendrite was placed in a capillary that was previously filled with a zinc sulfate solution. Under the applied field, the dendrite is acting as a BP_e; its anodic pole is dissolved by the oxidation, while deposition occurs at its cathodic pole.¹²⁹ These simultaneous reactivity leads to a linearly directed motion. Propulsion of zinc macro- and microswimmers at speeds of up to 80 $\mu\text{m s}^{-1}$ has been achieved.¹²⁹

Another strategy is based on the polarization of a BP_e, which triggers spatially separated oxidation and reduction reactions involving asymmetric gas bubble formation.¹³⁰ This in turn leads to a directional motion of the objects. Depending on the implied redox chemistry (choice of electroactive species in solution) and the device design, the speed can be controlled and the motion can be switched from linear to rotational.¹³⁰ Translational motion has been induced on millimeter-sized metal beads, and on micrometer-sized carbon beads in (PDMS) microchannels.¹³⁰ The same principle was adapted for the vertical propulsion of conductive beads in liquid filled capillaries.¹³¹ In this setup, bubbles are generated underneath a GC bead where the reduction of water to H₂ occurs, which in turn was enough to lift the bead.¹³¹ And by coupling the later system to ECL reaction at the anodic pole of a GC bead, it was possible to generate a light, which could be very useful for monitoring the micromotors.¹³²

In the frame of controlling the motion with space and time resolution, a bipolar electrochemical valve based on a chemo-mechanical feedback loop has been described.¹³³ This valve, which was in a sub-millimeter scale, operates in aqueous solutions by converting electrical energy into reversible motion via the electrochemical generation of hydrogen bubbles at the cathodic pole of a BP_e.¹³³ The design of the valve allows the storage and subsequent release of these bubbles by using a tube that is directly connected to the feeder anode, thus allowing the wireless activation of the motion.¹³³ This might be interesting for

1.5. Recent Micro- and Nano Applications of Bipolar Electrochemistry

certain applications for example in the field of microfluidics, where active compounds could be released on demand from one reservoir into another with subsequent mixing.

References

1. Goodridge, F., *Electrochim. Acta* **1977**, 22 (9), 929-933.
2. Fleischmann, M.; Ghoroghchian, J.; Rolison, D.; Pons, S., *J. Phys. Chem.* **1986**, 90 (23), 6392-6400.
3. Goodridge, F.; King, C. J. H.; Wright, A. R., *Electrochim. Acta* **1977**, 22 (10), 1087-1091.
4. Ndungu, P. G., PhD thesis, Drexel University, 2004.
5. Mavr , F. ; Anand, R. K.; Laws, D. R.; Chow, K.-F.; Chang, B.-Y.; Crooks, J. A.; Crooks, R. M., *Anal. Chem.* **2010**, 82 (21), 8766-8774.
6. Loget, G.; Kuhn, A., *Anal. Bioanal. Chem.* **2011**, 400 (6), 1691-1704.
7. Mano, N.; Heller, A., *J. Am. Chem. Soc.* **2005**, 127 (33), 11574-11575.
8. Bard, A. J.; Faulkner, L. R., *Electrochemical methods: Fundamentals and Applications, 2nd ed.*; John Wiley & Sons, Inc **2001**.
9. Mavr , F. ; Chow, K.-F.; Sheridan, E.; Chang, B.-Y.; Crooks, J. A.; Crooks, R. M., *Anal. Chem.* **2009**, 81 (15), 6218-6225.
10. Loget, G.; Kuhn, A., *Electrochemistry: Nanosystems Electrochemistry, Vol. 11 (Eds.: R. Compton, J. Wadhawan)*, RSC, **2012**.
11. Duval, J. F. L.; Buffle, J.; van Leeuwen, H. P., *The Journal of Physical Chemistry B* **2006**, 110 (12), 6081-6094.
12. Ulrich, C.; Andersson, O.; Nyholm, L.; Bj refors, F., *Anal. Chem.* **2009**, 81 (1), 453-459.
13. Bonvin, G.; Comninellis, C., *J. Appl. Electrochem.* **1994**, 24 (6), 469-474.
14. Cheng, C. Y.; Kelsall, G. H.; Pilone, D., *J. Appl. Electrochem.* **2005**, 35 (12), 1191-1202.
15. Kusakabe, K.; Morooka, S.; Kato, Y., *J. Chem. Eng. Jpn.* **1986**, 19 (1), 43-47.
16. King, C. J. H.; Wright, A. R., *Electrochim. Acta* **1977**, 22 (10), 1135-1139.
17. Yang, J.; Zhang, Q.; Wang, H.; Liu, Y., *Trans. Nonferrous Met. Soc. China* **1995**, 5, 29-35.
18. Comninellis, C.; Plattner, E.; Bolomey, P., *J. Appl. Electrochem.* **1991**, 21 (5), 415-418.
19. Kuhn, A.; Booth, J., *J. Appl. Electrochem.* **1980**, 10 (2), 233-237.
20. Kusakabe, K.; Morooka, S.; Kato, Y., *J. Chem. Eng. Jpn.* **1982**, 15 (1), 45-50.
21. Eardley, D. C.; Handley, D.; Andrew, S. P. S., *Electrochim. Acta* **1973**, 18 (11), 839-848.
22. Inagi, S.; Ishiguro, Y.; Shida, N.; Fuchigami, T., *J. Electrochem. Soc.* **2012**, 159 (11), G146-G150.
23. Duval, J. F. L.; Minor, M.; Cecilia, J.; van Leeuwen, H. P., *J. Phys. Chem. B* **2003**, 107 (17), 4143-4155.
24. Qian, S.; Duval, J. F. L., *J. Colloid Interface Sci.* **2006**, 300 (1), 413-428.
25. Fleischmann, M.; Ghoroghchian, J.; Pons, S., *J. Phys. Chem.* **1985**, 89 (25), 5530-5536.
26. Yen, S.-C.; Yao, C.-Y., *J. Electrochem. Soc.* **1991**, 138 (9), 2697-2703.

27. Duval, J. F. L.; van Leeuwen, H. P.; Cecilia, J.; Galceran, J., *J. Phys. Chem. B* **2003**, *107* (28), 6782-6800.
28. Duval, J.; Kleijn, J. M.; van Leeuwen, H. P., *J. Electroanal. Chem.* **2001**, *505* (1–2), 1-11.
29. Cox, J. T.; Guerrette, J. P.; Zhang, B., *Anal. Chem.* **2012**, *84* (20), 8797-8804.
30. Guerrette, J. P.; Oja, S. M.; Zhang, B., *Anal. Chem.* **2012**, *84* (3), 1609-1616.
31. Cattarin, S.; Musiani, M. M., *J. Electrochem. Soc.* **1995**, *142* (11), 3786-3792.
32. Keithley, R. B.; Carelli, R. M.; Wightman, R. M., *Anal. Chem.* **2010**, *82* (13), 5541-5551.
33. Plana, D.; Shul, G.; Stephenson, M. J.; Dryfe, R. A. W., *Electrochem. Commun.* **2009**, *11* (1), 61-64.
34. Plana, D.; Jones, F. G. E.; Dryfe, R. A. W., *J. Electroanal. Chem.* **2010**, *646* (1–2), 107-113.
35. Bouy, P.; Lachaux, H. D.; Conan, M., 1977, US Patents 4026782.
36. Pohto, G. R., 1977, US Patents 4017375.
37. Beck, T. R.; Rousar, I.; Thonstad, J., *MMTB* **1994**, *25* (5), 661-668.
38. Rousar, I.; Thonstad, J., *J. Appl. Electrochem.* **1994**, *24* (11), 1124-1132.
39. Divisek, J., *J. Appl. Electrochem.* **1984**, *14* (5), 663-674.
40. Litovka, Y. V.; Mikheev, V. V., *Theor. Found. Chem. Eng.*, **2006**, *40* (3), 305-310.
41. Pretorius, W.; Johannes, W.; Lempert, G., *Water S. A.* **1991**, *17* (2), 133-138.
42. Ivanova, N. D.; Gerasimchuk, A. I.; Vlasenko, N. E., *Russ. J. Appl. Chem.* **2002**, *75* (7), 1079-1081.
43. Kaun, T. D., 1992, US Patents 5162172
44. Bullock, K. R., *J. Electrochem. Soc.* **1995**, *142* (5), 1726-1731.
45. Karami, H.; Mousavi, M. F.; Shamsipur, M., *J. Power Sources* **2003**, *124* (1), 303-308.
46. Deng, C.; Shi, P. F.; Zhang, S., *Electrochem. Solid-State Lett.* **2006**, *9* (6), A303-A306.
47. Wiesener, K.; Ohms, D.; Benczúr-Ürmösy, G.; Berthold, M.; Haschka, F., *J. Power Sources* **1999**, *84* (2), 248-258.
48. Ohms, D.; Kohlhase, M.; Benczúr-Ürmösy, G.; Wiesener, K.; Harmel, J., *J. Power Sources* **2002**, *105* (2), 120-126.
49. Qian, P.; Zhang, H.; Chen, J.; Wen, Y.; Luo, Q.; Liu, Z.; You, D.; Yi, B., *J. Power Sources* **2008**, *175* (1), 613-620.
50. Hagg, C. M.; Skyllas-Kazacos, M., *J. Appl. Electrochem.* **2002**, *32* (10), 1063-1069.
51. Peled, E.; Golodnitsky, D.; Ardel, G.; Lang, J.; Lavi, Y., *J. Power Sources* **1995**, *54* (2), 496-500.
52. Livshits, V.; Blum, A.; Strauss, E.; Ardel, G.; Golodnitsky, D.; Peled, E., *J. Power Sources* **2001**, *97–98* (0), 782-785.
53. Karami, H.; Shamsipur, M.; Ghasemi, S.; Mousavi, M. F., *J. Power Sources* **2007**, *164* (2), 896-904.
54. Saakes, M.; Schellevis, D.; van Trier, D.; Wollersheim, M., *J. Power Sources* **1997**, *67* (1–2), 33-41.
55. Saakes, M.; Woortmeijer, R.; Schmal, D., *J. Power Sources* **2005**, *144* (2), 536-545.

56. Lim, H. S., 1986, US Patents 4567119.
57. Ovshinsky, S. R.; Smaga, J.; Higley, L. R.; Himmler, R.; Luesing, J.; Olszanski, T., 2007, US Patents 0212604A1.
58. Williams, M. T.; Briscoe, J. D.; Oweis, S. M., 1993, US Patents 5254415.
59. Mameri, N.; Yeddou, A. R.; Lounici, H.; Belhocine, D.; Grib, H.; Bariou, B., *Water Res.* **1998**, *32* (5), 1604-1612.
60. Mameri, N.; Lounici, H.; Belhocine, D.; Grib, H.; Piron, D. L.; Yahiat, Y., *Sep. Purif. Technol.* **2001**, *24* (1-2), 113-119.
61. Fosdick, S. E.; Crooks, R. M., *J. Am. Chem. Soc.* **2012**, *134* (2), 863-866.
62. Keddam, M.; Nóvoa, X. R.; Vivier, V., *Corros. Sci.* **2009**, *51* (8), 1795-1801.
63. Keddam, M.; Nóvoa, X. R.; Puga, B.; Vivier, V., *Eur. J. Environ. Civ. En.* **2011**, *15* (7), 1097-1103.
64. Andrade, C.; Martínez, I.; Castellote, M., *J. Appl. Electrochem.* **2008**, *38* (10), 1467-1476.
65. Munktel, S.; Tydén, M.; Höglström, J.; Nyholm, L.; Björefors, F., *Electrochem. Commun.* **2013**, *34*, 274-277.
66. Bradley, J.-C., 2000, US Patent 6120669.
67. Bradley, J.-C.; Chen, H.-M.; Crawford, J.; Eckert, J.; Ernazarova, K.; Kurzeja, T.; Lin, M.; McGee, M.; Nadler, W.; Stephens, S. G., *Nature* **1997**, *389* (6648), 268-271.
68. Bradley, J. C.; Dengra, S.; Gonzalez, G. A.; Marshall, G.; Molina, F. V., *J. Electroanal. Chem.* **1999**, *478* (1-2), 128-139.
69. Bradley, J.-C.; Crawford, J.; Ernazarova, K.; McGee, M.; Stephens, S. G., *Adv. Mater. (Weinheim, Ger.)* **1997**, *9* (15), 1168-1171.
70. Bradley, J.-C.; Crawford, J.; McGee, M.; Stephens, S. G., *J. Electrochem. Soc.* **1998**, *145* (3), L45-L47.
71. Bradley, J.-C.; Babu, S.; Carroll, B.; Mittal, A., *J. Electroanal. Chem.* **2002**, *522* (1), 75-85.
72. Bradley, J.-C.; Ma, Z.; Clark, E.; Crawford, J.; Stephens, S. G., *J. Electrochem. Soc.* **1999**, *146* (1), 194-198.
73. Bradley, J.-C.; Ma, Z.; Stephens, S. G., *Adv. Mater. (Weinheim, Ger.)* **1999**, *11* (5), 374-378.
74. Zhan, W.; Crooks, R. M., *J. Am. Chem. Soc.* **2003**, *125* (33), 9934-9935.
75. Chang, B.-Y.; Crooks, J. A.; Chow, K.-F.; Mavré, F.; Crooks, R. M., *J. Am. Chem. Soc.* **2010**, *132* (43), 15404.
76. Wei, W.; Xue, G.; Yeung, E. S., *Anal. Chem.* **2002**, *74* (5), 934-940.
77. Dhopeswarkar, R.; Hlushkou, D.; Nguyen, M.; Tallarek, U.; Crooks, R. M., *J. Am. Chem. Soc.* **2008**, *130* (32), 10480-10481.
78. Hlushkou, D.; Perdue, R. K.; Dhopeswarkar, R.; Crooks, R. M.; Tallarek, U., *Lab Chip* **2009**, *9* (13), 1903-1913.
79. Perdue, R. K.; Laws, D. R.; Hlushkou, D.; Tallarek, U.; Crooks, R. M., *Anal. Chem.* **2009**, *81* (24), 10149-10155.
80. Laws, D. R.; Hlushkou, D.; Perdue, R. K.; Tallarek, U.; Crooks, R. M., *Anal. Chem.* **2009**, *81* (21), 8923-8929.

81. Anand, R. K.; Sheridan, E.; Hlushkou, D.; Tallarek, U.; Crooks, R. M., *Lab Chip* **2011**, *11* (3), 518-527.
82. Sheridan, E.; Hlushkou, D.; Anand, R. K.; Laws, D. R.; Tallarek, U.; Crooks, R. M., *Anal. Chem.* **2011**, *83* (17), 6746-6753.
83. Sheridan, E.; Knust, K. N.; Crooks, R. M., *Analyst* **2011**, *136* (20), 4134-4137.
84. Anand, R. K.; Sheridan, E.; Knust, K. N.; Crooks, R. M., *Anal. Chem.* **2011**, *83* (6), 2351-2358.
85. Sheridan, E.; Hlushkou, D.; Knust, K. N.; Tallarek, U.; Crooks, R. M., *Anal. Chem.* **2012**, *84* (17), 7393-7399.
86. Knust, K. N.; Sheridan, E.; Anand, R. K.; Crooks, R. M., *Lab Chip* **2012**, *12* (20), 4107-4114.
87. Cao, Z.; Yobas, L., *Electrophoresis* **2013**, *34* (14), 1991-1997.
88. Klett, O.; Nyholm, L., *Anal. Chem.* **2003**, *75* (6), 1245-1250.
89. Ordeig, O.; Godino, N.; del Campo, J.; Muñoz, F. X.; Nikolajeff, F.; Nyholm, L., *Anal. Chem.* **2008**, *80* (10), 3622-3632.
90. Chow, K.-F.; Chang, B.-Y.; Zaccheo, B. A.; Mavré, F.; Crooks, R. M., *J. Am. Chem. Soc.* **2010**, *132* (27), 9228-9229.
91. Fosdick, S. E.; Berglund, S. P.; Mullins, C. B.; Crooks, R. M., *Anal. Chem.* **2013**, *85* (4), 2493-2499.
92. Bard, A. J., *Electrogenerated chemiluminescence*. CRC Press: 2004.
93. Richter, M. M., *Chem. Rev.* **2004**, *104* (6), 3003-3036.
94. Arora, A.; Eijkel, J. C. T.; Morf, W. E.; Manz, A., *Anal. Chem.* **2001**, *73* (14), 3282-3288.
95. Wu, M.-S.; Xu, B.-Y.; Shi, H.-W.; Xu, J.-J.; Chen, H.-Y., *Lab Chip* **2011**, *11* (16), 2720-2724.
96. Wu, M.-S.; Qian, G.-s.; Xu, J.-J.; Chen, H.-Y., *Anal. Chem.* **2012**, *84* (12), 5407-5414.
97. Jusková, P.; Neuzil, P.; Manz, A.; Foret, F., *Lab Chip* **2013**, *13* (5), 781-784.
98. Zhan, W.; Alvarez, J.; Crooks, R. M., *J. Am. Chem. Soc.* **2002**, *124* (44), 13265-13270.
99. Fosdick, S. E.; Crooks, J. A.; Chang, B.-Y.; Crooks, R. M., *J. Am. Chem. Soc.* **2010**, *132* (27), 9226-9227.
100. Chang, B.-Y.; Mavré, F.; Chow, K.-F.; Crooks, J. A.; Crooks, R. M., *Anal. Chem.* **2010**, *82* (12), 5317-5322.
101. Chow, K.-F.; Mavré, F.; Crooks, J. A.; Chang, B.-Y.; Crooks, R. M., *J. Am. Chem. Soc.* **2009**, *131* (24), 8364-8365.
102. Chow, K.-F.; Mavré, F.; Crooks, R. M., *J. Am. Chem. Soc.* **2008**, *130* (24), 7544-7545.
103. Chang, B.-Y.; Chow, K.-F.; Crooks, J. A.; Mavré, F.; Crooks, R. M., *Analyst* **2012**, *137* (12), 2827-2833.
104. Zhang, X.; Chen, C.; Li, J.; Zhang, L.; Wang, E., *Anal. Chem.* **2013**.
105. Guerrette, J. P.; Percival, S. J.; Zhang, B., *J. Am. Chem. Soc.* **2013**, *135* (2), 855-861.
106. Ulrich, C.; Andersson, O.; Nyholm, L.; Björefors, F., *Angew. Chem. Int. Ed.* **2008**, *47* (16), 3034-3036.

107. Ramakrishnan, S.; Shannon, C., *Langmuir* **2010**, 26 (7), 4602-4606.
108. Ramaswamy, R.; Shannon, C., *Langmuir* **2011**, 27 (3), 878-881.
109. Inagi, S.; Ishiguro, Y.; Atobe, M.; Fuchigami, T., *Angew. Chem. Int. Ed.* **2010**, 49 (52), 10136-10139.
110. Ishiguro, Y.; Inagi, S.; Fuchigami, T., *Langmuir* **2011**, 27 (11), 7158-7162.
111. Ishiguro, Y.; Inagi, S.; Fuchigami, T., *J. Am. Chem. Soc.* **2012**, 134 (9), 4034-4036.
112. Shida, N.; Ishiguro, Y.; Atobe, M.; Fuchigami, T.; Inagi, S., *ACS Macro Letters* **2012**, 1 (6), 656-659.
113. Bouchet, A.; Descamps, E.; Mailley, P.; Livache, T.; Chatelain, F.; Haguët, V., *Small* **2009**, 5 (20), 2297-2303.
114. Liu, J.; Hébert, C.; Pham, P.; Sauter-Starace, F.; Haguët, V.; Livache, T.; Mailley, P., *Small* **2012**, 8 (9), 1345-1349.
115. Liu, J.; Pham, P.; Haguët, V.; Sauter-Starace, F.; Leroy, L.; Roget, A.; Descamps, E.; Bouchet, A.; Buhot, A.; Mailley, P.; Livache, T., *Anal. Chem.* **2012**, 84 (7), 3254-3261.
116. Loget, G.; Zigah, D.; Bouffier, L.; Sojic, N.; Kuhn, A., *Acc.Chem.Res.* **2013**, in press, DOI: 10.1021/ar400039k.
117. Kumsapaya, C.; Bakaï, M.-F.; Loget, G.; Goudeau, B.; Warakulwit, C.; Limtrakul, J.; Kuhn, A.; Zigah, D., *Chem. Eur. J.* **2013**, 19 (5), 1577-1580.
118. Bradley, J.-C.; Ma, Z., *Angew. Chem. Int. Ed.* **1999**, 38 (11), 1663-1666.
119. Bradley, J.-C.; Babu, S.; Mittal, A.; Ndungu, P.; Carroll, B.; Samuel, B., *J. Electrochem. Soc.* **2001**, 148 (9), C647-C651.
120. Bradley, J.-C.; Babu, S.; Ndungu, P., *Fullerenes, Nanotubes and Carbon Nanostructures* **2005**, 13 (3), 227-237.
121. Babu, S.; Ndungu, P.; Bradley, J.-C.; Rossi, M. P.; Gogotsi, Y., *Microfluidics and Nanofluidics* **2005**, 1 (3), 284-288.
122. Warakulwit, C., PhD thesis, Kasetsart University and Bordeaux University, 2007.
123. Warakulwit, C.; Nguyen, T.; Majimel, J.; Delville, M.-H.; Lapeyre, V.; Garrigue, P.; Ravaine, V.; Limtrakul, J.; Kuhn, A., *Nano Lett.* **2008**, 8 (2), 500-504.
124. Loget, G.; Larcade, G.; Lapeyre, V.; Garrigue, P.; Warakulwit, C.; Limtrakul, J.; Delville, M. H.; Ravaine, V.; Kuhn, A., *Electrochim. Acta* **2010**, 55 (27), 8116-8120.
125. Loget, G.; Lapeyre, V. r.; Garrigue, P.; Warakulwit, C.; Limtrakul, J.; Delville, M.-H. l. n.; Kuhn, A., *Chem. Mater.* **2011**, 23 (10), 2595-2599.
126. Loget, G.; Kuhn, A., **2011**, French patent FR2969508.
127. Loget, G.; Roche, J.; Kuhn, A., *Adv. Mater. (Weinheim, Ger.)* **2012**, 24 (37), 5111-5116.
128. Loget, G.; Roche, J.; Gianessi, E.; Bouffier, L.; Kuhn, A., *J. Am. Chem. Soc.* **2012**, 134 (49), 20033-20036.
129. Loget, G.; Kuhn, A., *J. Am. Chem. Soc.* **2010**, 132 (45), 15918-15919.
130. Loget, G.; Kuhn, A., *Nat Commun* **2011**, 2, 535.
131. Loget, G.; Kuhn, A., *Lab Chip* **2012**, 12 (11), 1967-1971.
132. Sentic, M.; Loget, G.; Manojlovic, D.; Kuhn, A.; Sojic, N., *Angew. Chem. Int. Ed.* **2012**, 51 (45), 11284-11288.
133. Bouffier, L.; Kuhn, A., *Nanoscale* **2013**, 5 (4), 1305-1309.

Chapter 2

Bipolar Electrochemistry with Materials Science: Asymmetric Particles, Applications and Design

2.1. Asymmetric Particles

Asymmetric particles refer to particles that are composed of at least two components of different nature (i.e. chemistry, functionality, and/or polarity). The early work by Gasagrande *et al.* and subsequently De Gennes's Nobel lecture, in which he coined the term "Janus grains" in reference to the two faced Roman alleged god Janus, opened the way for exploring new types of asymmetric particles.¹⁻² De Gennes used the term "Janus grains" to describe particles with hemispherical amphiphilicity, meaning that, one half of the sphere is polar whereas the other is non-polar. This asymmetry offers efficient and distinctive capabilities for example to target complex self-assembled materials. After that, the term "Janus particles" was employed for describing a wide range of nano- and micro-sized particles that exhibit different chemical and physical properties in a one single object. In nature, we can find a number of analogues to the recently Janus particles developed in modern materials science. One example is the asymmetric structures of lipids, a most central building block of the biological molecular organization, that give rise to self-assembly into bilayers which is essential to the generation of biological shapes and sizes on the molecular level. The self-assembly of hydrophobins, a class of fungi proteins that are known to be an important factor in fungal development,³ generates Janus-like structures through eight cysteine residues in their primary structure.⁴ Due to this pattern, hydrophobins have an asymmetric arrangement

of hydrophilic and hydrophobic patches, which undergoes self-assembly in aqueous solution at the water/air interface breaking the surface tension of water.⁵

In literature, we can find a wide variety of synthetic asymmetric particles with different properties, sizes and shapes;⁶ and the high complexity of some of these particles can meet the requirement of a new-generation of building blocks for materials design and assembly.⁷ In this context, the terms Janus and patchy particles frequently appear for describing these particles, however, they are sometimes misused due to their structural similarity. Therefore, Du *et al.* reviewed the key feature of different asymmetric particles,⁸ and depending on their classification the term “Janus particles” (JPs) will be used for objects with equally phase-separated domains (Figure 2.1a, b) while the term “asymmetric patchy particles” (APPs) for objects with non-equally separated domains (Figure 2.1c). However, the term “asymmetric particles” (APS) can be employed for describing both Janus and asymmetric patchy particles.

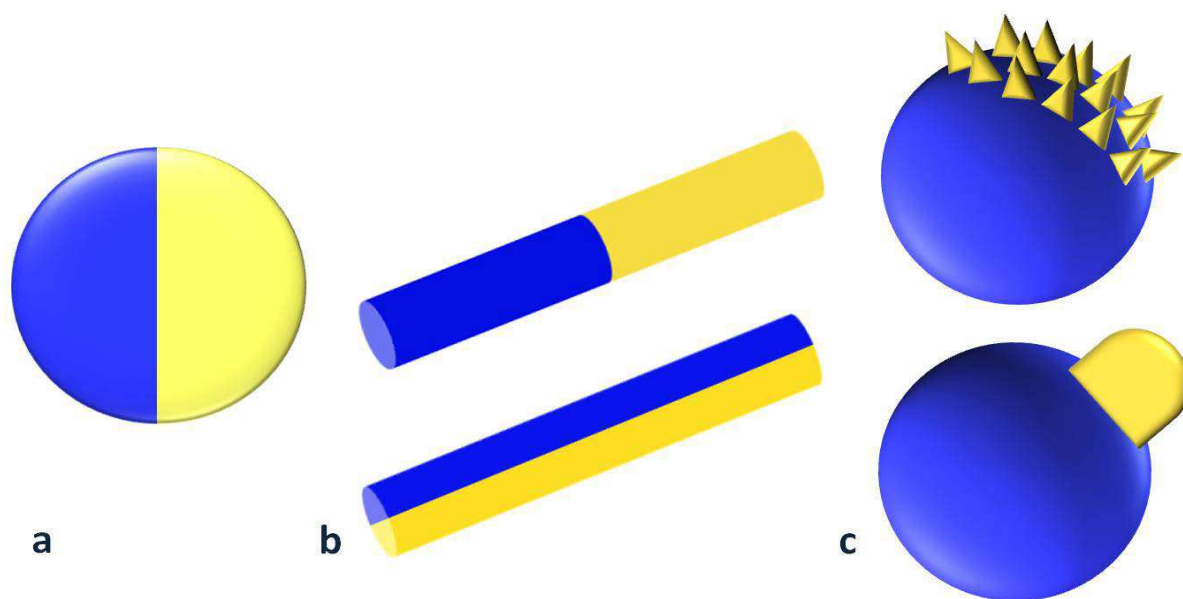


Figure 2.1 Schematic representation of asymmetric particles: a, b) Janus isotropic and anisotropic particles, respectively. c) Asymmetric patchy particles.

Asymmetric particles can be composed of different metallic, organic and/or inorganic materials, and can have isotropic or anisotropic shapes (Figure 2.1a and b, respectively). In recent years there has been great interest in the synthesis of more complex symmetric and asymmetric morphologies such as toroids and nanostructures with more complex domains, and a number of excellent reviews covering each of these particles have been published.⁸⁻⁹

However, only the asymmetric objects with different chemical and physical properties is of interest for the present chapter, starting with a view of the physical properties and applications of APs in the next section, and a brief description of synthetic approaches of these particles in section 2.3; the obtained experimental results will be presented in the following sections of this chapter.

2.2. Physical Properties and Applications

2.2.1. Adsorption at Interfaces

The asymmetry of Janus and patchy particles allows their strong adsorption at interfaces and this phenomenon attracted the attention of scientists to investigate and better understand this behavior. De Gennes advanced the popularity of Janus particles by describing the densely packed self-assembly of JPs at liquid-liquid or liquid-air interfaces. The films formed from “Janus grains” were reported as a “breathable skin” because interstices are always occurring between the grains, allowing the transport of the material between the two separated medium.¹⁰ Several theoretical and practical studies have been performed to predict the interfacial behavior of JPs.¹¹ A comprehensive theoretical study of the adsorption capabilities of JPs was reported by Binks *et al.* in 2001.¹² In this work they compared the adsorption of spherical JPs versus homogeneous particles at oil-water interface. Calculations concluded that the desorption energy of JPs was three times higher than for homogeneous particles.¹² Therefore, and in addition to the so-called Pickering effect (known for amphiphilic surfactants), JPs represent strong candidates as future emulsifiers. In a pioneering experimental work, Glaser *et al.* verified the qualitative confirmation of Bink’s theoretical prediction.¹³ It was shown that bi-metallic inorganic Au/Fe₃O₄ JPs exhibit a significantly higher interfacial activity at hexane-water interface and an efficiency to maintain their stability for an extended period of time as compared to respective homogeneous particles of the same size (Figure 2.2).¹³ Further contributions to theory and simulations appeared; discussing for example, the effect of the Janus balance (a dimensionless ratio between the work to transfer a JP from the oil-water interface into the oil phase and the work needed to move it into the water phase),¹⁴ similarly enhanced adsorption of the rod-shaped and the disk-shaped Janus objects,¹⁵⁻¹⁷ and the orientation of non-spherical JPs at interfaces.¹⁸⁻¹⁹ A

quantitative study to understand the effect of geometrical and chemical parameters on the configuration behaviors has also been done.²⁰ In addition to these examples, a simulation study using dissipative particle dynamics was used to study the mechanism of coalescence between two emulsion droplets stabilized with JPs.²¹

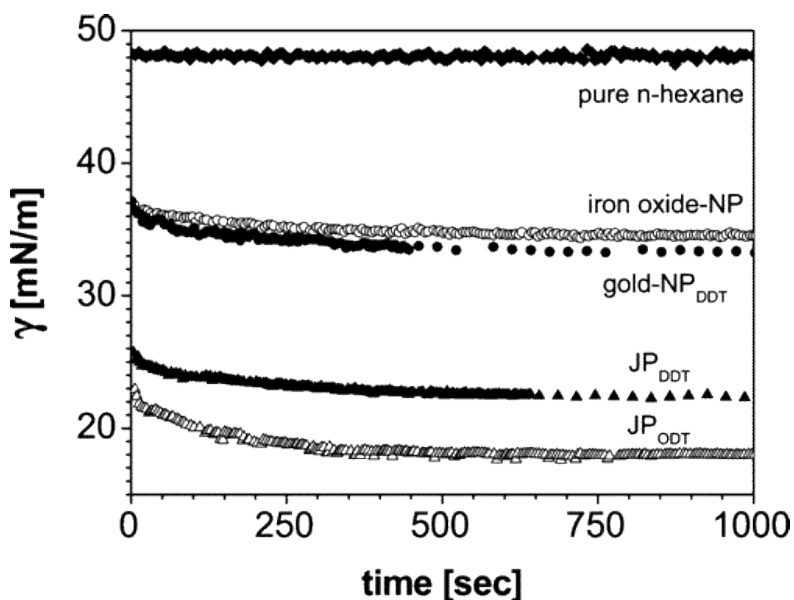


Figure 2.2 Interfacial tension vs. time (NP: homogeneous nanoparticles; JP: Janus particles. The gold moieties were modified using dodecanethiol (DDT) or octadecanethiol (ODT)), reprinted from Ref. (13).

Adams *et al.* reported a benchmark practical study in which they verified the importance of using well-defined JPs of limited roughness to be effective in stabilizing emulsions.²² It was found that asymmetrically metal-coated amphiphilic Janus microbeads unexpectedly displayed random orientations at air/water and water/oil interfaces, and this was a result of a relatively poor control of the roughness at the edge of the gold-glass boundary of the particles.²² Indeed, surface roughness or imperfections plays a crucial role and control the particle orientation, suggesting that only synthetic techniques where the surface roughness is kept to a minimum will be able to produce JPs that can truly exploit the full potential of their Janus nature.²² Capillary interactions (arising when distortions created by neighboring particles overlap) between irregular shape of micron-sized JPs have been investigated experimentally, and a brief review of the recent contributions was also stated.¹¹

2.2.2. Self-Assembly of Asymmetric Particles

The self-assembly (SA) of particles can spontaneously occur due to specific interactions with their environment, but it can also be triggered under the influence of, for example, external fields. SA is one of the unique properties of APs that is related to their asymmetric nature (structure and/or functionalization), and it is of fundamental interest for the fabrication of complex materials with new features within a hierarchical structure.

Amphiphilic APs, hydrophobic on one face and charged on the other, can spontaneously undergo a SA process.²³ Theoretical contributions based on simulations to predict the patterns of SA of APs have been proposed by different authors,²⁴⁻²⁶ which included in addition experimental investigations for the work from Jiang *et al.*²⁷ Practically, the first example of controlled SA of JPs was provided by Müller's and co-workers.²⁸ The authors observed the formation of supramicelles from amphiphilic particles composed of a polybutadiene (PBD) core and a compartmentalized corona consisting of a poly(methacrylic acid) (PMAA) and a polystyrene (PS) hemisphere. In aqueous solution the majority of the PS-PMAA Janus micelles form spherical supermicelles above a critical aggregation concentration of around 0.03 mg/L.²⁸ Controlled self-assembly of amphiphilic colloid, Janus discs,²⁹ and cylindrical JPs was also observed.³⁰ Pradhan *et al.* studied the SA of amphiphilic gold nanoparticles in various solvents.³¹ The formation of clusters with a size in the range of several hundreds of nanometers, depending on the solvent used was observed.³¹ Nie *et al.* showed that amphiphilic three-phase JPs with different volume fractions of the constituent phases form clusters with different aggregation numbers.³²

Dipolar JPs, with an opposite electric charge on their two hemispheres, also experience SA into clusters as demonstrated using simulations³³ in addition to experiments performed by Granick's group,^{27, 33} who observed the assembly of dipolar particles into chains in the aqueous phase, the chain length varied from three to eight particles.³³ The same behavior was also reported by Velev's group.³⁴⁻³⁵

Directed SA of JPs under external electric fields requires the particles to exhibit a surface charge. Velev's group investigated intensively the structure formation of ensembles of metallodielectric JPs (PS microspheres with 50% surface metal coating) using different AC electric field intensities and frequencies.³⁶⁻³⁹ At low field frequency and high intensity, the particles could move perpendicularly to the field lines due to unbalanced liquid flows around

each half of the particle.³⁶ The PS hemispheres were facing the field according to the direction of motion, and this was attributed to the fact that, the electric double layer of the gold-coated hemispheres experiences a much stronger electroosmosis, resulting in unbalanced liquid flows which force the particles to move by induced charge electrophoresis (Figure 2.3a and b).³⁶ Whereas at high field intensity (> 10 kHz) the JPs formed staggered chains parallel to the field direction (Figure 2.3c).³⁷ Chaudhary *et al.* employed the directed SA to induce vertical alignment of silica rods (~ 2 μm long) which followed by their SA through electroosmosis under an AC electric field, as a preparation for the tip-functionalization of the rods with gold.⁴⁰ Recently, Zhang *et al.* investigated the effect of medium conductivity, AC-field frequency, and JP surface chemistry on their assembly in aqueous suspensions.⁴¹ The results demonstrated that the assembly structures of JPs can be rapidly and actively controlled by tuning these parameters which can become useful for guiding the rapid synthesis of highly hierarchical structured materials from anisotropic building blocks.⁴¹

Particles with magnetic properties recently attracted the interest to understand their assembly under external magnetic fields. Smoukov *et al.* studied the assembly behavior of structures composed of JPs – polystyrene spheres with a thin magnetic iron shell evaporated on one hemisphere.⁴² Two types of structures were observed, staggered and double chains, depending on the thickness of the magnetic layer. The double chain structure was only observed for particles with 7–8 nm Fe layers, while the staggered chain structure was observed for particles with higher magnetic moments (34 nm-thick layer). The structures also had the advantage that the particle interactions could be disassembled on demand by remote demagnetization.⁴² In the same context, Ren *et al.* reported the field directed assembly of PS – iron oxide half-coated particles (Figure 2.3d, e).⁴³ The extent of iron oxidation was identified as the key parameter in determining the assembly behavior, i.e., formation of staggered chains, double chains, or no assembly).⁴³ In addition, the effects of particle volume fraction, thickness of the iron oxide cap, and assembly time on the final assembly behavior were investigated.⁴³

In disagreement with Smoukov *et al.* work,⁴² samples obtained at a specific average deposition rate with varying cap thickness showed the same assembly behavior.⁴³ The authors proposed that these two observations can be reconciled when the oxidation of the iron caps is taken into account.⁴³ Yuet *et al.* showed that superparamagnetic JPs form chain-like or mesh-

like structures in a uniform magnetic field.⁴⁴ They found that the complexity of the structures can be easily modified by the particle density and composition.⁴⁴

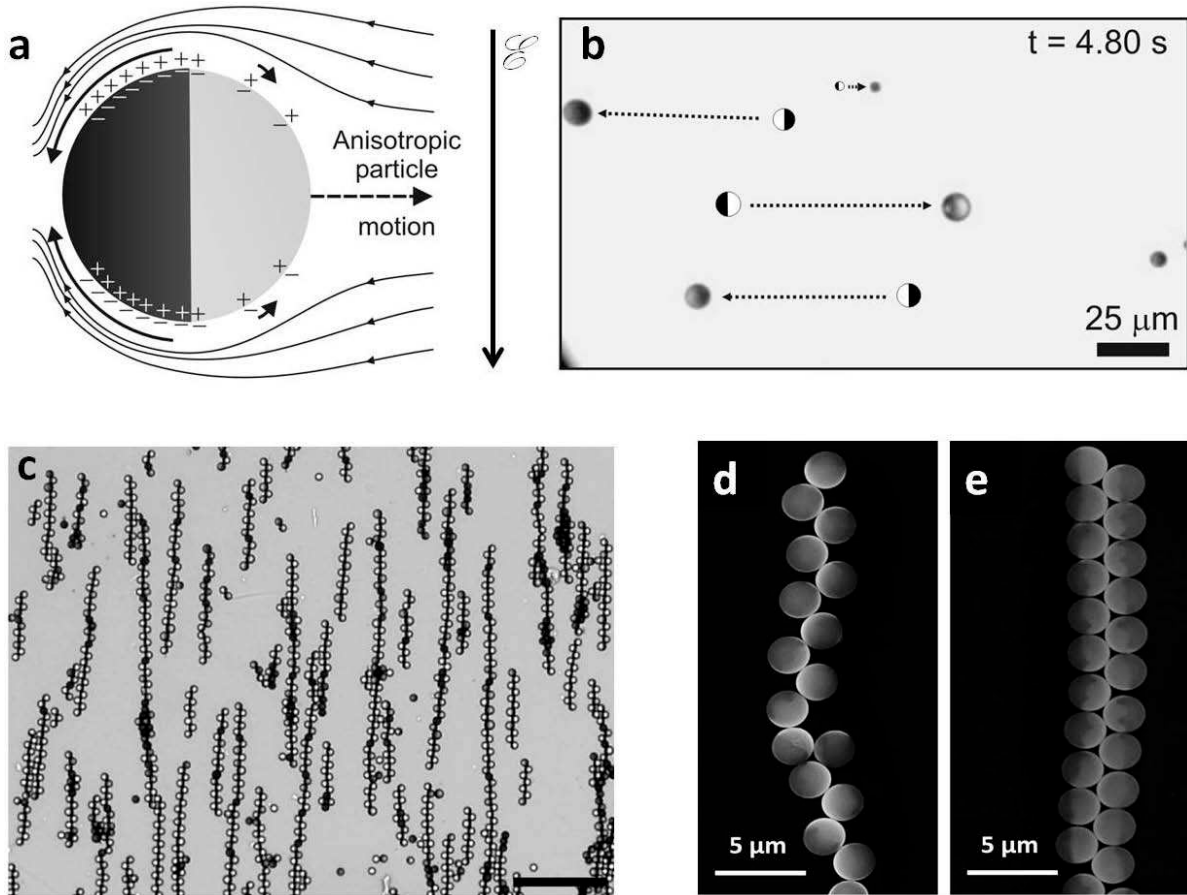


Figure 2.3 a) Scheme of the induced charge electrophoresis (ICEP). The electric double layer on the gold side (black hemisphere) is more strongly polarized and thus drives a stronger induced charged electroosmosis slip (arrows) than the PS side, resulting in ICEP motion in the direction of the dielectric side, b) Optical micrograph for the distances traveled by different JPs after 4.8 s of applying 14 kV/m field intensity and 1 kHz frequency. Both adapted from Ref. (36). c) Optical micrograph of staggered chains of 5.7 μm diameter JPs formed at 5.6 kV/m at 40 kHz AC field frequency. The scale bar is 70 μm , reprinted from Ref. (37). d, e) High-resolution SEM images of particle assemblies obtained after complete drying of the solution under continuous exposure to the magnetic field: (d) staggered chains structure and (e) double chains structure. Lighter areas on the particles are iron oxide caps, and darker areas are unmodified polystyrene particle, adapted from Ref. (43).

2.2.3. Applications of Janus Particles

The ability of amphiphilic JPs to get adsorbed at liquid-liquid or liquid-air interfaces that we discussed previously (section 2.2.1.) promotes the use of these particles as emulsion and foams stabilizing agents as an alternative to conventional surfactants.⁴⁵⁻⁴⁸ Micrometer-sized gold-silica JPs were used as an effective stabilizer of emulsions by adsorption of a monolayer at oil-water interface (Figure 2.4a). The resulted near-spherical and non-spherical oil droplets were found to be remarkably stable without coalescence for more than one year.⁴⁹ APs with arms were adapted by Meng *et al.* to emulsify water – toluene mixtures, forming oil-in-water emulsions at a very high internal phase content with rather low concentration of particles.⁵⁰ Müller's group indicated the superior performance of JPs in PS and poly(methyl methacrylate) (PMMA) emulsion relative to common stabilizer particles;⁵¹ and they also demonstrated very recently, that Janus micelles are well suited as supracolloidal dispersants for carbon nanotubes.⁵² In a novel extension to the encapsulation of inorganic materials into polymeric JPs, Teo *et al.* synthesized silica-PS asymmetric nanoparticles, with the polystyrene portion loaded with magnetic nanoparticles, which can be used to stabilize oil-water emulsions that can be spontaneously broken on application of an external magnetic field.⁵³ As solid surfactants, APs with different morphologies such as mushroom-like or nanosheets-like particles were also proposed as good emulsifiers for immiscible liquid mixtures.⁵⁴⁻⁵⁵

Furthermore, by selective functionalization of the “outer” and “inner” sides of the emulsion droplets with active compounds or catalysts, it was possible to manipulate the properly designed assemblies using external stimuli such as light or magnetic field to have optically different appearances.⁵⁶⁻⁵⁷ One-dimensional APs with a red and a green mirror at its opposite sides were selectively oriented at the interface according to the polarity which led to a homogeneous emulsion droplet.⁵⁶ Ou *et al.* employed Au-CNT (carbon nanotube) and Au-Ni-CNT micro-rods for stabilizing dichloromethane (DCM)/water emulsion droplets.⁵⁷ By functionalizing the Au tip with alkane-thiol it became more hydrophobic than CNT surface, hence a black sphere was formed when a drop of DCM was introduced into water dispersed with the Au-CNT nano-rods, as the CNTs pointed to the surrounding water (Figure 2.4b).⁵⁷ However, when the attached alkane-thiol was irradiated with UV light, the amphiphilicity inverted and the Au side oriented now to the water phase, consequently, the color of the droplet flipped from black to golden (Figure 2.4c).⁵⁷ Due to the presence of a Ni segment in

the Au-Ni-CNT hybrids, it was possible to manipulate and trap the emulsified droplet via an external magnetic field.⁵⁷

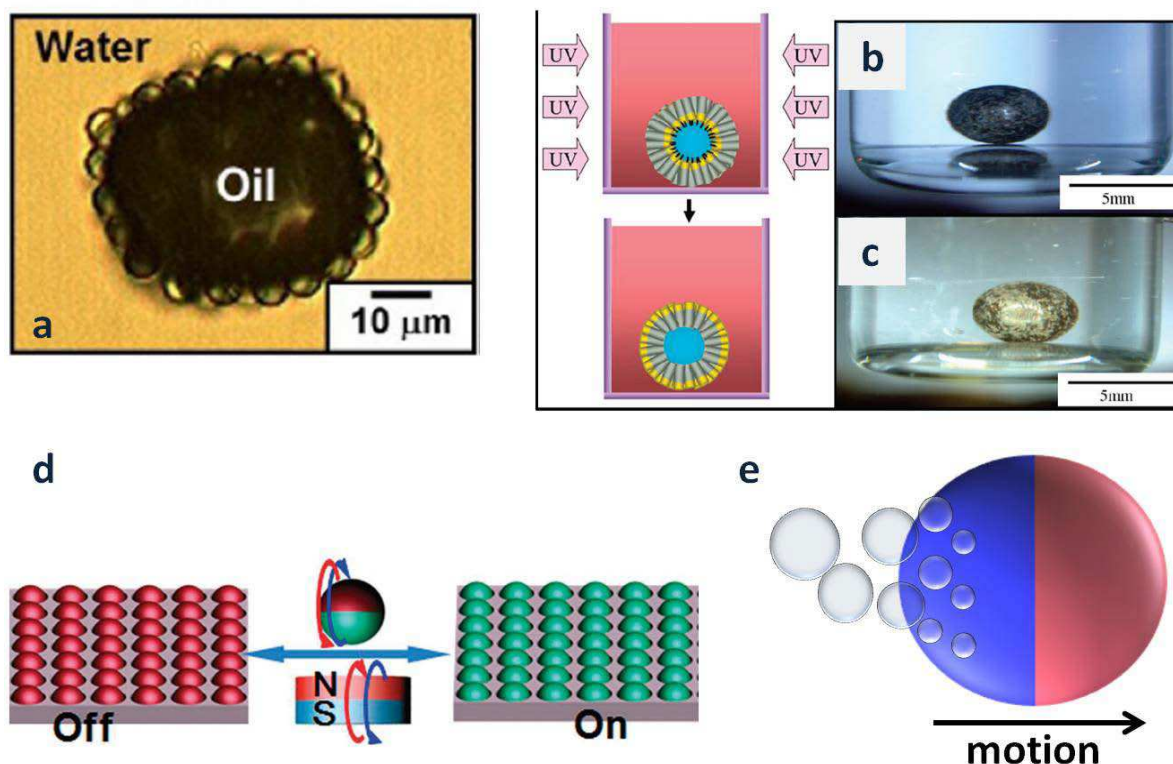


Figure 2.4 a) Optical image for oil-in-water emulsion stabilized with Au-SiO₂ Janus particles, adapted from Ref. (49). b, c) Optical images show the switched orientation of Au-CNT rods in oil-in-water emulsions before (black sphere) (b), and after (golden sphere) (c) the UV irradiation, adapted from Ref. (57). d) Schematic representation of a fluorescent switch of Janus particles controlled by varying the direction of an external magnetic field, each particle serves as an individual pixel. Adapted from Ref. (65). e) Induced motion of JP by bubbles production at one side of the particle.

Taking the advantage of orientation in external fields, APs with magnetic compartments or a large contrast in dielectric properties of both sides allow also their application as probes.⁵⁸⁻⁶¹ Microscopic spheres modified with a pH dependent charged groups, oriented under electric field only at a certain pH range, thus enabling the fabrication of a pH sensitive sensor.⁵⁸ Xu et al. achieved a significant improvement with dual-functional probes that are based on dumbbell Au-Fe₃O₄ nanoparticles (NPs).⁵⁹ The structure contained both a magnetic (Fe₃O₄) and an optically active plasmonic (Au) unit, which facilitated the attachment of different chemical functionalities for target-specific imaging and delivery applications.⁵⁹ Asymmetric magnetic fluorescent particles were designed to emit varying intensities of light in a manner

that depends on the particle orientation in an external electric field.⁶⁰ The Brownian motion of similar objects being placed into a specific environment led to their blinking depending on the surrounding conditions, thus enabling their use as modulated optical nanoprobe (MOONs).^{60, 62}

One of the very interesting applications of JPs is the fabrication of switchable devices for display technology such as electronic papers (e-papers). In this technique, microcapsules (acting as pixels) containing white and black particles with different charges are sandwiched between transparent electrodes. The presence of electric field causes the movement of one of the two kinds of particles within the microcapsules to the top electrode which changes the color of the pixel.⁶³ However, higher resolution and colored display can be performed by using JPs owning an electrical and optical asymmetry within single particle pixels. Nisisako *et al.* demonstrated the use of carbon black-titanium oxide Janus microspheres under an electric field to be suitable for e-paper.⁶⁴ Chen and coworkers introduced bifunctional magnetic-fluorescent hemispheres within single structures of JPs to develop a magnetically switchable display; the two hemispheres being able to endow themselves with excellent fluorescent and magneto-responsive features (Figure 2.4d).⁶⁵ Organic-inorganic magnetic APs also showed high performance and possibilities for e-papers.⁶⁶⁻⁶⁷

APs have also been employed for designing controlled self-propelled nano- and microswimmers.⁶⁸⁻⁷⁰ Such swimmers are of great interest for a wide range of application including ions sensing,⁷¹ cancer cell screening⁷² and drug delivery.⁷³⁻⁷⁴ By introducing reactive materials into the structure of particles, it is possible to generate the motion. The decomposition of hydrogen peroxide by metal surfaces such as platinum, is the most commonly used catalytic reaction which leads to the motion through several mechanisms such as bubble propulsion (Figure 2.4e) and self-electrophoresis.⁷⁵ The reported contributions from different groups in the frame of autonomous swimmers will be developed in details in chapter 3.

The interesting properties of JPs have attracted attention to be exploited also for biomedical applications like molecular imaging and bimolecular labeling, as well as drug delivery. In this field it is important to have spatially separated functionalities, uniform size, biocompatibility and efficient stimuli-response of JPs.⁷⁶ Lahann's group reported a novel type of microstructured bio-hybrid polymer materials with spatially-controlled affinity towards humane endothelial cells.⁷⁷ The formed cell-particle conjugates were detected directly and it

was possible to investigate.⁷⁷ In the same context, FePt-Au asymmetric NPs have been employed as probes, in order to study their application for in vitro molecular magnetic resonance imaging (MRI) of biological targets which demonstrated positive results.⁷⁸ A combined imaging and therapeutic method (theranostic) was developed by Hu and Gao.⁷⁹ They used JPs that have been loaded with a fluorescent dye at one side, and superparamagnetic NPs on the other side. The results demonstrated orientation control of the nanocomposites by external magnetic fields, cell imaging, and an innovative magnetolytic therapy on tumor cells.⁷⁹ Janus hydrogel particles with magnetic anisotropy were prepared and used to encapsulate mammalian cells inside the hydrogel part of the particles to maintain optical performance, and to reduce the contact between cells and magnetic particles.⁸⁰ A good biocompatibility, degradability and superparamagnetic properties of these JPs were shown.⁸⁰ For oral drug delivery, a differentially biodegradable polymer was introduced into the structure of JPs to end with particles that have two different polymers in the opposite hemispheres.⁸¹ In this work, a new type of stimuli-sensitive JPs was reported that allows the selective, pH-dependent degradation of individual compartments. Both compartments were initially stable at low pH (3.0), but only one compartment degraded at physiological pH after a defined time.⁸¹ Biocompatible polymeric Janus NPs were demonstrated by Xie *et al.* for the first time to encapsulate a hydrophobic drug (paclitaxel) on one side and a hydrophilic drug (doxorubicin), anticancer drugs, on the other side of the particles.⁸² In vitro release profile of drug-loaded NPs showed that more than 60% of each drug was released during the first 24 hours.⁸²

2.3. Synthetic Strategies for the Preparation of Asymmetric Particles

The past decade has witnessed a massive progress in developing various synthetic strategies for the preparation of APs with diverse functionalities, as well as scaling-up the quantity synthesized. However, we are not going to detail all these methods as it is outside the focus of the present thesis. Instead, a brief view will be given, and for full description of these strategies, several excellent reviews that cover the preparation of APs can be found in the literature.^{6, 8-9, 76, 83-90} Selective surface modification of particle monolayers immobilized on an interface is one of the first methods that has been employed to synthesize APs (Figure 2.5a). In this case, the part of the particles which is protected by the surface will not get modified.^{48, 91-99} It represents a simple procedure and can be adapted to variety of particles

with different sizes, and recently it has been extended to non-spherical micro-rods in order to modify at one tip.⁴⁰ A significant problem facing this technique is the difficulty to scale-up the production to the required level for industry, as the preparation is performed using a one or two dimensional interface. The deposition of materials within templates also provides simple procedure for synthesizing well defined APs.^{57, 100-102} For surface patterning of JPs, particle lithography¹⁰³ has been employed. Recently, microfluidic techniques (Figure 2.5b) have been shown as a promising tool for the production of JPs with remarkable control in shape and functionality. The general microfluidic setups include, for example, hydrodynamic channels to produce droplets,^{32, 44, 61, 64, 104-105} electro-hydrodynamic co-jetting¹⁰⁶⁻¹⁰⁹ and multi-barreled capillaries.¹¹⁰

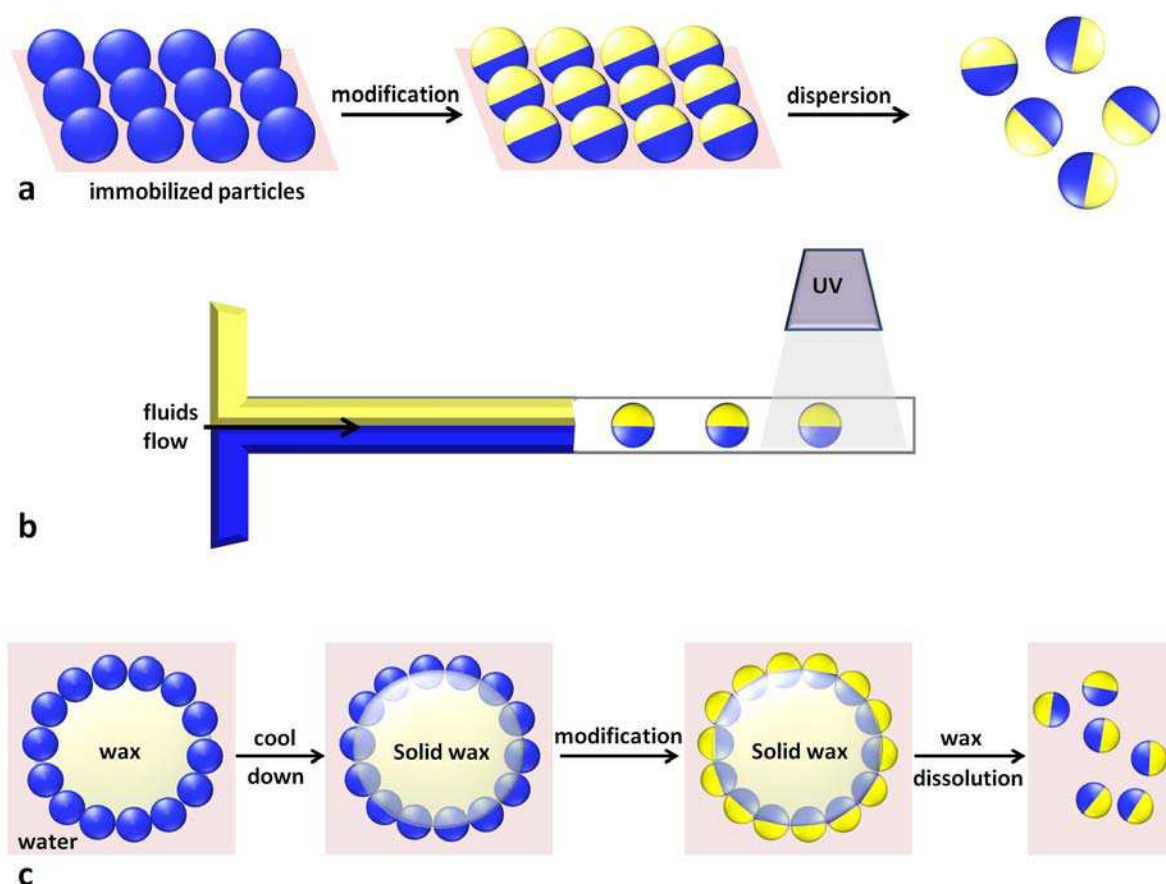


Figure 2.5 Schematic illustrations for the preparation of asymmetric particles. a) Modification of immobilized monolayer particles, b) Janus particles preparation by microfluidic techniques. c) Pickering emulsion based method.

On the other hand, the emulsion-based templates (Figure 2.5c) can be reported as bulk methods as they enable the synthesis of APs in large quantities at the interfaces of Pickering

emulsions.¹¹¹⁻¹¹⁸ Internal phase separation accompanied by solvent evaporation technique,^{66, 119} seeded emulsion,¹²⁰⁻¹²⁴ and dispersion polymerization¹²⁵ were also adapted to produce polymer-polymer JPs at a large scale. Other techniques such as block copolymer SA,¹²⁶ terpolymers SA¹²⁷ and spinning disk method,¹²⁸ can also be considered as bulk methods.

Another interesting approach is based on the irradiation of nano-¹²⁹ and microparticles¹³⁰ with light to induce the asymmetry.¹³¹ The technique uses UV or visible photons to efficiently break chemical bonds into photoactive molecules which induces rapid thin film deposition via very moderate beam intensities.¹³⁰ The deposition of transition metal ions on surfactant-stabilized single walled carbon nanotubes (SWCNTs) was activated by alternating electromagnetic (EM) fields in the radio frequency,¹³² microwave,¹³³ and optical regimes.¹³² The applied fields, similarly to bipolar electrochemistry method, develop polarization potentials at the tube extremities that readily drive electrochemical reactions in the presence of metal salts.¹³³ Several examples of APs exhibiting different shapes and scales that have been reported in the literature with various preparation techniques are shown in Figure 2.6.

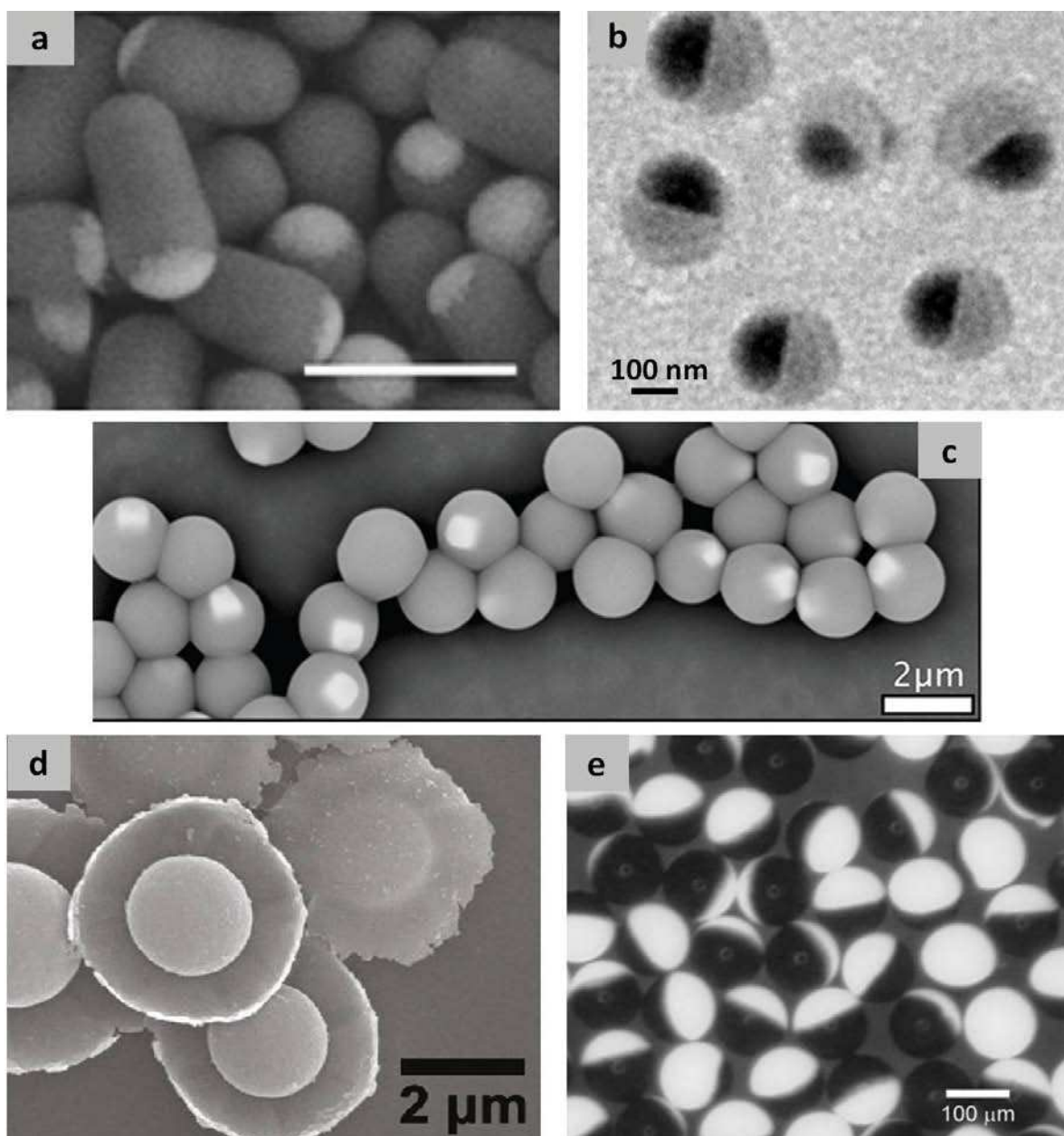


Figure 2.6 a) SEM image of gold-tip-coated silica rods by immobilization at interface, scale bar: 2 μm , adapted from Ref. (40). b) TEM micrograph of the acorn-shaped morphology of APs composed of two separated synthetic polymer batches prepared by seeded emulsion polymerization, adapted from Ref. (120). c) SEM image of organo-silica polymer spheres with a single hematite micromagnet embedded, obtained by seeded dispersion polymerization, adapted from Ref. (125). d) SEM image of asymmetric Janus polymer particles prepared by solvent evaporation in emulsion droplets, adapted from Ref. (119). e) Optical micrograph of monodisperse bicolor polymeric particles obtained from microfluidic technique, adapted from Ref. (64).

2.4. Capillary-Assisted Bipolar Electrodeposition

Capillary electrophoresis (CE) spread significantly during the past three decades, as it moved from a fundamental academic research field to a widely accessible and modern separation technique available in any analytical chemistry laboratory.¹³⁴ The developments of detectors based on fluorescence,¹³⁵ electrochemistry,¹³⁶ or mass spectrometry have led to various applications and sensitive detection of small organic or inorganic species, biomolecules as well as bioparticles.¹³⁷⁻¹³⁸ Recently, this technique has been employed for a novel application in materials science called “Capillary Assisted Bipolar Electrodeposition” (CABED) which has been demonstrated by Warakulwit *et al.* prior to the present thesis (see section 1.5.5.3.).¹³⁹⁻¹⁴⁰ By using the CABED technology, the bulk preparation of APs by bipolar electrodeposition¹⁴¹⁻¹⁴² was possible for the first time. As this setup was used in the present thesis for the modification of anisotropic objects (Figure 2.7), a description of the instrumentation will be given here before presenting the obtained results in the following sections.

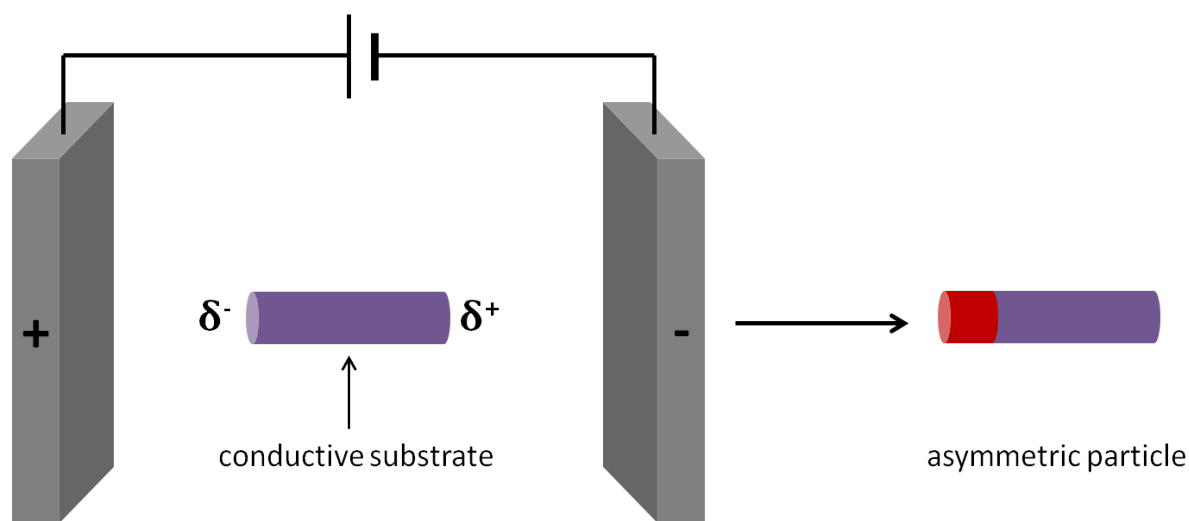


Figure 2.7 General principle of bipolar electrochemistry used to prepare asymmetric particles, adapted from Ref. (143).

2.4.1. Instrument Description

Most mentioned applications of the CE are based on the separation of analytes, which in turn depends on the electric charge and size of the analytes that travel through the capillary under an external electric field. The motion of the charged species in the CE is driven by the combination of two competitive forces. The first one is the electrophoretic flow (EPF), induced by the attraction of the charged species to the electrode of the opposite charge. Thus an analyte with a higher charge and a smaller size will have a better electrophoretic mobility. The second force is the electroosmotic flow (EOF), this one is induced by the negatively charged wall of the capillary, being rich in silanol groups because it is made of glass in our case, which develops a double layer by attracting the protons in the solution. These protons can be considered as a fixed or stationary layer that will direct the motion of the ions in the bulk toward the cathode under the influence of the applied electric field. Figure 2.8a shows a photograph the CE instrument used to perform our experiments. The capillary chamber usually consists of two vials containing the solvent, with an anode in the inlet, and a cathode in the outlet vial. The capillary is inserted into the chamber with both ends dipped into the electrode (platinum) compartments in such a way that the extremities are located outside from the hollow electrodes (Figure 2.8b). This is to prevent the bubbles generated during the electrolysis from entering the capillary. Before reaching the cathode, the capillary passes in front of a detector (UV-visible detector) which allows monitoring of the materials flow. The CE we used can provide a voltage of up to 30 kV, which induces an electric field of 100 kV/m with a 30 cm-long capillary as a typical length.

In this context, the intrinsic presence of favorable conditions for bipolar electrochemistry (very high voltage) allows using the CE setup not only as an analytical technique, but also as an experimental platform where high electric fields play a crucial role for the production of micro- or nanomaterials. Such high electric fields that are applied in a very safe way by the CE might be tricky with other setups because of issues related to the establishment of a high electric field across a short distance. On the other hand, the topic of electrochemical modification of the analyte during the separation through CE is by far under-investigated. The CABED has the advantage that electroosmotic flow promotes the transport of the analyte from the inlet to the outlet vial. Moreover, the small inside diameter (100 μm) of the capillary allows efficient dissipation of the heat generated by the application of such high voltages,¹³⁴ and provides a resistive current pathway that is valuable for faradaic reactions to occur.

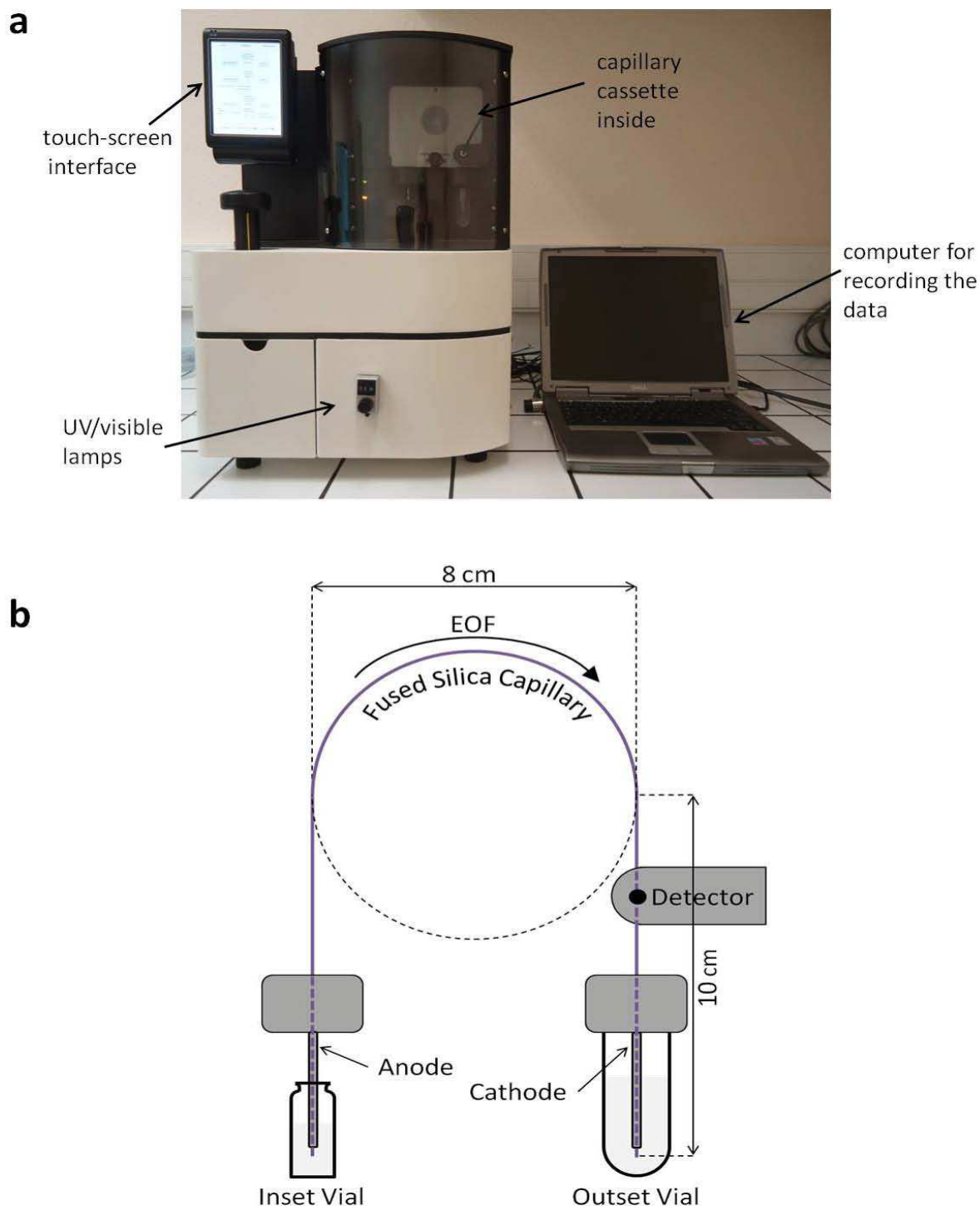


Figure 2.8 a) Photograph of the capillary electrophoresis set-up (Wyn-CE, WynSep) used in the experiments. b) Schematic illustration of the capillary inside the electrode compartments passing in front of the detector close to the cathode electrode, adapted from Ref. (143).

To modify our particles, carbon microtubes (CMTs) for example, the anodic vial is filled with a suspension of the tubes in a solution of the desired electroactive precursor that need to be

deposited. Application of the electric field will generate the EOF of the electrolyte which will carry the CMTs towards the cathodic vial (monitored by the detector which is connected to the computer) where the modified particles will be collected for further characterization.

2.4.2. Metal Deposition on Carbon Microtubes

The CABED was employed for the preparation of a complementary series of APs with respect to previous investigations from Warakulwit and Loget in order to show the versatility of this set-up.¹³⁹⁻¹⁴² The bipolar electrodeposition of metals on CMTs occurs when the tubes travel across the capillary, this leads to the fabrication of hybrid materials as a result of the localized metal reduction at the cathodic pole and the solvent oxidation (water) at the anodic pole of tubes (Figure 2.9).

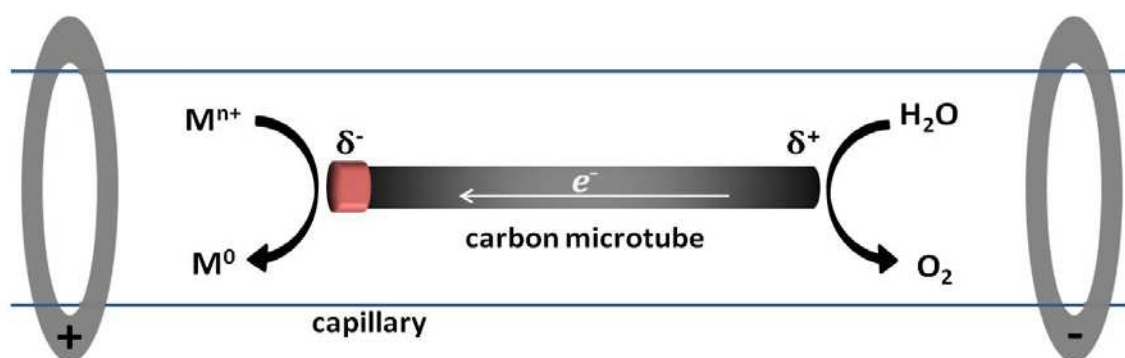


Figure 2.9 Schematic illustration of the modification of a CMT with a metal in the capillary during the CABED.

The major reason for choosing CMTs as a substrate was the suitable length (few tenth of μm), and width (few hundreds of nm (Figure 2.10b)) that they offer, which enable the easy visualization of the achieved modification by standard optical microscopy and SEM. These CMTs were produced by chemical vapor deposition using a porous aluminum oxide membrane serving as a template.¹³⁹ After an acidic digestion of the template (Figure 2.10a), the fairly homogeneous tubes were recovered as a powder.

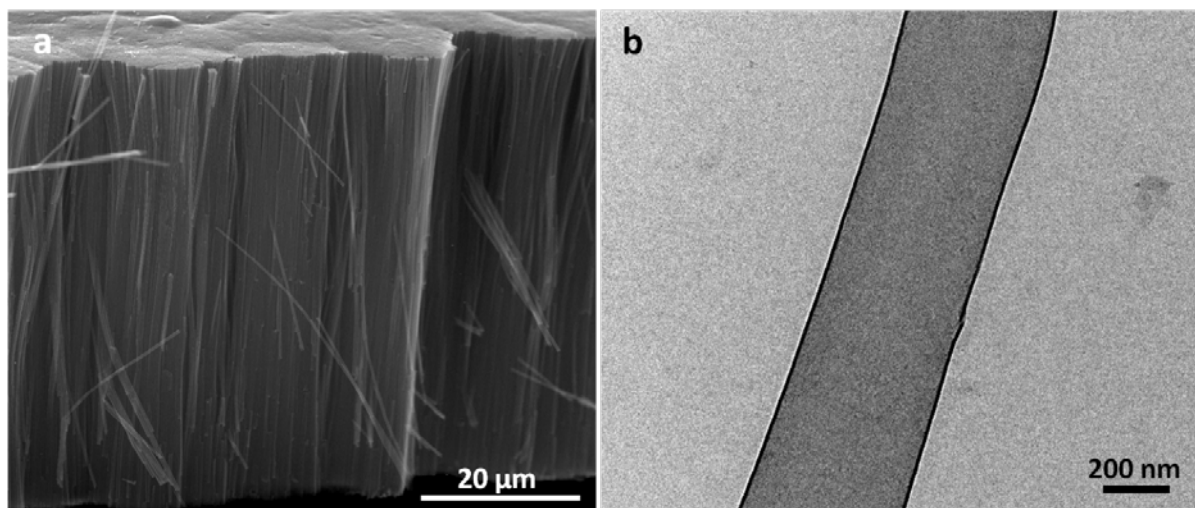


Figure 2.10 a) SEM image of the prepared CMTs sample after dissolving the aluminum oxide template. b) Transmission electron micrograph of a CMT.

Redox couple	E° (V vs. NHE)	ΔV_{\min} (V)	\mathcal{E} (V/m)
$\text{O}_2(\text{g}) / \text{H}_2\text{O}$	+ 1.23		
$[\text{Au}^{\text{III}}\text{Cl}_4]^- / \text{Au}(\text{s})$	+ 0.99	+ 0.24	12,000
$\text{Ag}^+ / \text{Ag}(\text{s})$	+ 0.80	+ 0.43	21,500
$[\text{Pt}^{\text{IV}}\text{Cl}_6]^{2-} / \text{Pt}(\text{s})$	+ 0.73	+ 0.50	25,000
$\text{Ni}^{2+} / \text{Ni}(\text{s})$	− 0.26	+ 1.49	74,500

Table 2.1 Formal standard potentials (E°) of relevant redox couples, the minimum potential (ΔV_{\min} , based on the difference between the E° of the metal reduction and water oxidation redox couples) and typical electric field (\mathcal{E} , based on a 20 μm -long CMT) values necessary to trigger the bipolar electrodeposition are given.

The electric field necessary for achieving the electrodeposition is inversely proportional to the length of the bipolar substrate as we discussed before in section 1.2. Thermodynamic calculations gathered in Table 2.1 shows that the electrodeposition of a range of metals from ionic precursors vs. the water oxidation needs typically electric fields of several tenths of kV per meter. The silver was selected to be reduced in a bulk on CMTs, because of its intermediate redox potential among the other metals.

The suspensions of CMTs were prepared by adding about 0.1 mg of CMTs to a 10 mM aqueous solution of either K_2SO_4 or Ag_2SO_4 ($V = 0.5$ mL). Prior to use, these mixtures were

sonicated in order to accelerate the formation of a suspension, but only for a short time (45 s) to avoid excessive breaking of the tubes. The capillary used was a fused silica capillary with a 100 μm diameter and 30 cm length. The suspensions were put in the inlet vial and introduced into the capillary by the hydrodynamic injection for 15 s. The short injection time was selected in order to maintain a low concentration and prevent clogging of the capillary, which has been previously observed with carbon substrates.¹⁴⁰ A potential of 10.1 kV was applied for 2 or 5 min, and a thermal regulation of the capillary ($T = 25 \pm 1^\circ\text{C}$) was maintained. The UV electronic absorption was monitored at the capillary outlet at a single wavelength. Figure 2.11 shows typical optical detection signals by light absorption measurement at $\lambda = 254$ nm recorded for 5 minutes when the potential is applied. The bottom signal which is a control experiment recorded with a solutions of Ag_2SO_4 has no detectable features; whereas the top trace corresponds to the solution containing Ag_2SO_4 and the CMTs. The latter exhibits typical spikes, assigned to the migration of the CMTs aggregates within the capillary.

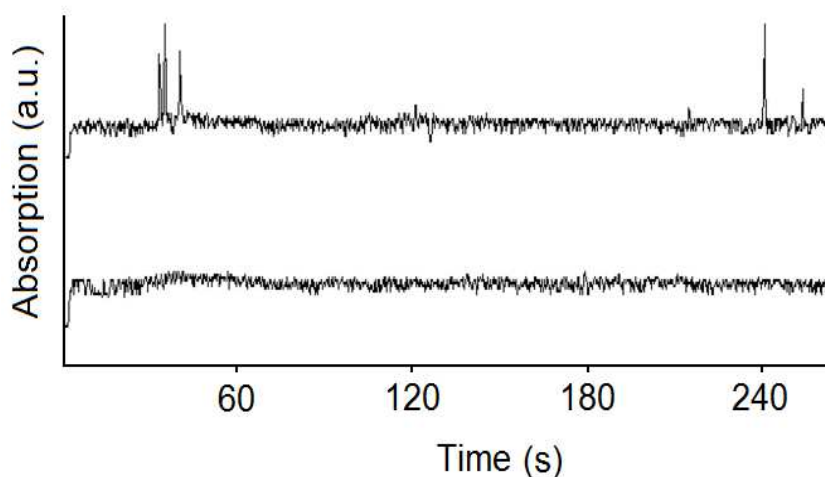


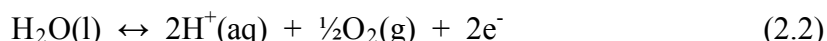
Figure 2.11 Typical optical detection signals at $\lambda = 254$ nm recorded from a 10 mM solution of Ag_2SO_4 with (top) and without CMTs (bottom), adapted from Ref. (143).

The CMTs are naturally collected in the outlet vial after travelling through the capillary. This causes a dilution of the suspension of CMTs and therefore a shorter run of 2 minutes was also performed for ease of characterization. The sample was then directly collected from the capillary, washed, and either dropped between two glass slides or transferred onto a conductive plate prior to characterization by optical microscopy and SEM.

The theoretical minimum potential value (ΔV_{\min}), required to induce the electrodeposition was calculated as the difference between the E° values of the two required redox reactions. If we consider the electroreduction of silver cations, the following reactions should occur at the extremities of the CMT:



at the cathodic pole and:



at the anodic pole. The electrodeposition can only take place when the applied electric field is high enough to promote simultaneously these two redox reactions. The E° values of the two reactions given in table 2.1, indicates that the necessary difference of polarisation potential generated between the two extremities of the CMT should be higher than $\Delta V_{\min} = 1.23 - 0.80 = 0.43$ V. It is noteworthy that this minimal thermodynamic value is based on standard conditions, but the real value should take into account non-standard conditions in terms of concentrations, pH, temperature, and pressure in addition to eventual overpotentials. The CMTs used in this study had a characteristic average length of 20 μm (Figure 2.12a). Therefore, an electric field of $\mathcal{E} \sim 33.7$ kV/m was applied which is higher than the theoretical estimated value (table 2.1) to trigger the silver electrodeposition on the CMTs.

The optical images of the CMTs collected at the capillary outlet (Figure 2.12b-d) show CMTs ($l = 12.3 - 18.2$ μm) exhibiting a single-point modification with a silver deposit. This selection of properly modified tubes is representative of the whole sample. Indeed, the effective polarization is directly proportional to the length of each CMT and as a general trend longer tubes exhibit a bigger deposit in comparison to smaller ones. This is clearly visible in Fig. 2.12 (right) because the Ag deposit on a long tube (b, $l \sim 17.2$ μm) is twice bigger than the one on a shorter CMT (d, $l \sim 12.3$ μm) with a typical diameter of 3.3 versus 2.1 μm .

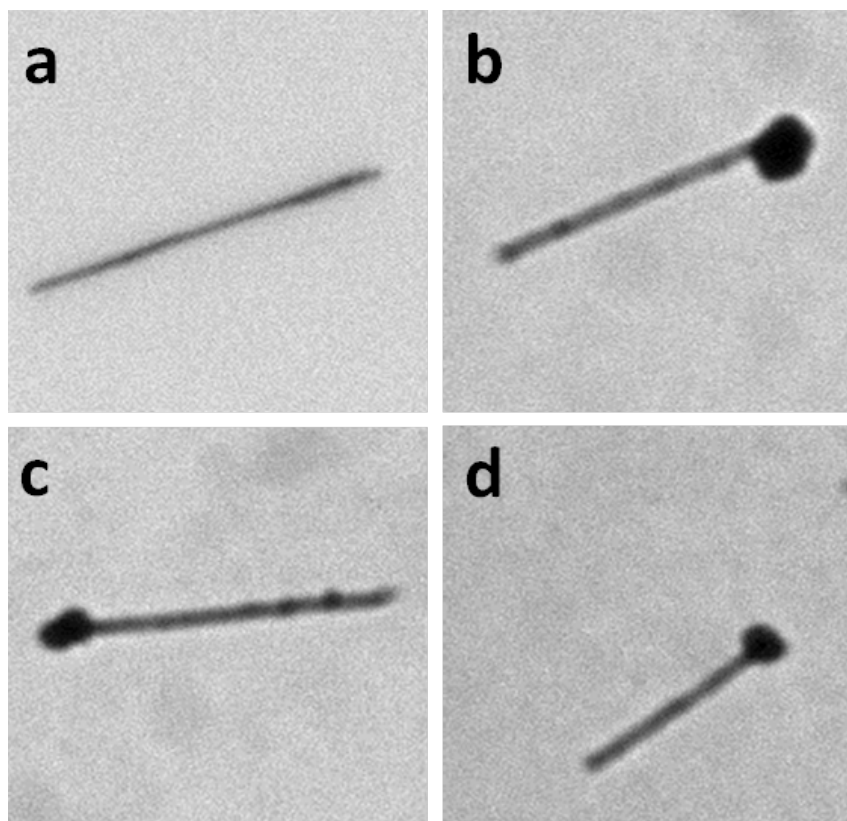


Figure 2.12 Transmission optical micrographs (magnification 50 times) of an unmodified CMT (a) and selection of CMTs modified with a silver deposit (b-d) using capillary assisted bipolar electrodeposition. Square size = $24 \times 24 \mu\text{m}$. Adapted from ref. (143).

The data obtained by optical microscopy allow concluding on the successful metal deposition, but scanning electronic microscopy (SEM, Hitachi, TM-1000) was performed in addition in order to image the hybrid Ag/CMTs with higher contrast and resolution. Figure 2.13 shows three representative images of modified CMTs, as well as a high resolution zoom centered on a silver deposit. These images are perfectly consistent with the previous optical ones; moreover they allow analyzing in more details the shape of the silver deposits, which can vary from polycrystalline (a) to a more regular hexagonal crystal structure (b-d). Several other, more dendritic, morphologies have also been observed. The same relationship between the length of the tube and the size of the deposit is obtained when comparing the $7.6\mu\text{m}$ -long CMT (deposit with hexagonal shape with $1 \mu\text{m}$ length) and the $16.8\mu\text{m}$ -long CMT (deposit with $1.8 \mu\text{m}$ length).

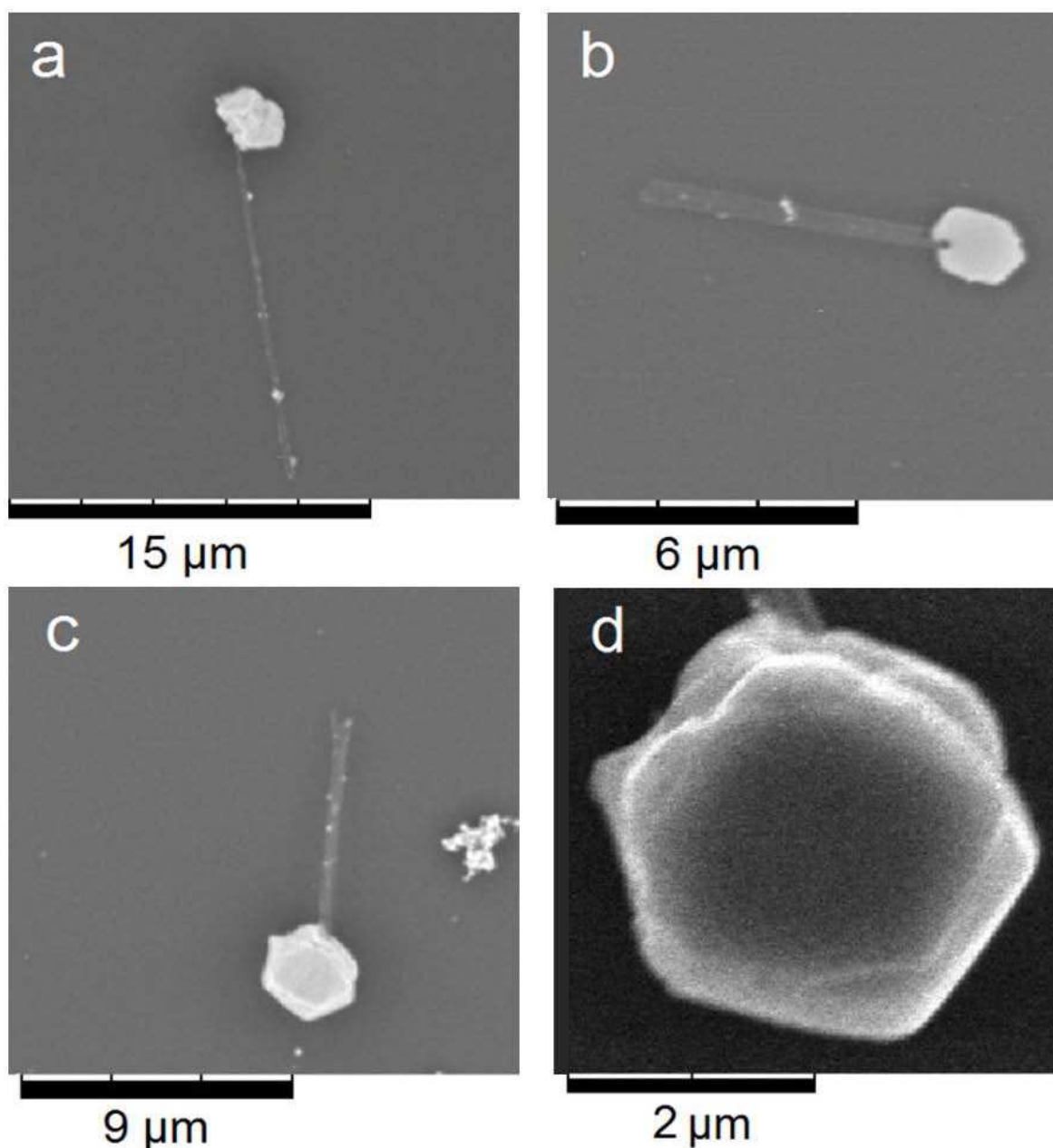


Figure 2.13 Scanning electron microscopy images of silver modified CMTs, with a high resolution zoom centered on a silver deposit (d). Adapted from Ref. (143).

The chemical nature of the deposit has been confirmed by energy-dispersive X-ray spectroscopy measurements (EDX, FEI Quanta 200, Figure 2.14). A spectrum was collected at a position centered on the deposit (a) and a negative control was recorded far away (b). The two major signals at 3.0 and 3.2 keV were assigned to Ag, whereas no detectable Ag traces are present in the control, but only signals corresponding to the supporting glass slide. It is

noteworthy that no measurable oxidation of the Ag deposit has been evidenced by EDX for the objects once they have left the capillary.

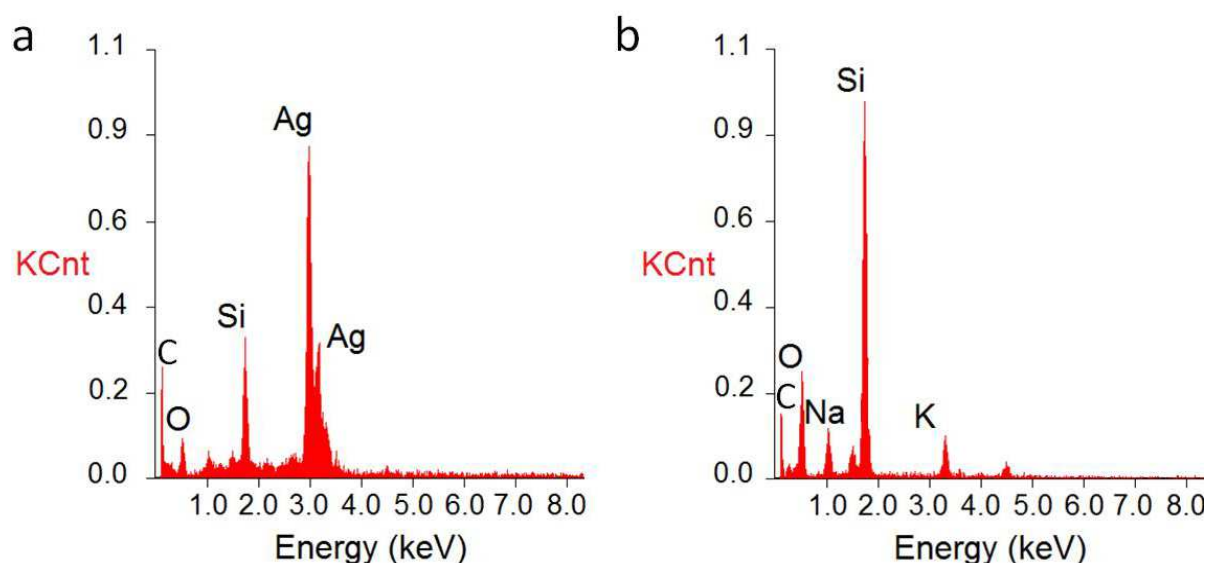
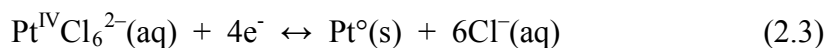


Figure 2.14 EDX spectra recorded for the deposit located at the end of the CMTs (a) and an unmodified carbon tube (b). Adapted from Ref. (143).

Thus, the results showed the successful modification of CMTs with silver. The resulting asymmetric hybrid materials obtained through the single-point deposition of silver at one extremity of a CMT could find interesting applications in the field of surface-enhanced Raman spectroscopy or even tip-enhanced Raman spectroscopy.

In order to prepare other CMT-hybrids that have a high functionality, we chose to deposit platinum asymmetrically on one end of the CMTs using the CABED. The same procedure was followed to perform the electrodeposition process. The suspension of CMTs was obtained this time by the addition of CMTs (0.3 mg) to absolute ethanol (1.25 mL). The suspension was sonicated for 1 min and after 30 min of sedimentation; 0.5 mL of the supernatant was taken and added to 1.5 mL of a freshly prepared 60 mM H_2PtCl_6 solution in ultrapure water. The addition of the salt increases the ionic strength, which might result in the aggregation of the CMTs, and therefore the suspensions were sonicated for few seconds and directly employed for the bipolar electrodeposition process analogous to what has been described previously. The following reaction is supposed to occur at the cathodic pole of CMTs:



By considering the water oxidation at the anodic pole of the CMTs, and as shown in table 2.1, it is clear that an electric field of at least 25 kV/m must be applied to induce the deposition of platinum onto a 20 μm -long CMT. We applied a slightly larger electric field (30 kV/m for 4 min) to be sure that all CMTs are getting modified. This corresponds to a good compromise because the difference of potential (ΔV_{min}) between both sides of the CMT is higher than the thermodynamic threshold value of the bipolar reactions but still reasonable in order to avoid H_2 bubbles evolution that may generate at the same pole than the platinum deposit which will possibly disturb our experiment and may cause detaching of the Pt cluster from the CMTs' extremity.

The experiments showed clear evidence for the asymmetric deposition of platinum at one end of the tubes as revealed under optical microscope (Figure 2.15a) with a good yield. Samples have been prepared at quite high dilution in order to avoid superposition of several tubes. The modified carbon tubes have also been characterized by SEM and a representative picture is given in Figure 2.15b. Three successfully functionalized small tubes with a length between 5 and 8 μm can be observed and at high magnification (inset) a typical Pt particle is visible. The asymmetrically functionalized CMTs with platinum will be used later to directly generate a movement by applying an external stimulus (section 3.2.2.).

To summarize, the CABED was properly adapted to perform localized deposition of silver and platinum onto CMTs. The process can be also applied to generate such micro- and nanoobjects with a variety of other materials. Indeed, the high power supply combined with electromigration through the capillary allows the straight-forward preparation of hybrid materials, avoiding experimental problems linked to gas evolution, ohmic heating, and uncontrollable convection.

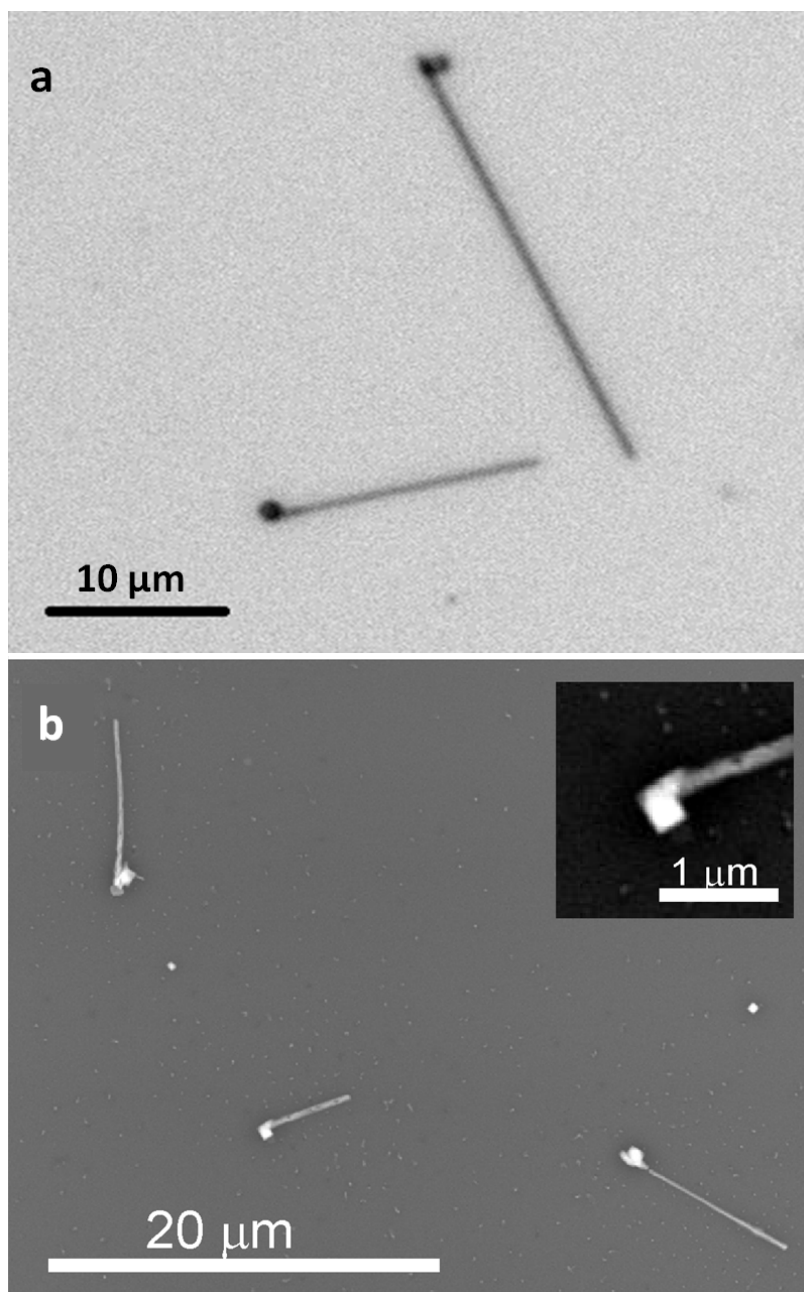


Figure 2.15 Optical micrograph (a) and a scanning electron microscopy image (b) of platinum modified CMTs. Inset: magnified SEM image of the platinum deposit. Adapted from Ref. (144).

2.5. Up-Scaling the Production Using the Bipolar Cell

In spite of the mentioned positive aspects of the CABED specially in terms of using high electric fields and the bulk preparation of APs, two main disadvantages of the technology can still be considered. The first one is the need to use the CE which is somehow an expensive instrument. The second one is the limited reaction volume which is conditioned by the capillary inner diameter (100 μm). This makes the process insufficient for producing high quantities of such particles for industrial applications. One of the main goals of this thesis is the fabrication of new APs at a large scale by bipolar electrochemistry. Therefore, a bipolar cell which has been introduced by Kuhn's group¹⁴⁵⁻¹⁴⁶ for the first time for the real bulk preparation of APs prior to the present thesis was adapted for this purpose. The cell design will be described first, and the obtained results will be presented in the following sections in addition to technology development which allowed the generation of more complex nano-and microstructures.

2.5.1. Cell Description

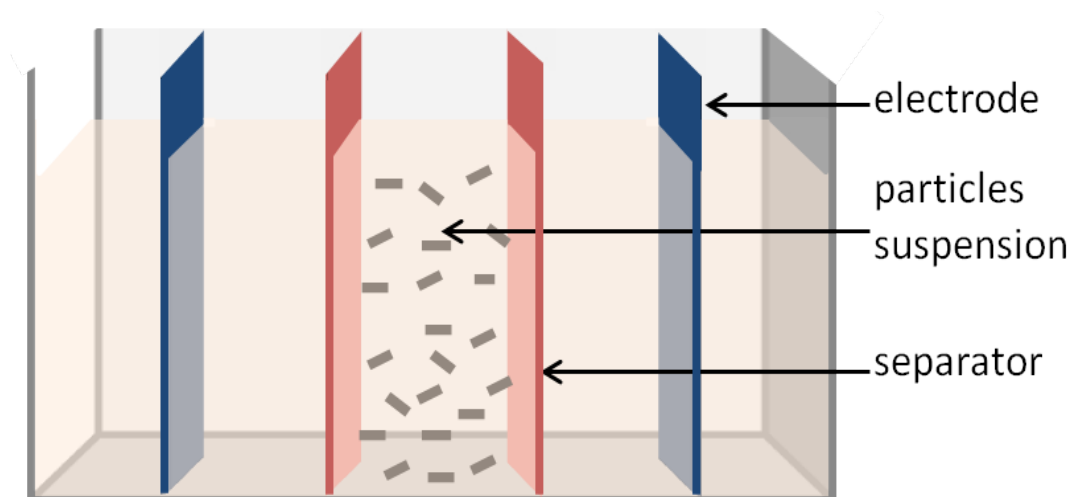


Figure 2.16 Schematic illustration of the bipolar electrodeposition cell (side view).

The cell initially composed of a single unit that has been separated by two membranes to isolate a middle reaction compartment where the substrate suspension is located, and two outer compartments in which the feeder electrodes are positioned (Figure 2.16). Gold or graphite sheets were used as feeder electrodes which are connected to a high voltage power

supply. The separators were made of either sintered glass or polymer which allowed different permeability and mechanical stability. The membranes were also included in the setup to minimize convection that originates from the Joule effect and the bubbles released at the electrodes. In this way the electrodes are separated from the objects that have to be modified. Cold ethanol (or an alternative solvent) was poured in the outer compartments thus the application of high electric fields is possible for a suitable time before the reaction medium became affected by the increased temperature.

Several cells made from various materials and exhibiting different dimensions have been used to perform the bipolar electrodeposition experiments that will be present in the following sections. Figure 2.17 shows three cell designs that were mainly used. Transparent materials such as PMMA, glass or polyethylene (PE) were employed in order to be able to visualize the bubble formation at the feeder electrodes. The PMMA/ polypropylene (PP) cell design (Figure 2.17a) allows changing the position of the separators, which enable the use of different reaction volumes, and the electrodes as well which allow tuning the applied electric fields. The polymer membranes were fixed in the cell by using Teflon (polytetrafluoroethylene (PTFE)) or silicon paste. The membranes were usually kept in pure water (18.2 M Ω .cm) to avoid their shrinkage which may lead to their detachment from the cell body. The PE/glass cell (Figure 2.17b, analogous to the capillary electrophoresis but at a significantly larger scale in terms of capillary diameter) consists in two PE cuvettes which are connected by a squared glass capillary; the later acting as the reaction compartment where the suspension of substrates was filled, and it was fixed to the cuvettes with silicon. The glass cell includes sintered glass separators (3 mm thickness and porosity 2) which were built into the cell structure (Figure 2.17c). This kind of separators causes a high EOF, but also gives a good insulation of the modified objects from the feeder electrodes. The middle part of the cell was surrounded at the bottom by an outer compartment used to control the reaction temperature. Four feeder electrodes were used in order to apply different orientations of the electric field. The suspension of the substrate under investigation was usually inserted into the reaction compartments prior to the experiment. The electric field was applied for a certain time via the feeder electrodes, immersed in the solvent or supporting electrolyte, which were connected to the high power supplier (Consort E 862 6000 V – 150 mA, Sodilec MCN 350 V, or Heinzinger PNC 30,000 – 20 ump). After the experiment, the sample was recovered, drop coated, dried and washed on a glass slide or a metallic plate for characterization under the microscope.

2.5. Up-Scaling the Production Using the Bipolar Cell

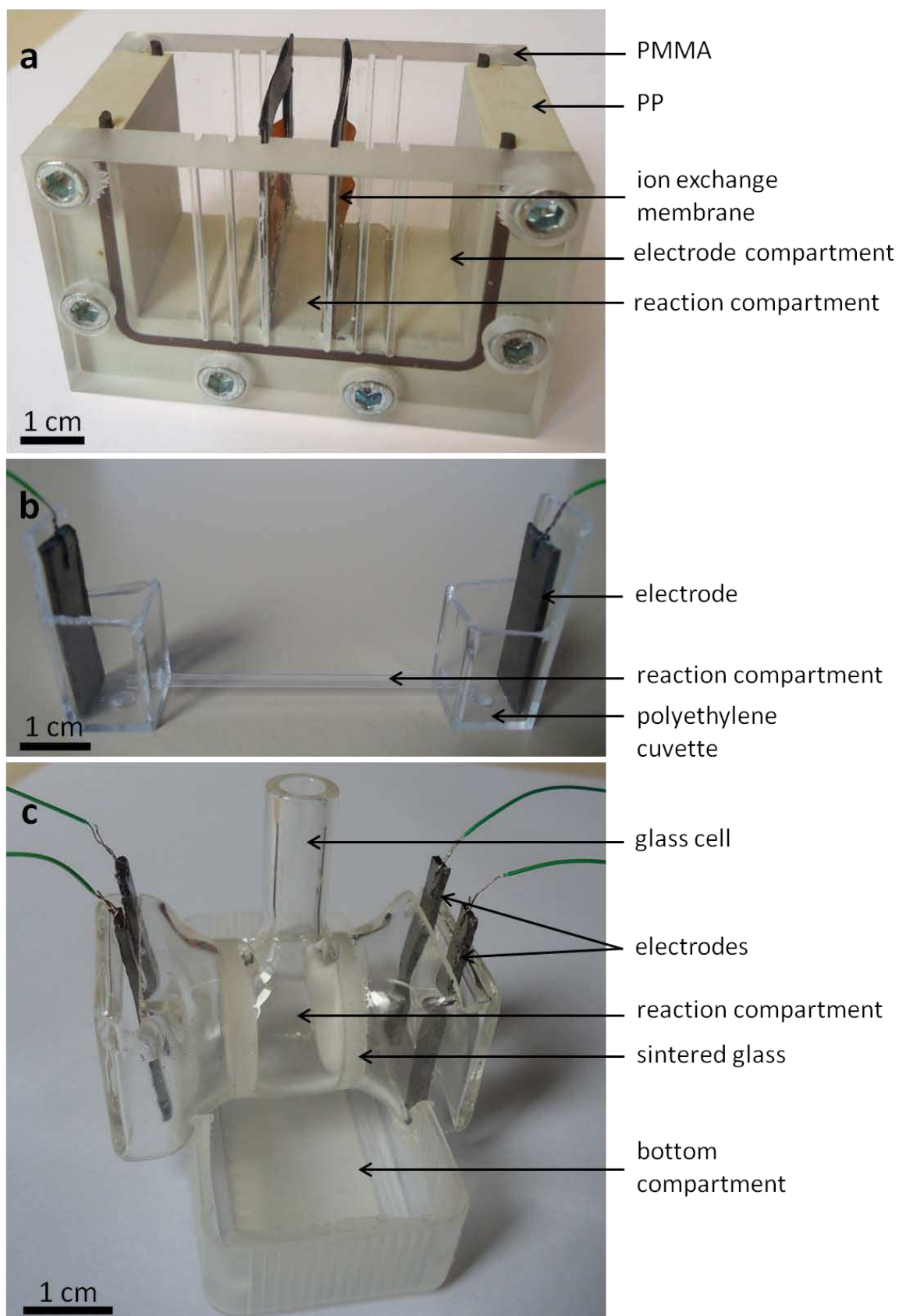


Figure 2.17 Bipolar electrodeposition cells. a) PMMA/PP cell. b) PE/glass cell. c) Glass cell.

2.5.2. Metal Electrodeposition on Anisotropic Substrates

In order to check the efficiency of the bipolar cell and the sample reproducibly with the new technology, we decided to modify first CMTs with platinum, as we already did by CABED. The suspension of CMTs was prepared exactly in the same way as previously described during the CABED and 0.5 mL was added to 1.5 mL of 1 or 60 mM of a freshly prepared H_2PtCl_6 solution in ultrapure water. The mixture was poured into the reaction compartment of the PMMA/PP cell (Figure 2.17a). The membranes in this cell were separated by 1 cm, and the gold plates feeder electrodes have been spaced by 2 cm distance. About 6 mL of cold ethanol ($T \sim -10^\circ\text{C}$ after immersing for 1 min in liquid nitrogen) were added to the electrode compartments. After the application of 30 kV/m electric field for 4 min, the sample was recovered from the middle compartment for investigation.

The resulted particles showed the platinum deposit at one extremity of the CMTs as revealed under the optical (Zeiss, Imager M1) and scanning electron microscopes (Figure 2.18). The morphology of the resulting hybrids was also similar to those obtained using CABED (Fig. 2.15). The modified CMTs in Figure 2.18a, b and f were produced using 1 mM concentration; while the others (Figure 2.18c-e) were produced with 60 mM H_2PtCl_6 . Careful examination of the samples highlights two slightly different topologies. We observed that some tubes shown in Figure 2.18a, c and e are modified in a symmetrical way with the Pt particle being centered with respect to the long axis of the tube. On the other hand, other tubes shown in Figure 2.18b, d and f have been modified in a non-symmetrical fashion as the particle is positioned slightly off the long axis of the tube. Indeed, the CMTs/Pt particles that were prepared by the CABED, also have shown these two different topologies (Figure 2.15). As we briefly mentioned before, the presence of the platinum in the structure of this hybrids enables their use as microswimmers in the presence of external fuel. The different Pt topologies will play a key role with respect to this application as we are going to discuss in the next chapter (section 3.1.2.), therefore, an explanation of the mechanism which may lead to these topologies will now be proposed.

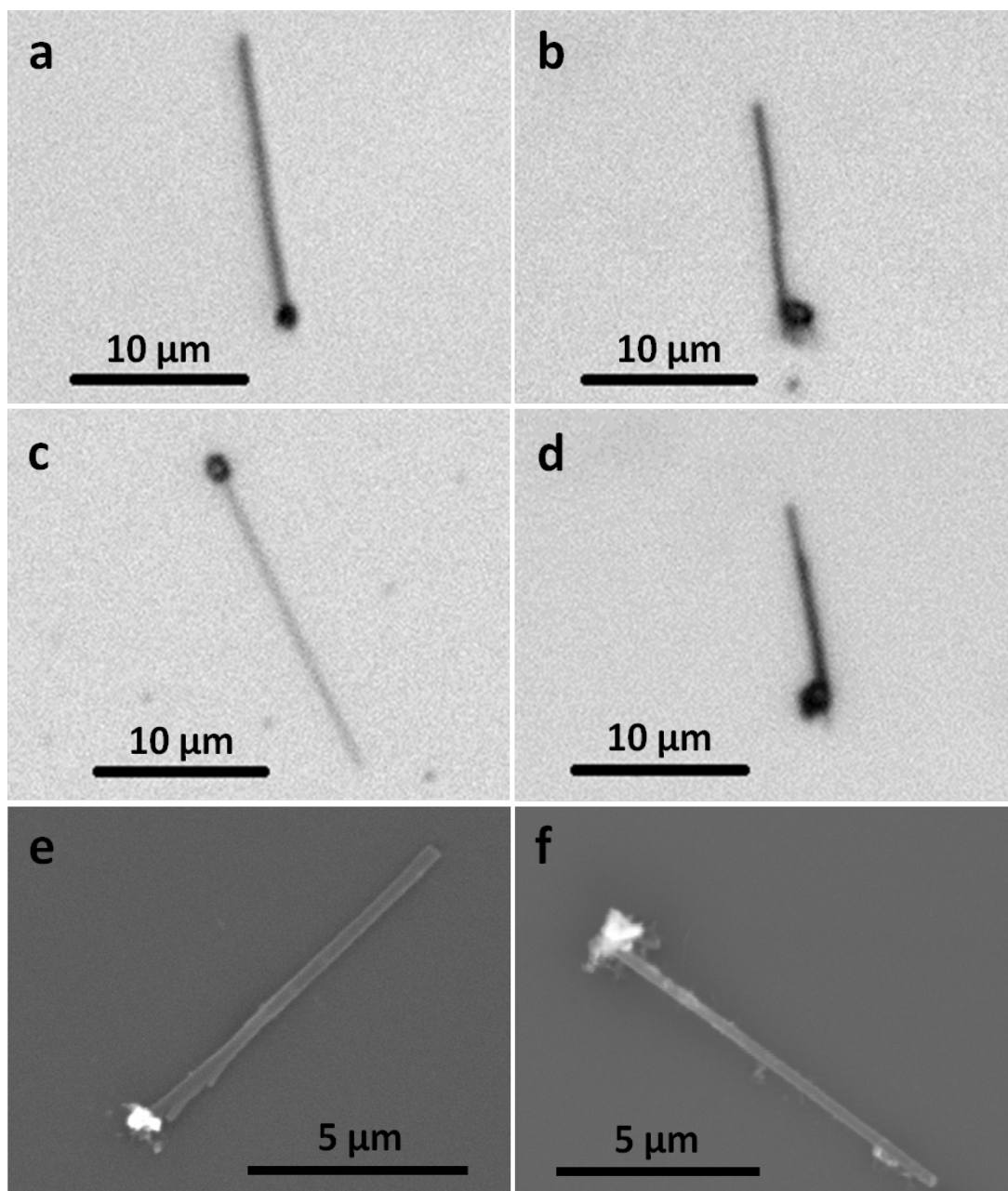


Figure 2.18a-d) Optical micrographs of platinum modified CMTs using 1 mM (a and b), and 60 mM (C and d) of H_2PtCl_6 solution. e, f) SEM images of CMT/Pt AP obtained from 60 mM (e) and 1 mM (f) H_2PtCl_6 solution.

The different topologies might be explained on the basis of a mixed influence of two competing kinetic parameters, which are the electromechanical alignment time and the kinetic activation of the bipolar reaction, respectively. Indeed, a linear potential sweep is applied in order to reach the sufficient electric field value for electrodeposition when $\Delta V > \Delta V_{\min}$. Theoretically, this potential ramp should last for a sufficient time to allow an alignment of the tubes along the direction of the electric field before reaching the threshold

value where the bipolar reaction starts. In this case, the experiment should lead theoretically to the formation of a centered deposit of the Pt (Fig. 2.19a) with respect to the tube axis, because the nucleation point is located at the point of maximum polarization. But the reality is more complicated as the alignment of the CMT in electric field depends on three main variables: the initial orientation and length of each tube, as well as the viscosity of the surrounding environment (the latter depending on another series of variables: solvent, temperature, nature and concentration of the supporting electrolyte).

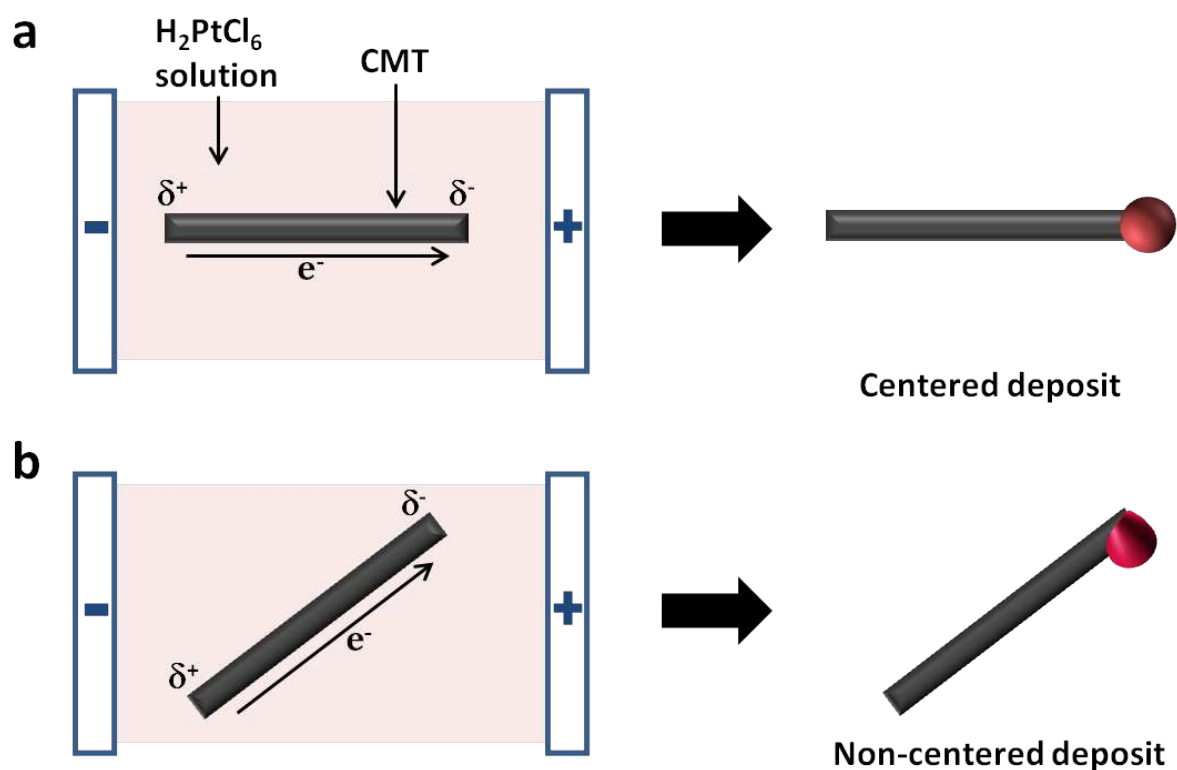


Figure 2.19 Schematic illustration explaining the origin of different deposit locations obtained for CMTs as a function of their orientation in the electric field at the beginning of the electrodeposition process. (a) Aligned parallel to the electric field and (b) non-aligned with the electric field.

The interesting point is that by adjusting the experimental conditions (as we will see in section 2.5.3), it is possible to tune the electrodeposition topology (centered versus non-centered). The initial orientation of the tubes is a statistical distribution, but the subsequent alignment could be favored by applying an initial potential difference lower than the threshold value necessary for the bipolar reaction, followed by a potential step above the

threshold value once the tubes are all aligned. As a consequence, the solvent choice is of first importance as the timescale of reorientation of the CMT could be either very short in water or substantially longer by adding a co-solvent with a higher viscosity. A precise control of the monodispersity of the tube length does not seem to be necessary as two opposite factors influence the alignment: First, the length of the tube directly influences the polarization between both extremities of the CMT. All tubes are exposed to the same electric field (30 kV/m) and that means that the polarization of a 20 μm long carbon tube is twice as large as the polarization of a 10 μm tube. This polarization is the driving force of the alignment, but mechanical counter forces also depend on the length of the tubes. Indeed, the longer CMTs exhibit a larger surface area in contact with the surrounding environment and, therefore, are more affected by the solvent viscosity contribution, which slows down the alignment. Experimentally we find that these two contributions do not seem to be of the same magnitude, because the longer CMTs have a higher tendency to be functionalized in a non-centered fashion, meaning that they need more time to orientate in the electric field and during this time the deposition already occurs at the point of highest polarization, which in this case is not located at the center of the tube end, but at the edge. Consequently the Pt electrodeposition resulting from the reduction of H_2PtCl_6 directly grows from the most favorable nucleation site and generates an off-centered Pt/CMT hybrid as illustrated in Figure 2.19b.

The bulk preparation of metal hybrids was also done with another carbon substrate than the CMTs. Carbon fibers (CFs), were also employed for the bipolar electrodeposition. They are less conductive than CMTs due to their fabrication process that can result in fibers with different morphologies and characteristics (hence different conductivity) depending on the operating conditions.¹⁴⁷ For this purpose, a cell similar to the one shown in Figure 2.17b, with a 5 cm long and 1 mm inner diameter glass capillary was used. In this cell, the majority of the potential drop occurs inside the capillary, where the particles will be modified. This is due to the small diameter of the capillary with respect to the cuvettes and also the absence of separating membranes.

Prior to use, CFs (grade: P100 from Goodfellow) have been washed several times with ethanol and pure water in order to remove any possible contaminations. All the compartments of the cell were filled with the solution of the metal salt, and carbon the CFs were inserted manually into the glass capillary. The voltage was applied through the feeder electrodes made of graphite sheets, for a certain time. The samples were collected on a conductive substrate

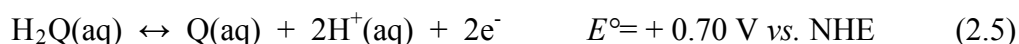
and washed several times with pure water, then fixed from the middle to the substrate with a tiny spot of glue to avoid its loss during scanning electron microscopy (high vacuum).

Two metals have been deposited on the CFs, platinum and nickel. The Pt was deposited first from a 10 mM of H_2PtCl_6 solution on CFs (2.72–3 mm long and 10 μm diameter (\emptyset)), by applying 0.54 kV/m for 50–60 min. The SEM images in Figure 2.20a shows the cathodic pole of four CFs with a successful Pt deposit at the extremity. It is noteworthy that the applied potential generates a maximum polarization of ~ 1.5 V along the extremities of the CFs in order to trigger the Pt electrodeposition, which is about three times higher than the value ($\Delta V_{\text{max}} \sim 0.6$ V) applied on 20 μm long CMTs. This may refer to the higher conductivity of the CMTs compared to the CFs.

The same procedure was followed for depositing nickel on 1 cm long CFs, from 5 mM NiSO_4 solution. The following reaction is supposed to occur at the cathodic pole of the CF:



The reduction of Ni^{2+} from its aqueous solution was investigated in the presence of either water or hydroquinone as two different redox couples that can be oxidized at the anodic pole of the fibers. The oxidation of water (eq. 2.2) was performed in the first experiment. In the second experiment, a solution of hydroquinone was added to the reaction mixture and in this case, the following reaction will take place at the anodic pole of the CF:



The principle difference in these two experiments is only the value of the applied potential which will control the morphology of the resulted deposit. Indeed, the standard potential of $\text{O}_2/\text{H}_2\text{O}$ redox couple (+ 1.23 V vs. NHE) is significantly higher than that of $\text{Q}/\text{H}_2\text{Q}$ couple (eq. 2.5), which thermodynamically favors the reduction of nickel cations in the presence of hydroquinone, and allows easier formation of the deposit in this case. The estimated theoretical threshold values for nickel electrodeposition on a 1cm long CF is about 0.15 and 0.053 kV/m without and with hydroquinone, respectively. Figure 2.20b shows a CF that has been modified with a Ni cluster in the presence of water after the application of 0.3 kV/m for 15 min. No evidence for any deposit formation was observed in the later case when applying a field that is less than 0.26 kV/m. However, a marked and long deposition (~ 1 mm) was monitored on the CF in the presence of hydroquinone (Figure 2.20c) when applying only 0.2 kV/m for 15 min. This is because the fiber experiences a much higher potential than

necessary for the polarization which let the deposition begins earlier on the fiber than the previous one (Fig. 2.20b) which is by comparison more localized at the end of the fiber.

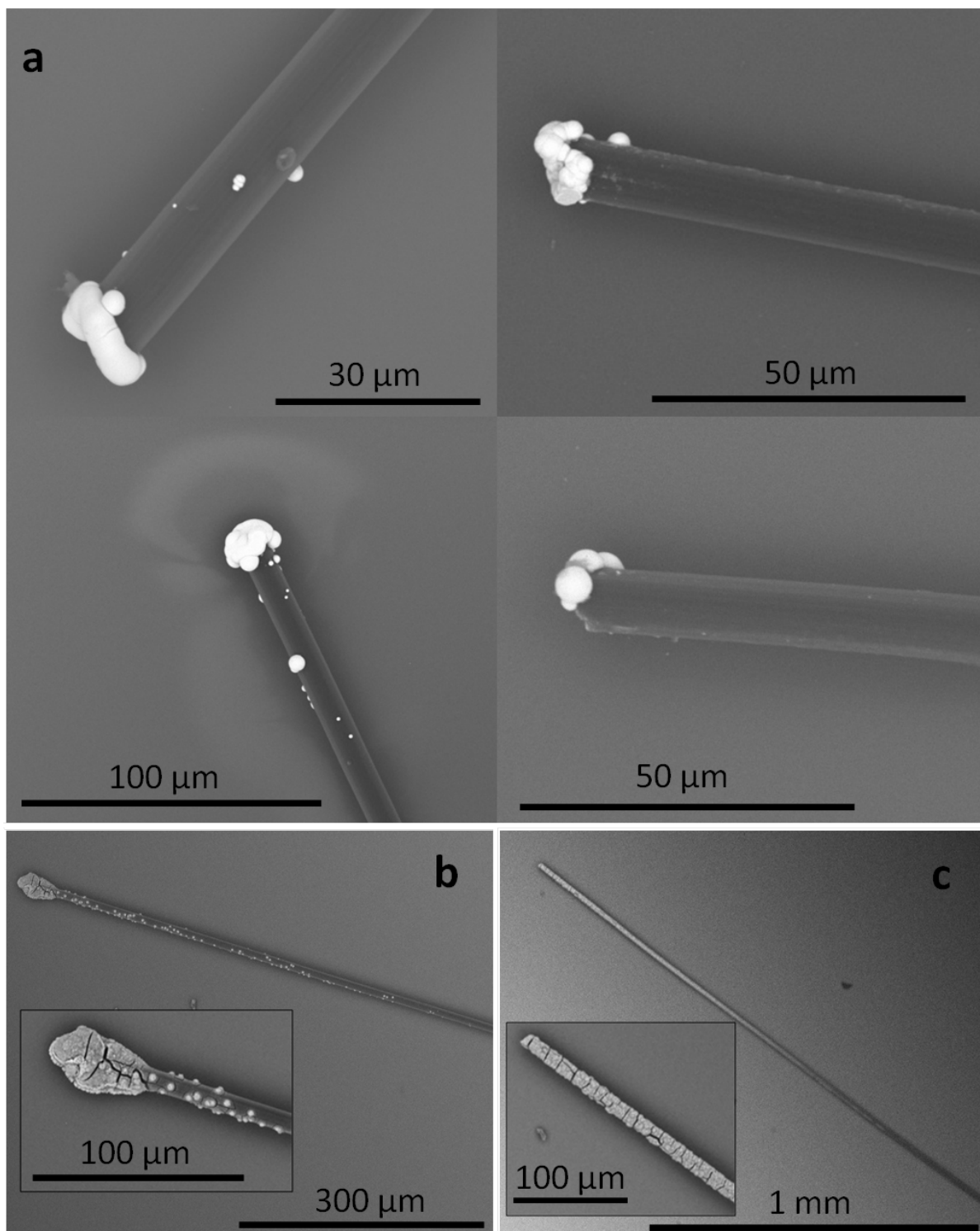


Figure 2.20 SEM images of carbon fibers modified with platinum (a), and nickel (b-c). Inset: magnified SEM image of the nickel deposit formed in the absence (b), and presence (c) of hydroquinone.

The prepared APs with nickel (ferromagnetic material) can be very interesting swimmers candidates as they can be controlled and guided under the application of an adequate magnetic field (external magnet for example). One can note that in addition to the hydrophobic property of the CFs, the modification with Ni could enhance their self-assembly which is an attractive functionality with possible application further.

2.5.3. Topo-Selectivity of the Metal Cluster

The electrodeposition of metals on carbon substrates by bipolar electrochemistry gave access, as we showed in the previous sections, to APs that have been modified with two different topologies which have a crucial role in certain applications. Therefore, we decided to control the resulted topology by controlling the alignment of the objects in the electric field during the bipolar electrodeposition process. These topologies will be referred to as centered and non-centered topology as a function of the orientation of the metal deposit with respect to the main axis of the carbon substrate.

2.5.3.1. Control of the Topology of the Metal on Carbon Fibers

In a proof-of-principle experiment, we first tested the concept of alignment on a millimetric scale using carbon fibers. The precise electrodeposition of copper on CFs was investigated. Similar procedure and setup (Figure 2.17b) that have been used to modify CFs with Pt and Ni were employed for this purpose. All compartments of the electrochemical cell were filled with a solution of 10 mM CuSO₄ in ultrapure water. The CFs were introduced into the glass capillary and mechanically oriented either parallel or diagonal with respect to the capillary long axis (Figure 2.21), and hence, with respect to the direction of the applied electric field. The voltage was applied to polarize the CFs and trigger electrodeposition of copper at their cathodic pole as following:



If we consider the oxidation of water at the anodic pole ($E^{\circ} = + 1.23 \text{ V}$), the polarization has to generate a potential difference of approximately 0.9 V. This means that we need theoretically to apply an electric field of 0.385 kV/m to induce both reactions simultaneously

at the two extremities of a 2.34 mm long CF. As we were far from the standard conditions, we applied a higher electric field to be sure to modify asymmetrically the fiber with a copper cluster. In order to produce a centered topology, two CFs (2.34 and 2.50 mm long) were oriented inside the capillary until being perpendicular to both feeder electrodes (gold plates). The electric field (0.7 kV/m) was applied for an appropriate time (40 min) in order to produce a large copper deposit with a sufficient size for ease of characterization. It is noteworthy that the deposition time is of course adjustable. The used CFs were relatively long; therefore, they will not change their alignment under the effect of the applied field. Since the nucleation starts at the point of maximum polarization, which is in this case localized around the end of the fiber, the growth of the copper cluster will lead to a centered deposition.

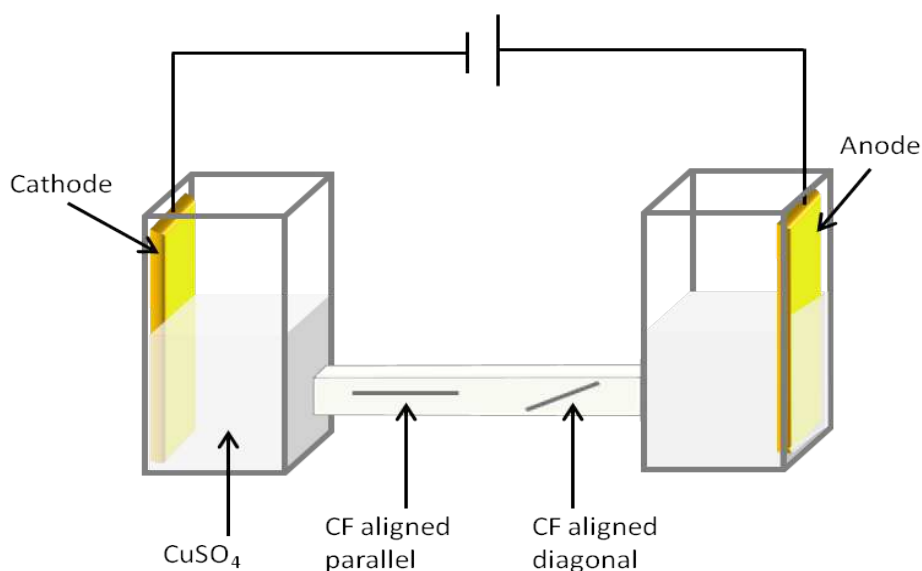


Figure 2.21 Schematic representation of the bipolar cell used to modify carbon fibers with copper. The fiber is aligned parallel (left), or diagonal (right) with respect to the capillary long axis, adapted from Ref. (148).

One can note that the applied potential is almost twice as high as the thermodynamic threshold value required for the electrochemical reaction. This value is however still moderate enough to limit the formation of oxygen bubbles at the anodic side of the fiber. In fact, the slow production of these bubbles allows their continuous dissolution in the electrolyte thus preventing the evolution of too big bubbles, which might disturb the experiment and ultimately stop the current flow, since the capillary diameter is relatively narrow (1 mm). Investigation of these CFs at the end of the experiment under SEM showed

clear evidence for asymmetric deposition of copper at one end of the fibers with a perfectly centered localization of the cluster with respect to the fiber axis (Figure 2.22a, b). The chemical composition of the Cu deposit was further analyzed by EDX spectroscopy (JEOL, 840A) as shown in Figure 2.22c. A strong signal around 1 keV, besides two other signals at 8 and 9 keV, was observed, which confirms that the deposit is indeed copper. The weak signal assigned to carbon comes from the underlying carbon fiber and the supporting grid, while the tiny gold signal most likely originates from the gold sputtering of the sample prior to SEM imaging.

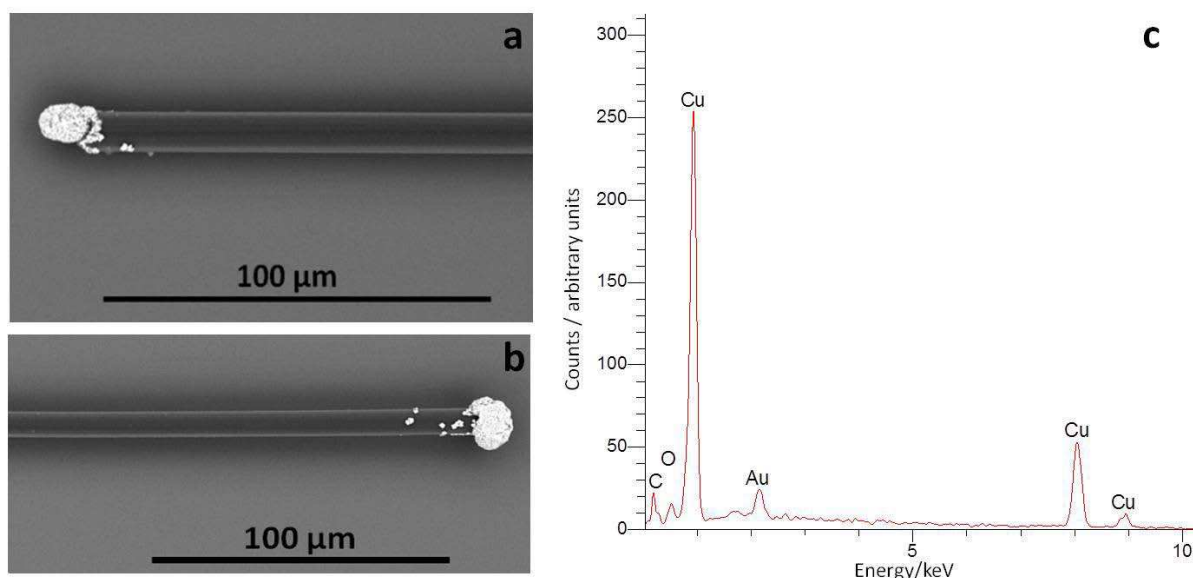


Figure 2.22 SEM images of a carbon fiber (2.34 mm, a, and 2.50 mm, b, long) modified with a centered copper cluster. c) EDX spectra recorded for the deposit on the end of the carbon fiber in b, adapted from Ref. (148).

We followed the same procedure in order to prepare carbon fibers with a non-centered topology of the metal deposit. For that, a 2.33 mm-long CF (almost the same length as the first fiber (Fig. 2.22a) modified with a centered topology) was inserted into the capillary and mechanically oriented with a significant angle between the fiber axis and the direction of the applied electric field. From the previous experiment one can predict that a value of 0.7 kV/m (even though it was not investigated as a minimum value required for the electrodeposition in that case) should be enough to modify this carbon fiber. However, no metal deposition was observed on this fiber as revealed under the scanning electron microscope (Figure 2.23a). This is because the effective length, which is responsible for the polarization of the fiber, is

significantly shorter than the real length (2.33 mm), because it depends on the orientation angle of the fiber in the field.

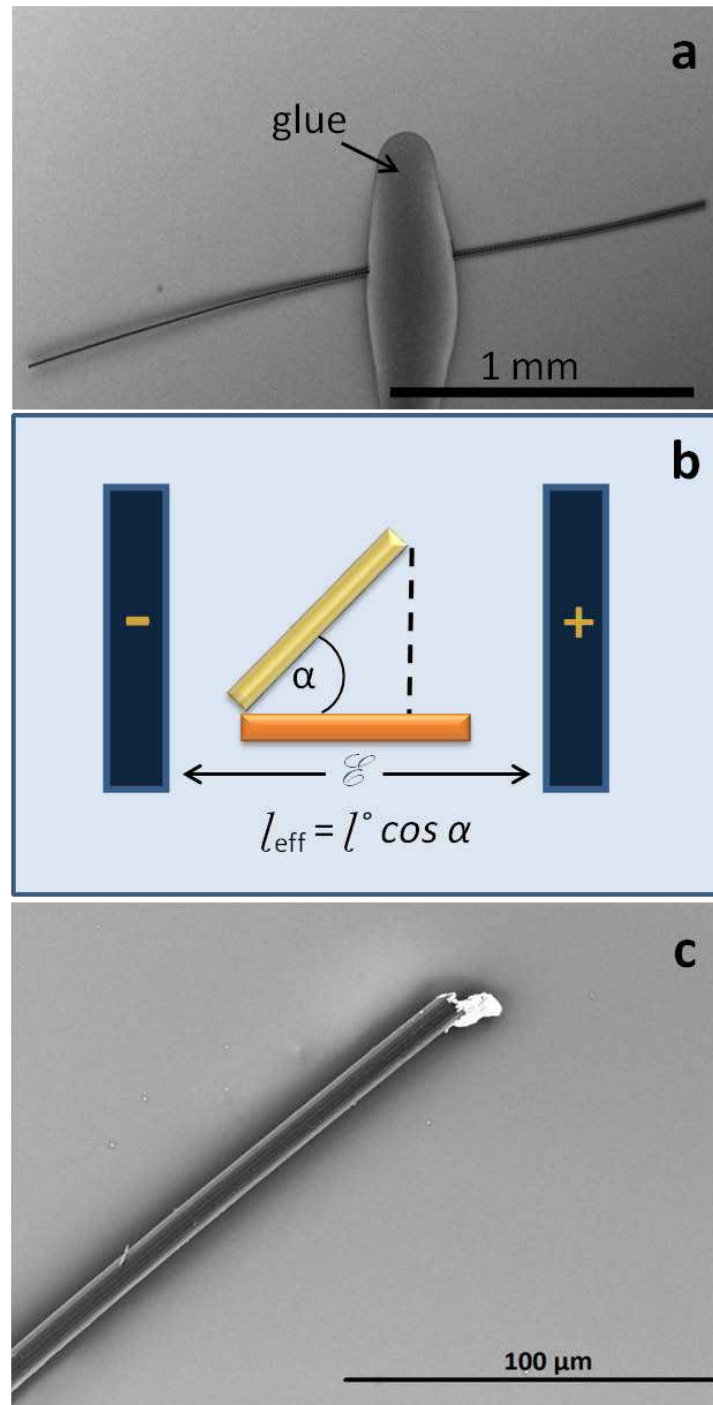


Figure 2.23 a) SEM image of 2.33 mm-long unmodified CF after submitting to the electric field (0.7 kV/m) for 40 min in CuSO_4 solution. b) Schematic illustration of the effect of orientation angle on the effective length of CFs in the electric field. (c) SEM picture of a modified carbon fiber (1.86 mm long) with a non-centered topology of copper deposit. b and c, adapted from Ref. (148).

Figure 2.23b schematically illustrates two carbon fibers with the same length but different orientations. The first one (orange) is aligned parallel to the electric field, so the effective length (l_{eff}) of this fiber is the same as the real length (l). The second fiber (golden) has a marked angle α with respect to the electric field vector; therefore, the effective length equals the real length multiplied by cosine α . As a consequence, in the second case, a higher electric field needs to be applied to ensure a comparable driving force for the electrodeposition. Therefore, and because the resulting topology depends, in principle, on the angle of orientation of the carbon fiber in the field, we used a shorter fiber (1.86 mm) that allowed a higher α in the narrow capillary (1 mm diameter), and we applied also a higher electric field (0.92 kV/m) which could generate the maximum polarization at the very edge of the extremity of the fiber. As a result, a well-pronounced noncentered localization of the microcluster has been observed by SEM (Figure 2.23c). From these modified macroscopic objects, we concluded that bipolar electrochemistry is well-adapted to asymmetrically modify the carbon fibers with a controlled topology of copper metal by the alignment of the fibers in the electric field. This is a first key step towards generating a highly controlled orientation of the deposit with respect to the fiber axis. After these preliminary experiments, we explored the possibility of extending this concept to objects with smaller dimensions, particularly at the microscale.

2.5.3.2. Control of the Topology of the Metal on Carbon Microtubes

It is indeed more complicated to modify microscale objects in comparison to millimetric ones with such a specific topology, since it is not possible to align them at a certain angle with respect to the electric field by a simple mechanical manipulation as in the case of the macroscopic CFs. Figure 2.24 shows the bipolar electrochemical cell that has been designed to electrically align the CMTs in the field. The feeder electrodes, spaced by a distance of 4.3 cm, were positioned in the outer compartments which have been filled with dimethylsulfoxide (DMSO). The suspension of CMTs in DMSO was poured in the middle compartment. The lower outside reservoir was filled with cold ethanol to freeze the DMSO at the appropriate time of the experiment. The mechanism of the CMT alignment during the experiment depends on two parameters: the applied potential and the viscosity of the surrounding medium. Two successive potential steps were applied instead of a single linear potential ramp. The first potential step should be high enough to orientate the CMTs;

however, it has to be lower than the threshold value necessary for the bipolar electrodeposition. The second potential step should be higher than the thermodynamic threshold value required for the modification. At the end of the first potential step and before the second potential step, the viscosity of the medium surrounding the tubes should be increased in order to immobilize the tubes at a certain angle with respect to the orientation of the initially applied electric field.

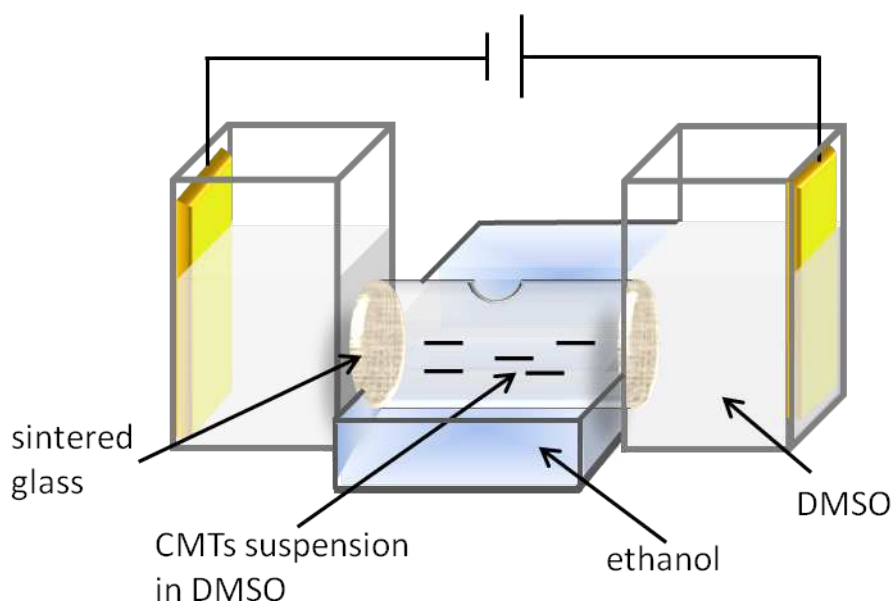


Figure 2.24 Scheme of the bipolar cell designed for asymmetric modification of CMTs with copper metal.

The sample of CMTs used in this work contains a population of tubes with a length ranging from 10 to 30 μm . In order to estimate a suitable value for the initial potential step, the alignment of the tubes was monitored under a transmission optical microscope by increasing gradually the applied potential between the two electrodes. An electric field of 12 kV/m was found to be large enough to orientate the tubes along the direction of the electric field. Figure 2.25a shows three carbon tubes with a length of 15 to 20 μm which adopt a random orientation in a DMSO solution before applying the field. As soon as an appropriate electric field was applied (Fig. 2.25b), the tubes get polarized and orientated in a perfect parallel alignment with respect to the applied field. Although a field of 12 kV/m seems to be high, such a value is much lower than the theoretical threshold value necessary for bipolar electrodeposition of copper (45 kV/m for a CMT of 20 μm according to eq. 1.4). The second tunable parameter governing the orientation of the tubes is the viscosity, which in turn

depends on many other factors such as the nature of the solvent, temperature, nature and concentration of the electrolyte. The main reason for choosing DMSO was its relatively high viscosity (1.996 cP at 20 °C) compared to water (0.894 cP at 25 °C), the high temperature freezing point (18 °C) and the good miscibility with water, which is essential during the collection of the modified objects at the end of the experiment. In this way it has been possible to maintain the orientation of the tubes, once they have been aligned by the first electric field.

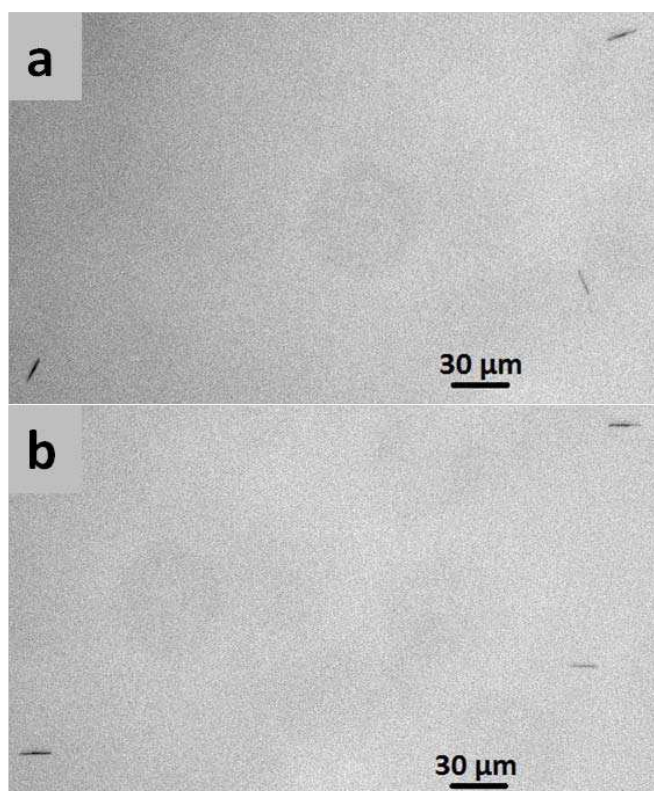


Figure 2.25 Optical micrographs showing the CMTs alignment: a- before, b- during application of the first potential step, adapted from Ref. (148).

The preliminary step to align the CMTs is essential for modifying the microtubes with a coaxial topology of the copper deposit. When changing slightly the design of the electrochemical cell (by using a cell similar to the one showed in Fig. 2.17c) it was possible to change the orientation of the electric field between the first and the second potential step. A new set of electrodes (gold plates) consisting of two independent and addressable electrodes, has been integrated in the cell set-up. This led to a final set of four electrodes instead of two (Figure 2.26). The middle part of the cell was filled with the suspension of

CMTs which was prepared in a 10 mM $\text{Cu}(\text{OAc})_2$ in DMSO solution, whereas pure DMSO was used to fill both feeders electrode compartments. In order to synthesize copper modified tubes with a centered topology of the deposit, all four electrodes were connected and the first potential step was applied with a slightly higher amplitude (14 kV/m for 30 s) than what we estimated previously (Figure 2.26a). The latter value was selected to be sure that also the shortest tubes get well aligned. Then, the viscosity of the solvent (DMSO) was increased in the middle compartment containing the tubes. Half a minute was long enough to allow the orientation of the tubes in the field. During this time a solution of cold ethanol ($T \sim -10^\circ\text{C}$) was poured in the compartment located under the center part. This led to an increase in viscosity and eventually to freezing of the CMTs suspension. In this way it was possible to keep the alignment of the carbon tubes parallel to the field before the electrodeposition step. The second potential step was also applied using simultaneously the four electrodes with an electric field of 90 kV/m for 8 minutes. With this alignment mode of the tubes, a symmetric maximum polarization around the extremity of the tube was generated, triggering the nucleation of the deposit at this point and finally leading to objects modified with a centered metal cluster (Figure 2.26a). During the course of these experiments, the DMSO was maintained at a low temperature. After the electrodeposition, the solution was allowed to warm up before collecting and characterizing the CMTs.

When the same procedure was employed, but by connecting only two of the four electrodes during the first potential step, a diagonal electric field with respect to the cell axis was generated (Figure 2.26b). After aligning and freezing the orientation of the tubes, the field of the second potential step was aligned parallel to the cell axis by connecting all four electrodes. As a consequence, in this case the CMTs axis and the electric field will not be parallel during the electrodeposition step, but tilted by a certain angle. This was the key element for generating a maximum polarization at the edge of the carbon tube tip. The nucleation of the copper deposit at this point of maximum polarization results in a non-centered metal cluster (Figure 2.26b).

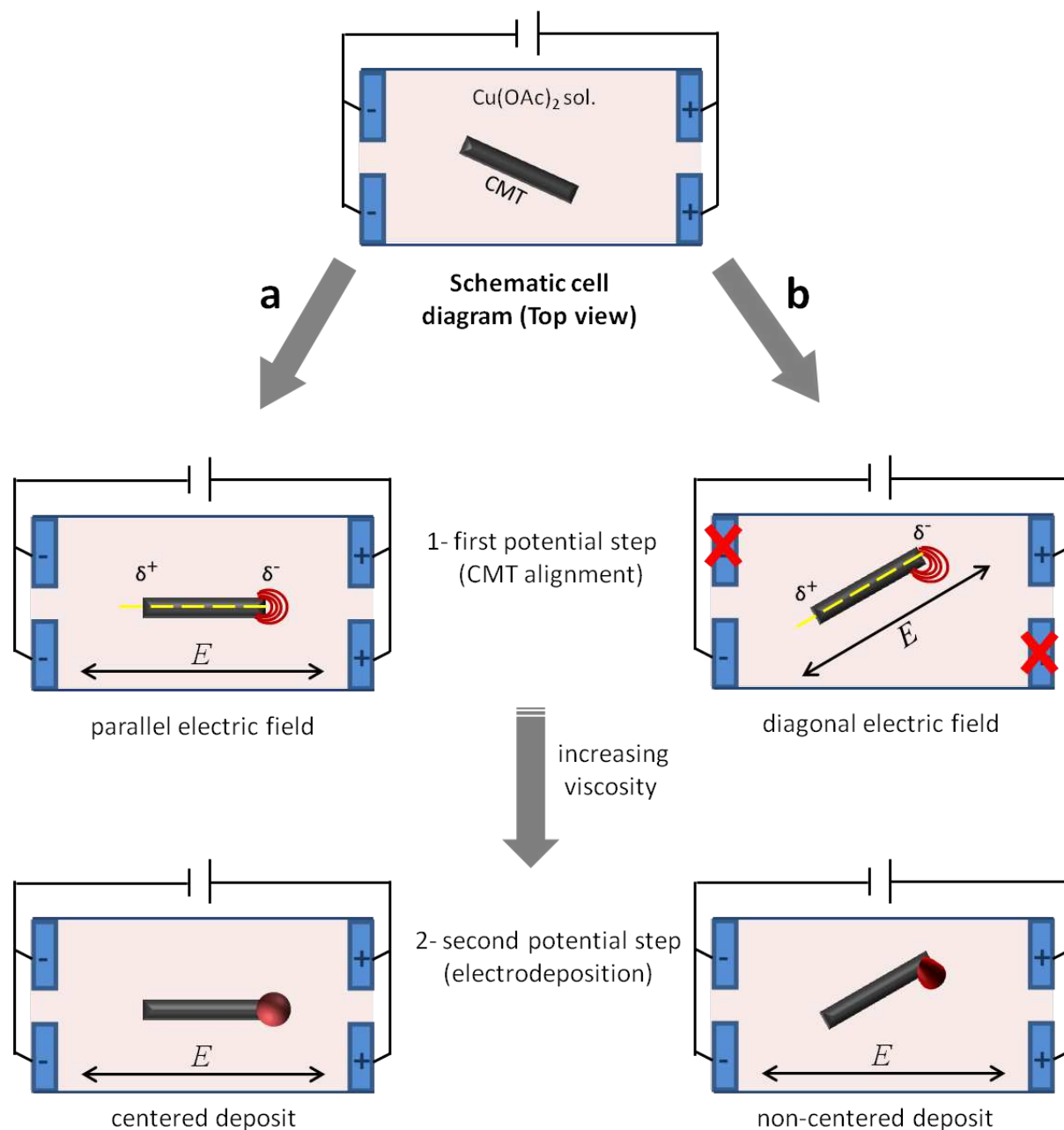


Figure 2.26 Schematic illustrations (top view) of the electrodes connection in the bipolar cell during the first and second potential step to control a CMT alignment in the electric field and the resulting, centered (a), and non-centered (b) deposits. The red curved lines indicate the maximum polarization potential around the tube extremity.

For both types of experiments described above, the solution has been collected after the second potential step, the tubes were washed with water and their morphology has been investigated by optical and scanning electron microscopy. Figure 2.27 shows SEM images of four representative carbon microtubes with different length collected from the first

experiment, all being modified at one end with a centered deposit. Practically, around 40% of the CMTs were modified with copper (global yield) and about 75% of these tubes exhibited a centered deposit. The non-quantitative conversion yield can be explained by several origins. The first reason is the possible detachment of the copper deposit from the tube during the washing procedure. Secondly, the conductivity of the tubes, which varies depending on their morphology and the presence of defects, might be in some cases too low for bipolar electrodeposition. In the extreme case of an insulating tube, no deposition can occur and even for conducting tubes their intrinsic conductivity has to be larger than that of the surrounding medium to induce an efficient deposition. The third reason is linked to the calculation of the potential drop as a function of CMTs size. The shortest tubes might experience a potential difference between the two ends that is below the threshold value.

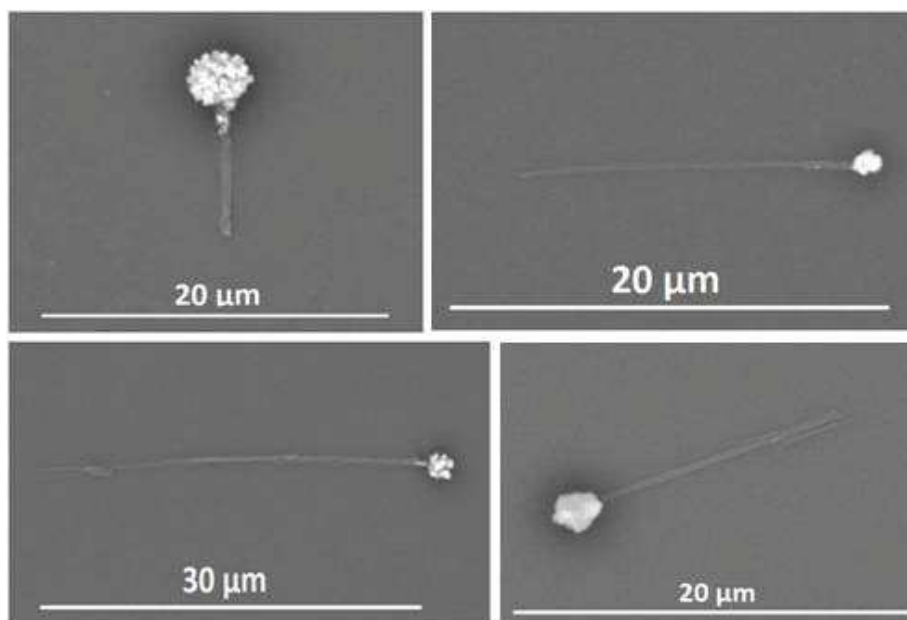


Figure 2.27 Selection of SEM pictures showing toposelective bipolar electromodification of carbon microtubes with a centered copper deposit, reprinted from Ref. (148).

Looking at the SEM pictures of the resulting CMTs from the second experiment (Figure 2.28), it is obvious that the site-selective non-centered topology is highly controllable. The total percentage of the modified CMTs was estimated to be around 35% by optical microscopy. 70 % of them were modified with a non-centered topology. The presence of the CMTs modified with a centered deposit mode is most likely due to the local melting of DMSO around these microtubes, which cannot be directly observed by eye. In that case the tubes can partially or totally realign under the effect of the field applied during the second

potential step. The total product yield of this experiment (35%) was lower than the previous one (40%) for modifying the tubes with a centered metal topology. This difference is quite expected according to what we discussed concerning the orientation angle (Figure 2.23b) between the CMTs and the applied field, which changes the effective length of the tubes. Since we applied the same potential difference in both experiments, the number of CMTs which were polarized with a sufficient potential for electrodeposition was higher in the case of the tubes aligned parallel to the external electric field than the others which were in a diagonal alignment with respect to the field.

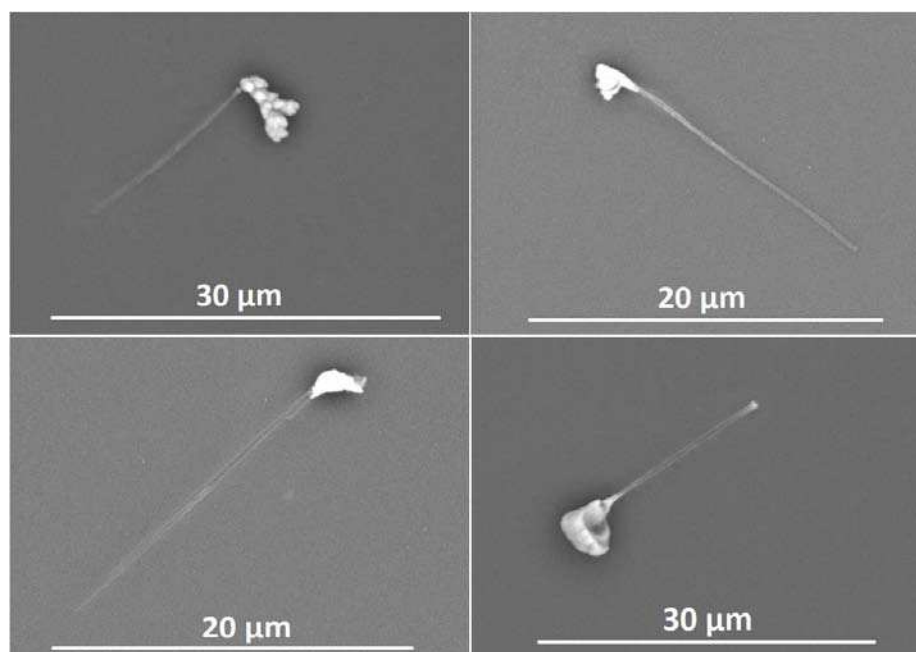


Figure 2.28 Selection of copper modified CMTs (SEM images) with a non-centered topology of the deposit, reprinted from Ref. (148).

In a last set of experiments it was possible to modify CMTs with a more complex and tunable copper structure by combining sequentially both topologies (centered & non-centered electrodeposition). An experiment analogue to the one used to prepare the non-centered deposition was carried out, using the same conditions in terms of electric field (the electrodeposition lasted for 6.5 min.), but the DMSO was allowed to melt during the second potential step. Thus the alignment of the tubes was diagonal with respect to the electric field during the first part of the electrodeposition process (as long as DMSO was frozen), but as soon as the solvent started to melt, a reorientation of the carbon tubes occurred (Figure 2.29a). Investigation of the collected tubes at the end of the experiment revealed a copper

deposit with a typical L shape, resulting from this change of orientation. Figure 2.29b shows SEM images of representative CMTs exhibiting such an L shape structure. This last experiment illustrates that the concept of modulating the alignment of the objects in the electric field is a very efficient strategy to generate controlled topologies of copper clusters at one end of the CMTs when using bipolar electrochemistry to trigger the deposition.

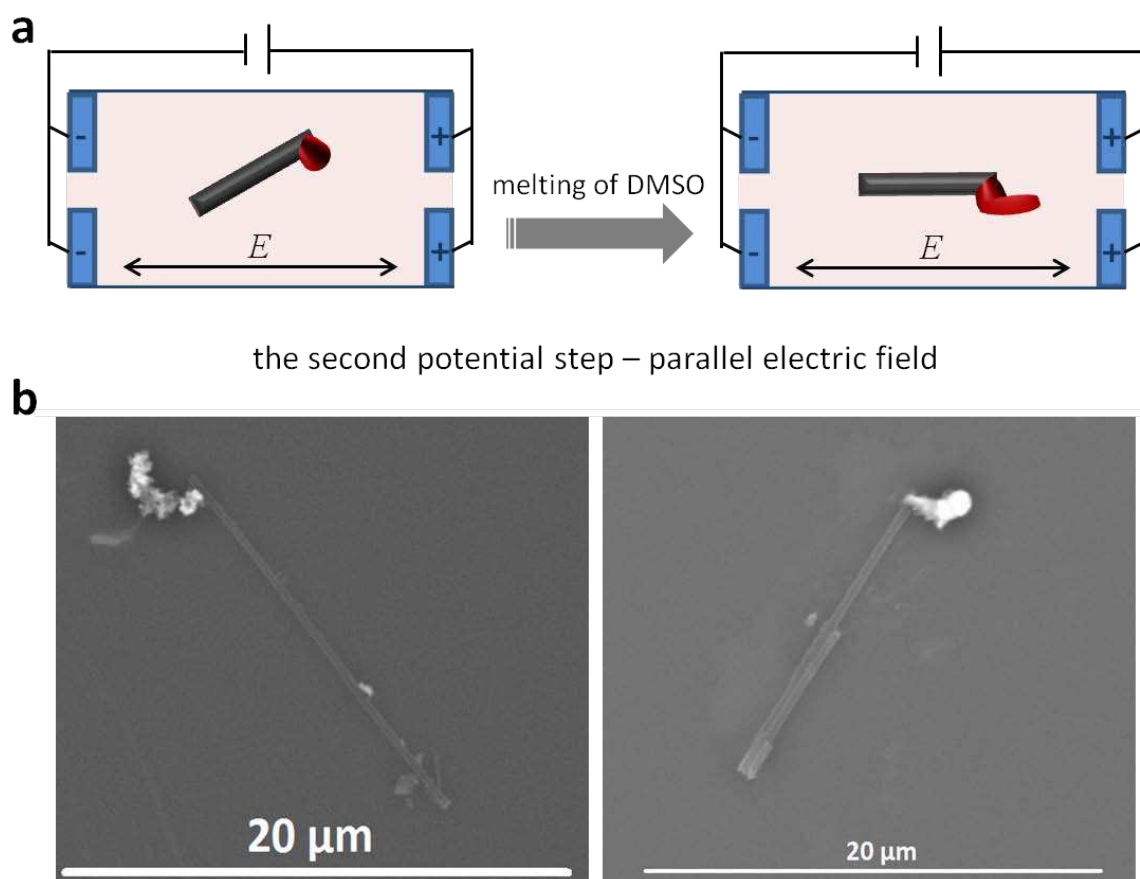


Figure 2.29 a) Scheme shows the resulted topology from realignment of the CMT under the effect of the applied field during the electrodeposition of non-centered cluster. b) SEM images for CMTs modified with a controlled sequence of a first non-centered and a second centered copper deposit, reprinted from Ref. (148).

We demonstrated here the fine-tuning of the local orientation of the metal deposit by carefully choosing the experimental conditions during bipolar electrochemistry. The experiments were performed with carbon substrates and copper, but this concept can be adapted to a wide range of substrates and materials leading to a large library of microscale hybrid materials. Such controlled topologies might be of importance for the design of electronic devices,¹⁴⁹ where a variety of specific electric connections are required, especially

at the microscale, when conventional electrodeposition approaches are experimentally challenging because of the necessity of a direct electric contact between the conductive objects which need to be modified and the external power supply. In addition, these topologies can be exploited to control the mode of motion of swimmers, in case we have, for example, platinum, instead of copper as we will discuss in section 3.2.2.

2.5.4. Electrodeposition of an Inorganic Functional Layer on Graphite Rods.

The bipolar electrodeposition strategy that has been shown so far always involves a direct electron transfer from the substrate (BPe) to a metal ion which undergoes an electroreduction. However, an indirect bipolar electrodeposition (IBED) is also possible to prepare APs. In this case, the deposits are triggered indirectly at the reactive pole of the BPe by local reactions. They can be induced by the dissolution of the BPe itself,¹⁴⁶ or a local pH change,¹⁵⁰ or even from reducing electroactive species that can further react locally with another soluble precursor to generate the deposit.¹⁵¹ We will now focus on the latter case in the following section.

The IBED process was adapted for the selective deposition of a functional inorganic layer, able to promote chemical light emission on a Janus object. We were able to deposit water-insoluble Prussian Blue (PB), $\text{Fe}^{\text{III}}_4[\text{Fe}^{\text{II}}(\text{CN})_6]_3$, and related compounds.¹⁵²⁻¹⁵³ PB is a well-known coordination compound with many interesting applications, either as a pigment¹⁵⁴ or in the field of analytical chemistry, especially for chemical¹⁵⁵⁻¹⁵⁶ and biological sensors.¹⁵⁷⁻¹⁵⁹ In this context the activity of PB with respect to luminol chemiluminescence (CL) has been explored.¹⁶⁰ CL refers to the emission of light from a chemical reaction, which can occur in solid, liquid or gas systems.¹⁶¹ Generally, the chemical reaction generates an excited and unstable state of a chemical compound that will emit light when relaxing to its fundamental state.¹⁶² CL can serve as a sensitive analytical reporter signal, which has been used for a variety of assays, including CL-based sensors for detecting different kinds of compounds ranging from inorganic and biological molecules to drugs.¹⁶³ One can therefore imagine that the asymmetric modification of objects with such a functional layer might find original applications for example in the field of analytical chemistry or for tracking the trajectories of autonomous microswimmers.

Prior to bipolar electrodeposition, preliminary experiments have been performed to investigate the formation of PB by classic chemical reaction as well as conventional electrodeposition, using aqueous solutions of ferric- or ferrocyanide with FeCl_2 or FeCl_3 . PB paste was chemically prepared first in order to check its activity towards CL. This was performed by simple mixing of 2:3 vol. of 1M $\text{K}_4[\text{Fe}(\text{CN})_6]$ and 1M of FeCl_3 , respectively. PB precipitated directly and was separated from the supernatant by centrifugation at 15,000 rpm for 3 min. The paste was washed by adding pure water and the resulting mixture was sonicated for 3 min prior to another centrifugation. The washing step was repeated 10 times in order to remove any traces of unreacted precursors. The prepared paste (Figure 2.30) was used later for investigating the CL.



Figure 2.30 Optical image of PB paste prepared by the chemical reaction of $\text{K}_4[\text{Fe}(\text{CN})_6]$ with FeCl_3 in aqueous solution.

The classic electrodeposition of PB is usually carried out from aqueous solutions containing ferric (Fe^{III}) and ferricyanide ($[\text{Fe}^{\text{III}}(\text{CN})_6]^{3-}$) ions.¹⁶⁴ We tested the possibility to deposit PB on our bipolar substrate (graphite rod, from Goodfellow) by cyclic voltammetry from a solution containing 4 mM of $\text{K}_3[\text{Fe}(\text{CN})_6]$ and FeCl_3 in 0.1 M KCl and HCl. The deposition was performed by applying 200 scans (scan range 0.4 to 0.8 V versus Ag/AgCl) with a scan rate of 40 mV/s, and under a nitrogen gas atmosphere. Figure 2.31a shows representative cyclic voltammograms of PB growth by applying 200 successive cycles where a characteristic cathodic peak at ~ 0.75 V is visible. These data are in good agreement with the reported literature.¹⁵⁵ Optical micrograph of PB deposit on the graphite rod can be seen in Figure 2.31b.

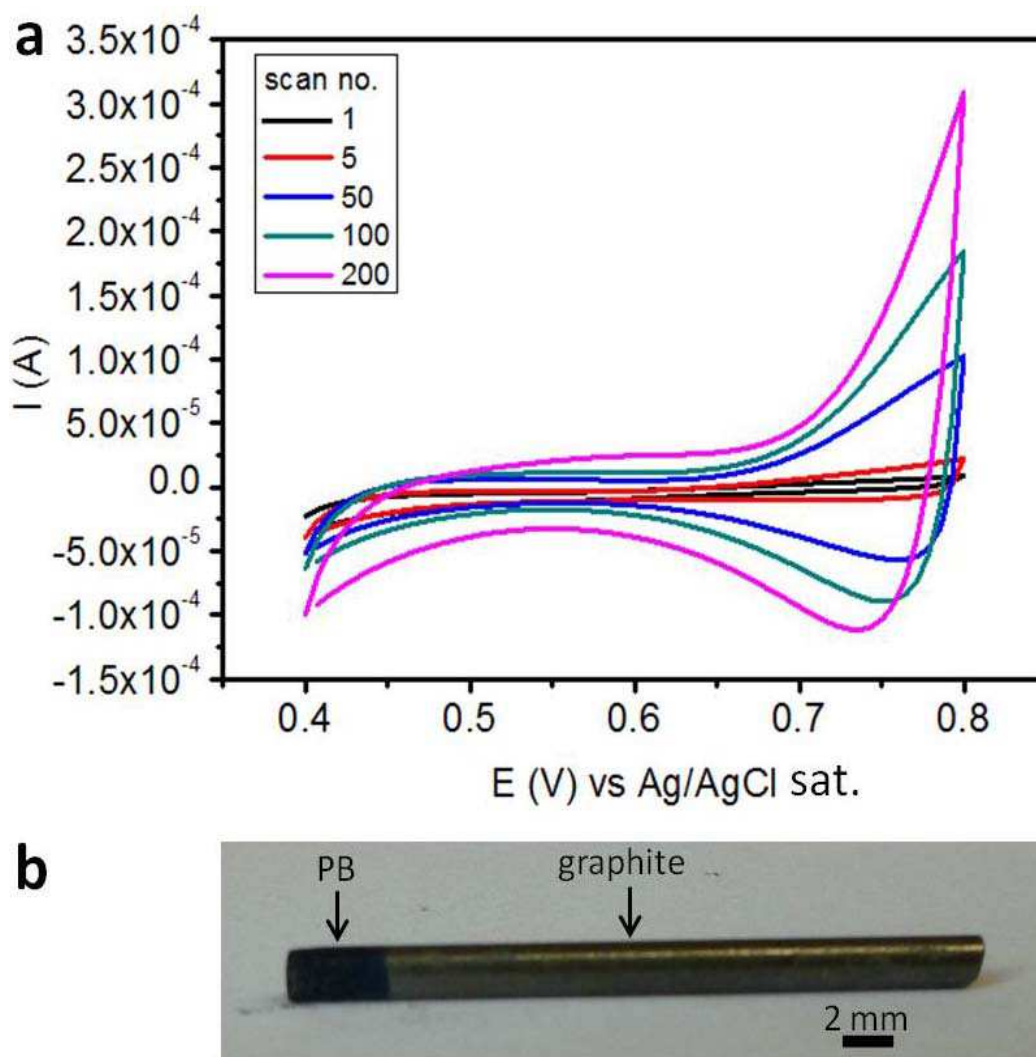


Figure 2.31 a) Representative cyclic voltammograms of PB growth on graphite rod ($\varnothing = 2$ mm). b) Optical image of the graphite rod showing PB deposit on its end after 200 cycles with cyclic voltammetry (CV).

For bipolar electrodeposition of PB on graphite rods, a cell similar to the one in Fig. 2.17b with a 3 mm in diameter, and 3 cm long plastic capillary was used. Graphite sheets were used as feeder electrodes and the graphite rod ($\varnothing = 2$ mm) was positioned in between. The cell was filled with a fresh solution of FeCl_3 and $\text{K}_3[\text{Fe}(\text{CN})_6]$ (10 mM) and the electric field was applied with a DC power supply (Sodilec MCN 350 V). At the end of the experiment the modified rods were washed several times with ultrapure water to remove salt residues.

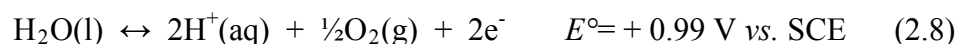
In order to estimate the sufficient electric field for bipolar electrodeposition, it is important to understand the mechanism of PB deposition. Chronopotentiometric investigations in an equimolar ferric–ferricyanide mixture reveal two plateaus at $\sim +0.7$ V and $+0.4$ V versus

SCE,¹⁶⁵ which have been assigned to the reduction of the one-to-one complex of $\text{Fe}^{\text{III}}[\text{Fe}^{\text{III}}(\text{CN})_6]$, discovered by Ibers et al.,¹⁶⁶ and of Fe^{3+} cations in this mixture, respectively. Two possible mechanisms have been reported for PB deposition, depending on the applied potential. First, PB can be deposited at + 0.7 V via the reduction of the ferric–ferricyanide complex ($\text{Fe}^{\text{III}}[\text{Fe}^{\text{III}}(\text{CN})_6]$). Secondly, around + 0.4 V, the precipitation of PB occurs due to reduction of Fe^{3+} to Fe^{2+} , the latter reacting with $[\text{Fe}^{\text{III}}(\text{CN})_6]^{3-}$.¹⁶⁴ Herein we use these mechanisms in order to electrogenerate PB by a wireless approach. For the purpose of illustration we now consider the second mechanism to explain our approach. Applying IBED for the localized and asymmetric deposition of PB involves the electrogeneration of Fe^{2+} ions at the cathodically polarized side of the rod, with concomitant oxidation of water at the anodic pole of the rod. The following half reactions need to be considered:

Ferric ion reduction at one side:



Water oxidation at the opposite side:



Based on the difference in formal potentials of the involved redox couples (0.46 V), an electric field of at least 0.023 kV/m theoretically needs to be applied to trigger PB deposition onto one extremity of a 2 cm-long rod. For reasons of clarity, Figure 2.32 illustrates only the second mechanism of PB electrodeposition. An electric field of 0.063 kV/m was applied across the solution for 30 min. The oxidation of water at the anodic pole of the rod releases electrons, which are employed for reducing Fe^{3+} cations into Fe^{2+} at the cathodic pole. Then, the latter undergo a local chemical reaction with $[\text{Fe}^{\text{III}}(\text{CN})_6]^{3-}$ ions, leading to the controlled deposition of the insoluble form of PB, $\text{Fe}^{\text{III}}_4[\text{Fe}^{\text{II}}(\text{CN})_6]_3$, at the cathodic pole of the rod.¹⁶⁴

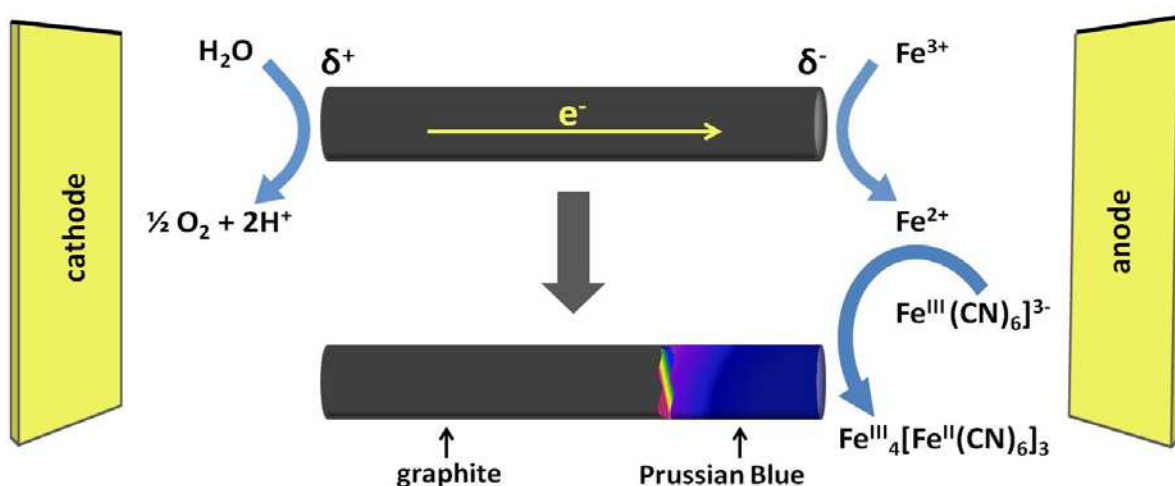


Figure 2.32 Illustration of the mechanism of indirect bipolar electrodeposition of Prussian Blue (PB), reprinted from Ref. (151).

Figure 2.33a shows a 2 cm long rod, modified at one end with a PB deposit. The general aspect of the deposit is visibly not homogeneous along the rod, as indicated by the color change, especially at the left part of the deposit. This can be explained by variations of the thickness of the inorganic layer, as well as differences in its chemical composition. Furthermore the composition of PB is notoriously variable due to the presence of lattice defects, and the exact color depends also on the particle size of the pigment. In bipolar electrochemistry, the apparent potential along the bipolar electrode varies (see section 1.5.3.), in contrast to conventional electrochemistry, where the potential of the working electrode stands at a fixed value which is fully controlled with respect to the reference electrode. The potential drop in the solution and around the object (which in turn depends on several other parameters like concentration and mobility of ions), also favors variations in the chemical composition of the deposit.

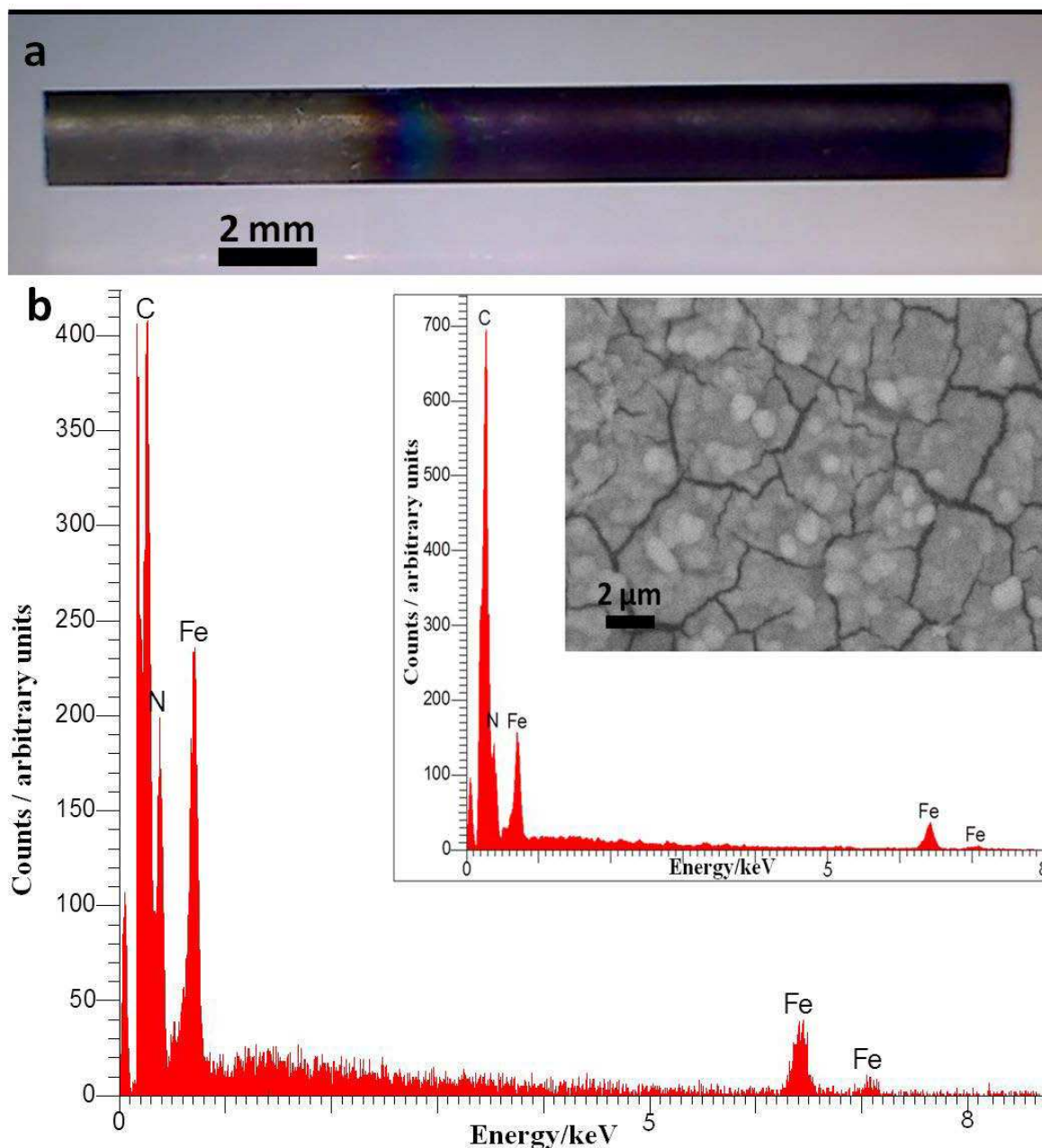


Figure 2.33 a) Optical image of graphite rod modified under 0.063 kV/m electric field and 10 mM Conc. of reactants, b) EDX spectra of the deposit recorded on the right end of the rod. Inset: EDX recorded on the middle of the modified rod and SEM image of the deposit, adapted from Ref. (151).

Indeed, the color arises directly from the exact chemical nature of the local precipitate, which is governed by a combination of several competing mechanisms at different potential values. Based on the first chronopotentiometric plateau (+ 0.7 V versus SCE) for the deposition of

PB¹⁶⁵ and from a thermodynamic point of view, the first mechanism should govern the reaction towards the middle of the rod, where the potential difference is lower (eq. 1.2).

The second proposed mechanism at + 0.4 V versus SCE¹⁶⁵ requires a higher potential difference, and is therefore more likely to occur at the extremity of the rod. Between these two extreme locations, most likely a mixture of both mechanisms is responsible for the deposit formation, and this would also have an influence on its morphology and stoichiometry, comparable to what has been reported in a different context for the generation of material gradients by bipolar electrochemistry.¹⁶⁷⁻¹⁷¹ Further analysis of the chemical composition of the resulting deposit was performed on this rod by EDX analysis (Figure 2.33b). The spectrum was collected at a position located at around 3 mm from the right end of the rod. Three significant signals assigned to carbon, nitrogen and iron were observed at 0.3, 0.4 and 0.7 keV respectively, as well as two other smaller contributions at 6.4 and 7.1 keV for iron. The carbon signal essentially originates from the rod. EDX data was also collected for the deposit located near the middle of the rod (Fig. 2.33b, inset). The same signals as in the first spectra were observed with a lower intensity, except the one for carbon which increased, due to the thinner PB layer. This analysis is in agreement with the composition of PB.¹⁷² SEM images (Figure 2.33b, inset) of the deposit revealed the presence of cracks, which have typically been reported by Itaya et al. for anhydrous PB films on electrodes.¹⁶⁵

Modifications were also carried out using lower electric fields (0.03 kV/m instead of 0.063 kV/m) for a longer time (2 h 40 min) and at lower salts concentrations (4 mM) (Figure 2.34a), in order to understand the influence of these parameters and compare the results with rods obtained under the conditions of Figure 2.33a. In this case the deposits showed a range of different colors. This indicates again the simultaneous presence of different electrodeposition mechanisms along the rod, leading to compounds that do not have the ideal PB stoichiometry. Most likely the nature of the chemical structure generated on the rod at low potentials is different from the one obtained at higher potential values, where the dark-blue color is observed. It is noteworthy that in control experiments where only FeCl₃ or K₃[Fe^{III}(CN)₆] was present, under otherwise identical conditions to that used to modify the rod in Fig. 2.33a, absolutely no deposit was formed (Figure 2.34b, c, respectively).

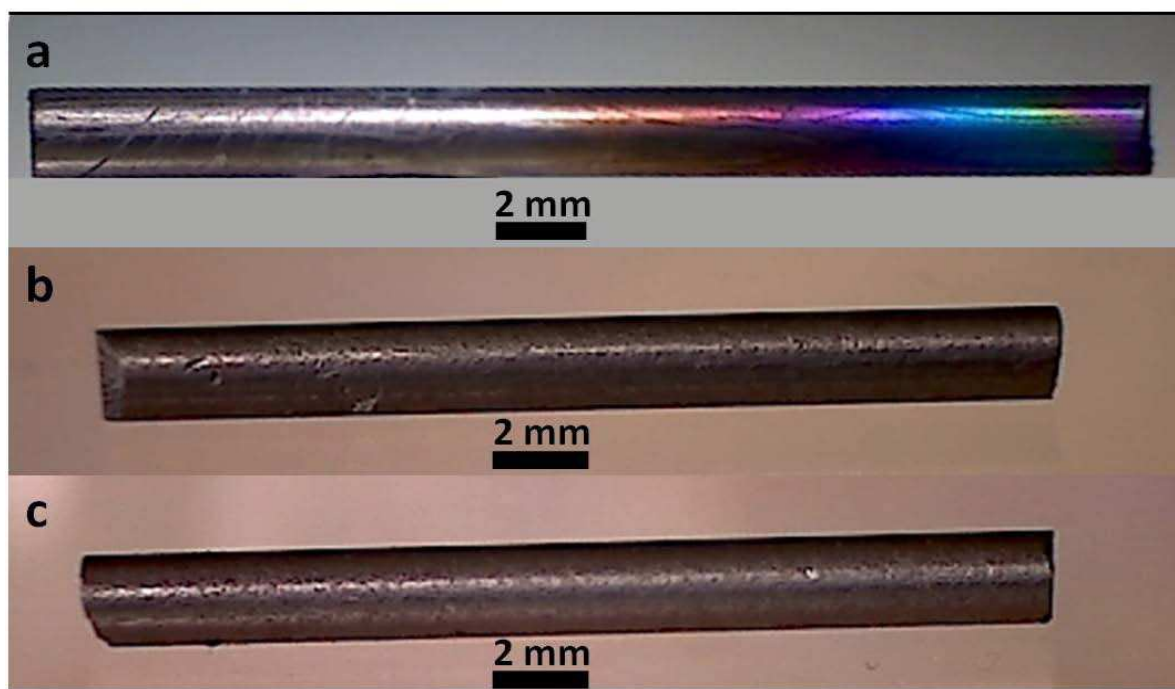


Figure 2.34 Optical images of graphite rods submitted to different experimental conditions. a) Modified under electric field of 0.03 kV/m, and 4 mM of FeCl_3 and $\text{K}_3[\text{Fe}^{\text{III}}(\text{CN})_6]$, adapted from Ref. (151). b), and c) Submitted to 0.063 kV/m electric field in the presence of 10 mM of FeCl_3 or $\text{K}_3[\text{Fe}^{\text{III}}(\text{CN})_6]$, respectively.

After this set of characterization experiments the activity of PB deposit with respect to the promotion of luminol CL was investigated. For this, a stock solution of 22 mM of luminol in 1M NaOH was prepared. 1 mL of this solution was diluted with pure water to reach a final concentration of 5.5 mM of luminol. 10 mL of hydrogen peroxide (30%) was added just before recording the luminescence. The deposit was immersed in the solution after switching off the light, and CL was detected as a function of time. Figure 2.35a shows the mechanism responsible for this light emission. The oxidation of luminol can be promoted by PB in the presence of dissolved oxygen in alkaline aqueous solutions.¹⁶⁰ Hydrogen peroxide decomposition triggered by cations is also known as an ingredient for luminol CL.¹⁶¹ The overall reaction leads to the formation of an amino-phthalate dianion in an excited state, which emits light when returning to the ground state.¹⁶² The CL activity of PB paste that has been prepared prior to bipolar electrodeposition experiments was tested first. A glass rod was coated with a layer of the paste and put in a vial, after the solution of luminol/ H_2O_2 was poured on it, CL was clearly visible (Fig. 2.35 b, c).

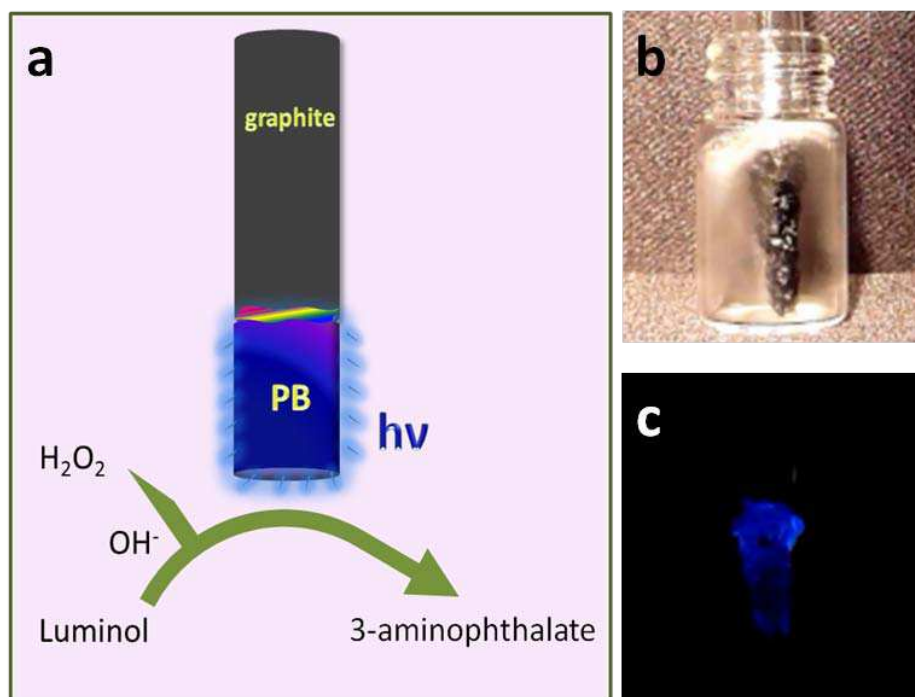


Figure 2.35 a) Illustration of luminol chemiluminescence, localized at the Prussian Blue modified end of a graphite rod. Pictures of PB paste stuck on a glass rod before (b) and after (c) putting the solution of luminol/ H_2O_2 and switching off the light.

The end of the rods modified with PB by bipolar electrochemistry was then investigated for CL. Two snapshots extracted from a movie, showing graphite rod modified with PB at the higher potential are gathered in Figure 2.36. The first one has been recorded before (Figure 2.36a) and the other one (Figure 2.36b) during exposure of the modified part to a solution containing luminol and hydrogen peroxide. The dark-blue part of the deposit at the bottom gives an intense CL signal, while the upper one (green to blue) generated no significant blue light. This difference is most likely related to the changes in the chemical structure of the deposit along the rod as discussed before, and also due to variations in the deposit thickness, increasing from the middle towards the end of the rod. The typical lifetime of the CL signal for the objects used in this study was of the order of a few seconds, until complete consumption of the PB layer. However this lifetime can be increased by prolonging the bipolar electrodeposition, leading to thicker PB layers. The activity of graphite rods modified at lower potential values (0.03 kV/m), like that in Figure 2.34a, was also investigated. No CL could be observed in these cases, suggesting that the highly colored deposit is indeed of different chemical nature.

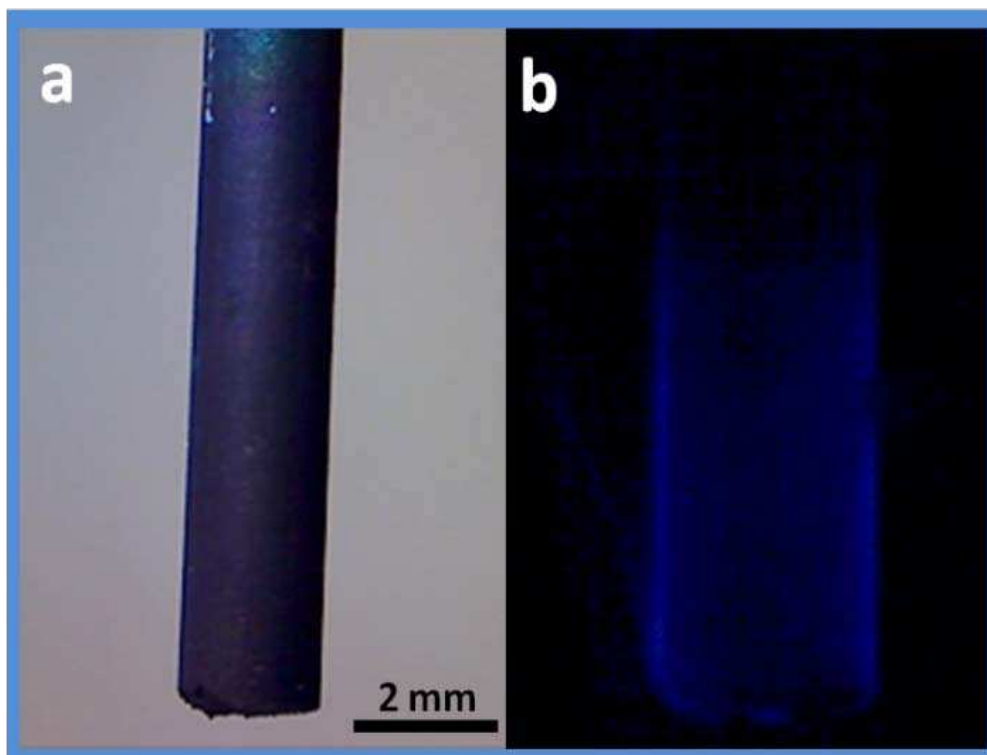


Figure 2.36 Snapshots of the Prussian-Blue-modified end of a graphite rod recorded a) before and b) during immersion in luminol/H₂O₂ solution with switched-off light, reprinted from Ref. (151).

To conclude, functional inorganic layers, PB, were successfully deposited electrochemically for the first time in a wireless set-up at one end of graphite rods, exhibiting high activity towards luminol CL. These proof-of-principle experiments open up new perspectives for the straightforward generation of functionalized light-emitting objects. Such objects might find interesting applications either as sensors or catalytic swimmers,¹⁷³ taking advantage of PB's activity with respect to the decomposition of hydrogen peroxide, which can act in this way simultaneously as a chemical fuel for controlled propulsion¹⁴⁴ and as a reactant for CL, thus resulting in an autonomous chemiluminescent swimmer.

2.5.5. Bipolar Electrogeneration of Single Crystals

During the experiments that have been performed in order to explore the possibility to modify carbon fibers (CFs) with various metals, we observed an interesting phenomenon. Among the several morphologies of the resulting deposits single crystals were detected. We decided to investigate this phenomenon in detail, which was characterized later as an electrocrystallization process.

Electrocrystallization refers to a variety of electrochemical deposition processes that marked the birth of modern electrochemistry.¹⁷⁴⁻¹⁷⁵ It may be broadly defined as the process (or result) of a direct or indirect electrochemical influence on crystallization.¹⁷⁶ (i) A direct electrochemical influence may be exerted if the value of the electrode potential dominates the type of nucleation and the growth kinetics for electrodeposition of a metal. (ii) Electrochemical reactions may indirectly alter the local reaction environment (e.g. the pH) and hence the nature of the reaction product. For example, in an unbuffered electrolyte the occurrence of hydrogen evolution as a side reaction at the cathode may result in the co-deposition of metal oxides/hydroxides in the metal deposit.¹⁷⁶ In many processes, both of these influences are experienced to some extent, i.e. there is a significant coupling between electrochemical and chemical steps in the overall reaction sequence.¹⁷⁶ The properties of a solid phase are linked to the crystallographic structure.¹⁷⁴ Many parameters can influence this structure such as electrode potential or current density, respectively, temperature, metal ion concentration, additives and electrolyte convection.^{174, 177} In contrast to physical crystallization where metal crystals are formed by solidification of the liquid metal or by condensation of the metal vapor, in electrocrystallization the mass transfer is accompanied by charge transfer.¹⁷⁸

The first experiments were performed in a bipolar cell having two ion exchange membranes, the CFs were placed in between, and the feeder electrodes (gold plates) were spaced by 6 cm. Solutions of 60 mM of HAuCl_4 , or 10 mM of H_2PtCl_6 in pure water were prepared. The metal precursor solution was poured in the reaction compartment whereas the feeder electrodes compartments were filled with cold water. The voltage was applied in order to trigger the oxidation of water at the anodic pole and the metal deposition at the cathodic pole of the CF. At the end of the experiment, the modified fibers were collected, washed several times, and prepared for the characterization similar to what has been described before in section 2.5.2. Figure 2.37a shows a 150 μm long CF that was modified in the presence of

HAuCl₄ solution with a single crystal at one extremity and also in the middle after applying 300 V for 7 min. In this case the proposed reaction at the cathodic pole of the CF was the reduction of AuCl₄¹⁻ into Au metal as following:

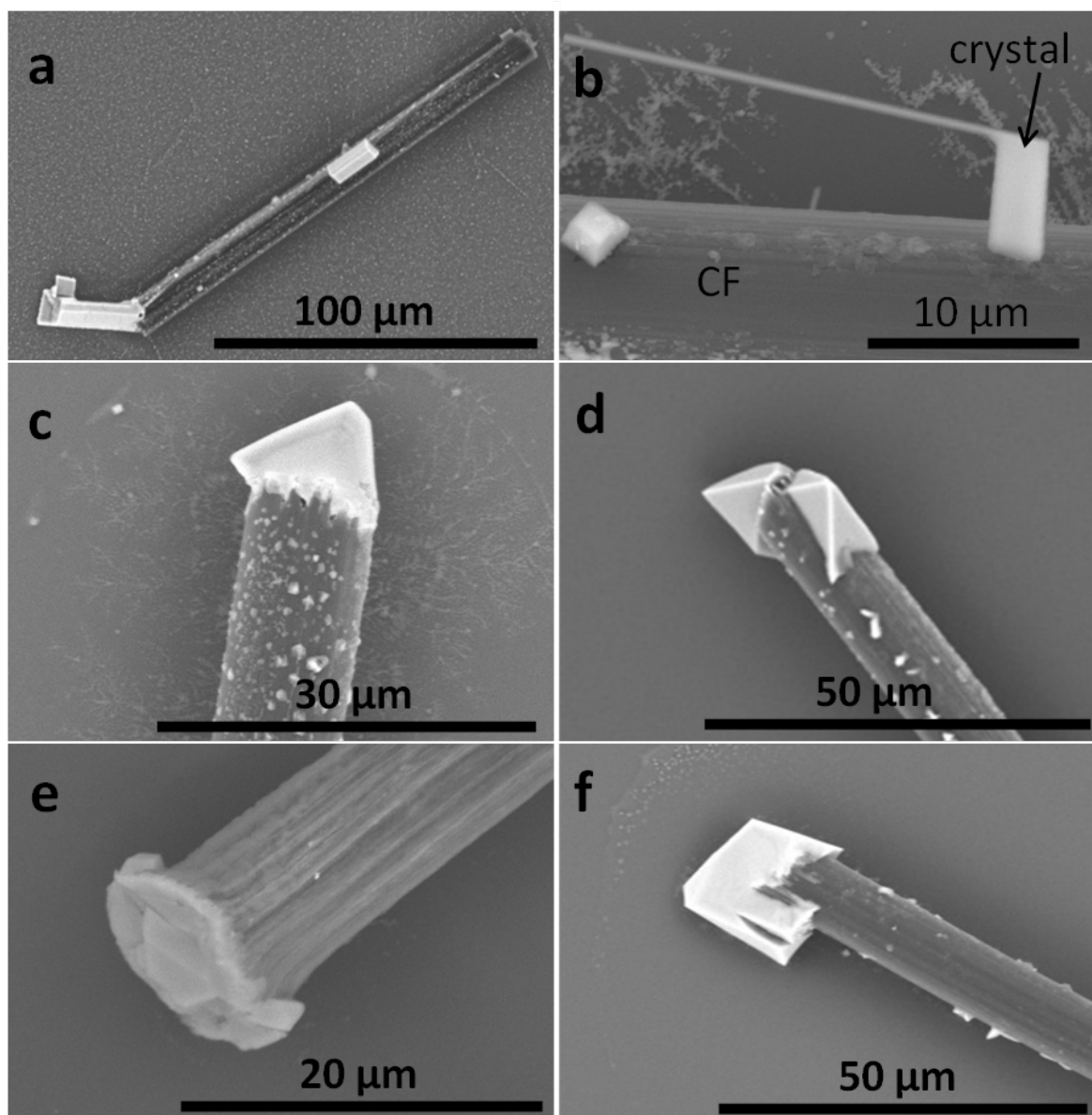
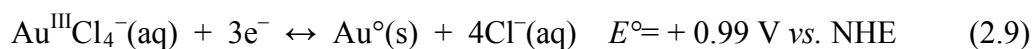


Figure 2.37 SEM images of a carbon fiber modified with gold (a) and platinum (b-f) crystalline species under different experimental conditions.

Simultaneously, the same procedure was performed with platinum by applying 22 V for 14 min in order to modify a 4 mm-long CF with Pt. In this case several crystals were observed along the CF, and a zoom on two of them is shown in Figure 2.37b. Since we already

deposited Pt on CMTs and CFs as we showed previously, this deposit morphology was surprising and we decided to further investigate this intriguing crystal formation phenomenon.

For this, we used the bipolar cell (see Fig. 2.17b) containing a glass capillary (5 cm long, and 1 mm diameter) connected to both PE cuvettes, since it is easier to manipulate and recover the modified fibers without breaking or detaching the deposit from the sample. The cell was filled with the H_2PtCl_6 solution and CFs in the range of 2.2 – 3.3 mm in length were inserted inside the capillary. The potential (27 V) was applied through the gold feeder electrodes for ~ 60 min. The recovered fibers from different experiments are illustrated in Figure 2.37c-f. The CFs were perfectly modified with single crystals at one extremity. The shape and the length (l_{dep}) of the crystal are different from one fiber to another in Fig. 2.37. They are ranging from rectangular prisms (a, $l_{\text{dep}} \sim 15, 30 \mu\text{m}$) in the case of gold species, to hammer (b, $l_{\text{dep}} \sim 6 \mu\text{m}$), pyramidal (c, $l_{\text{dep}} \sim 12 \mu\text{m}$, and d, $l_{\text{dep}} \sim 15 \mu\text{m}$), flower (e, $l_{\text{dep}} \sim 13 \mu\text{m}$) and cubic (f, $l_{\text{dep}} \sim 20 \mu\text{m}$) like structures in the case of platinum species.

It is noteworthy that the resulting crystals were not always located at the cathodic pole, but many times they appeared at the anodic pole of the carbon fiber. This was completed by observing sometimes two different morphologies with different contrast under the scanning electron microscope, which was assigned to different compositions characterizing these deposit structures. Figure 2.38a shows SEM image of one example of a CF that was simultaneously modified at one end with the two morphologies. A rhombic crystal ($l_{\text{dep}} \sim 30 \mu\text{m}$) is located at the very end of the fiber together with several, more amorphous deposits alongside the fiber. The latter displayed a higher contrast under SEM than the large crystal, which tends to indicate a higher electron density in that region (possibly metallic Pt). After this characterization, the fiber was washed ten times during ~ 30 min with pure water to check the solubility of the rhombic deposit in case it is a soluble salt instead. A very slight decrease in the crystal size was observed under the optical microscope. Pt metal is a well known catalyst for the hydrogen peroxide decomposition which generates intensive oxygen bubbles when dipping for example a Pt wire in an H_2O_2 solution (Figure 2.38b). By taking advantage of this reaction, we tested the same fiber, which still had the crystal on it, by immersing the modified end in a solution of 30% hydrogen peroxide under the optical microscope.

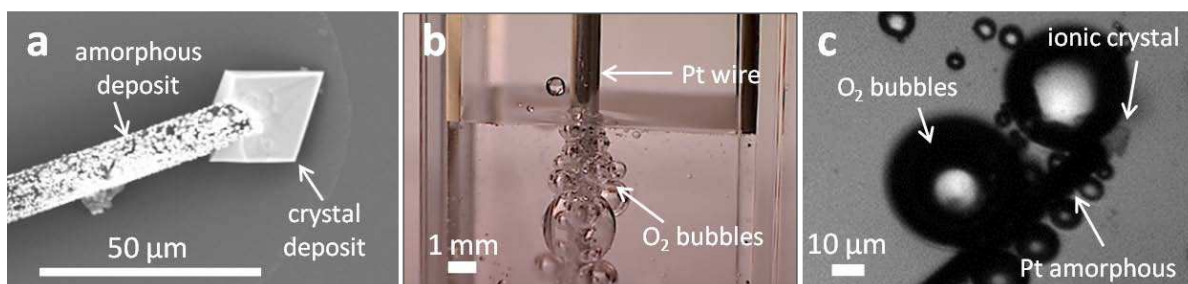


Figure 2.38 a) SEM picture of a CF modified with different deposit morphologies. b) Optical image of a platinum wire dipped in a solution of 30% H_2O_2 leading to intensive oxygen bubbles release. c) Optical micrograph of the modified end of the fiber immersed in a 30% H_2O_2 solution.

As one can see in Figure 2.38c, a lot of O_2 bubbles were released alongside the amorphous deposit, but not from the crystal at the extremity of the fiber. We can conclude from this experiment that the amorphous deposit is the metallic form of platinum, while the crystal is not, and also that this end was definitely the cathodic pole of the BPe because the Pt reduction occurred at this side (note: the anodic pole did not show any kind of deposit for this fiber). Some other CFs, like the ones in Fig. 2.37d and e, showed the crystal formation at one pole and the amorphous deposit at the other pole. To be sure that the CFs are not acting as a nucleation site for generating the crystals even in the absence of the electric field, a control experiment was performed. The same procedure that has been used to modify the CFs with Pt was exactly followed, except that no potential was applied in this case. After ~ 60 min, the fibers were recovered and prepared for investigation under SEM which revealed no crystals.

The batch of CFs that we used, contains a certain number of CFs that are not easy to be modified by bipolar electrochemistry, and this might be attributed to variations in conductivity that depends on their fabrication process¹⁷⁹ as discussed before. Also, due to the small diameter of the CFs ($10\ \mu\text{m}$), they can be quite fragile, hence, very easy to break.

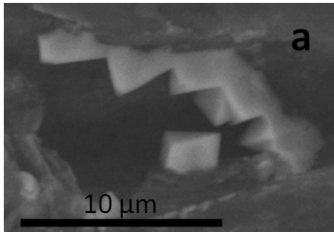
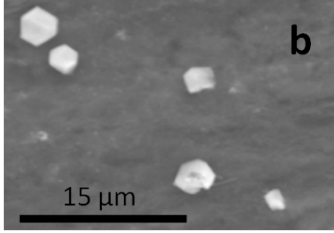
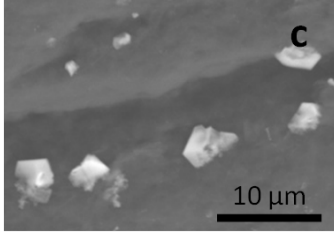
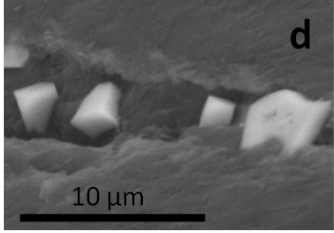
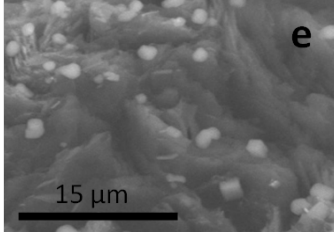
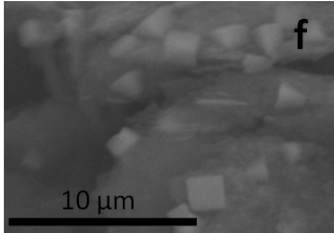
H_2PtCl_6 Conc./mM	E_{appl}/V	Deposition time/min	Ionic platinum crystals modified rods
10	22	60	
60	12.5	64	
60	12.5	64	
60	10	71	
60	10	480	
60	8	129	

Table 2.1 The experimental conditions that have been used in order to modify graphite rods with ionic platinum crystals and the SEM images of the resulted objects.

Therefore, in order to check the reproducibility of the crystals, and to be fully sure whether they are growing at the cathodic or anodic pole (especially when we are below the thermodynamic threshold value for Pt electrodeposition, which make it difficult to recognize the poles), we decided to work with another substrate that showed a better conductivity and is also easier to handle. Graphite rods ($\varnothing = 0.5$ mm) were chosen for this purpose because the larger dimension helps to discriminate which pole has acted as a cathode or anode by maintaining their alignment at the end of the experiment. The same bipolar set-up was used, except that in this case we used graphite sheets as feeder electrodes. Different experimental conditions were investigated in order to modify the graphite rods, the conditions and the SEM pictures of the resulting deposits are gathered in Table 2.1. The same length of the rods (3 mm) and salt concentration (60 mM) was employed, except for the first entry in the Table (a) which corresponds to a 3.3 mm-long rod and 10 mM concentration. The modified rods showed many times a successful generation of the crystals, however, similarly to the CFs, they are not always located on one extremity of the rod and appeared also alongside the rod's surface.

Let us first discuss the hypotheses that can explain the nature of these crystals. From the simple test of the crystal in contact with hydrogen peroxide solution (Fig. 2.38c), we excluded the possibility that it is a Pt^0 metal crystal. So, the only remaining possibility was the formation of an ionic crystal. The Pt compound that we used here is the hexachloroplatinic acid form (H_2PtCl_6) in which the platinum ion has an oxidation state of Pt^{IV} and it is present in the solution as a negatively charged metal complex (PtCl_6^{2-}). According to this, we propose two different hypotheses which both depend on the presence of the electric field: (1) The crystallization is a result of the PtCl_6^{2-} ions migration towards the positively charged (anodic) pole of the BPe. This will lead to a local accumulation of the ions at the anodic pole, and at a certain point when this concentration exceeds locally the limit of solubility, then the ions will start to crystallize. In this case, no electron transfer occurs, but the electric field is necessary for polarizing the substrate (graphite rod, for example) and enhancing the electrostatic accumulation of ions at the anodic pole. (2) The electrocrystallization is due to the reduction of PtCl_6^{2-} ions at the cathodic pole of the BPe into PtCl_4^{2-} in which the platinum has the oxidation state of Pt^{II} according to the following reaction:



Then, a local preconcentration of $\text{Pt}^{\text{II}}\text{Cl}_4^{2-}$ ions at the cathodic pole leads to their crystallization at this side of the BPe. Accordingly, first there is an electron transfer process which is followed by a local accumulation and crystallization.

In comparison to the conditions that have been used to modify the CFs in Fig. 2.37c-f, we studied the effect of a potential decrease on the size of the single crystal at the end of the rods. Hypothesis (2) implies that the Pt ion electrodeposition into Pt^0 will compete with the electrocrystallization process. Moreover, in most cases, the crystal appeared when the applied potential was close to the thermodynamic threshold value for Pt electrodeposition. Therefore, we tried to reach a potential that is below this value to prevent a complete electroreduction of the salt into Pt^0 metal. Also a lower potential may help generating a bigger single crystal by slowing down the crystallization allowing the ions to get arranged in into their final structure. Table 2.1a shows a series of crystals (each one has $l_{\text{dep}} \sim 5 \mu\text{m}$) that have been localized at the anodic pole of the graphite rod. The salt concentration was then increased to 60 mM for the following experiments and we considered simultaneously both hypotheses. In the latter cases, the higher concentration should promote a faster accumulation of the ions (PtCl_6^{2-} and/or PtCl_4^{2-}). However, we observed that this leads to the formation of more individual crystals but with a smaller size. It is well known that increasing the concentration speeds up the rate of three-dimensional nucleation and decreases the diameter of the final crystals.¹⁷⁸ By allowing the experiment to run for a longer time, the average crystals sizes increased again (Table 2.1d), but at very long reaction times (8 h) a lot of very small crystals were generated instead (e), in contrast to the bigger sizes observed when the experiment time was decreased to ~ 2 h (f). This behavior might be attributed to the local pH change around the graphite rod in the bipolar cell during the experiment. The longer time will generate a higher pH gradient, which may result in the dissolution of the deposited crystals leading to a smaller size at the end.

For this set of experiments, the applied potential value was decreased down to 8 V, which corresponds to the theoretical threshold value for Pt^{IV} deposition into Pt^0 (8.3 V) in this set-up, but this did not seem to influence the electrocrystallization process.

The modified rods were also characterized by using different techniques. The chemical composition of the big crystal in Table 2.1d (right side) was investigated by EDX spectroscopy (Figure 2.39a). The spectra show three significant signals assigned to carbon, platinum, and chlorine at 0.25, 2.1, and 2.6 keV respectively. In addition, gold signal was

overlapping with Pt at 2.1 keV, and was generated by the coating of the sample prior to SEM observation. Three other small contributions at 1.1, 2.8, and 3.3 keV belonging to Na, Cl, and K respectively, were also detected. The carbon signal essentially originated from the rod. The analysis confirmed that the crystal is composed of Pt and Cl. The small contributions of Na and K are not really understood, but most likely they might be present as impurities in the original hexachloroplatinic acid salt (Sigma-Aldrich, impurities not specified).

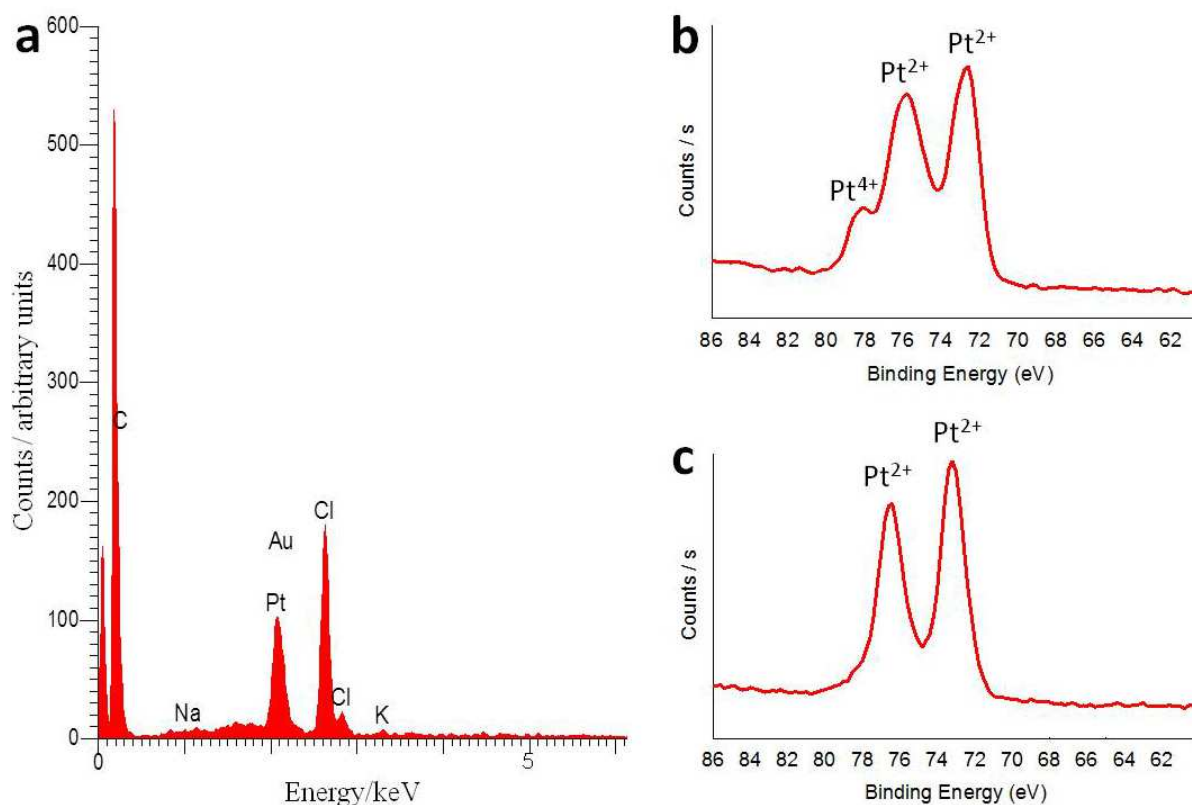


Figure 2.39 a) EDX – spectra for a crystal located at the anodic pole of a graphite rod. b, c) XPS Pt 4f spectra of crystals located at the anodic (b), and cathodic (c) poles of the same graphite rod.

The EDX analysis confirmed the presence of Pt in the crystal; however, this technique cannot provide information regarding the oxidation state of the elements. Therefore, we characterized the crystals in Table 2.1b, and 2.1c (b, c being the anodic and cathodic pole, respectively of a single graphite rod) using X-ray photoelectron spectroscopy (XPS, (Escalab VG 220i XL)). Figure 2.39b gives the X-ray photoelectron spectrum of Pt 4f regions for the crystals located at the anodic pole of the graphite rod. By comparing this data to the one reported in the literature that explored the XPS for a mixture of Pt^{II} and Pt^{IV},¹⁸⁰ we can

recognize one doublet which is most likely corresponded to Pt^{II} with a binding energy of 72.6 and 75.8 eV. The peak at 78.0 eV is strongly in agreement with the theoretical value for Pt^{IV} . The spectrum recorded at the cathodic pole of the rod (Fig. 2.39c) highlights a characteristic doublet with a binding energy at 73.2 and 76.4 eV which is in favor of Pt^{II} . The XPS data confirm our previous conclusion that there is no metallic platinum (Pt^0) in the structure of the crystals. As both Pt oxidation states (II and IV) appeared in the collected spectra, it is difficult to conclude whether only PtCl_4^{2-} or PtCl_6^{2-} is composing the crystals. In the same time we have to consider that Pt^{IV} may be reduced into Pt^{II} under prolonged X-ray bombardment.¹⁸¹⁻¹⁸² This means that the peaks assigned to Pt^{II} might be either original ones or generated from the reduction of Pt^{IV} ions, especially for the sample exists at the anodic pole of the rod (Fig. 2.39b) where a peak of Pt^{IV} is presented. However, as the doublet recorded at the cathodic pole (Fig. 2.39c) is more in favor of Pt^{II} with no signs to Pt^{IV} , it seems to indicate the presence of both chemical structures (PtCl_4^{2-} or PtCl_6^{2-}) at the opposite ends of the rod. And if this is the case, it can give us an explanation for the different data collected from the two poles. In other words, the first hypothesis (crystal formation is due to an electrostatic accumulation of PtCl_6^{2-} ions) might be valid at the anodic pole, while the second hypothesis (electroreduction of PtCl_6^{2-} ions into PtCl_4^{2-} and accumulation of the later leads to crystal formation) is valid at the cathodic pole of the BPe. It is noteworthy that the chlorine (Cl 2p) is also present with a characteristic peak at a typical energy (198.23 eV) in good agreement with a chloroplatinum complex.

In addition to the previous investigations, X-ray diffraction (XRD) was employed in order to get information about the crystallographic structure of our sample. For this, the CF that has been modified with a cubic crystal (Figure 2.37f) has been selected (the crystal most likely grew at the anodic pole of the fiber because it was possible to observe an amorphous deposit similar to a metallic Pt form at the opposite pole of the CF). Figure 2.40a shows the XRD pattern for this crystal. The fiber fixed into the sample holder was spinning during the analysis in order to collect the data from the different sides of the crystal. The pattern of spots that can be observed in Fig. 2.40a is characteristic for the crystal structure. The collected data refer to a cubic structure of the crystal with a lattice parameter of $a = 9.751 \text{ \AA}$. Figure 2.40b is a control pattern recorded with an unmodified CF where no diffraction spots can be identified.

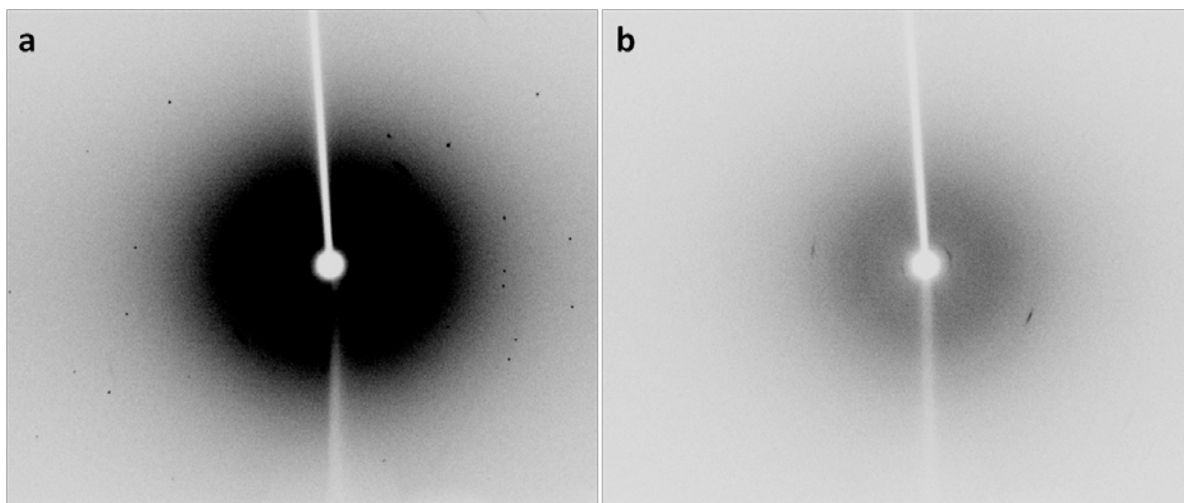


Figure 2.40 X-ray diffraction patterns for a single cubic crystal (a), and a CF as control sample (b).

By looking into the literature, one can see that Pt^{II} in K_2PtCl_4 for example has a tetragonal crystal structure with lattice parameters that are $a = b = 7.025 \text{ \AA}$, $c = 4.144 \text{ \AA}$.¹⁸³ On the other hand, Pt^{IV} in K_2PtCl_6 has a cubic crystal structure with a lattice parameter of $a = 9.743 \text{ \AA}$.¹⁸⁴ If we compare the results that have been obtained for our crystal ($a = 9.751 \text{ \AA}$) to those reported in the literature, it is clear that our sample is more consistent with the lattice structure model of the K_2PtCl_6 , which most likely matches with the Pt^{IV} oxidation state that was observed at the anodic pole of the graphite rod with the XPS analysis.

This electrocrystallization phenomenon is possibly applicable to other ions and conductive substrates, such as in the case of gold crystal (Fig. 2.37a). Therefore, at that stage, the experiments need to be further investigated in order to identify the parameters that are controlling the process.

In order to conclude, we have shown here for the first time that electrocrystallization of ionic compounds is possible using bipolar electrochemistry on carbon substrates. Even though the phenomenon is not fully understood yet, it opens up new perspectives for electrocrystallization of organic, inorganic and also biologic compounds in the nanoscale, e.g. proteins. One can imagine generating a single crystal of a protein at the end of a substrate and going directly to XRD for studying its crystallographic structure, without using complicated and long procedures. In addition, using bipolar electrochemistry allows preparing a lot of crystal-modified objects simultaneously (bulk procedure).

2.5.6. Generation of Different Metal Morphologies on a Single Substrate

Under certain conditions during the bipolar experiments, the metal electrodeposition was found to generate different morphologies alongside an individual substrate (BPe). Copper metal was selected in order to study this phenomenon. The control of morphological variation in electrodeposition is an important issue because the electrodeposition process is used for the production of many devices in industry and in various scientific fields.¹⁸⁵ The physical nature of the deposit can influence not only the functional properties, but also the chemical analysis.¹⁸⁶ Copper electrodeposits represent one of the processes that have been widely investigated.¹⁸⁷⁻¹⁸⁹

The potential gradient alongside the BPe during the bipolar electrochemistry experiment provides a suitable environment for the generation of material gradients (see section 1.3.5.). This concept also seems to play an important role for generating different metal morphologies on a single object.

Carbon fibers were employed as a substrate for asymmetric electrodeposition of copper at their extremities. A bipolar setup and procedure similar to the one that have been described to modify the CFs with Cu in section (2.5.3.1.) were used. The solution of CuSO_4 (5 mM) in pure water was poured into the cell compartments. A long CF (1 cm) was inserted into the capillary (5 cm long), and the voltage (17 V) was applied for 40 min. Figure 2.41 shows a representative SEM image of the cathodic pole of one modified fiber with a long (~ 1 mm) deposition. The zoom on the different sections of the deposit under the electron microscope highlights different copper morphologies on the fiber. The deposits varied in their shape and size depending on their position on the fiber because the potential is different. Starting from the right side of the deposit in Figure 2.41, we can recognize crystal structures (a), which varies to amorphous (b), dendritic (c) and porous (d) copper deposits when moving towards the end of the fiber. In fact, this variation in the Cu morphology was not observed before when we were modifying the CFs with a controlled Cu cluster (section 2.5.3.1.), most probably because we were using much shorter (~ 2 mm) fibers and the applied potential was possibly insufficient. Therefore, we performed several experiments, with different lengths of the CF (0.5 – 1 cm) using almost the same potential, which revealed that the relatively long fibers generate more different morphologies. The ΔV_{\min} required for the Cu electrodeposition on a 1 cm-long fiber is 0.9 V, while the applied ΔV_{\max} at the extremities of the fiber in Fig. 2.41 was 3.5 V, which is about four times higher. As this polarization increases from the

middle of the CF towards the end, this might explain the difference in the size and morphology of the deposit.¹⁸⁷ The small crystalline structure in (a) is located in the lower potential area which might be close to the thermodynamic threshold value for Cu electrodeposition leading to an electrocrystallization phenomenon similar to what has been described before with Pt (section 2.5.5.). The next region (b) shows the Cu grains with a big size compared to the deposits in (c) and (d), but with fewer nucleation sites for initiating the growth.¹⁹⁰ The active sites increase significantly when moving towards the area submitted to a higher potential, which leads to the formation of more dendritic and porous or dispersed copper deposits.¹⁸⁷ However, we have to consider that it is not easy to control these morphologies, since they are very sensitive to the experimental conditions such as concentration, pH, electric field (which affects the ion migration), dissolved oxygen, impurities and etc.¹⁸⁸⁻¹⁹⁰ Therefore, the process is still under investigation and the effect of some parameters such as concentration will be studied further.

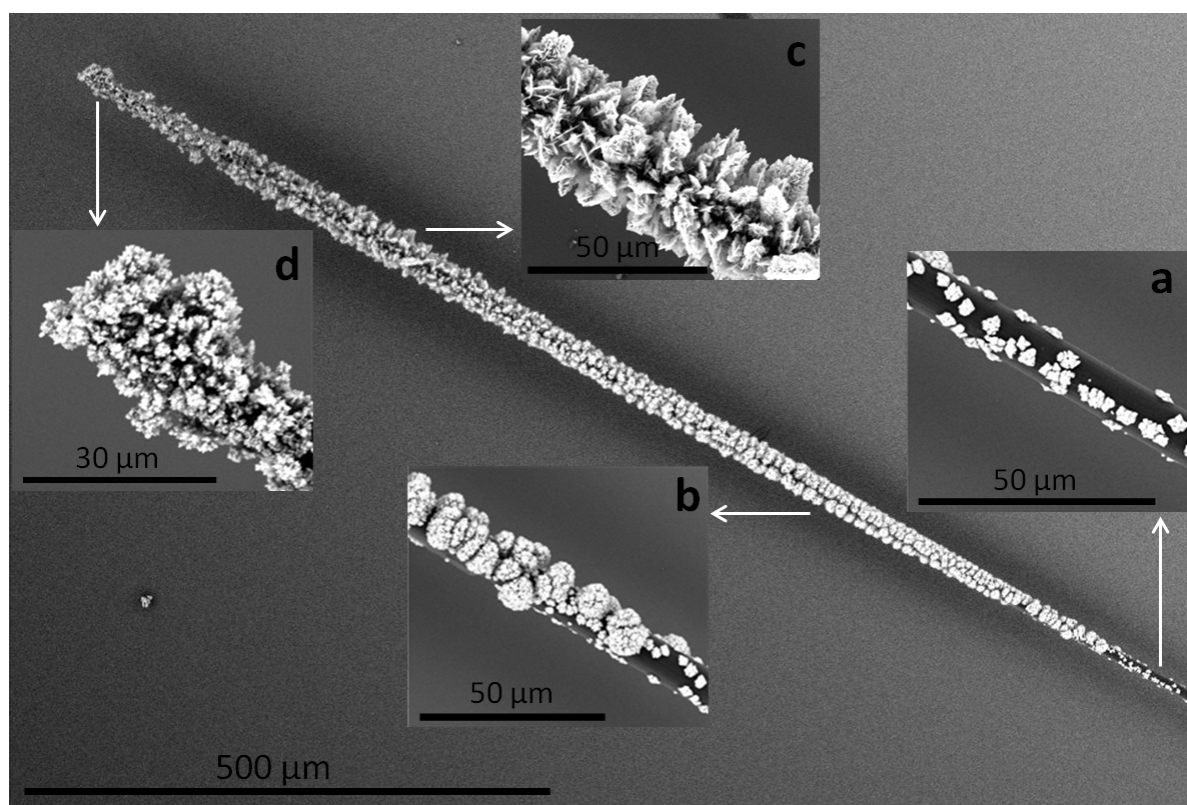


Figure 2.41 SEM image of a carbon fiber modified with four distinctly different copper morphologies by bipolar electrochemistry. Insets: SEM pictures of the zoom on the different sections of the deposit.

This methodology demonstrates the effective generation of several morphologies of copper at the same time on a single substrate by bipolar electrochemistry, which can be extended to other different metals. The method provides a simple way to study the structure of the deposits simultaneously and also to determine the potential that is responsible for producing a certain morphology, which is important especially for industrial applications.

2.6. Technology Development and Surface Microstructuration

The design of the bipolar cells that has been used for the preparation of APs such as the PMMA/PP, and glass cells (Figure 2.17a and c, respectively) is significantly improving the bulk technology as shown by the library of modified particles that were generated. However, the way of fixing the separators (in case of polymer membranes) and the porosity (for the sintered glass membranes) usually resulted in an uncontrolled convection of the solutions between the three compartments of the cell. Therefore, it became essential to develop a proper cell by introducing independent reaction compartment instead of fixing the membranes to the walls of the cell using PTFE, which could not really prevent the fluid flow from the outer compartments to the middle one and vice versa.

A bipolar cell with a new independent reaction compartment was first fabricated manually with glass. This design has been further improved by using PP as illustrated in Figure 2.42a. The reaction compartment (Fig. 2.42b) is made of a PP container open from the two sides that are facing the feeder electrodes. The ion exchange membranes (spaced by 1.6 cm) are fixed by two plastic windows which are connected tightly to the body by plastic screws. In this way, it is possible to totally separate the solution in the reaction compartment from those in the electrode compartments, which means that no convection will occur at least during the time required for bipolar electrodeposition. This has several advantages for the reaction solution: (1) it minimizes the pH changes (which is important for some reactions) and bubble evolution that result from oxidation and reduction of the solvent at the feeder electrodes. (2) it keeps the concentration at an accurate value by preventing the dilution. (3) it avoids contamination by other ions than the reactants in the case of using supporting electrolyte in the outer compartments which might affect the potential value required for the electrodeposition at the bipolar electrode. (4) it maintains the viscosity (especially for solvents with a relatively low freezing point), which is important to keep the orientation or

alignment of the BPe in particular for the site selective deposit. (5) it facilitates the handling and recovering of the modified sample and finally (6) it controls efficiently the microstructuration of spherical surfaces. The later point is of main interest and we are going to discuss it below.

Interest in nano- and microstructuration of surfaces has grown significantly over the past several years, due to their potentially broad applications in different fields such as biological and chemical sensors.¹⁹¹⁻¹⁹² We will show here that bipolar electrochemistry can be adapted to the straightforward micro- and nanostructuration of conductive objects.

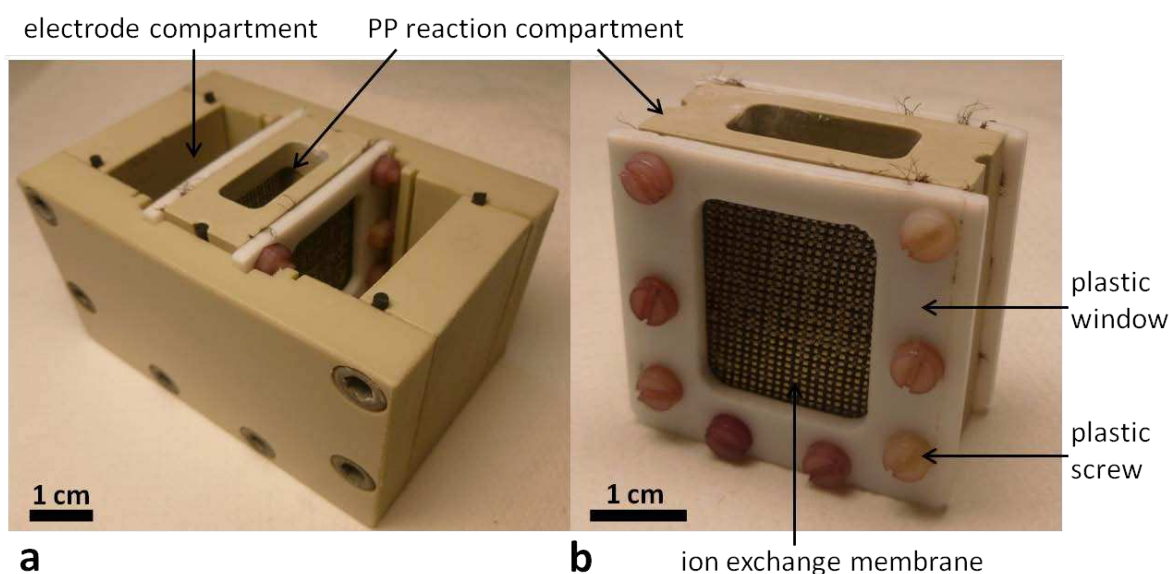


Figure 2.42 Bipolar cell made out of polypropylene (a) with an independent reaction compartment (b).

In the frame of preparing JPs, the bulk synthesis of particles that exhibit a hemispherical metal coating was recently demonstrated using bipolar electrochemistry.¹⁴⁶ Most metal deposits are generated from a cationic metal precursor; however, when a negatively charged metal ion at low ionic strength is used instead, the mode of mass transfer during the bipolar electrochemistry can generate a metal ring on the conductive surface.

As we explained in chapter one (section 1.2.), when a conductive object is submitted to an external electric field, a generated polarization potential (ΔV_x) gradient along the object divides its surface into cathodic and anodic areas. When a charged metal ion is dissolved in the solution and can only undergo an electroreduction at the cathodic pole of the BPe, the

mass transfer dominated by the migration of ions (no convection) needs to be considered (Figure 2.43). In order to understand this mechanism, let us consider first two different metal ions, a simple cation such as Cu^+ and a negatively charged metal complex such as PtCl_6^{2-} that are migrating under the effect of the applied electric field. In the case of Cu^+ , the ions migrate towards the cathodic feeder electrode, and when they arrive in front of the cathodic part of the BPe, they will experience a polarization (ΔV_x) that is higher than ΔV_{min} required for Cu^+ reduction. Therefore the electrodeposition occurs in this area, leading to the formation of a metallic hemisphere (Figure 2.43a).

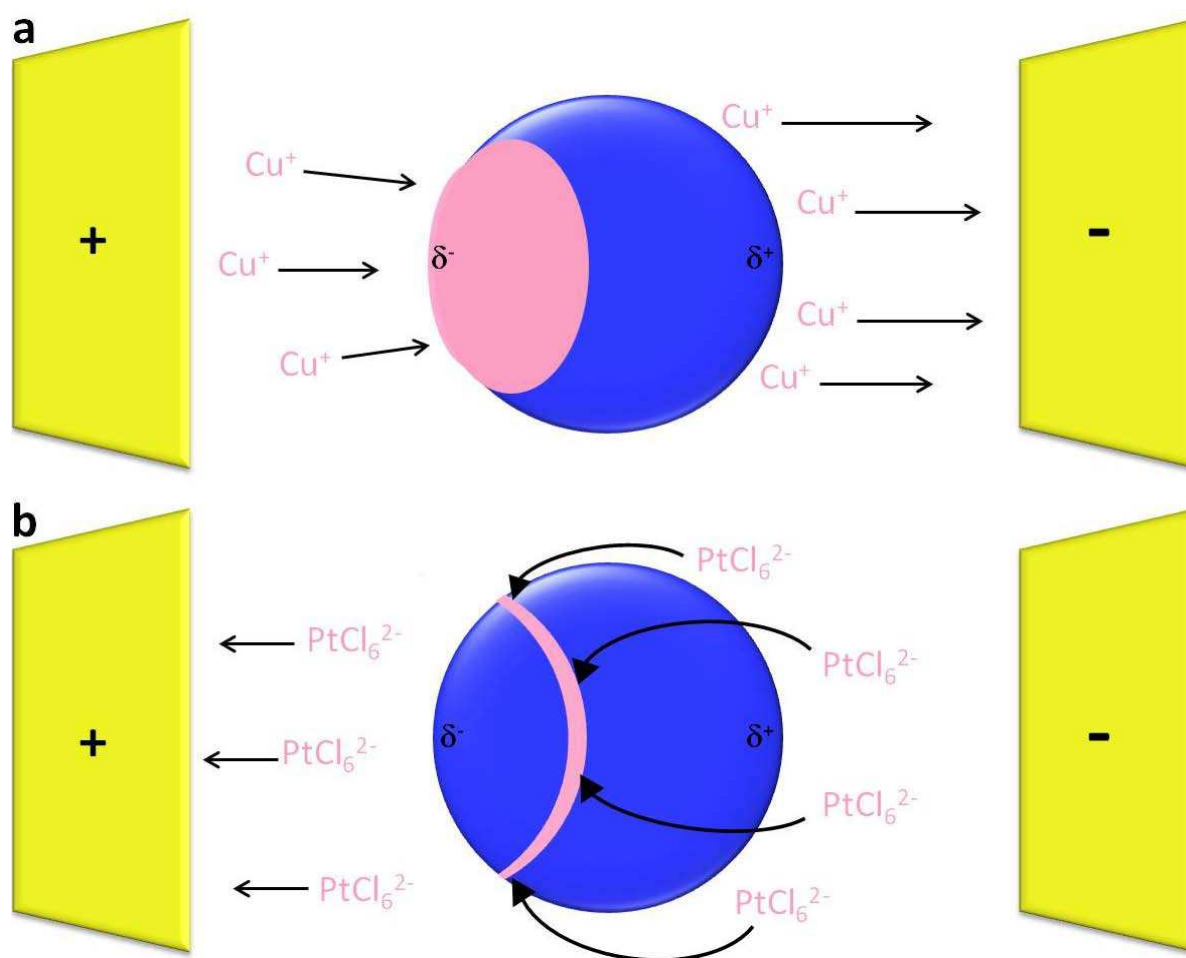


Figure 2.43 Illustration of the proposed bipolar electrodeposition mechanism when using cations (a), and anions (b), under the effect of ions migration (the arrows). The pink area refers to the deposit location.

On the other hand, the migration of the negative PtCl_6^{2-} ions takes place in the opposite direction. These ions migrate towards the anodic feeder electrode, which means they arrive from the backside of the BPe towards its cathodic pole (Figure 2.43b). Therefore, as soon as

they reach a position with a sufficient polarization ($\Delta V_x > \Delta V_{\min}$, at the boundary between the cathodic and anodic zone of the BPe), they will deposit. As a result the metal ions in this region are depleted and cannot be replaced due to the shadow effect, and this leads to the generation of a metal ring at this boundary. It is noteworthy that the presence of convection during the electrodeposition directs metal anions to the cathodic pole extremity, which minimizes the migration effect leading to the formation of JPs¹⁴⁶ instead of rings.

The PtCl_6^{2-} anion was employed to structure the surface of 200 – 400 μm diameter glassy carbon beads (GCBs, from Alfa-Aesar) with a metal ring. In contrast to anisotropic particles which keep their larger dimension oriented under the effect of the applied voltage, isotropic ones easily rotate in solution during the bipolar experiment. Therefore, a gel is usually used in order to trap them mechanically to enable a site selective modification. A suspension of 30 mg of GCBs was added to 6 mL of the gel (ethyl cellulose in EtOH). 0.25 mM H_2PtCl_6 was added and the mixture was stirred until the beads were well dispersed. 4 mL of the resulting mixture was introduced into the reaction compartment of the cell in Figure 2.42. 1 mM of NH_4Cl in ethanol was used as supporting electrolyte and was cooled for 1 min in liquid nitrogen and then added inside the electrode compartments. The gold feeder electrodes were spaced by 3.3 cm distance, and a 42 kV/m electric field was imposed for 20 s. After modification, the gel was taken out from the reaction compartment before washing and recovering the modified beads (see appendix 1 for the experimental details of the gel preparation and washing step of the modified beads).

SEM picture of the recovered particles is shown in Figure 2.44. The Pt rings were successfully deposited on the beads with relatively good yield, which confirms the mechanism of ring formation when using negatively charged species.¹⁹³ The process can be extended to other complex anions such as $\text{Au}^{\text{III}}\text{Cl}_4^-$. In the latter case, one can functionalize further the gold deposit by forming a functional self-assembly monolayer (SAM) such as optically active compounds for example. Also the generation of more complex structures is possible and is currently under investigation. This mechanism opens up many opportunities for the electrochemical design of very complex structures ranging from microstructured barcodes to optically active nanostructures.

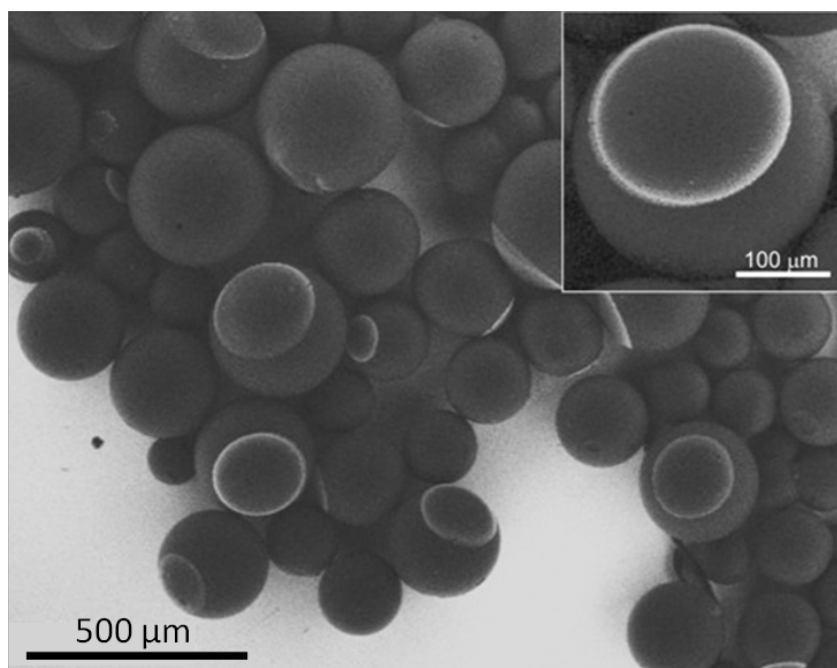


Figure 2.44 SEM picture of glassy carbon microbeads modified with a platinum ring. Inset: SEM picture of a zoom on one ringed particle. Adapted from Ref. (193).

References

1. Casagrande, C.; Fabre, P.; Raphaël, E.; Veyssié, M., *Europhys. Lett.* **1989**, 9 (3), 251.
2. de Gennes, P. G., *Science* **1992**, 256 (5056), 495-497.
3. Wessels, J. G. H., *Mycologist* **2000**, 14 (4), 153-159.
4. Sunde, M.; Kwan, A. H. Y.; Templeton, M. D.; Beever, R. E.; Mackay, J. P., *Micron* **2008**, 39 (7), 773-784.
5. Linder, M. B., *Curr. Opin. Colloid Interface Sci.* **2009**, 14 (5), 356-363.
6. Pawar, A. B.; Kretzschmar, I., *Macromol. Rapid Commun.* **2010**, 31 (2), 150-168.
7. Glotzer, S. C.; Solomon, M. J., *Nat. Mater.* **2007**, 6 (7), 557-562.
8. Du, J.; O'Reilly, R. K., *Chem. Soc. Rev.* **2011**, 40 (5), 2402-2416.
9. He, J.; Liu, Y.; Hood, T. C.; Zhang, P.; Gong, J.; Nie, Z., *Nanoscale* **2013**, 5 (12), 5151-5166.
10. de Gennes, P. G., *Rev. Mod. Phys.* **1992**, 64 (3), 645-648.
11. Botto, L.; Lewandowski, E. P.; Cavallaro, M.; Stebe, K. J., *Soft Matter* **2012**, 8 (39), 9957-9971.
12. Binks, B. P.; Fletcher, P. D. I., *Langmuir* **2001**, 17 (16), 4708-4710.
13. Glaser, N.; Adams, D. J.; Böker, A.; Krausch, G., *Langmuir* **2006**, 22 (12), 5227-5229.
14. Jiang, S.; Granick, S., *The Journal of Chemical Physics* **2007**, 127 (16), 161102-4.
15. Nonomura, Y.; Komura, S.; Tsujii, K., *J. Oleo Sci.* **2004**, 53 (12), 607-610.
16. Nonomura, Y.; Komura, S.; Tsujii, K., *Langmuir* **2004**, 20 (26), 11821-11823.
17. Ruhland, T. M.; Gröschel, A. H.; Ballard, N.; Skelhon, T. S.; Walther, A.; Müller, A. H. E.; Bon, S. A. F., *Langmuir* **2013**, 29 (5), 1388-1394.
18. Park, B. J.; Lee, D., *Soft Matter* **2012**, 8 (29), 7690-7698.
19. Kumar, A.; Park, B. J.; Tu, F.; Lee, D., *Soft Matter* **2013**, 9 (29), 6604-6617.
20. Park, B. J.; Lee, D., *ACS Nano* **2012**, 6 (1), 782-790.
21. Fan, H.; Striolo, A., *Soft Matter* **2012**, 8 (37), 9533-9538.
22. Adams, D. J.; Adams, S.; Melrose, J.; Weaver, A. C., *Colloid Surface A* **2008**, 317 (1-3), 360-365.
23. Ramanathan, M.; Shrestha, L. K.; Mori, T.; Ji, Q.; Hill, J. P.; Ariga, K., *Phys. Chem. Chem. Phys.* **2013**, 15 (26), 10580-10611.
24. Zhang; Glotzer, S. C., *Nano Lett.* **2004**, 4 (8), 1407-1413.
25. Li, W.; Gunton, J. D., *Langmuir* **2013**.
26. Liu, Y.; Li, W.; Perez, T.; Gunton, J. D.; Brett, G., *Langmuir* **2012**, 28 (1), 3-9.
27. Jiang, S.; Chen, Q.; Tripathy, M.; Luijten, E.; Schweizer, K. S.; Granick, S., *Adv. Mater. (Weinheim, Ger.)* **2010**, 22 (10), 1060-1071.
28. Erhardt, R.; Zhang, M.; Böker, A.; Zettl, H.; Abetz, C.; Frederik, P.; Krausch, G.; Abetz, V.; Müller, A. H. E., *J. Am. Chem. Soc.* **2003**, 125 (11), 3260-3267.
29. Walther, A.; Drechsler, M.; Muller, A. H. E., *Soft Matter* **2009**, 5 (2), 385-390.
30. Walther, A.; Drechsler, M.; Rosenfeldt, S.; Harnau, L.; Ballauff, M.; Abetz, V.; Müller, A. H. E., *J. Am. Chem. Soc.* **2009**, 131 (13), 4720-4728.
31. Pradhan, S.; Xu, L.; Chen, S., *Adv. Funct. Mater.* **2007**, 17 (14), 2385-2392.

32. Nie, Z.; Li, W.; Seo, M.; Xu, S.; Kumacheva, E., *J. Am. Chem. Soc.* **2006**, *128* (29), 9408-9412.
33. Hong, L.; Cacciuto, A.; Luijten, E.; Granick, S., *Nano Lett.* **2006**, *6* (11), 2510-2514.
34. Cayre, O.; Paunov, V. N.; Velev, O. D., *Chem. Commun.* **2003**, (18), 2296-2297.
35. Cayre, O.; Paunov, V. N.; Velev, O. D., *J. Mater. Chem.* **2003**, *13* (10), 2445-2450.
36. Gangwal, S.; Cayre, O. J.; Bazant, M. Z.; Velev, O. D., *Phys. Rev. Lett.* **2008**, *100* (5), 058302.
37. Gangwal, S.; Cayre, O. J.; Velev, O. D., *Langmuir* **2008**, *24* (23), 13312-13320.
38. Gangwal, S.; Pawar, A.; Kretzschmar, I.; Velev, O. D., *Soft Matter* **2010**, *6* (7), 1413-1418.
39. Velev, O. D.; Gangwal, S.; Petsev, D. N., *Annu. Rep. Prog. Chem., Sect. C*, **2009**, *105* (0), 213-246.
40. Chaudhary, K.; Chen, Q.; Juárez, J. J.; Granick, S.; Lewis, J. A., *J. Am. Chem. Soc.* **2012**, *134* (31), 12901-12903.
41. Zhang, L.; Zhu, Y., *Langmuir* **2012**, *28* (37), 13201-13207.
42. Smoukov, S. K.; Gangwal, S.; Marquez, M.; Velev, O. D., *Soft Matter* **2009**, *5* (6), 1285-1292.
43. Ren, B.; Ruditskiy, A.; Song, J. H.; Kretzschmar, I., *Langmuir* **2012**, *28* (2), 1149-1156.
44. Yuet, K. P.; Hwang, D. K.; Haghighooie, R.; Doyle, P. S., *Langmuir* **2010**, *26* (6), 4281-4287.
45. Binks, B. P.; Murakami, R., *Nat. Mater.* **2006**, *5* (11), 865-869.
46. Hunter, T. N.; Pugh, R. J.; Franks, G. V.; Jameson, G. J., *Adv. Colloid Interface Sci.* **2008**, *137* (2), 57-81.
47. Binks, B. P., *Curr. Opin. Colloid Interface Sci.* **2002**, *7* (1-2), 21-41.
48. Andala, D. M.; Shin, S. H. R.; Lee, H.-Y.; Bishop, K. J. M., *ACS Nano* **2012**, *6* (2), 1044-1050.
49. Fujii, S.; Yokoyama, Y.; Miyanari, Y.; Shiono, T.; Ito, M.; Yusa, S.-i.; Nakamura, Y., *Langmuir* **2013**, *29* (18), 5457-5465.
50. Meng, X.; Guan, Y.; Zhang, Z.; Qiu, D., *Langmuir* **2012**, *28* (34), 12472-12478.
51. Walther, A.; Hoffmann, M.; Müller, A. H. E., *Angew. Chem. Int. Ed.* **2008**, *47* (4), 711-714.
52. Gröschel, A. H.; Löbbling, T. I.; Petrov, P. D.; Müllner, M.; Kuttner, C.; Wieberger, F.; Müller, A. H. E., *Angew. Chem. Int. Ed.* **2013**, *52* (13), 3602-3606.
53. Teo, B. M.; Suh, S. K.; Hatton, T. A.; Ashokkumar, M.; Grieser, F., *Langmuir* **2011**, *27* (1), 30-33.
54. Tanaka, T.; Okayama, M.; Minami, H.; Okubo, M., *Langmuir* **2010**, *26* (14), 11732-11736.
55. Liang, F.; Shen, K.; Qu, X.; Zhang, C.; Wang, Q.; Li, J.; Liu, J.; Yang, Z., *Angew. Chem. Int. Ed.* **2011**, *50* (10), 2379-2382.
56. Link, J. R.; Sailor, M. J., *Proc. Natl. Acad. Sci USA* **2003**, *100* (19), 10607-10610.
57. Ou, F. S.; Shaijumon, M. M.; Ajayan, P. M., *Nano Lett.* **2008**, *8* (7), 1853-1857.
58. Takei, H.; Shimizu, N., *Langmuir* **1997**, *13* (7), 1865-1868.

59. Xu, C.; Xie, J.; Ho, D.; Wang, C.; Kohler, N.; Walsh, E. G.; Morgan, J. R.; Chin, Y. E.; Sun, S., *Angew. Chem. Int. Ed.* **2008**, *47* (1), 173-176.
60. Behrend, C. J.; Anker, J. N.; McNaughton, B. H.; Brasuel, M.; Philbert, M. A.; Kopelman, R., *J. Phys. Chem. B* **2004**, *108* (29), 10408-10414.
61. Chen, C.-H.; Abate, A. R.; Lee, D.; Terentjev, E. M.; Weitz, D. A., *Adv. Mater.* **2009**, *21* (31), 3201-3204.
62. Behrend, C. J.; Anker, J. N.; Kopelman, R., *Appl. Phys. Lett.* **2004**, *84* (1), 154-156.
63. Rogers, J. A.; Bao, Z.; Baldwin, K.; Dodabalapur, A.; Crone, B.; Raju, V. R.; Kuck, V.; Katz, H.; Amundson, K.; Ewing, J.; Drzaic, P., *Proc. Natl. Acad. Sci USA* **2001**, *98* (9), 4835-4840.
64. Nisisako, T.; Torii, T.; Takahashi, T.; Takizawa, Y., *Adv. Mater.* **2006**, *18* (9), 1152-1156.
65. Yin, S.-N.; Wang, C.-F.; Yu, Z.-Y.; Wang, J.; Liu, S.-S.; Chen, S., *Adv. Mater.* **2011**, *23* (26), 2915-2919.
66. Yabu, H.; Kanahara, M.; Shimomura, M.; Arita, T.; Harano, K.; Nakamura, E.; Higuchi, T.; Jinnai, H., *ACS Appl. Mater. Interfaces* **2013**, *5* (8), 3262-3266.
67. Lee, S. Y.; Yang, S., *Angew. Chem. Int. Ed.* **2013**, 8160-8164.
68. Ozin, G. A.; Manners, I.; Fournier-Bidoz, S.; Arsenault, A., *Adv. Mater.* **2005**, *17* (24), 3011-3018.
69. Paxton, W. F.; Sen, A.; Mallouk, T. E., *Chem. Eur. J.* **2005**, *11* (22), 6462-6470.
70. Wang, J., *ACS Nano* **2009**, *3* (1), 4-9.
71. Kagan, D.; Calvo-Marzal, P.; Balasubramanian, S.; Sattayasamitsathit, S.; Manesh, K. M.; Flechsig, G.-U.; Wang, J., *J. Am. Chem. Soc.* **2009**, *131* (34), 12082-12083.
72. Balasubramanian, S.; Kagan, D.; Jack Hu, C.-M.; Campuzano, S.; Lobo-Castañón, M. J.; Lim, N.; Kang, D. Y.; Zimmerman, M.; Zhang, L.; Wang, J., *Angew. Chem. Int. Ed.* **2011**, *50* (18), 4161-4164.
73. Gao, W.; Kagan, D.; Pak, O. S.; Clawson, C.; Campuzano, S.; Chuluun-Erdene, E.; Shipton, E.; Fullerton, E. E.; Zhang, L.; Lauga, E.; Wang, J., *Small* **2012**, *8* (3), 460-467.
74. Wu, Y.; Wu, Z.; Lin, X.; He, Q.; Li, J., *ACS Nano* **2012**, *6* (12), 10910-10916.
75. Ebbens, S. J.; Howse, J. R., *Soft Matter* **2010**, *6* (4), 726-738.
76. Kaewsaneha, C.; Tangboriboonrat, P.; Polpanich, D.; Eissa, M.; Elaissari, A., *ACS Appl. Mater. Interfaces* **2013**, *5* (6), 1857-1869.
77. Yoshida, M.; Roh, K.-H.; Mandal, S.; Bhaskar, S.; Lim, D.; Nandivada, H.; Deng, X.; Lahann, J., *Adv. Mater.* **2009**, *21* (48), 4920-4925.
78. Choi, J.-s.; Jun, Y.-w.; Yeon, S.-I.; Kim, H. C.; Shin, J.-S.; Cheon, J., *J. Am. Chem. Soc.* **2006**, *128* (50), 15982-15983.
79. Hu, S.-H.; Gao, X., *J. Am. Chem. Soc.* **2010**, *132* (21), 7234-7237.
80. Zhao, L. B.; Pan, L.; Zhang, K.; Guo, S. S.; Liu, W.; Wang, Y.; Chen, Y.; Zhao, X. Z.; Chan, H. L. W., *Lab Chip* **2009**, *9* (20), 2981-2986.
81. Hwang, S.; Lahann, J., *Macromol. Rapid Commun.* **2012**, *33* (14), 1178-1183.
82. Xie, H.; She, Z.-G.; Wang, S.; Sharma, G.; Smith, J. W., *Langmuir* **2012**, *28* (9), 4459-4463.

83. Hu, J.; Zhou, S.; Sun, Y.; Fang, X.; Wu, L., *Chem. Soc. Rev.* **2012**, *41* (11), 4356-4378.
84. Lattuada, M.; Hatton, T. A., *Nano Today* **2011**, *6* (3), 286-308.
85. Loget, G.; Kuhn, A., *J. Mater. Chem.* **2012**, *22* (31), 15457-15474.
86. Mao, Z.; Xu, H.; Wang, D., *Adv. Funct. Mater.* **2010**, *20* (7), 1053-1074.
87. Rodríguez-Fernández, D.; Liz-Marzán, L. M., *Part. Part. Syst. Char.* **2013**, *30* (1), 46-60.
88. Walther, A.; Muller, A. H. E., *Soft Matter* **2008**, *4* (4), 663-668.
89. Walther, A.; Müller, A. H. E., *Chem. Rev.* **2013**, *113* (7), 5194-5261.
90. Dendukuri, D.; Doyle, P. S., *Adv. Mater. (Weinheim, Ger.)* **2009**, *21* (41), 4071-4086.
91. Fujimoto, K.; Nakahama, K.; Shidara, M.; Kawaguchi, H., *Langmuir* **1999**, *15* (13), 4630-4635.
92. Lu, Y.; Xiong, H.; Jiang, X.; Xia, Y.; Prentiss, M.; Whitesides, G. M., *J. Am. Chem. Soc.* **2003**, *125* (42), 12724-12725.
93. Gong, J.; Zu, X.; Li, Y.; Mu, W.; Deng, Y., *J. Mater. Chem.* **2011**, *21* (7), 2067-2069.
94. Ho, C.-C.; Chen, W.-S.; Shie, T.-Y.; Lin, J.-N.; Kuo, C., *Langmuir* **2008**, *24* (11), 5663-5666.
95. Paunov, V. N.; Cayre, O. J., *Adv. Mater.* **2004**, *16* (9-10), 788-791.
96. Ye, S.; Carroll, R. L., *ACS Appl. Mater. Interfaces* **2010**, *2* (3), 616-620.
97. Cui, J.-Q.; Kretzschmar, I., *Langmuir* **2006**, *22* (20), 8281-8284.
98. Pawar, A. B.; Kretzschmar, I., *Langmuir* **2009**, *25* (16), 9057-9063.
99. Petit, L.; Manaud, J.-P.; Mingotaud, C.; Ravaine, S.; Duguet, E., *Mater. Lett.* **2001**, *51* (6), 478-484.
100. Park, S.; Lim, J.-H.; Chung, S.-W.; Mirkin, C. A., *Science* **2004**, *303* (5656), 348-351.
101. Lim, J. K.; Ciszek, J. W.; Huo, F.; Jang, J.-W.; Hwang, S.; Mirkin, C. A., *Nano Lett.* **2008**, *8* (12), 4441-4445.
102. Zhang, H.; Nunes, J. K.; Gratton, S. E. A.; Herlihy, K. P.; Pohlhaus, P. D.; DeSimone, J. M., *New Journal of Physics* **2009**, *11* (7), 075018.
103. Snyder, C. E.; Yake, A. M.; Feick, J. D.; Velegol, D., *Langmuir* **2005**, *21* (11), 4813-4815.
104. Shepherd, R. F.; Conrad, J. C.; Rhodes, S. K.; Link, D. R.; Marquez, M.; Weitz, D. A.; Lewis, J. A., *Langmuir* **2006**, *22* (21), 8618-8622.
105. Yu, Z.; Wang, C.-F.; Ling, L.; Chen, L.; Chen, S., *Angew. Chem. Int. Ed.* **2012**, *51* (10), 2375-2378.
106. Lee, K. J.; Park, T.-H.; Hwang, S.; Yoon, J.; Lahann, J., *Langmuir* **2013**, *29* (20), 6181-6186.
107. Roh, K.-H.; Martin, D. C.; Lahann, J., *J. Am. Chem. Soc.* **2006**, *128* (21), 6796-6797.
108. Bhaskar, S.; Roh, K.-H.; Jiang, X.; Baker, G. L.; Lahann, J., *Macromol. Rapid Commun.* **2008**, *29* (20), 1655-1660.
109. Roh, K.-H.; Martin, D. C.; Lahann, J., *Nat. Mater.* **2005**, *4* (10), 759-763.
110. Maeda, K.; Onoe, H.; Takinoue, M.; Takeuchi, S., *Adv. Mater.* **2012**, *24* (10), 1340-1346.

111. Gu, H.; Yang, Z.; Gao, J.; Chang, C. K.; Xu, B., *J. Am. Chem. Soc.* **2004**, *127* (1), 34-35.
112. Hong, L.; Jiang, S.; Granick, S., *Langmuir* **2006**, *22* (23), 9495-9499.
113. Jiang, S.; Schultz, M. J.; Chen, Q.; Moore, J. S.; Granick, S., *Langmuir* **2008**, *24* (18), 10073-10077.
114. Liu, B.; Zhang, C.; Liu, J.; Qu, X.; Yang, Z., *Chem. Commun.* **2009**, (26), 3871-3873.
115. Ning, Y.; Wang, C.; Ngai, T.; Tong, Z., *Langmuir* **2013**, *29* (17), 5138-5144.
116. Perro, A.; Meunier, F.; Schmitt, V.; Ravaine, S., *Colloid Surfaces A* **2009**, *332* (1), 57-62.
117. Suzuki, D.; Tsuji, S.; Kawaguchi, H., *J. Am. Chem. Soc.* **2007**, *129* (26), 8088-8089.
118. Perro, A.; Reculosa, S.; Pereira, F.; Delville, M.-H.; Mingotaud, C.; Duguet, E.; Bourgeat-Lami, E.; Ravaine, S., *Chem. Commun.* **2005**, (44), 5542-5543.
119. Wang, Y.; Zhang, C.; Tang, C.; Li, J.; Shen, K.; Liu, J.; Qu, X.; Li, J.; Wang, Q.; Yang, Z., *Macromolecules* **2011**, *44* (10), 3787-3794.
120. Misra, A.; Urban, M. W., *Macromol. Rapid Commun.* **2010**, *31* (2), 119-127.
121. Tang, C.; Zhang, C.; Liu, J.; Qu, X.; Li, J.; Yang, Z., *Macromolecules* **2010**, *43* (11), 5114-5120.
122. Tang, C.; Zhang, C.; Sun, Y.; Liang, F.; Wang, Q.; Li, J.; Qu, X.; Yang, Z., *Macromolecules* **2013**, *46* (1), 188-193.
123. Rahman, M. M.; Montagne, F.; Fessi, H.; Elaissari, A., *Soft Matter* **2011**, *7* (4), 1483-1490.
124. Xu, S.; Ma, W.-F.; You, L.-J.; Li, J.-M.; Guo, J.; Hu, J. J.; Wang, C.-C., *Langmuir* **2012**, *28* (6), 3271-3278.
125. Sacanna, S.; Rossi, L.; Pine, D. J., *J. Am. Chem. Soc.* **2012**, *134* (14), 6112-6115.
126. Ian, W.; GuoJun, L., *Sci. China Life Sci.* **2013**, 1-27.
127. Wolf, A.; Walther, A.; Müller, A. H., *Polymer Preprints* **2010**, *51* (1), 616-617.
128. Ghosh, A.; Sheridan, N. K.; Fischer, P., *Small* **2008**, *4* (11), 1956-1958.
129. Loget, G.; Lee, T. C.; Taylor, R. W.; Mahajan, S.; Nicoletti, O.; Jones, S. T.; Coulston, R. J.; Lapeyre, V.; Garrigue, P.; Midgley, P. A.; Scherman, O. A.; Baumberg, J. J.; Kuhn, A., *Small* **2012**, *8* (17), 2698-2703.
130. Hugonnot, E.; Delville, M.-H.; eacute; egrave; ne; Delville, J.-P., *Appl. Surf. Sci.* **2005**, *248* (1-4), 470-474.
131. Reiche, H.; Dunn, W. W.; Bard, A. J., *J. Phys. Chem.* **1979**, *83* (17), 2248-2251.
132. Duque, J. G.; Eukel, J. A.; Pasquali, M.; Schmidt, H. K., *J. Phys. Chem. C* **2009**, *113* (43), 18863-18869.
133. Duque, J. G.; Pasquali, M.; Schmidt, H. K., *J. Am. Chem. Soc.* **2008**, *130* (46), 15340-15347.
134. Jorgenson, J. W.; Lukacs, K. D., *Anal. Chem.* **1981**, *53* (8), 1298-1302.
135. Starke, H. R.; Yan, J. Y.; Zhang, J. Z.; Muhlegger, K.; Effgen, K.; Dovichi, N. J., *Nucleic Acids Res.* **1994**, *22* (19), 3997-4001.
136. Wallingford, R. A.; Ewing, A. G., *Anal. Chem.* **1987**, *59* (14), 1762-1766.
137. Kašička, V., *Electrophoresis* **2012**, *33* (1), 48-73.
138. Nyholm, L., *Analyst* **2005**, *130* (5), 599-605.

139. WARAKULWIT, C., PhD thesis, Kasetsart University and Bordeaux University, 2007.
140. Warakulwit, C.; Nguyen, T.; Majimel, J.; Delville, M.-H.; Lapeyre, V.; Garrigue, P.; Ravaine, V.; Limtrakul, J.; Kuhn, A., *Nano Lett.* **2008**, *8* (2), 500-504.
141. Loget, G.; Larcade, G.; Lapeyre, V.; Garrigue, P.; Warakulwit, C.; Limtrakul, J.; Delville, M. H.; Ravaine, V.; Kuhn, A., *Electrochim. Acta* **2010**, *55* (27), 8116-8120.
142. Loget, G.; Lapeyre, V.; Garrigue, P.; Warakulwit, C.; Limtrakul, J.; Delville, M.-H.; Kuhn, A., *Chem. Mater.* **2011**, *23* (10), 2595-2599.
143. Fattah, Z.; Garrigue, P.; Goudeau, B.; Lapeyre, V.; Kuhn, A.; Bouffier, L., *Electrophoresis* **2013**, *34* (14), 1985-1990.
144. Fattah, Z.; Loget, G.; Lapeyre, V.; Garrigue, P.; Warakulwit, C.; Limtrakul, J.; Bouffier, L.; Kuhn, A., *Electrochim. Acta* **2011**, *56* (28), 10562-10566.
145. Loget, G.; Kuhn, A., **2011**, French patent FR2969508.
146. Loget, G.; Roche, J.; Kuhn, A., *Adv. Mater.* **2012**, *24* (37), 5111-5116.
147. Al-Saleh, M. H.; Sundararaj, U., *Carbon* **2009**, *47* (1), 2-22.
148. Fattah, Z.; Garrigue, P.; Lapeyre, V.; Kuhn, A.; Bouffier, L., *J. Phys. Chem. C* **2012**, *116* (41), 22021-22027.
149. Bradley, J.-C.; Crawford, J.; McGee, M.; Stephens, S. G., *J. Electrochem. Soc.* **1998**, *145* (3), L45-L47.
150. Loget, G.; Roche, J.; Gianessi, E.; Bouffier, L.; Kuhn, A., *J. Am. Chem. Soc.* **2012**, *134* (49), 20033-20036.
151. Fattah, Z.; Roche, J.; Garrigue, P.; Zigah, D.; Bouffier, L.; Kuhn, A., *ChemPhysChem* **2013**, *14* (10), 2089-2093.
152. Ozeki, T.; Matsumoto, K.; Hikime, S., *Anal. Chem.* **1984**, *56* (14), 2819-2822.
153. Izatt, R. M.; Watt, G. D.; Bartholomew, C. H.; Christensen, J. J., *Inorg. Chem.* **1970**, *9* (9), 2019-2021.
154. Samain, L.; Silversmit, G.; Sanyova, J.; Vekemans, B.; Salomon, H.; Gilbert, B.; Grandjean, F.; Long, G. J.; Hermann, R. P.; Vincze, L.; Strivay, D., *J. Anal. At. Spectrom.* **2011**, *26* (5), 930-941.
155. Voronin, O. G.; Hartmann, A.; Steinbach, C.; Karyakin, A. A.; Khokhlov, A. R.; Kranz, C., *Electrochem. Commun.* **2012**, *23*, 102-105.
156. Karyakin, A. A.; Puganova, E. A.; Budashov, I. A.; Kurochkin, I. N.; Karyakina, E. E.; Levchenko, V. A.; Matveyenko, V. N.; Varfolomeyev, S. D., *Anal. Chem.* **2004**, *76* (2), 474-478.
157. Karyakin, A. A.; Karyakina, E. E., *Russ. Chem. Bull.* **2001**, *50* (10), 1811-1817.
158. Salazar, P.; Martín, M.; O'Neill, R. D.; Roche, R.; González-Mora, J. L., *Colloid Surface B* **2012**, *92*, 180-189.
159. Karyakin, A. A.; Kotel'nikova, E. A.; Lukachova, L. V.; Karyakina, E. E.; Wang, J., *Anal. Chem.* **2002**, *74* (7), 1597-1603.
160. Qin, W.; Zhang, Z.; Zhang, C., *Microchim. Acta* **1998**, *129* (1-2), 97-101.
161. Barni, F.; Lewis, S. W.; Berti, A.; Miskelly, G. M.; Lago, G., *Talanta* **2007**, *72* (3), 896-913.
162. Marquette, C.; Blum, L., *Anal. Bioanal. Chem.* **2006**, *385* (3), 546-554.

163. Zhang, Z.; Zhang, S.; Zhang, X., *Anal. Chim. Acta* **2005**, *541* (1–2), 37-46.
164. Karyakin, A. A., *Electroanalysis* **2001**, *13* (10), 813-819.
165. Itaya, K.; Ataka, T.; Toshima, S., *J. Am. Chem. Soc.* **1982**, *104* (18), 4767-4772.
166. Ibers, J. A.; Davidson, N., *J. Am. Chem. Soc.* **1951**, *73*, 476-478.
167. Ulrich, C.; Andersson, O.; Nyholm, L.; Björefors, F., *Angew. Chem. Int. Ed.* **2008**, *47* (16), 3034-3036.
168. Ishiguro, Y.; Inagi, S.; Fuchigami, T., *Langmuir* **2011**, *27* (11), 7158-7162.
169. Shida, N.; Ishiguro, Y.; Atobe, M.; Fuchigami, T.; Inagi, S., *ACS Macro Letters* **2012**, *1* (6), 656-659.
170. Ramakrishnan, S.; Shannon, C., *Langmuir* **2010**, *26* (7), 4602-4606.
171. Munktel, S.; Tydén, M.; Högström, J.; Nyholm, L.; Björefors, F., *Electrochem. Commun.* **2013**, *34*, 274-277.
172. Duncan, J. F.; Wigley, P. W. R., *J. Chem. Soc.* **1963**, 1120-1125.
173. Sentic, M.; Loget, G.; Manojlovic, D.; Kuhn, A.; Sojic, N., *Angew. Chem. Int. Ed.* **2012**, *51* (45), 11284-11288.
174. Plieth, W., *J. Solid State Electrochem.* **2011**, *15* (7-8), 1417-1423.
175. Budevski, E.; Staikov, G.; Lorenz, W. J., *Electrochim. Acta* **2000**, *45* (15–16), 2559-2574.
176. Walsh, F. C.; Herron, M. E., *J. Phys. D: Appl. Phys.* **1991**, *24* (2), 217.
177. Winand, R., *J. Appl. Electrochem.* **1991**, *21* (5), 377-385.
178. Winand, R., *Electrochim. Acta* **1994**, *39* (8–9), 1091-1105.
179. Tibbetts, G. G.; Lake, M. L.; Strong, K. L.; Rice, B. P., *Compos. Sci. Technol.* **2007**, *67* (7–8), 1709-1718.
180. Grasset, F.; Alphonse, P.; Labrug; egrave; re, C.; Darriet, J.; Rousset, A., *Mater. Res. Bull.* **1999**, *34* (12-13), 2101-2108.
181. Karhu, H.; Kalantar, A.; Väyrynen, I. J.; Salmi, T.; Murzin, D. Y., *Appl. Catal. A Gen.* **2003**, *247* (2), 283-294.
182. Yong, C.; Ke-Zhen, G.; Ren-Yuan, Q., *Acta Chim. Sin.* **1985**, *3* (1), 26-34.
183. Mais, R. H. B.; Owston, P. G.; Wood, A. M., *Acta Cryst. B* **1972**, *28* (2), 393-399.
184. Ohba, S.; Saito, Y., *Acta Crystallogr. C* **1984**, *40* (10), 1639-1641.
185. Nishikawa, K.; Chassaing, E.; Rosso, M., *J. Electrochem. Soc.* **2013**, *160* (4), D183-D187.
186. Wang, H. M.; Chen, S. F.; O'Keefe, T. J.; Degrez, M.; Winand, R., *J. Appl. Electrochem.* **1989**, *19* (2), 174-182.
187. Nikolić, N. D.; Popov, K. I.; Pavlović, L. J.; Pavlović, M. G., *Surf. Coat. Technol.* **2006**, *201* (3–4), 560-566.
188. Kuhn, A.; Argoul, F., *J. Electroanal. Chem.* **1994**, *371* (1–2), 93-100.
189. Nikolić, N. D.; Popov, K. I.; Pavlović, L. J.; Pavlović, M. G., *J. Electroanal. Chem.* **2006**, *588* (1), 88-98.
190. Song, S.; Ortega, C. M.; Liu, Z.; Du, J.; Wu, X.; Cai, Z.; Sun, L., *J. Electroanal. Chem.* **2013**, *690*, 53-59.
191. Liu, S.; Tang, Z., *J. Mater. Chem.* **2010**, *20* (1), 24-35.
192. Mubeen, S.; Zhang, T.; Yoo, B.; Deshusses, M. A.; Myung, N. V., *J. Phys. Chem. C* **2007**, *111* (17), 6321-6327.

193. Roche, J.; Loget, G.; Zigah, D.; Fattah, Z.; Goudeau, B.; Bouffier, L.; Arbault, S.; Kuhn, A., *in preparation* **2013**.

Chapter 3

Bipolar Electrochemistry and Swimmers

3.1. Microswimmers: Principles, Synthesis and Applications

Autonomous microswimmers are of enormous interest not only from an academic point of view, but also for future practical applications ranging from miniaturized motors to nanomedicine. These applications require a precise control of the direction and the speed of the swimmers which can be classified based on the source of the fuel that induces their locomotion.

3.1.1. Biocatalytic Swimmers

Biological motors are powered by spontaneous chemical reactions involving molecules as a source of energy, most commonly adenosine triphosphate (ATP), to generate a mechanical motion and perform various functions. Protein motors represent one of the well known natural systems that can overcome the viscosity forces and Brownian motion.¹⁻² They include dyneins (responsible for ciliary and flagellar motility) and kinesins (cargo carrier within the cell), which move by numerous steps along the microtubule protofilament “tracks” without dissociating themselves and rely on these interactions with the track filament to control their directionality (Figure 3.1a).^{1, 3-5} Another example of protein motors is the myosins which are responsible for muscle contractions.³⁻⁴ Circular motion of asymmetric microswimmers, *e.g.*, bacteria⁶⁻⁷ and spermatozoa can also be cited and was investigated using numerical simulations.⁸

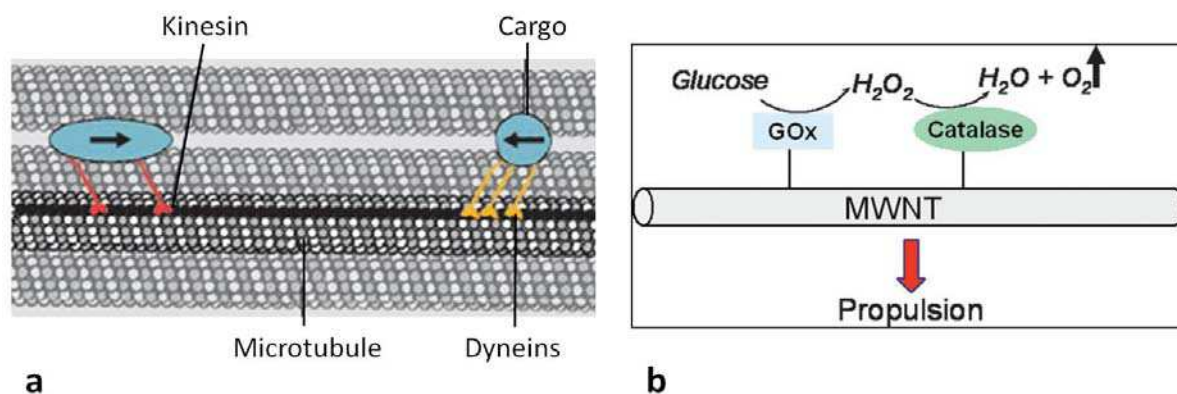


Figure 3.1 a) Scheme of the cargo transport by kinesin and dyneins along a microtubule, adapted from Ref. (4). b) A biohybrid propulsion system of MWCNTs-enzymes, the conversion of glucose by GOx produces H_2O_2 , which is decomposed by catalase to generate dioxygen gas bubbles which propel the MWCNTs, reprinted from Ref. (20).

Inspired by the remarkable performance of biological motors and pumps, researchers have developed synthetic systems in order to compete with natural ones.^{3, 9-12} For instance, the use of gold, polystyrene, and glass beads as cargo which was nonspecifically (electrostatic/hydrophobic interactions) attached to kinesin, showed unidirectional transport of the beads regardless of material and size.¹³ The interaction between microtubules and micro-machined structures was also proposed in order to simulate the movement of biomolecular motors in a microfluidic environment.¹⁴ Bacterial flagella was used as bioactuators, to propel 10 μm polystyrene beads by several *S. marcescens* bacteria attached to them.¹⁵ Integrated living organisms into micromotor devices allowed the use of the new systems for several applications as sensors¹⁶⁻¹⁷ and “molecular shuttles” for cargo transport and release.¹⁸

On the other hand, some biological compounds were exploited to power artificial swimmers. A carbon microfiber that was coated at one end with glucose oxidase (GOx, anode), and at the other with bilirubin oxidase (cathode), was powered by glucose and oxygen. This construction creates a shorted biofuel cell in which the net bioelectrochemomechanical power-generating reaction of glucose and oxygen is directly converted into propulsive mechanical power of the fiber.¹⁹ Covalent attachment of the enzymes GOx and catalase to multiwalled carbon nanotubes (MWCNTs) enables the tandem catalytic conversion of glucose and H_2O_2 formed to power autonomous movement of the nanotubes through the released O_2 gas (Figure 3.1b).²⁰ This system provides exciting opportunities towards both

autonomous nanoscale transport within biological microenvironments and in exploring the behavior of complex multienzyme ensembles.²⁰

3.1.2. Chemically Powered Swimmers

The growing interest in the field of artificial swimmers which are inspired basically by nature is reflected from the increasing number of publications during the past two decades. The motion of most swimmers is generated by the conversion of a locally available chemical fuel into mechanical energy with the help of catalysts that are localized on one part of the swimmer.²¹⁻²² Self-electrophoresis and bubble-based propulsion represent the principle mechanisms that are responsible for motion.²³ In H_2O_2 solutions, the self-electrophoresis mechanism have been proposed to dominate the propulsion of bimetallic rods (Figure 3.2a) in the size range of a few micrometers and below.²⁴ The synthesis of these rods is usually carried out by metal electrodeposition through a microchannel alumina membrane as a sacrificial template which is later dissolved in order to recover the individual rods.²⁵ Different metal segments can be introduced into the composition of the rods with one metal being the cathodic pole for H_2O_2 reduction, and the other one the anodic pole for H_2O_2 oxidation.²⁵⁻²⁶ The direction of current flow, and therefore motion can be predicted from the mixed potential values of each metal in the medium.²³ In the presence of the fuel, the rods act as BPeS as it is called by Mallouk *et al.* where the cathode is the metal segment with the more positive mixed potential and the anode is the other one.²³ A simple example is shown in Figure 3.2c where a Au/Pt nanorod can preferentially catalyze the reduction and oxidation reactions of H_2O_2 at the Au (cathode) and Pt²⁶ (anode) ends of the nanorod, respectively.²⁴ This results in an asymmetric distribution of protons near the ends of the rod, which in turn creates an electric field in the solution near the metal rod.²⁴ The protons then migrate in the electrical double layer at the metal-solution interface from Pt to Au for charge balance, inducing the motion in the opposite direction.²³

Modifications to the nanorod structure and medium composition were demonstrated by Wang group in order to increase the efficiency and propulsion speed of the rod.²⁷ The first improvement was obtained by incorporating carbon nanotubes (CNTs) within the Pt segment of catalytic nanowires, which raised the average rod translation velocity to $43 \mu\text{m s}^{-1}$ in 5% w/v hydrogen peroxide solutions.²⁷ Further acceleration to $94 \mu\text{m s}^{-1}$ was observed upon

adding hydrazine to the peroxide fuel.²⁷ A dramatic acceleration of bisegment nanowire motors up to $150 \mu\text{m s}^{-1}$, corresponding to more than 75 body-lengths/s, was achieved by using a cathodic Ag/Au alloy instead of a gold segment.²⁸

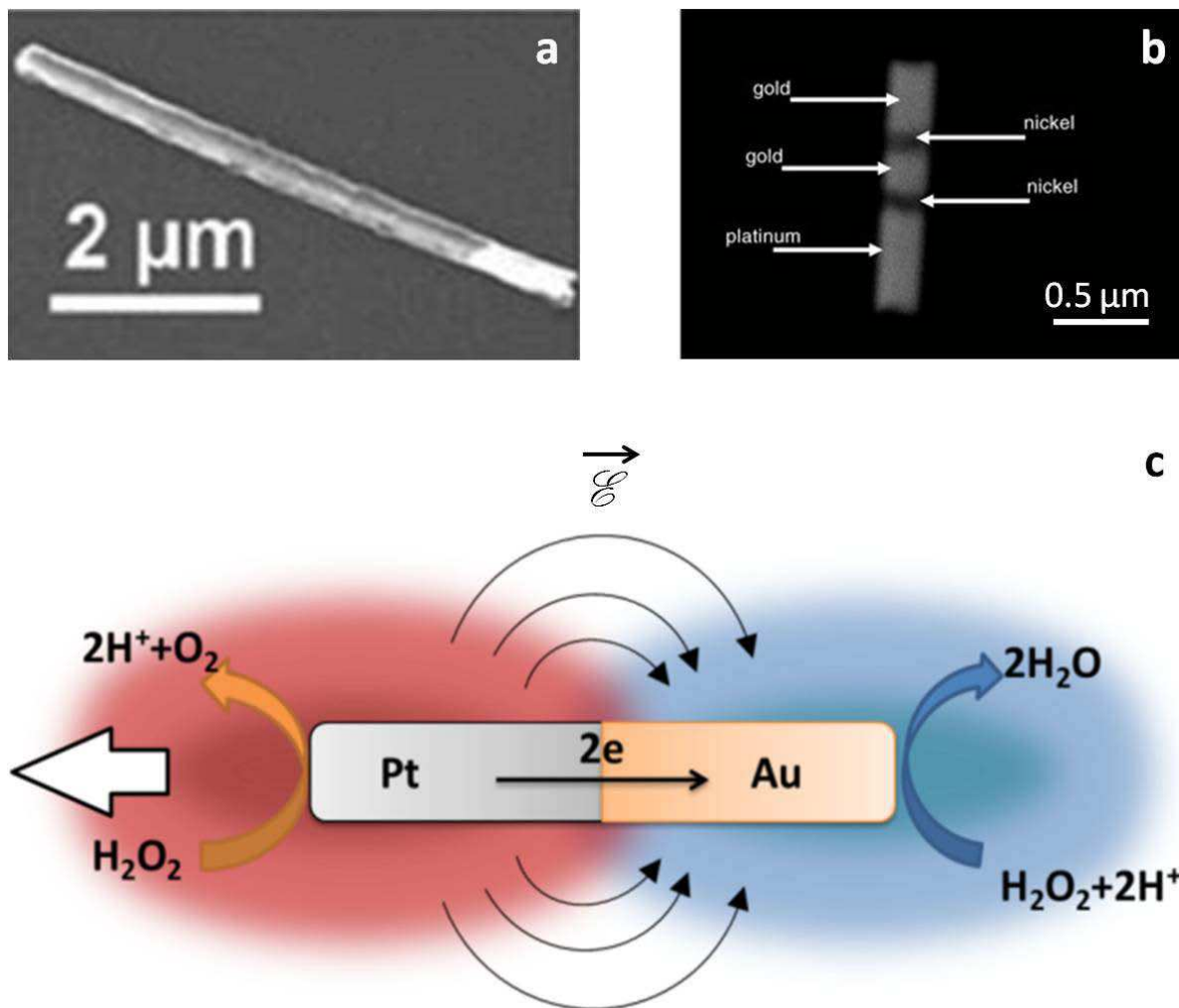


Figure 3.2 a) SEM image of Au/Ni nanorod, adapted from Ref. (27). b) SEM image of a striped metallic nanorod with platinum, nickel, gold, nickel, and gold segments, adapted from Ref. (30). c) Illustration of the self-electrophoretic propulsion mechanism for a Au/Pt catalytic nanomotor. Red and blue represent high and low proton concentrations, respectively. The electric field \mathcal{E} points from the anode (Pt) end to the cathode (Au). The white arrow indicates the direction of motion of the motor, adapted from Ref. (24).

Zacharia *et al.* adopted the porosity of the catalytic segment surface (Ni) to enhance the speed of the nanorods.²⁹ By introducing magnetic parts (Figure 3.2b), it is also possible to control the direction of the nanorods by using an external magnetic field.³⁰ Several applications have been reported for the use of nanorods in, for example, chemical cargo transport,³¹ cargo

manipulation within microfluidic channels,³² and sensing.³³ The circular motion for a Au/Ni rod has been reported.²⁵ In the same context, gold gear-like structures with platinum deposited on the tooth regions that lead to its rotation in H₂O₂ solution.³⁴ The aqueous solutions of Br₂ or I₂ were recently used by Liu *et al.* to power Pt/Cu nanorods based on the self-electrophoresis mechanism.³⁵ Janus nanomotors consisting of Au/Ni bimetallic were also demonstrated by Wheat *et al.* to swim at speeds comparable to rod-shaped motors with the same dimensions and composition.³⁶

The self-propulsion through bubble formation mechanism was demonstrated first by Whitesides's group in connection to the spontaneous movement of centimeter-scale hemicylindrical polydimethylsiloxane (PDMS) "boats" with a platinum strip on their rear at air-water interfaces.³⁷ The plate moved under the impulse of bubbles generated by the platinum-catalyzed decomposition of hydrogen peroxide.³⁷ The mechanism was then employed to power Pt-coated spherical silica microbead motors,³⁸ Au-Pt-Au nanorotors,³⁹ and Pt-Ni-Au nanojets.⁴⁰ The advantage of bubble-propelled micromachines consists in their high power and ability to operate in salt-rich environments, in which the catalytic electrophoretic of nanomotors is limited.⁴¹ Recent efforts focus on the fabrication of tubular microjet engines in the range of micrometer size. These microjets consist of mono- or multilayer microtubes with a catalytic film located at the inner surface of the tubes.^{10, 42-43} Upon the presence of the chemical fuel, gas bubbles grow at the catalytic surface which release later from the wider tubular openings, leading to the object motion towards the opposite opening. Figure 3.3a shows the propulsion of a gold microjet based on immobilized catalase at its inner surface which decomposes the H₂O₂ fuel and generates O₂ bubbles.⁴⁴

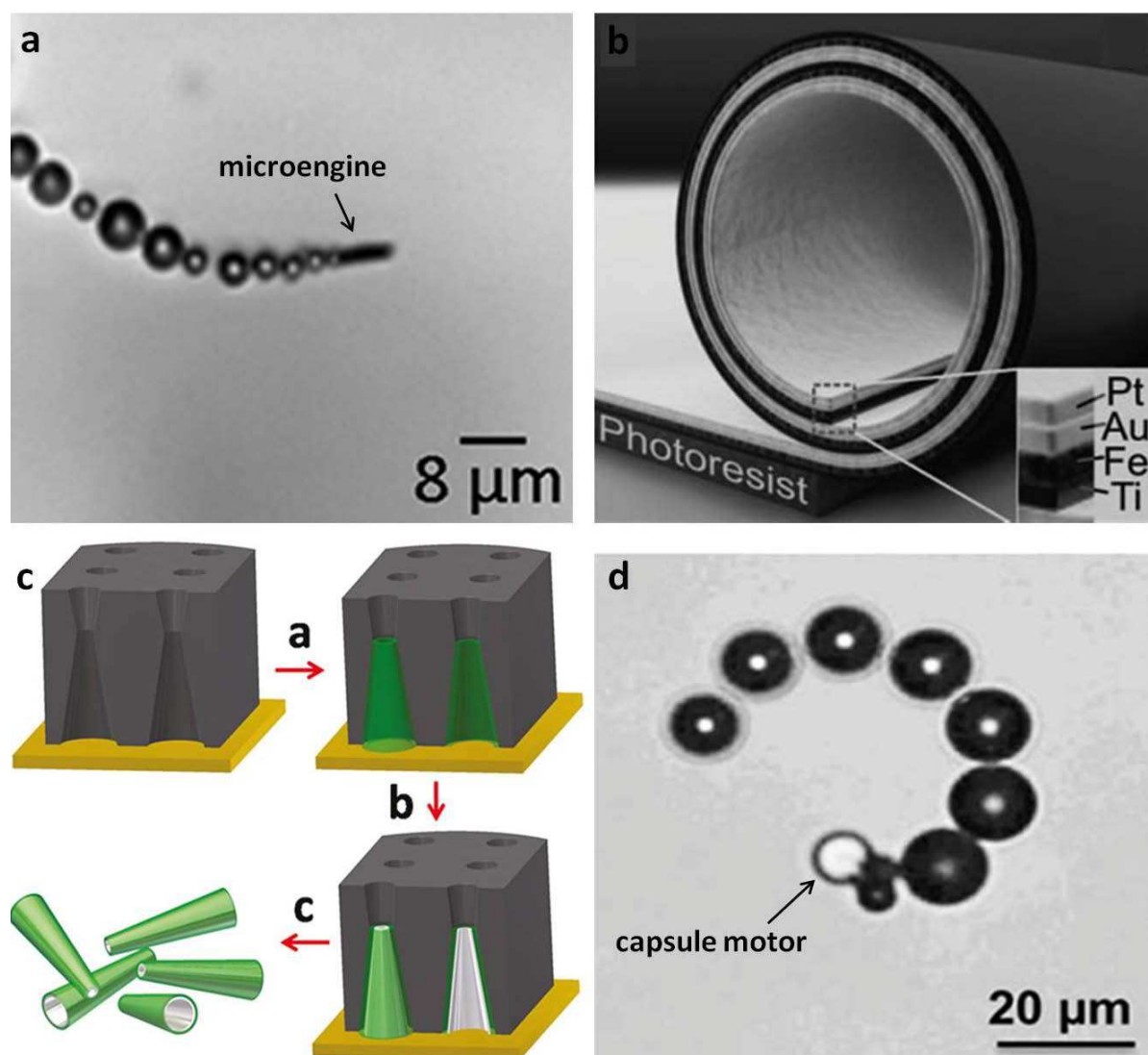


Figure 3.3 a) Optical micrograph of a gold microengine in 2% H_2O_2 solution, adapted from Ref. (44). b) Scheme of the catalytic rolled-up tubular microjet engine consists of (from inner to outer layer) Pt/Au/Fe/Ti multilayers on a photoresist sacrificial layer, reprinted from Ref. (45). c) Preparation of bilayer polyaniline (PANI)/Pt microtubes using polycarbonate membranes: (a) deposition of the PANI microtube, (b) deposition of the Pt microtube, and (c) dissolution of the membrane and release of the bilayer microtubes, reprinted from Ref. (48). d) Optical image displaying circular motion of a capsule motor, the capsule motor is visible in white and the dark bubbles are the oxygen bubble tails, reprinted from Ref. (51).

Rolled-up technique was developed by Schmidt's group for the fabrication of microtubular motors.⁴⁶⁻⁴⁷ Multimetallic thin films can be rolled-up into microtubes by selectively etching a polymer sacrificial pattern fabricated by photolithography and deposition on photoresist substrates, with an inner catalytic active layer (Figure 3.3b).⁴⁶ This method allows the deposition of different materials, and incorporation of a ferromagnetic (Fe/Co) layer into the

tube wall enabling magnetic remote control of the motility direction of the catalytic microjets.¹

Casting materials into molds of microtubes is another method that has been developed by Wang's group to prepare micromotors. The sequential deposition of platinum and gold on an etched silver wire template followed by dicing and dissolution of the template resulted in a conical tube microjet.⁴¹ The shape of the tubes is usually cylindrical or conical depending on the template used. Figure 3.3c depicts the process of polyaniline (PANI)/platinum bilayer microtubular engines fabrication through polycarbonate membrane.⁴⁸ Aniline polymerization on the inner wall of the membranes is followed by platinum layer electrodeposition inside the PANI tube, which also leads to conical bilayer structures after the dissolution of the template.⁴⁸ PANI/Zn microjets were fuelled using acidic solutions such as HCl to oxidize zinc at the inner layer and generate hydrogen bubbles to power the motors.⁴⁹ The prepared motors displayed an ultrafast propulsion up to 100 body length/s.⁴⁹ Hydrogen gas generated from the reaction of Al with water was also employed to propel Ga/Al Janus micromotors.⁵⁰ A Janus polyelectrolyte hollow capsule that has been functionalized asymmetrically with Pt patches generating a circular motion of the capsule in H₂O₂ solution (Figure 3.3d).⁵¹

The microjets were exploited for microdrilling biomaterials,⁴⁷ transport and drug release,⁵² capture and isolation of cancer cells in complex media,⁵³ and protein transport.⁵⁴ Synthetic microengines that were functionalized with a bioreceptor were shown to be extremely useful for the rapid, real-time isolation of *Escherichia coli* (*E. coli*) bacteria from peroxide fuel containing environmental, food and clinical samples.⁵⁵ In the same context, by using enzyme-powered artificial “microfish” in H₂O₂ medium, Orozco *et al.* demonstrated a novel nanotechnological alternative for assessing the water quality and indicating the presence of aquatic pollutants by following the change in the propulsion behavior of the micro-engines.⁴⁴

3.1.3. Externally Stimulated Swimmers

Fuel-free nanomotors are essential for certain applications such as in-vivo biomedical transport and drug-delivery, when chemical fuels, e.g. H₂O₂, are not allowed to be used because of toxicity issues. Therefore, the interest to fabricate swimmers that can be propelled by external stimuli is continuously increasing. A synthetic micro-swimming flagella that is remotely controlled was reported by Dreyfus *et al.*⁵⁶ The spermatozoa like motion of a string

of magnetic particles connected together by short flexible joints was used to transport a red blood cell attached to the string under an alternating magnetic field.⁵⁶ Similar moving structures have also been shown by spontaneous self-assembly of magnetic beads at the water/air interface.⁵⁷ Screw-shaped artificial motors in a centimeter⁵⁸ and micrometer scale,⁵⁹ were propelled using a homogeneous magnetic field. Figure 3.4a, b shows SiO₂ micro helical structures that have been prepared by the vapor deposition technique.⁵⁹ Then, a thin layer of a ferromagnetic material is usually deposited onto the surface and hence one-half of the dispersed helices.⁵⁹ When dissimilar boundary conditions exist at the two ends of an object, tumbling motion can be generated that leads to the propulsion of the object.⁶⁰ This concept has been applied for controlled propulsion of doublets of paramagnetic beads with different or similar size,⁶¹ as well as ferromagnetic nanowires⁶⁰ using a uniform rotating magnetic field. Flexible metal nanowires that have been introduced by Wang's were used as magnetic swimmers.⁶²⁻⁶³ A template electrodeposition approach was employed for the sequential deposition of Au, Ag, and Ni segments into the alumina membrane micropores (Figure 3.4c).⁶² Subsequent dissolution of the template and release of the nanowires are followed by partial dissolution of the central silver segment in hydrogen peroxide to create the flexibility.⁶²⁻⁶³ The magnetic-based nanomotors have been used for directing drug delivery in biological media,⁶³ single cell manipulation,⁶⁴ and also generating complex helical metal microstructures for "surface writing".⁶⁵

The electric field is another attractive option to induce motion. The application of a DC field usually provokes electrophoretic forces which drive the charged particles towards the electrode of opposite charge. This phenomenon was exploited to propel semiconductor diodes ('particles', pumps,⁶⁶ and nanowire⁶⁷) under spatially uniform AC electric fields. The DC voltage induced between the electrodes of each diode as a result of rectification of the AC field leads to an electro-osmotic flow of the adjacent liquid which propel the diodes towards either the cathode or the anode depending on its surface charge (Figure 3.4d).⁶⁶ The specific direction of motion with regards to the diode cathode and anode indicated that the DC field along the diode was responsible for its mobility.⁶⁶ Both translational,⁶⁶⁻⁶⁷ and rotational⁶⁶ motions were reported using this mechanism, which might be useful to perform practical tasks in future. The electric field was also adapted to generate different modes of propulsion through different mechanisms using bipolar electrochemistry⁶⁸ as we discussed in section 1.5.6., as well as to drive Janus particles (section 2.2.2.).⁶⁹

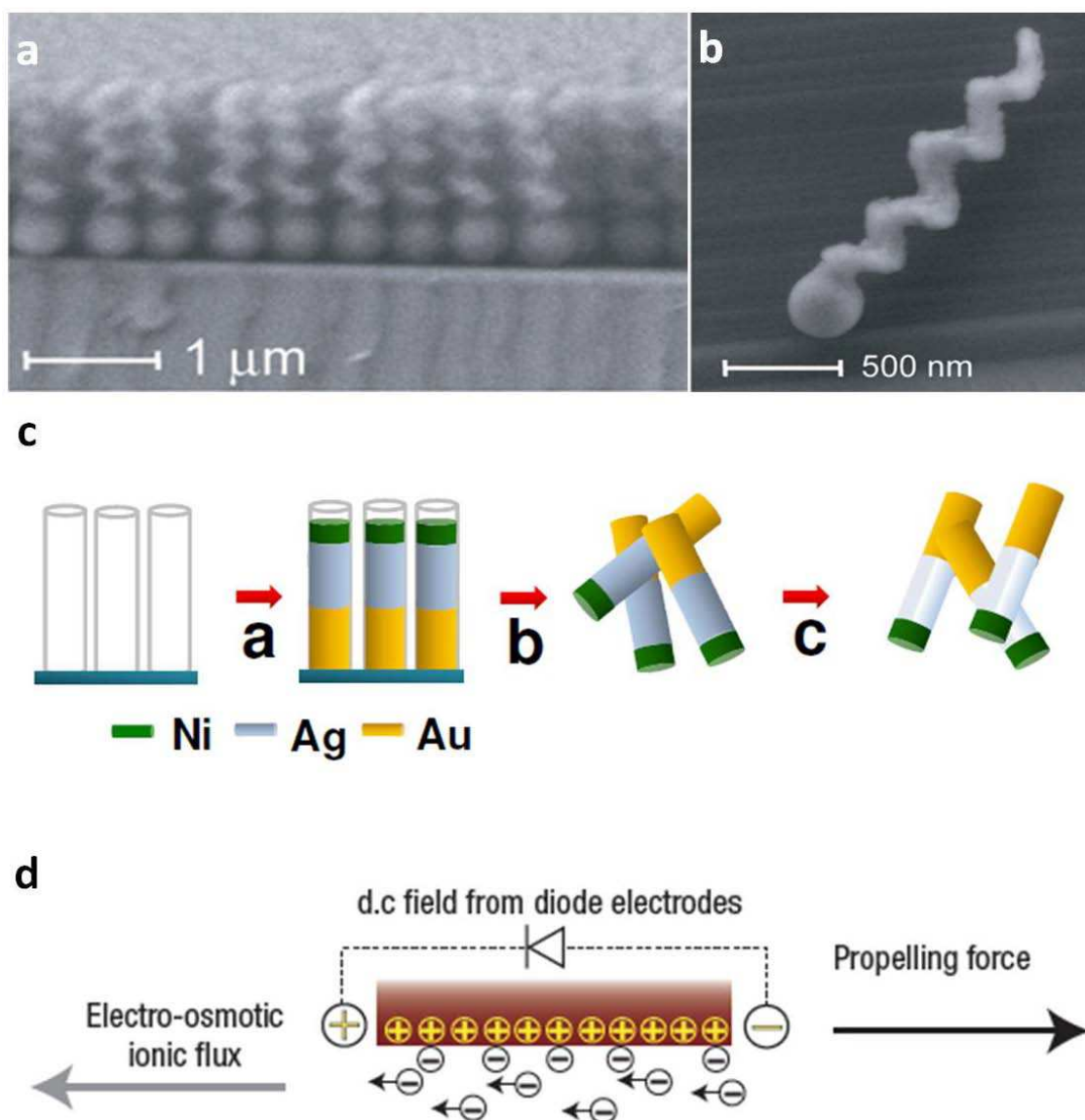


Figure 3.4 a) SEM image of a wafer section with a nanostructured film containing SiO_2 screw structures, b) SEM image of an individual glass screw with nanostructured helicity, adapted from Ref. (59). c) Template based electrochemical preparation of the Au/Ag/Ni nanowire swimmer: a) Sequential template deposition of gold, silver and nickel segments on the sputtered silver layer of the alumina membrane template; b) removal of the sputtered silver layer and dissolution of the alumina template; c) partial dissolution of the silver segment. Reprinted from Ref. (62 SI). d) Schematic illustration of the propulsion mechanism of diodes in an AC. electric field, reprinted from Ref. (66).

The key point for generating the motion in all presented swimmers is the asymmetry that was provided either by the chemical composition, shape, or even charge distribution along the objects. However, long procedures, as well as complex techniques were necessary to produce such asymmetry. In this frame, bipolar electrochemistry represents an attractive method for

generating the required asymmetry for self-propulsion motors as we are going to show in the following.

3.2. Asymmetric Swimmers Designed by Bipolar Electrochemistry

The patchy functional particles that have been prepared by bipolar electrochemistry (see chapter 2) are very attractive as autonomous swimmers, due to the high asymmetry exhibited in the chemical composition along their structure, as we will show in the two following sections.

3.2.1 Magnetically Driven Motion

The modified CF with a Ni cluster at one extremity that was prepared using a bipolar cell (section 2.5.2.) was collected after the experiment and then positioned in a transparent glass square capillary (1 mm in diameter) filled with pure water. The capillary was observed under the objective of an optical microscope with a graphic paper used as a ruler to measure the displacement; and a commercial camera was also used in order to record the motion of the Ni modified fiber. A CMT/Ni motor propulsion was already reported previously; however, it was difficult to follow the object in a 3 dimension focus in order to have a perfect image of the motor.⁷⁰ Therefore, we recorded the movement on a macro-scale motor (1 cm-long CF) in two directions (x and y) under the effect of an external permanent magnetic field. When the magnet was approached close to one face of the capillary, the Ni cluster was attracted to this face pulling the CF towards the magnet (Fig. 3.5a). Moving the magnet along the axial axis of the capillary was also investigated. In this case, it was possible to drive the CF-Ni hybrid parallel to the walls of the capillary (Fig. 3.5c). A series of optical micrographs showing the controlled motion of the CF-Ni hybrid from one capillary face to the other, as well as along the capillary with a velocity of 0.54 mm/s, are demonstrated in Figure 3.5b, d, respectively. One can note that the typical speed can potentially be tuned by playing on the size of the ferromagnetic cluster or the strength of the external magnet.

This experiment proves that the bipolar electrochemistry is a simple process compared to the others techniques discussed previously to fabricate magnetic swimmers. In addition, its versatility can be adapted to combine different materials in the structure of the hybrids. This

approach can be used to separate, for example, conducting and insulating CNTs as the later ones will not act as a BP_e and therefore will not get modified. Then, it will be possible to separate the conductive tubes from the mixture using a magnetic field and recover the CNTs after acidic digestion of the Ni cluster. On the other hand, the modified objects might find interesting application in microfluidic devices as their external manipulation is possible.

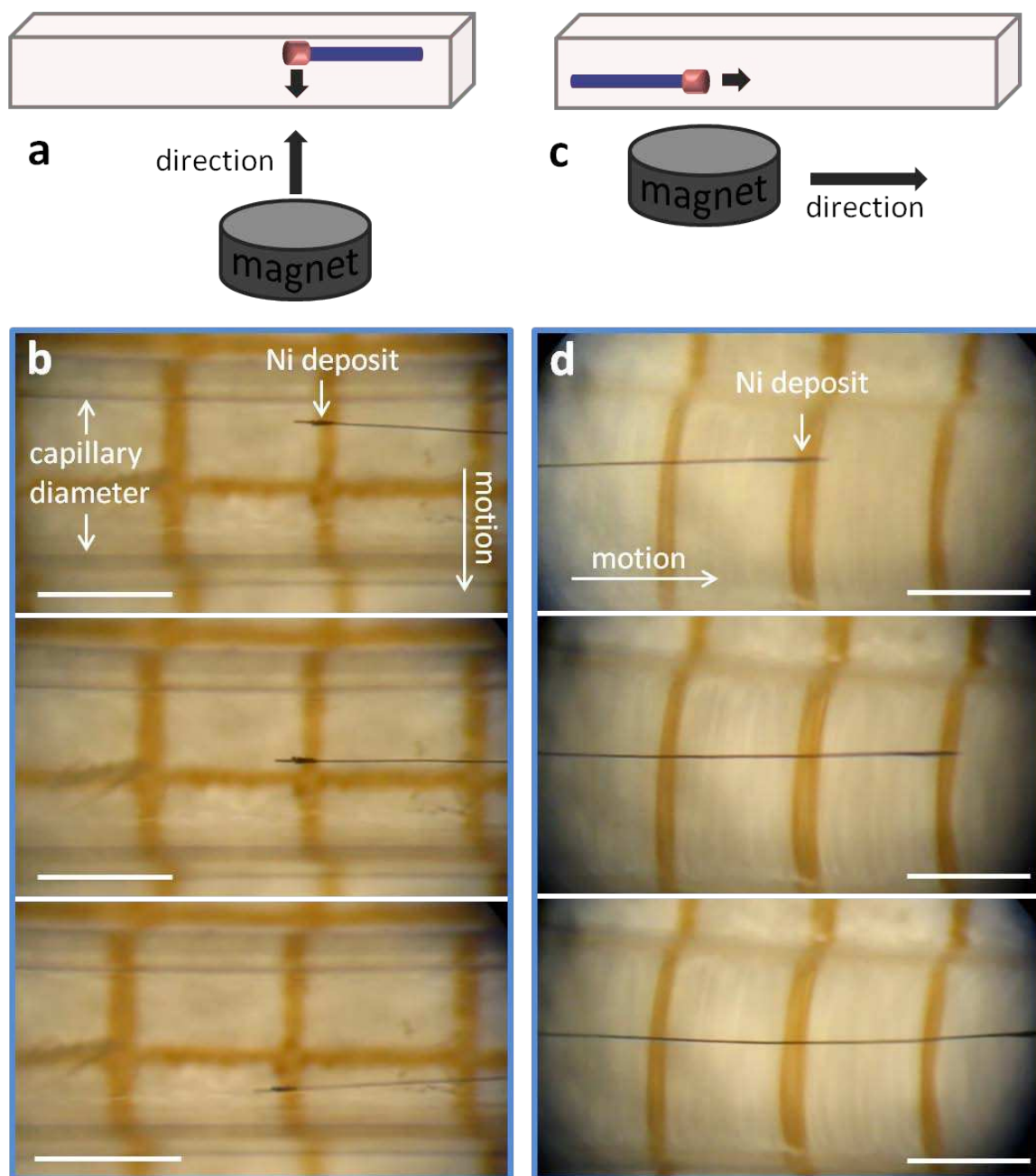
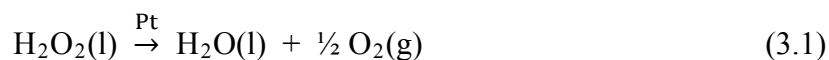


Figure 3.5 a, c) Schemes showing the manipulation of the CF/Ni hybrid in y (a), and x (c) direction with a permanent magnet. b, d) Series of optical micrographs showing the movement of a Ni modified CF suspended in water inside the capillary upon application of an external magnet against one face (b), and alongside the long axis (d) of the capillary. Scale bar: 1 mm.

3.2.2. Chemically Induced Motion

Platinum metal is a well-known catalyst which has been extensively used for the decomposition of hydrogen peroxide into water and oxygen according to the following equation:



This property explains the frequent integration of a platinum moiety for building different swimmers in order to induce the motion through the bubble propulsion mechanism as we discussed in section 3.1.2. This mechanism was employed here to study the movement of CMTs/Pt hybrids that were modified asymmetrically using the bipolar electrochemistry (section 2.4.2. and 2.5.2.). We first tested the ability of the newly prepared material to decompose hydrogen peroxide. Dioxygen bubble generation was immediately observed as soon as the Pt/CMT hybrid was in contact with the reactant solution. The rate of bubble production can be tuned by adjusting the hydrogen peroxide content and concentrated solutions like 30% H_2O_2 generated a very high activity. Depending on the exact location of the catalyst cluster, the propulsion of these objects was either following a linear or a circular trajectory.

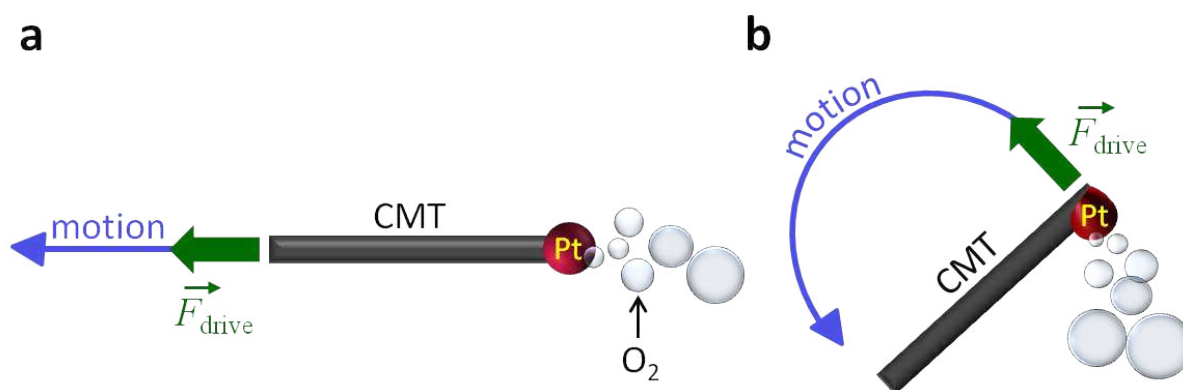


Figure 3.6 Schematic illustrations of the propulsion mechanism of platinum-modified CMTs with a centered (a), and non-centered (b) Pt deposit.

Figure 3.6a and b gives a schematic representation of the mechanisms responsible for the motions of CMT modified with a centered Pt and non-centered Pt deposit, respectively. A Pt particle perfectly centered at the middle of a CMT extremity results in an axial production of

O₂ bubbles which generates a local mechanical perturbation and induces a driving force \vec{F} parallel to the axis of the tube.³⁸ This ideal situation leads to a subsequent movement of the object in the direction of its unmodified end and therefore generates a linear motion. By contrast, a non-centered deposit will generate bubbles anisotropically with respect to the tube axis. As a result, the mode of motion does change from a translation to a rotation because \vec{F} is now oriented diagonally with respect to the tube. Then, the motion takes place in the opposite direction of the oxygen bubbles generated on the platinum catalyst.³⁹

For observing the movement of the modified CMTs, the suspension was drop coated on a glass slide and the CMTs/Pt objects were observed with the transmission optical microscope. 5 μ L of a solution of 30 wt.% hydrogen peroxide in water was then added onto the tubes. The propulsion of a CMT is experimentally very challenging to image for several reasons. (i) The generation of a large quantity of bubbles is necessary to move the microhybrid, but these bubbles disturb the optical resolution by changing instantly the nature of the local environment surrounding the CMT. (ii) The propulsion usually takes place in a three dimensional configuration, (xyz), and the optical microscope is only able to focus on a single plane (xy). (iii) The rate of bubble formation and the acceleration of the CMT do not take place at the same timescale and it is therefore very frequent that the CMT moves out of the focal plane of the microscope. However, we could record several videos with a CCD camera for visualizing the swimmers according to the described procedure. Figure 3.7 shows a representative optical micrograph of a CMT in motion. Four dioxygen bubbles can be distinguished after their successive formation from right to left, resulting in the efficient propulsion of the carbon tube towards the bottom-left corner of the picture.⁷¹ As mentioned previously, this linear mode of motion is directly controlled by the centered topology of the platinum deposit on the CMT.

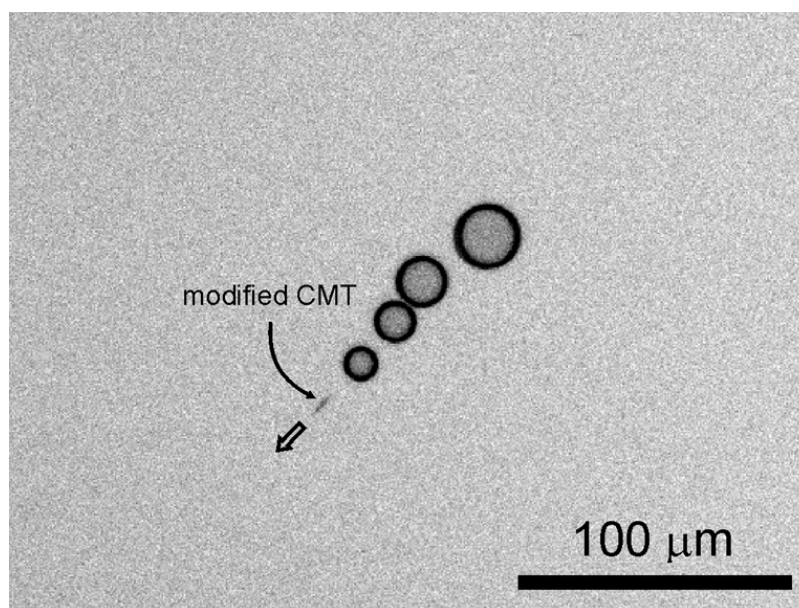


Figure 3.7 Linear motion of the microswimmer leaving a train of bubbles behind observed under the optical microscope, reprinted from Ref. (71).

However, when the Pt deposit was non-centered, rotational motion of the CMT was observed. Figure 3.8 shows a selection of six high magnification optical images of a CMT performing one anticlockwise turn. These data were extracted from a large set of images in which the microhybrid is rotating several times around the unfunctionalized extremity of the microtube. A time interval of 2.01 ± 0.14 s/turn was estimated from 10 full turns which allows calculating a speed of 29.9 ± 2.1 rpm (or a frequency of ~ 0.50 Hz). The sequence of images in Figure 3.8 clearly ensures that the driving force of the rotation is the non-symmetric O_2 formation, as the CMT is rotating in the opposite direction with respect to the bubble evolution.

The presented motors demonstrate a straightforward modification approach using bipolar electrochemistry with respect to other methods where complex procedures are required in order to generate such swimmers, especially for rotational motion.³⁹ The prepared swimmers were able to undergo dominantly either linear or rotational propulsion based on the platinum topology on the CMT. The speed of these chemical motors can easily be enhanced by introducing surfactants during the bipolar electrodeposition experiment, which leads to a porous metal deposit,⁷²⁻⁷³ hence, a higher surface area for O_2 production. Further functionalization of such pores with other molecules⁷² may lead to a new generation of, for

example, catalytic swimmer sensors which can find interesting applications in analytical chemistry.

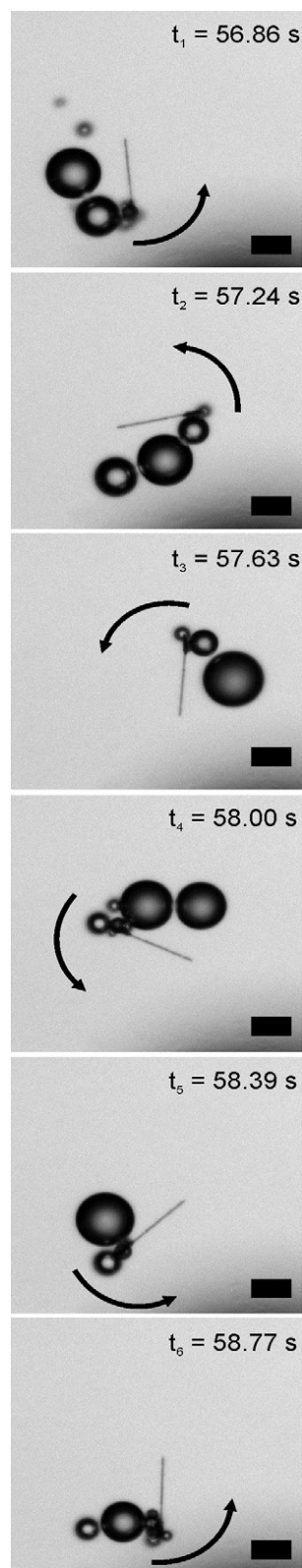
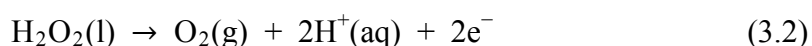


Figure 3.8 Series of optical micrographs of a counter clockwise rotating microswimmer. Scale bar 10 μm , reprinted from Ref. (71).

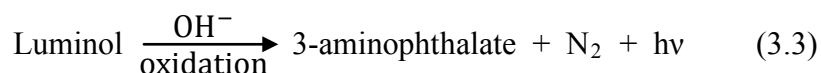
3.3. Bubble Induced Motion of the Lighting Up Bipolar Swimmers Under External Electric Field

The intrinsic asymmetry of the swimmers described in the two previous sections arises from their preparation by bipolar electrodeposition of either a Ni or a Pt moiety (i.e. structural asymmetry). By contrast, The asymmetry which is the key for generating controlled motion of the objects can equally be provided directly by the bipolar electrochemistry itself which induces a (electro)chemical break of symmetry at the opposite ends of the BPe (see section 1.5.6.) leading to propulsion of the object driven by water splitting. Following the trajectory of the swimmer in real time requires to functionalize the swimmers with a fluorophore⁵⁹ and to use efficient microscopes in many cases.⁶⁴ Therefore, working with a swimmer that is self-emitting light would be conceptually very interesting for this purpose. In that context, we adapted bipolar electrochemistry not only to drive the object propulsion but also to trigger a simultaneous light emission by mean of electrogenerated chemiluminescence (ECL) coupled to the electrochemical fuelling reaction on the same object. ECL consists in the emission of light resulting from an initial electrochemical reaction. A typical model ECL system is based on the oxidation of luminol (5-Amino-2,3-dihydro-1,4-phthalazine-dione or 3-aminophthalhydrazide) in alkaline solution in the presence of hydrogen peroxide in order to promote blue light emission.⁷⁴ Luminol and its derivatives⁷⁵ are widely used in biochemical and clinical analysis such as enzymatic assays and immunoassays.⁷⁶⁻⁷⁷ For example, luminol ECL coupled to oxidase-catalysed reactions generating hydrogen peroxide constitutes a sensitive and versatile analytical strategy. ECL has not only been exploited in combination with bipolar electrochemistry for analytical purposes,⁷⁸⁻⁷⁹ but also to design the first light emitting electrochemical swimmer involving $[\text{Ru}(\text{bpy})_3]^{2+}$ and tripropylamine (TPrA).⁸⁰

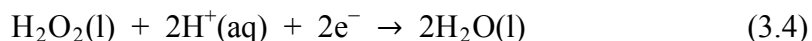
The present work will show that this methodology can be generalized with another ECL system based on luminol, allowing tuning the wavelength of light emission. Moreover, all previously described bipolar-driven motions were reported in neutral or acidic aqueous solutions with cathodic bubbles generation (H_2 evolution).⁸⁰⁻⁸² In contrast, this first example in an alkaline solution proceeds through an alternative mechanism based on H_2O_2 oxidation and allows the light emission at the same BPe pole (anode) than the bubble production as following:



3.3. Bubble Induced Motion of the Lighting Up Bipolar Swimmers



These oxidation reactions are compensated with the reduction of hydrogen peroxide at the cathodic pole:



The produced O_2 bubbles at the anodic pole are responsible for generating the motion of the object which performed in this case in a vertical motion as depicted in Figure 3.9.

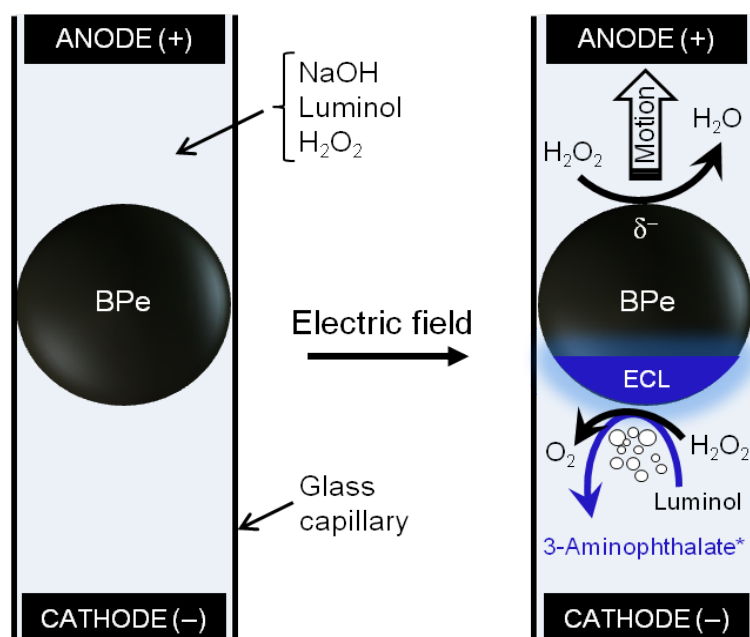


Figure 3.9 Scheme showing the electrochemical reactions occurring and the blue electrogenerated chemiluminescence (ECL) during the vertical motion of a spherical bipolar electrode with luminol as a luminophore, adapted from Ref. (83).

Simultaneous generation of gas bubbles and of ECL could be theoretically achieved when the interfacial difference of potential alongside a BPe becomes sufficiently high. A preliminary experimental feasibility was therefore performed by recording cyclic voltammetry (CV) on a glassy carbon electrode, and it has been combined with a simultaneous monitoring of the ECL intensity by using a photomultiplier tube. Figure 3.10a shows typical CVs recorded at 0.1 V/s in 0.1 M NaOH with H_2O_2 (1 %). Hydrogen peroxide is essentially electro-oxidized to oxygen at $\sim +0.5$ V and reduced to hydroxide anions at ~ -1.25 V vs. Ag/AgCl. Both processes are irreversible and involve two electrons. By comparison, the value of the current corresponding to the electroactivity of a pure NaOH solution is much lower. CV was

recorded again for the mixture after the addition of 0.01 M luminol solution, the later exhibited an irreversible oxidation peak at + 0.3 V vs. Ag/AgCl (Figure 3.10b).⁸³ The electrochemical measurement has also been combined with a simultaneous monitoring of the ECL intensity (see appendix 2 for experimental details). As expected, the oxidation step is responsible for the ECL process starting right at the foot of the anodic wave and with a maximum intensity observed at + 0.5 V vs Ag/AgCl. Even if the presence of H_2O_2 is not compulsory to achieve luminol luminescence, H_2O_2 is promoting the molecular ECL mechanism which involves the formation of intermediate endoperoxide species.⁸⁴

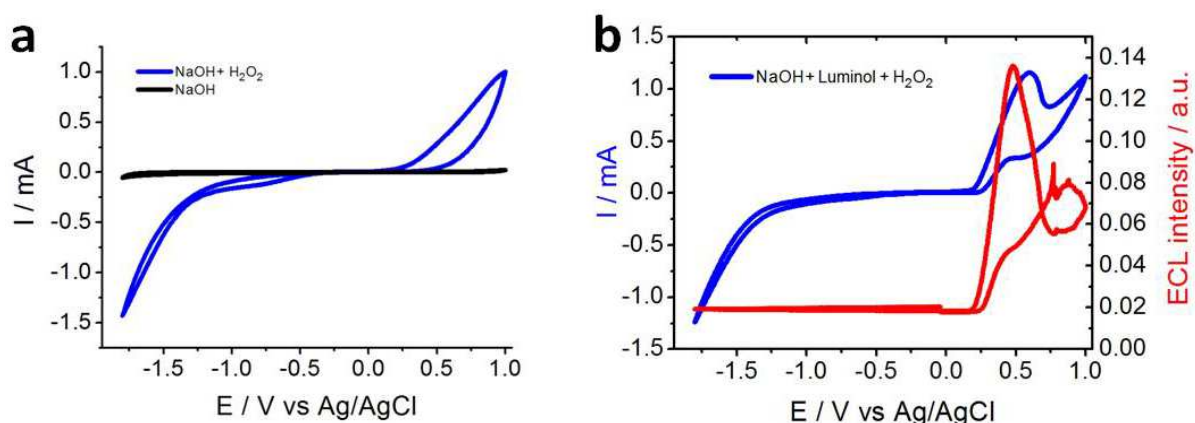


Figure 3.10 Cyclic voltammograms recorded in 0.1 M sodium hydroxide with and without 1% H_2O_2 (a) and with 0.01 M luminol combined with ECL detection (b). Scan rate 0.1 V/s.

Luminol ECL has never been investigated under bipolar electrochemistry conditions. This is why a proof-of-feasibility experiment was first performed with a graphite rod ($l=1$ cm; $\varnothing=2.0$ mm). This BPe was positioned in a PDMS bipolar electrochemical cell (see appendix 3 for details about fabrication process) depicted in Figure 3.11a and immersed in a 0.1 M NaOH solution containing luminol (0.01 M) and 1% H_2O_2 . Applying an electric field of about 0.15 kV/m was sufficient to generate an intense blue light emission typical for luminol ECL ($\lambda=425$ nm) and the light was recorded in the dark (Figure 3.12b). In fact, ECL emission was so intense that it was also easily seen under natural light with the naked eye or recorded with a commercial camera (Figure 3.12 a). Increasing the value of the electric field could also allow extending the region where ECL is promoted because a longer part of the BPe is submitted to a sufficient polarization. This phenomenon is illustrated in Figure 3.12c–f where the value of the applied electric field is 0, 0.13, 0.20 and 0.27 kV/m, respectively. This

successful preliminary experiment has clearly demonstrated that ECL of luminol can be achieved in a bipolar setup.

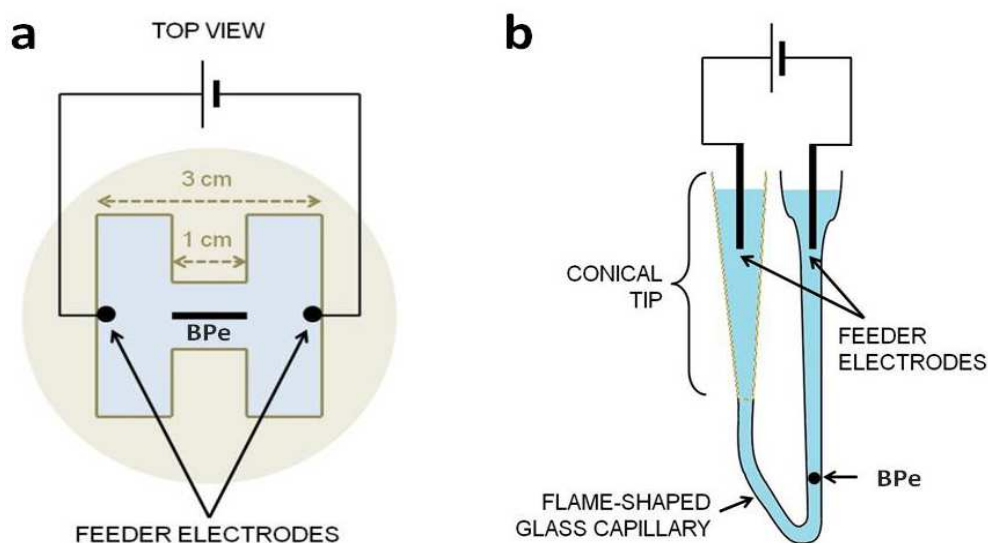


Figure 3.11 Schematic illustrations of the designed bipolar electrochemical cell. a) PDMS cell used for the graphite rod. b) U-shaped cell assembled from a Pasteur pipette glass capillary connected with a conical tip.

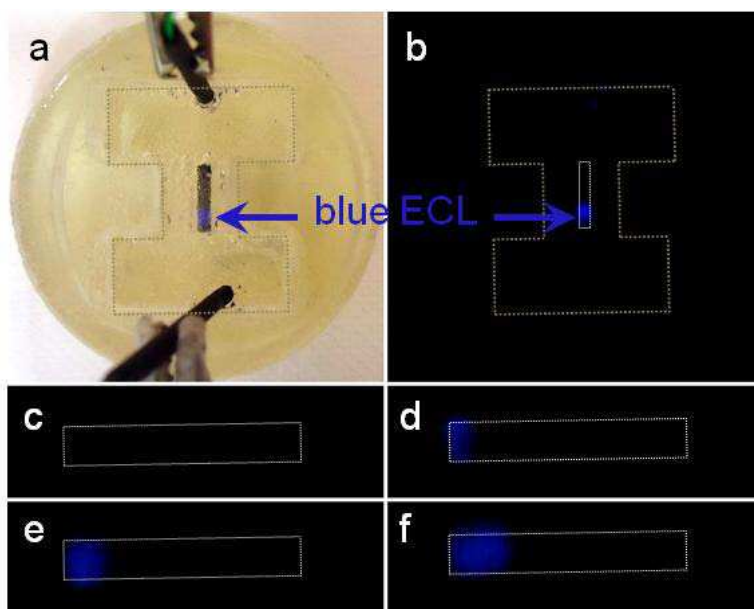


Figure 3.12 Optical images showing luminol ECL promoted by bipolar electrochemistry on a 1 cm-long graphite bar. Images were recorded (a) under natural light or (b-f) in the dark with a commercial camera. The applied potential value is 0.3 kV/m (a,b), and varies from 0 to 0.13, 0.20 and 0.27 kV/m (c, d, e and f respectively). The location of the BPe is indicated with a white line. Reprinted from Ref. (83).

The next step corresponded to scaling down the size of the BPe to prepare a light-emitting swimmer. For that, a graphite bead of 1 mm in diameter was selected in line with previous results.⁸² The electrochemical cell was home-made by combining a glass capillary and a conical tip in order to separate both feeder electrodes by ~ 10 cm inside a U-shaped cell (Figure 3.11b). The cell was filled with the solution mixture and the bead was inserted into the arm of the cell. For the vertical motion experiments, a typical voltage of 250–300 V over a distance of 10 cm was applied (electric field of 2.5 – 3.0 kV/m). First attempts to drive the motion based on the production of gas bubbles underneath the bead were executed under visible light. Oxygen bubbles clearly form at the anodic pole of the BPe facing the feeder cathode (Fig. 3.9 and Fig. 3.13a). The gas production and the light emission are produced simultaneously at the same pole of the BPe resulting in a “rear” blue light emitting bead. The generation of oxygen bubbles arises from H_2O_2 oxidation but, in addition the decomposition of luminol produces also N_2 bubbles (eq. 3.3)⁸⁵ which can contribute to the propulsion of the BPe. Therefore it is noteworthy that the ECL reaction may potentially generate itself the movement of the bead.

Figure 3.13b shows the carbon bead located at its initial position in the capillary alongside a graduated ruler. After switching off the light, the vertical motion of the bead could be easily followed due to luminol ECL. Figure 3.13c–e illustrates the vertical position of the bead right after applying the electric field (c), and after 12 and 40 s (d and e respectively). The motion of the bead has been studied and reveals an inhomogeneous speed when following the variation of the vertical position as a function of time. An average speed of about 0.1 mm/s has been observed for the present work concerning blue light emitting swimmers (Fig. 3.13f). As a general trend, one can notice that the BPe progressively slows down during the course of vertical motion. This is due to the slightly conical shape of the bipolar cell (Fig. 3.11b), which favors the escape of bubbles from underneath the carbon bead after reaching a certain height in the capillary.

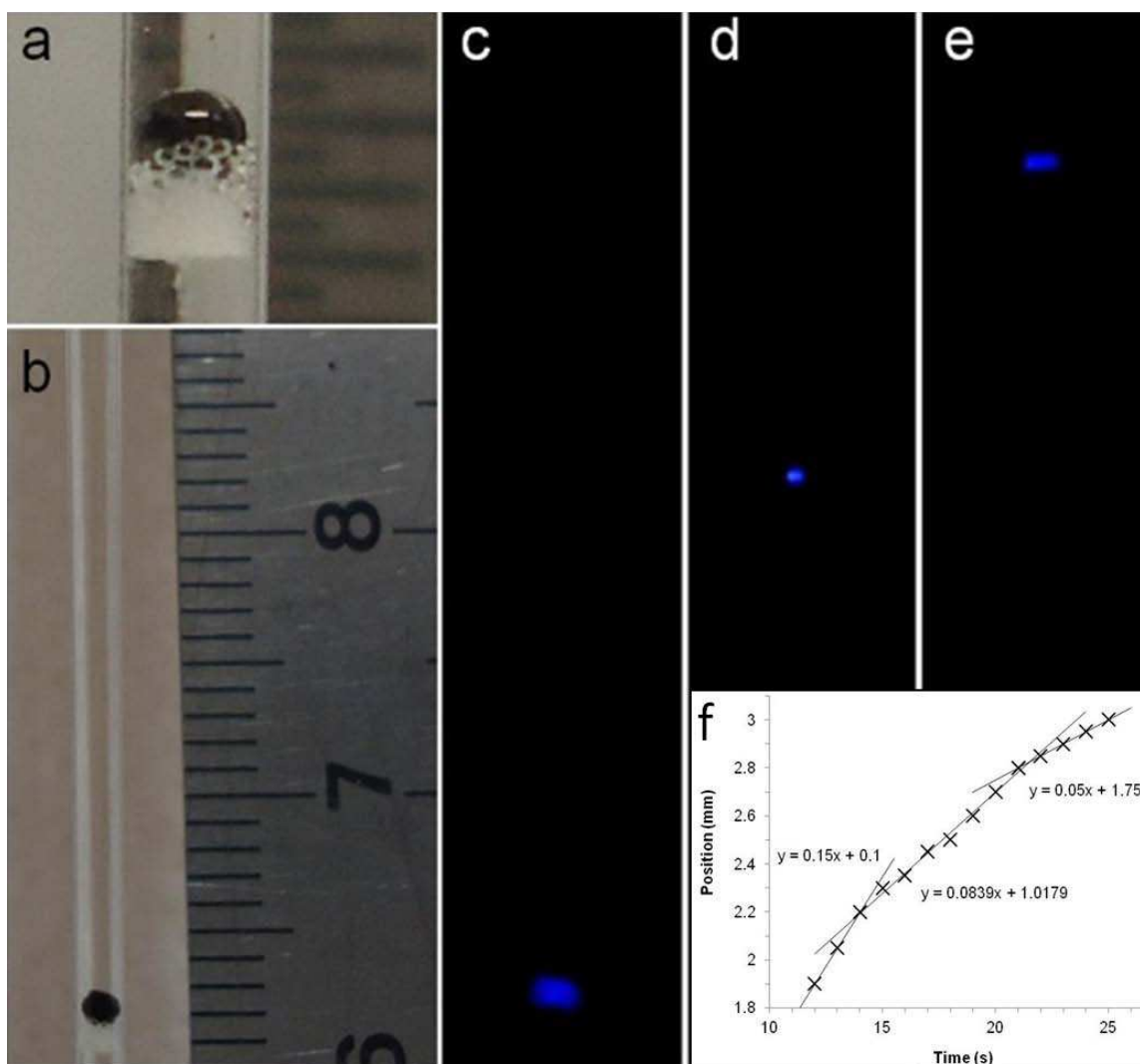


Figure 3.13 Snapshots showing the vertical motion of a blue light emitting carbon bead (1 mm diameter). a) Zoom on the gas evolution at the bottom part of the bead. b) Position of the bead in the capillary. c-e) Recording the ECL emitting bead in the dark at 0, 12 and 40 seconds after applying an electric field of 2.5 kV/m. f) Plot showing the variation of the vertical position of the bead as a function of time (followed by luminol ECL). Reprinted from Ref. (83).

To conclude, redox-driven motion within a capillary under bipolar electrochemistry conditions with concomitant generation of ECL has been generalized by using luminol-based luminescence. The motion and light emission has to be compared to the first described system involving $[\text{Ru}(\text{bpy})_3]^{2+}$ and TPrA. The later was based on cathodic hydrogen production and red light production at the “front” of the BPe. In contrast, the reported new system takes advantage of O_2 evolution and blue light electrogeneration at the “rear” end of the carbon bead. This finding opens the door to the possible design in the near future of

functional systems combining multi-wavelength light emission. Luminol is not only capable of promoting ECL, but also chemiluminescence which involves catalytically active iron cations.⁸⁶ This strategy could potentially lead to new applications in the field of chemical or biochemical sensing with a possible example being the modulation of the speed of light emitting swimmers by substrate-driven enzymatic generation of H₂O₂. The significant difference between all the previous motors that have been powered in the electric field and the present work is that, they were based on the cathodic pole for bubble production to propel the objects.⁸⁰⁻⁸² In our case, as the anodic pole is responsible for powering the motor and the cathodic pole is free, we may apply this advantage in microfluidic devices, for example, for *in situ* metallic depollution by electrodeposition of toxic metals at the cathodic pole of the motor during its motion.

References

1. Wang, J.; Manesh, K. M., *Small* **2010**, *6* (3), 338-345.
2. Ozin, G. A.; Manners, I.; Fournier-Bidoz, S.; Arsenault, A., *Adv. Mater.* **2005**, *17* (24), 3011-3018.
3. Patra, D.; Sengupta, S.; Duan, W.; Zhang, H.; Pavlick, R.; Sen, A., *Nanoscale* **2013**, *5* (4), 1273-1283.
4. Goel, A.; Vogel, V., *Nat Nano* **2008**, *3* (8), 465-475.
5. Vale, R. D., *Cell* **2003**, *112* (4), 467-480.
6. Phuyal, K.; Kim, M. J., *Phys. Fluids* **2013**, *25* (1), 011901-9.
7. DiLuzio, W. R.; Turner, L.; Mayer, M.; Garstecki, P.; Weibel, D. B.; Berg, H. C.; Whitesides, G. M., *Nature* **2005**, *435* (7046), 1271-1274.
8. Mijalkov, M.; Volpe, G., *Soft Matter* **2013**, *9* (28), 6376-6381.
9. Wang, J., *ACS Nano* **2009**, *3* (1), 4-9.
10. Wang, J.; Gao, W., *ACS Nano* **2012**, *6* (7), 5745-5751.
11. Hess, H.; Vogel, V., *Rev. Mol. Biotechnol.* **2001**, *82* (1), 67-85.
12. Limberis, L.; Magda, J. J.; Stewart, R. J., *Nano Lett.* **2001**, *1* (5), 277-280.
13. Konrad, J. B.; Roland, S.; Peter, M.; Eberhard, U., *Nanotechnology* **2001**, *12* (3), 238.
14. Ma, T.-C.; Lin, C. H.; Lin, C.-T.; Chen, C.-S., *AIP Conf. Proc.* **2010**, *1233* (1), 684-689.
15. Behkam, B.; Sitti, M., *Appl. Phys. Lett.* **2007**, *90* (2), 023902-3.
16. van den Heuvel, M. G. L.; Dekker, C., *Science* **2007**, *317* (5836), 333-336.
17. Hess, H.; Bachand, G. D.; Vogel, V., *Chem. Eur. J.* **2004**, *10* (9), 2110-2116.
18. Schmidt, C.; Vogel, V., *Lab Chip* **2010**, *10* (17), 2195-2198.
19. Mano, N.; Heller, A., *J. Am. Chem. Soc.* **2005**, *127* (33), 11574-11575.
20. Pantarotto, D.; Browne, W. R.; Feringa, B. L., *Chem. Commun.* **2008**, 1533-1535.
21. Paxton, W. F.; Sen, A.; Mallouk, T. E., *Chem. Eur. J.* **2005**, *11* (22), 6462-6470.
22. Ebbens, S. J.; Howse, J. R., *Soft Matter* **2010**, *6* (4), 726-738.
23. Wang, Y.; Hernandez, R. M.; Bartlett, D. J.; Bingham, J. M.; Kline, T. R.; Sen, A.; Mallouk, T. E., *Langmuir* **2006**, *22* (25), 10451-10456.
24. Wang, W.; Chiang, T.-Y.; Velegol, D.; Mallouk, T. E., *J. Am. Chem. Soc.* **2013**, *135* (28), 10557-10565.
25. Fournier-Bidoz, S.; Arsenault, A. C.; Manners, I.; Ozin, G. A., *Chem. Commun.* **2005**, 441-443.
26. Paxton, W. F.; Kistler, K. C.; Olmeda, C. C.; Sen, A.; St. Angelo, S. K.; Cao, Y.; Mallouk, T. E.; Lammert, P. E.; Crespi, V. H., *J. Am. Chem. Soc.* **2004**, *126* (41), 13424-13431.
27. Laocharoensuk, R.; Burdick, J.; Wang, J., *ACS Nano* **2008**, *2* (5), 1069-1075.
28. Demirok, U. K.; Laocharoensuk, R.; Manesh, K. M.; Wang, J., *Angew. Chem. Int. Ed.* **2008**, *47* (48), 9349-9351.
29. Zacharia, N. S.; Sadeq, Z. S.; Ozin, G. A., *Chem. Commun.* **2009**, 5856-5858.
30. Kline, T. R.; Paxton, W. F.; Mallouk, T. E.; Sen, A., *Angew. Chem.* **2005**, *117* (5), 754-756.

31. Sundararajan, S.; Lammert, P. E.; Zudans, A. W.; Crespi, V. H.; Sen, A., *Nano Lett.* **2008**, *8* (5), 1271-1276.
32. Burdick, J.; Laocharoensuk, R.; Wheat, P. M.; Posner, J. D.; Wang, J., *J. Am. Chem. Soc.* **2008**, *130* (26), 8164-8165.
33. Kagan, D.; Calvo-Marzal, P.; Balasubramanian, S.; Sattayasamitsathit, S.; Manesh, K. M.; Flechsig, G.-U.; Wang, J., *J. Am. Chem. Soc.* **2009**, *131* (34), 12082-12083.
34. Catchmark, J. M.; Subramanian, S.; Sen, A., *Small* **2005**, *1* (2), 202-206.
35. Liu, R.; Sen, A., *J. Am. Chem. Soc.* **2011**, *133* (50), 20064-20067.
36. Wheat, P. M.; Marine, N. A.; Moran, J. L.; Posner, J. D., *Langmuir* **2010**, *26* (16), 13052-13055.
37. Ismagilov, R. F.; Schwartz, A.; Bowden, N.; Whitesides, G. M., *Angew. Chem.* **2002**, *114* (4), 674-676.
38. Gibbs, J. G.; Zhao, Y. P., *Appl. Phys. Lett.* **2009**, *94* (16), 163104-3.
39. Qin, L.; Banholzer, M. J.; Xu, X.; Huang, L.; Mirkin, C. A., *J. Am. Chem. Soc.* **2007**, *129* (48), 14870-14871.
40. Zhao, G.; Pumera, M., *Langmuir* **2013**, *29* (24), 7411-7415.
41. Manesh, K. M.; Cardona, M.; Yuan, R.; Clark, M.; Kagan, D.; Balasubramanian, S.; Wang, J., *ACS Nano* **2010**, *4* (4), 1799-1804.
42. Wan, G.; Solovev, A. A.; Huang, G. S.; Maitz, M. F.; Huang, N.; Mei, Y. F., *J. Mater. Chem.* **2012**, *22* (26), 12983-12987.
43. Manjare, M.; Yang, B.; Zhao, Y. P., *J. Phys. Chem. C* **2013**, *117* (9), 4657-4665.
44. Orozco, J.; García-Gradilla, V.; D'Agostino, M.; Gao, W.; Cortés, A.; Wang, J., *ACS Nano* **2013**, *7* (1), 818-824.
45. Solovev, A. A.; Mei, Y.; Bermúdez Ureña, E.; Huang, G.; Schmidt, O. G., *Small* **2009**, *5* (14), 1591-1694.
46. Sanchez, S.; Solovev, A. A.; Mei, Y.; Schmidt, O. G., *J. Am. Chem. Soc.* **2010**, *132* (38), 13144-13145.
47. Solovev, A. A.; Xi, W.; Gracias, D. H.; Harazim, S. M.; Deneke, C.; Sanchez, S.; Schmidt, O. G., *ACS Nano* **2012**, *6* (2), 1751-1756.
48. Gao, W.; Sattayasamitsathit, S.; Orozco, J.; Wang, J., *J. Am. Chem. Soc.* **2011**, *133* (31), 11862-11864.
49. Gao, W.; Uygun, A.; Wang, J., *J. Am. Chem. Soc.* **2012**, *134* (2), 897-900.
50. Gao, W.; Pei, A.; Wang, J., *ACS Nano* **2012**, *6* (9), 8432-8438.
51. Wu, Y.; Wu, Z.; Lin, X.; He, Q.; Li, J., *ACS Nano* **2012**, *6* (12), 10910-10916.
52. Wu, Z.; Wu, Y.; He, W.; Lin, X.; Sun, J.; He, Q., *Angew. Chem. Int. Ed.* **2013**, *52* (27), 7000-7003.
53. Balasubramanian, S.; Kagan, D.; Jack Hu, C.-M.; Campuzano, S.; Lobo-Castañón, M. J.; Lim, N.; Kang, D. Y.; Zimmerman, M.; Zhang, L.; Wang, J., *Angew. Chem. Int. Ed.* **2011**, *50* (18), 4161-4164.
54. Orozco, J.; Cortés, A.; Cheng, G.; Sattayasamitsathit, S.; Gao, W.; Feng, X.; Shen, Y.; Wang, J., *J. Am. Chem. Soc.* **2013**, *135* (14), 5336-5339.
55. Campuzano, S.; Orozco, J.; Kagan, D.; Guix, M.; Gao, W.; Sattayasamitsathit, S.; Claussen, J. C.; Merkoçi, A.; Wang, J., *Nano Lett.* **2012**, *12* (1), 396-401.

56. Dreyfus, R.; Baudry, J.; Roper, M. L.; Fermigier, M.; Stone, H. A.; Bibette, J., *Nature* **2005**, *437* (7060), 862-865.
57. Snezhko, A.; Belkin, M.; Aranson, I. S.; Kwok, W. K., *Phys. Rev. Lett.* **2009**, *102* (11), 118103.
58. McNaughton, B. H.; Anker, J. N.; Kopelman, R., *J. Magn. Magn. Mater.* **2005**, *293* (1), 696-701.
59. Ghosh, A.; Fischer, P., *Nano Lett.* **2009**, *9* (6), 2243-2245.
60. Zhang, L.; Petit, T.; Lu, Y.; Kratochvil, B. E.; Peyer, K. E.; Pei, R.; Lou, J.; Nelson, B. J., *ACS Nano* **2010**, *4* (10), 6228-6234.
61. Tierno, P.; Golestanian, R.; Pagonabarraga, I.; Sagués, F., *J. Phys. Chem. B* **2008**, *112* (51), 16525-16528.
62. Gao, W.; Sattayasamitsathit, S.; Manesh, K. M.; Weihs, D.; Wang, J., *J. Am. Chem. Soc.* **2010**, *132* (41), 14403-14405.
63. Gao, W.; Kagan, D.; Pak, O. S.; Clawson, C.; Campuzano, S.; Chuluun-Erdene, E.; Shipton, E.; Fullerton, E. E.; Zhang, L.; Lauga, E.; Wang, J., *Small* **2012**, *8* (3), 460-467.
64. Sakar, M. S.; Steager, E. B.; Kim, D. H.; Kim, M. J.; Pappas, G. J.; Kumar, V., *Appl. Phys. Lett.* **2010**, *96* (4), 043705-3.
65. Manesh, K. M.; Campuzano, S.; Gao, W.; Lobo-Castanon, M. J.; Shitanda, I.; Kiantaj, K.; Wang, J., *Nanoscale* **2013**, *5* (4), 1310-1314.
66. Chang, S. T.; Paunov, V. N.; Petsev, D. N.; Velev, O. D., *Nat. Mater.* **2007**, *6* (3), 235-240.
67. Calvo-Marzal, P.; Sattayasamitsathit, S.; Balasubramanian, S.; Windmiller, J. R.; Dao, C.; Wang, J., *Chem. Commun.* **2010**, *46* (10), 1623-1624.
68. Loget, G.; Zigah, D.; Bouffier, L.; Sojic, N.; Kuhn, A., *Acc. Chem. Res.* **2013**, *46* (11), 2513-2523.
69. Gangwal, S.; Cayre, O. J.; Bazant, M. Z.; Velev, O. D., *Phys. Rev. Lett.* **2008**, *100* (5), 058302.
70. Loget, G.; Larcade, G.; Lapeyre, V.; Garrigue, P.; Warakulwit, C.; Limtrakul, J.; Delville, M. H.; Ravaine, V.; Kuhn, A., *Electrochim. Acta* **2010**, *55* (27), 8116-8120.
71. Fattah, Z.; Loget, G.; Lapeyre, V.; Garrigue, P.; Warakulwit, C.; Limtrakul, J.; Bouffier, L.; Kuhn, A., *Electrochim. Acta* **2011**, *56* (28), 10562-10566.
72. Lee, Y.-J.; Park, D.-J.; Park, J.-Y.; Kim, Y., *Sensors* **2008**, *8* (10), 6154-6164.
73. Choi, K. S.; McFarland, E. W.; Stucky, G. D., *Adv. Mater.* **2003**, *15* (23), 2018-2021.
74. Forry, S. P.; Wightman, R. M., *Electrogenerated Chemi-luminescence, (Ed.: A. J. Bard), CRC Press* **2004**, 273-300.
75. Tian, D.; Zhang, H.; Chai, Y.; Cui, H., *Chem. Commun.* **2011**, *47* (17), 4959-4961.
76. Chen, X.-m.; Su, B.-y.; Song, X.-h.; Chen, Q.-a.; Chen, X.; Wang, X.-r., *TrAC Trends in Analytical Chemistry* **2011**, *30* (5), 665-676.
77. Chai, Y.; Tian, D.; Wang, W.; Cui, H., *Chem. Commun.* **2010**, *46* (40), 7560-7562.
78. Chow, K.-F.; Mavré, F. o.; Crooks, R. M., *J. Am. Chem. Soc.* **2008**, *130* (24), 7544-7545.
79. Wu, M.-S.; Yuan, D.-J.; Xu, J.-J.; Chen, H.-Y., *Chemical Science* **2013**, *4* (3), 1182-1188.

80. Sentic, M.; Loget, G.; Manojlovic, D.; Kuhn, A.; Sojic, N., *Angew. Chem. Int. Ed.* **2012**, *51* (45), 11284-11288.
81. Loget, G.; Kuhn, A., *Nat. Commun.* **2011**, *2*, 535.
82. Loget, G.; Kuhn, A., *Lab Chip* **2012**, *12* (11), 1967-1971.
83. Bouffier, L.; Zigah, D.; Adam, C.; Sentic, M.; Fattah, Z.; Manojlovic, D.; Kuhn, A.; Sojic, N., *ChemElectroChem* **2014**, in press.
84. Sakura, S., *Anal. Chim. Acta* **1992**, *262* (1), 49-57.
85. Koizumi, Y.; Nosaka, Y., *J. Phys. Chem. A* **2013**, *117* (33), 7705-7711.
86. Fattah, Z.; Roche, J.; Garrigue, P.; Zigah, D.; Bouffier, L.; Kuhn, A., *ChemPhysChem* **2013**, *14* (10), 2089-2093.

Chapter 4

Bipolar Electrochemistry with Soft Materials: Deoxyribonucleic Acid (DNA)

4.1. Introduction to DNA: Structure, Charge Transport and Conductivity

4.1.1. DNA Structure

DNA is a long biopolymer made from repeating units called nucleotides.¹ A nucleotide is composed of a nucleobase (Adenine or guanine, double-ringed class of molecules, called purines. Cytosine or thymine, single-ringed molecules, called pyrimidines), a five-carbon sugar deoxyribose and at least one phosphate group (Figure 4.1).¹ DNA was first discovered and isolated by Friedrich Miescher in 1868 when he was doing experiments on the chemical composition of leukocytes.² The double-helical structure of DNA (Figure 4.1Inset) was proposed in 1953 by James Watson and Francis Crick³ based on Chargaff's analysis of the bases content (the ratio of the amounts of adenine to thymine, and the ratio of guanine to cytosine, are always very close to unity)⁴ of a number of DNA samples from different organisms, as well as through X-ray analysis of DNA fibers.³ Both of the two DNA helical chains are coiled around the same axis, and each with a radius of around 1 nanometer, with one backbone identified as 3' and the other 5' which refers to the direction that the 3rd and 5th carbon on the sugar molecule are facing.³

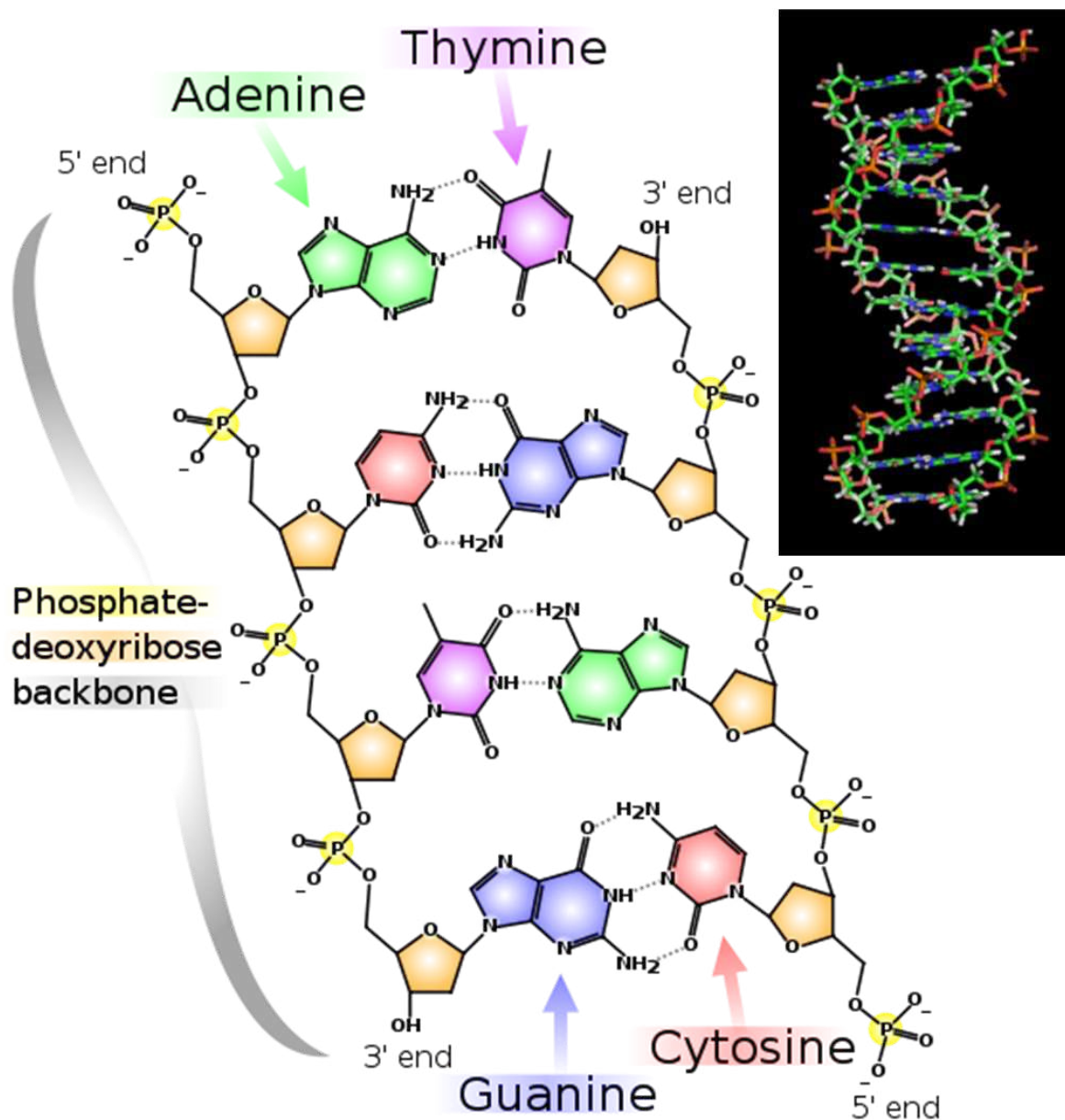


Figure 4.1 Chemical structure of DNA. Hydrogen bonds are shown as dotted lines. Inset: A section of DNA, the bases lie horizontally between the two spiraling strands. Reprinted from Ref. (1).

The base pairs (bps), guanine-cytosine and adenine-thymine, are linked by hydrogen bonds, and the distance between each two base pairs is 0.34 nm along the chains.³ The complementary nature of this based-paired structure provides a backup copy of all genetic information encoded within double-stranded DNA.²

4.1.2. DNA Charge Transport (CT) and Conductivity

The use of molecular recognition processes and the self-assembly of molecules into supramolecular structures⁵ is essential for nanoscale constructions. The conductivity of such structures is of importance in the field of nanotechnology especially for applications related to electrochemical signal transduction. DNA, in particular, shows great potential as a template for self-assembly of well defined nanostructures.⁶⁻⁷ However, DNA conductivity which is essential, e.g., for the design of biomolecular electric circuits⁸⁻¹⁰ and also for biological and medical applications,¹¹⁻¹⁵ is still a controversial point among scientists. In 1962, Eley and Spivey suggested that π - π interactions of the stacked base pairs in double-stranded (ds) DNA might serve as a pathway for charge transfer processes.¹⁶ The reason behind this idea was the similarities that they observed between stacked DNA base pairs and stacked graphite sheets: same planarity, with an inter-plane stacking distance of 3.4 Å for each one and made of aromatic molecules/residues.¹⁶ Evidence of DNA-mediated CT was reported in a 1993 experiment involving oxidative quenching of a DNA-bound metal complex through the DNA base stack.¹⁷⁻¹⁸ This pioneer work from Barton's group suggested that DNA is an efficient medium for coupling electron donors and acceptors over very long distances (> 40 Å).¹⁷ However, a later work contradicted this proposition when different donors and acceptors were used.¹⁹ The possibility that DNA may act as a molecular wire stimulated experimental and theoretical studies, resulting in the emergence of three views regarding the mechanism of long-distance DNA-mediated CT.²⁰ All the mechanisms involve an electron moving from a donor (D) orbital to an acceptor (A) orbital (Figure 4.2).²¹ The variations arise from the location of the orbitals that mediate this transition and also the pathways that are coupled to it.²¹ The mechanisms include: (a) superexchange or tunneling (charge is transported in one step by long-distance tunneling from D to A via the “bridging” DNA bases as shown in Fig. 4.2a);²⁰⁻²¹ (b) classic hopping (the charge resides on one base or several adjacent bases (Fig. 4.2b, c) and thermal fluctuations activate the charge motion along the DNA duplex);^{20, 22} (c) multistep random walk (from D to A involving short-distance tunneling intervals linked by nucleotide sequences serving as charge “resting” sites).²⁰

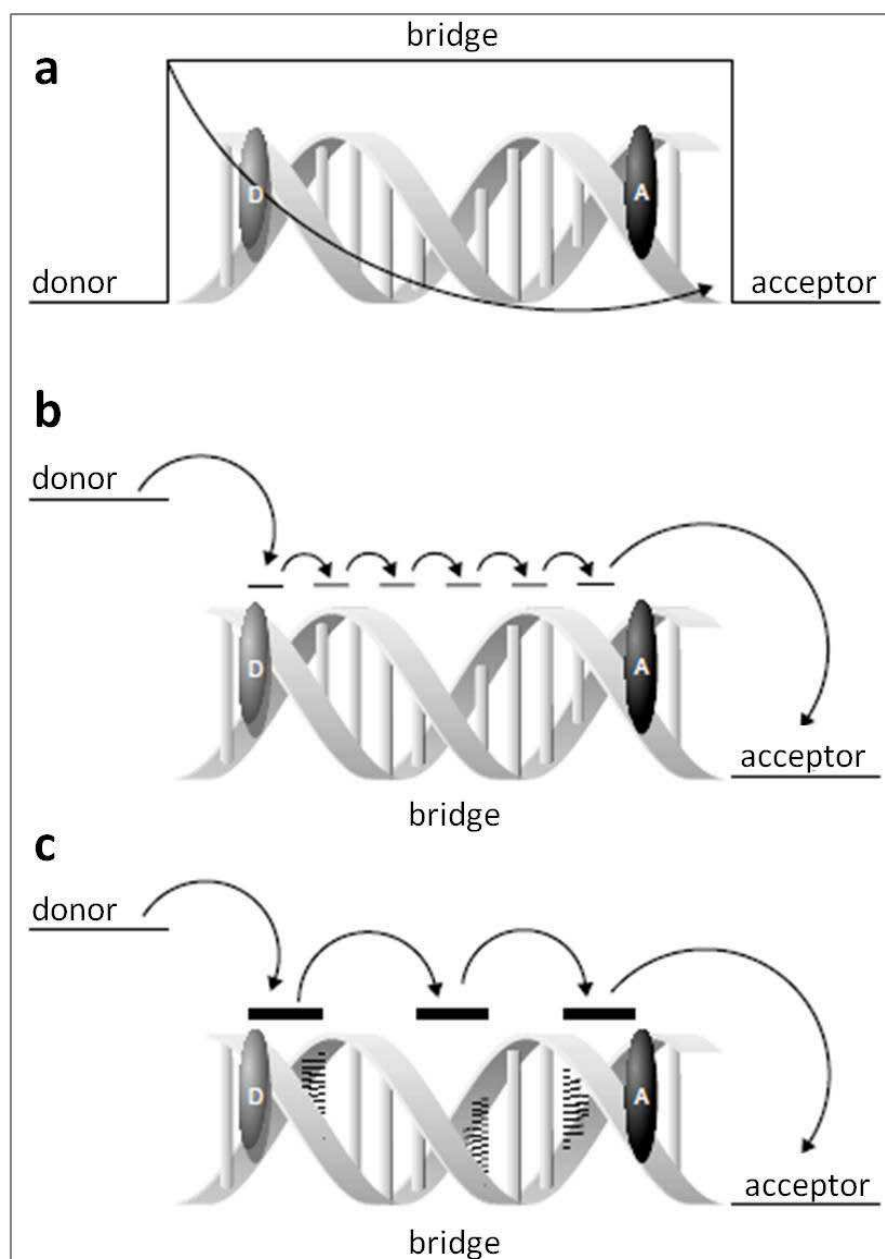


Figure 4.2 Schematic representations of three possible mechanisms for charge transport through DNA.²² (a) Superexchange: the charge tunnels from the donor (D) to the acceptor (A) through the bridge in a nonadiabatic process. An exponential decrease in the rate of charge transport with increasing length of the bridge is predicted. (b) Hopping: charge occupies the bridge in travelling from donor to acceptor by hopping between discrete molecular orbitals on the bridge. If the rate of charge migration is faster than trapping, the charge should be able to migrate over long distances before getting trapped. (c) Domain hopping: charge occupies the bridge by delocalizing over several bases, or a domain. This domain hops along the bridge to travel from donor to acceptor. As in a pure hopping mechanism, the charge should be able to travel long distances before getting trapped.²² Adapted from Ref. (22).

Recently, Paleček and Bartošík stated in their review that tunneling appears to be inefficient because of dynamic structural fluctuations of DNA.²⁰ The studies have shown that the dominant mechanism for charge (radical cation) migration in DNA is multistep hopping.²⁰ This mechanism takes place according to a complex process in which the charge (resulting from one-electron oxidation of DNA) can migrate over long distances by hopping through the double helix until it is irreversibly trapped in a reaction that damages DNA bases.^{20, 23} The efficiency of hopping is determined by specific nucleotide sequences. The reaction occurs usually at a guanine residue yielding primarily 8-oxo-7,8-dihydroguanine (8-oxoG) since the guanine has the lowest oxidation potential of all DNA bases.²⁴⁻²⁵ If no suitable guanine is available, the reaction may occur at two-thymine (TT) sections in which both T's can be damaged.²³ For more information about the CT mechanisms, we refer the reader to recent reviews.^{18, 20-21, 26}

Many experimental approaches have been employed in order to investigate the CT reactions through DNA, and most of the factors that affect the rate and efficiency of the reaction are well understood.¹⁸ Indeed, the nature of the CT bridge must be considered, DNA sequence, and the introduction of perturbations such as base mismatches between the donor and the acceptor, among other factors, can alter the rate of the reaction and the yield of CT products.¹⁸ Details concerning the experimental studies of the CT in DNA and the factors affecting this process were reported by different groups and can be found in the literature.²⁷⁻⁴⁰

The issue of whether DNA is intrinsically conducting is still an open question. The experimental outcomes are amazingly different, covering all possible results: from insulating, semiconducting to conducting, as reviewed by Endres *et al.*⁴¹ One difficulty is to perform reproducible and easily interpretable experiments at nanoscale dimensions. In addition, there is a large variety of experimental conditions that are usually adapted and on which the results strongly depend.⁴¹ Different techniques such as conductive atomic force microscopy (AFM),⁴²⁻⁴³ scanning tunneling microscopy (STM),⁴⁴⁻⁴⁸ and nanogap junctions⁴⁹⁻⁵⁰ have been employed in order to study DNA conductivity as illustrated in Figure 4.3. However, all these approaches represent indirect methods to prove the ability of DNA to conduct electricity and further work is clearly needed in order to address this property. In this context, bipolar electrochemistry might be used as a straightforward technique for investigating DNA conductivity, as we are going to discuss in the next section.

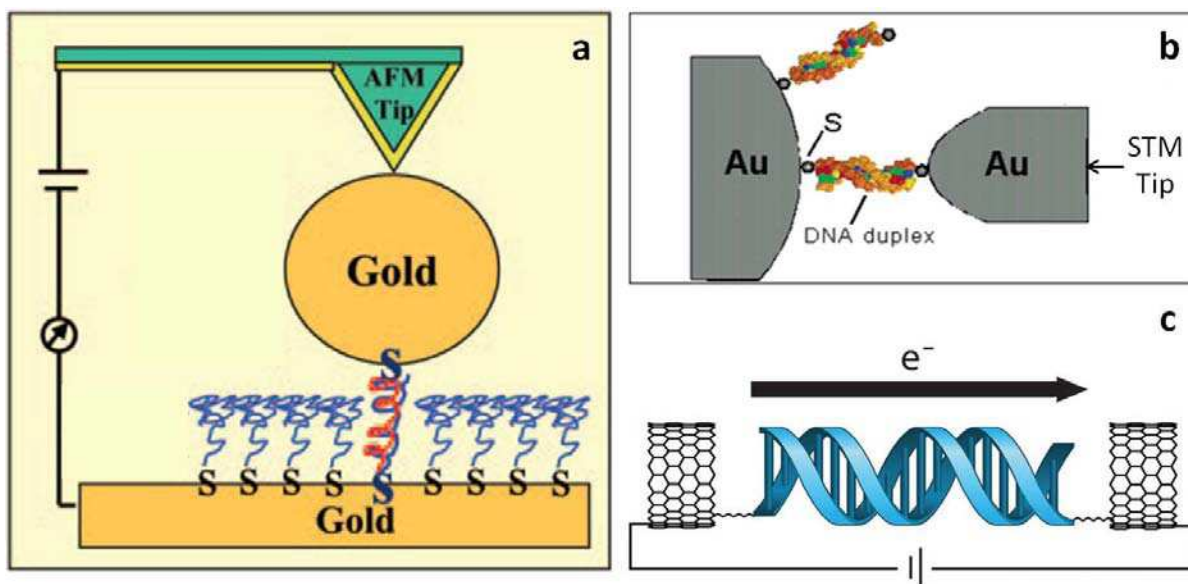


Figure 4.3 Schematic illustrations of some techniques that have been used for measurement of single-molecule DNA conductivity through molecular contacts. a) An individual 26-mer DNA molecule on a gold electrode is in contact with AFM tip via a gold nanoparticle, adapted from Ref. (42). b) A gold STM tip is slowly brought into contact with a thiol-modified DNA surface (8-mer), allowing to build a histogram of conductance over many different orientations, adapted from Ref. (48). c) One DNA duplex is covalently attached by amide bonds across a gap that has been cut in a carbon nanotube placed in an electrical circuit. Current flow through the CNT–DNA device is a reflection of DNA CT through the single DNA duplex that bridges the gap and can be used to make fundamental measurements of DNA conductivity.¹⁸ Reprinted from Ref. (18).

4.2. Bipolar electrochemistry for Asymmetric Metal deposition on DNA

In contrast to all previously mentioned approaches that have been used to study DNA conductivity, bipolar electrochemistry represents an inexpensive and simple method that can be useful for this purpose. Based on the principle of bipolar electrochemistry (section 1.2.), the conductivity of the substrate should be higher than its surrounding medium in order to get it sufficiently polarized and behave as a BPe. Therefore, if we apply an efficient potential ($\Delta V > \Delta V_{\min}$) along the DNA and if its conductivity is higher than the solution conductivity, then oxidation and reduction reactions may occur at both DNA extremities. In the presence of metal cations M^{n+} , the formation of metal deposit at its cathodic pole (Figure 4.4) will be a strong evidence of the intrinsic conductivity of DNA.

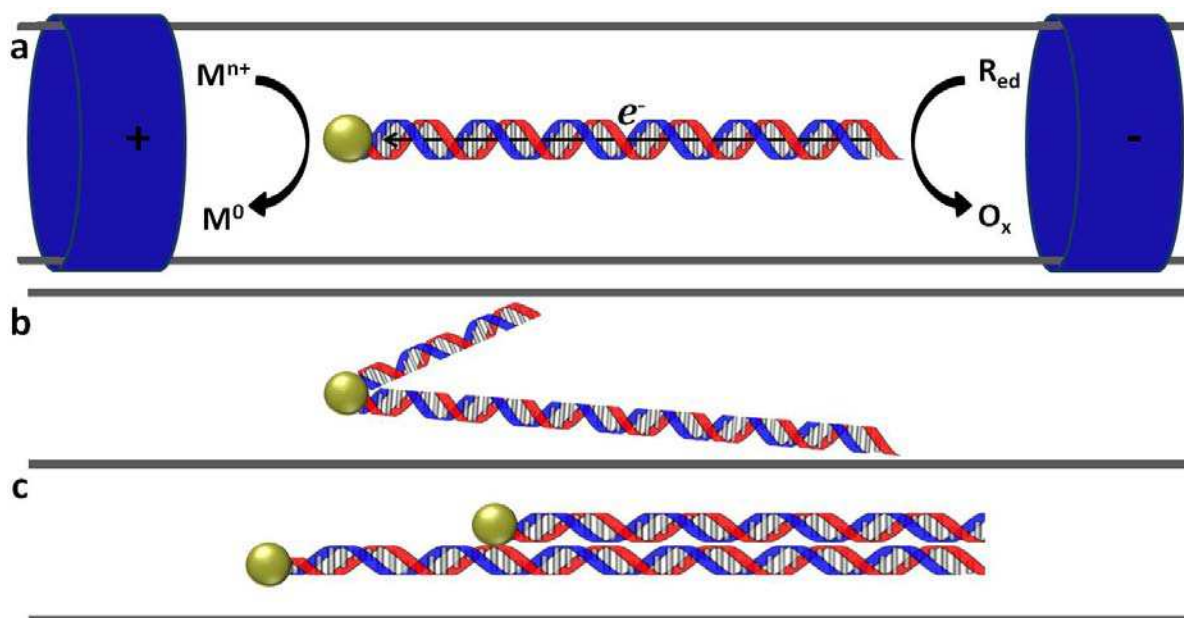


Figure 4.4 Schematic representations of double-stranded (ds) DNA modified with a metal particle if DNA has a sufficient conductivity with a value that is higher than that of the surrounding solution during bipolar electrochemistry. Moreover, the resulting morphology will depend on how it travels in the capillary: a) Straight dsDNA, b) Folded dsDNA, and c) dsDNA bundle.

The CABED setup and the same procedure that has been described in section 2.4. was employed in order to investigate this process. Capillary electrophoresis is indeed a safe tool that is commonly adopted for DNA analysis without deformation of its structure.⁵¹ Different

other setups employing bipolar cells and home built capillary configurations were also used alternatively to CABED, but because of some practical experimental issues we stopped working with them and focused only on CABED. A commercial double-stranded lambda DNA (*cl857 Sam7* isolated from *E. coli* strain is provided in 10 mM Tris-HCl (pH 7.5), 10mM NaCl and 1 mM EDTA, Promega) that is relatively long (48,502 bps, length $\sim 16.5 \mu\text{m}$) at a concentration of 465 $\mu\text{g/mL}$ was chosen for easier polarization and visualization under transmission electronic microscope (TEM). Figure 4.5 shows a TEM image of the DNA that was not exposed to the electric field. Several bundles as well as individual dsDNA can be seen clearly. The inset shows a high resolution TEM picture of a single dsDNA, with a diameter of $\sim 2 \text{ nm}$ which is comparable to the theoretical value (2 nm) if we consider the resolution of the TEM microscope.

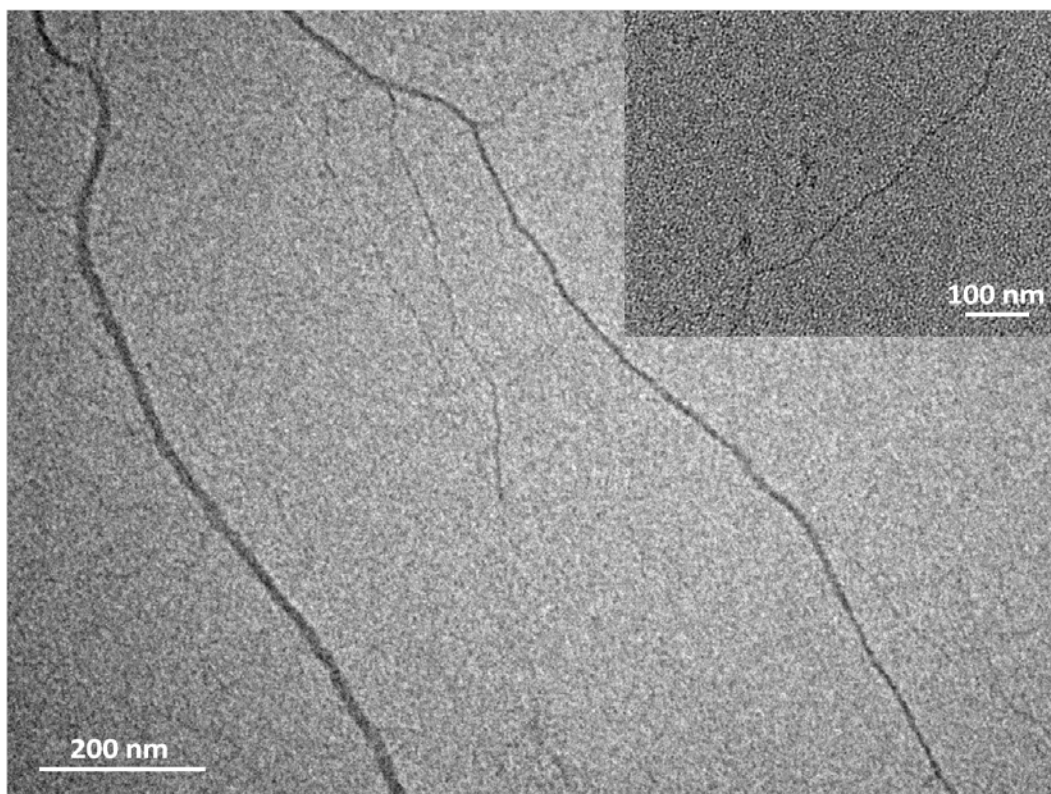


Figure 4.5 TEM image showing several bundles of dsDNA that have been branched in some parts into individual dsDNA. Inset: high resolution TEM image of a single dsDNA after sonication of the sample for 10 s before drop coating it onto the grid.

DNA samples, either simply diluted in pure water or mixed with an aqueous metal salt solution, were sonicated for 10 s in order to disperse the DNA strands and minimize the formation of bundles before injecting into the CE. It is noteworthy that CABED can also

directly participate in stretching the DNA strands during the experiment, leading to a less coiled configuration. The electric field was applied for about 1 min and the DNA absorbance was monitored at 260 nm (Figure 4.6). At the end of the experiment, the sample was collected from the capillary and directly dropped onto a TEM grid (200 mesh from Agar scientific) and left for ~ 1 min to settle down. Then, the excess of solution was carefully removed from the bottom side of the grid by using a filter paper. The grid was then washed several times with pure water using the same procedure. The dried sample was investigated later with a high resolution TEM microscope (Hitachi H7650).

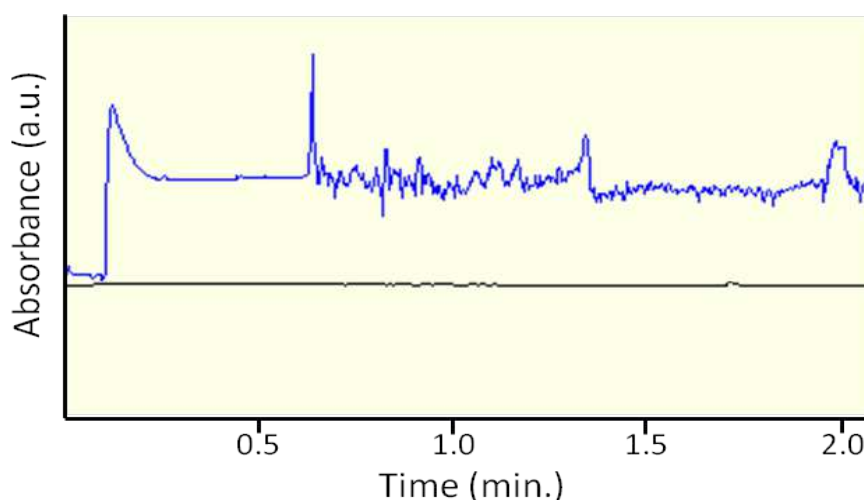


Figure 4.6 Typical trace of absorbance at $\lambda = 260$ nm, recorded with pure water (black line), and $24 \mu\text{g}/70 \mu\text{L}$ diluted solution of Lambda DNA in H_2O (blue line) during two minutes under 50 kV/m electric field.

DNA imaging is very challenging due to its small diameter (2 nm), especially in the absence of staining agents which are usually used to enhance the DNA contrast with respect to the grid surface.⁵² Different preparation methods as well as DNA concentrations were tested before being able to observe regularly DNA under the TEM. Uranyl acetate ($\text{UO}_2(\text{C}_2\text{H}_3\text{O}_2)_2$) was used for DNA staining, however, as this compound is able to bind indifferently to both negatively and positively charged groups in the specimen,⁵³ it didn't improve the visualization in our case. Therefore all the pictures that will be presented in the following were taken without any staining. Different metal salts have been used in order to deposit the corresponding metals from their aqueous solutions asymmetrically at the cathodically polarized DNA extremity. Gold chloride $[\text{Au}^{\text{III}}\text{Cl}_4]^-$ was first chosen among different metals, since it is very easy to reduce ($E^\circ = + 0.99 \text{ V vs. NHE}$), thus facilitating the overall bipolar

reaction involving also water oxidation at the anodic pole of the DNA strands. Investigation of the collected samples under the TEM showed a clear gold deposition along the DNA as well as over different areas of the grid. Therefore, a control experiment was performed in order to check whether the generation of such deposits takes also place in the absence of electric field. Unfortunately, the formation of Au deposits is also observed even if no potential is applied, which might be attributed to the spontaneous reduction of the Au^{3+} ions by the guanine or the thymine within the DNA structure. Following this result, we decided to work with another metal that has a lower reduction potential. Copper chloride (CuCl) which has a standard reduction potential of $E^\circ = +0.52 \text{ V vs. NHE}$, was the second metal precursor that we investigated. Unfortunately, the same problem of spontaneous reduction appeared again and has been attributed to disproportionation of the cuprous cation, therefore we stopped working with Cu^{1+} .

Such problems were not encountered when Cu^{2+} ($E^\circ = +0.34 \text{ V vs. NHE}$) was used instead, which encouraged us to continue with this species. A solution of 5 mM CuSO_4 and $24 \mu\text{g}/70 \mu\text{L}$ of DNA was employed for the CE experiment by applying an electric field of 103 kV/m for 1 min . Investigation of the recovered samples showed in many cases DNA strands attached to a dark nanoparticle at its extremity. Figure 4.7 shows TEM images of an individual dsDNA connected to a $\sim 50 \text{ nm}$ big deposit. Due to the length of the DNA ($16.5 \mu\text{m}$) and its low contrast with respect to the grid surface, we did not succeed to follow the strand over this large distance and image its other, supposedly unmodified end.

In order to verify the metal electrodeposition process at one extremity of DNA, we performed another set of experiments with a different metal salt. Nickel sulfate has been used for this purpose. Ni^{2+} has a much lower reduction potential ($E^\circ = -0.26 \text{ V vs. NHE}$), hence, by using the same electric field (driving force) and also the same salt concentration as in the case of Cu^{2+} , the final Ni deposit should have a smaller size. Tuning the deposit size is also possible by using different concentrations of the Ni^{2+} salt. However, in the later case we have to consider that by changing the metal ion concentration, we are changing the conductivity of the surrounding solution, which will affect the faradaic current through the BPe (DNA).

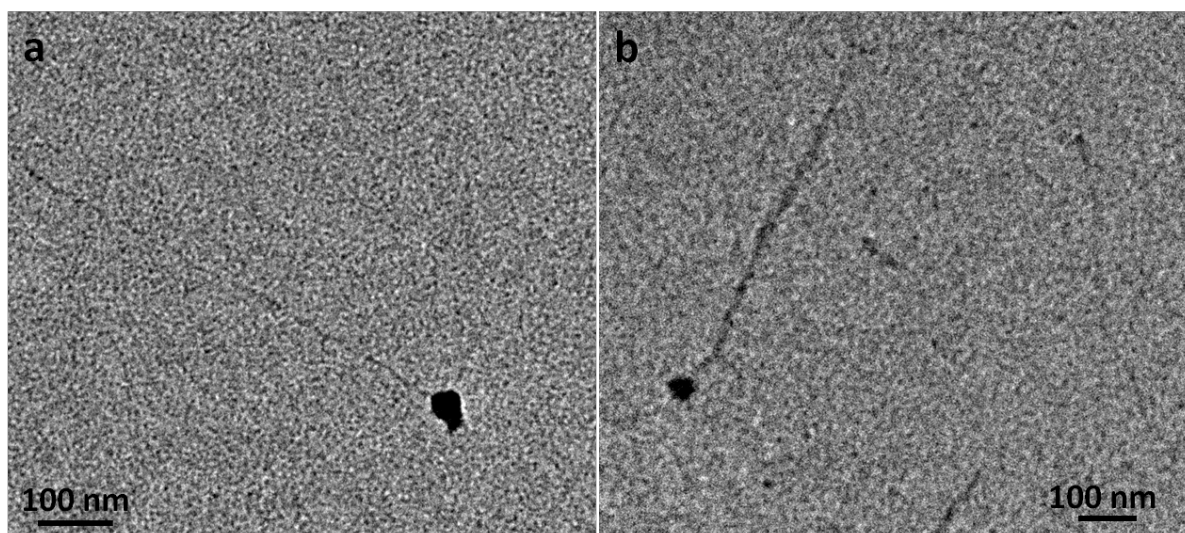


Figure 4.7 TEM images of a dsDNA collected from the CE after exposure to the electric field in the presence of copper sulfate.

The same concentration of DNA as well as an electric field identical to the one applied with Cu^{2+} was used in the all experiments with Ni^{2+} except for the one in Figure 4.8b. The latter was carried out with $1.9 \mu\text{g}/70 \mu\text{L}$ DNA and $\mathcal{E} = 158 \text{ kV/m}$ applied to a PDMS cell, similar to the one in Figure 3.12a, with a much smaller reaction compartment and also in the presence of cation exchange membranes instead of using the CE. The NiSO_4 concentration was varied from 1 – 5 mM in the experiments. Figure 4.8 shows TEM pictures of the DNA that has been exposed to the electric field by varying the concentrations of Ni^{2+} salt from 1 (a) to 3.3 (b) and 5 mM (c,d) respectively. Different morphologies of the collected samples were observed under the TEM. Deposits that are just localized at the extremity of the DNA can be seen in Fig.4.8a and b, whereas a nanoparticle localized along the DNA and not at its extremity is visible in Fig.4.8c. The latter may be generated if the DNA strand is folded during its journey in the CE (Fig.4.4b). In this case, if the longer part of the folded DNA experiences a sufficient reactivity at its ends, deposition might be possible as well. The last morphology presented in Fig.4.8d is obtained when DNA is moving in a bundle through the CE. In such a case each individual dsDNA that has been branched from the main bundle can be modified with a single metal particle at its extremity as depicted in Figure 4.4c.

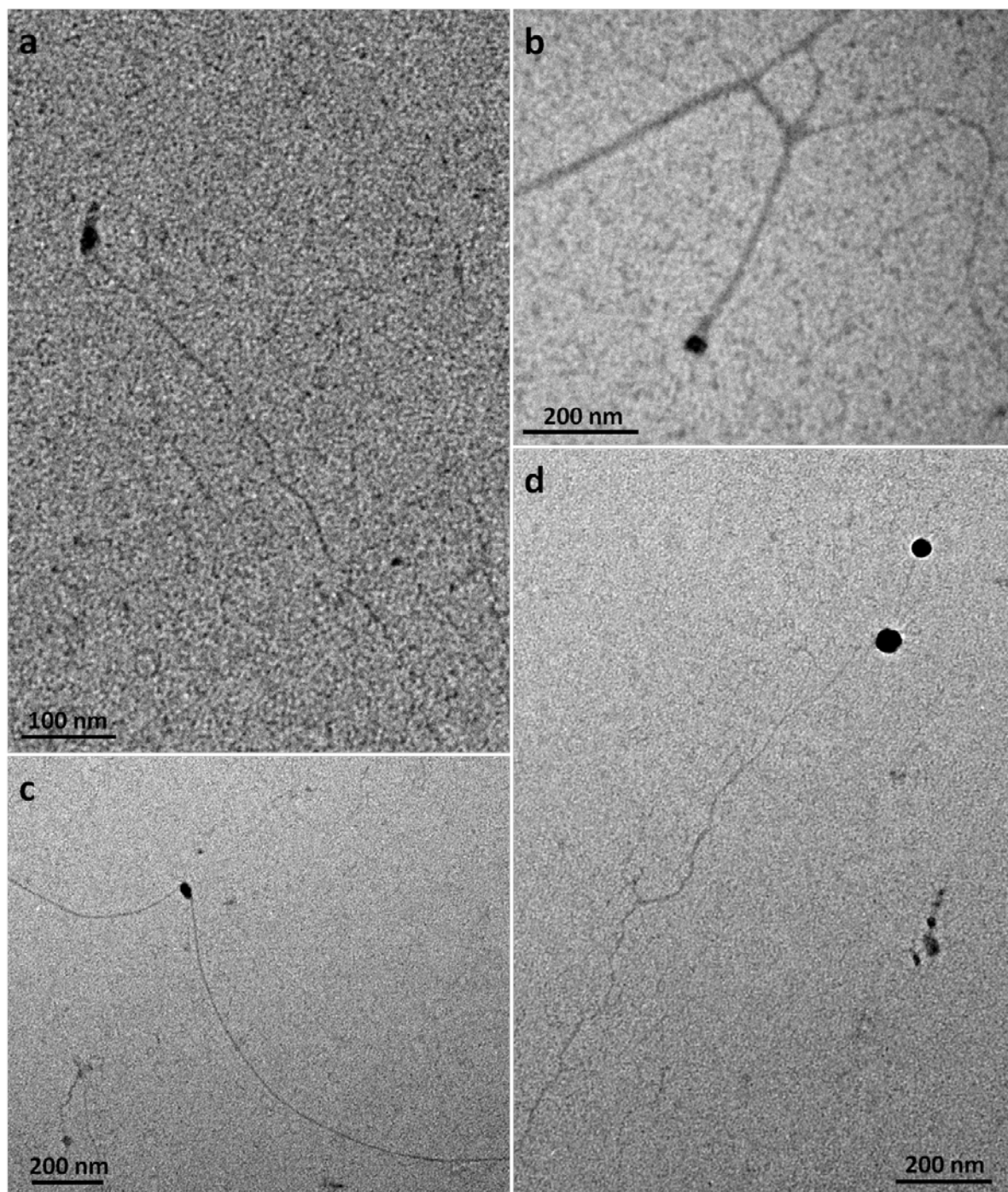


Figure 4.8 TEM pictures of the DNA recovered after the CABED in the presence of nickel sulfate. a) Single dsDNA with one cluster at its end. b) A big bundle of DNA with a single deposit. c) dsDNA with a nanoparticle that is not located at the extremity. d) DNA bundle with two particles at the extremities of the individual dsDNA.

The typical size of the deposit varies from 20-30 nm in Fig.4.8a and b, up to ~ 50 nm in c and d, respectively, with increasing the Ni^{2+} concentration. However this was not always the case, which might be attributed to the possible presence of DNA strands with different lengths.

Also when comparing the deposit lengths in Fig.4.8c and d with the ones that have been generated with the same concentration (5 mM) of CuSO₄ in Fig.4.7a, b (~50 nm), no significant difference can be seen.

Another attempt to tune the driving force and to facilitate the Cu electrodeposition process in order to generate a bigger deposit was tried by introducing other counter reactions than water oxidation at the anodic pole of the DNA. For this, ferrocenemethanol (FcMeOH), hydroquinone (H₂Q) and 3,4-ethylenedioxythiophene (EDOT) were used together with the copper sulfate solution in the presence of DNA during the CABED. Investigation of the resulting samples as well as a series of control experiments revealed the formation of dirty samples with an unexplained imaging noise for all selected counter ions which prevented the clear visualization of the modification. In fact, the low percentage of clearly reproducible samples is one of the major problems that we were facing during this work. This might be due sometimes to the experimental setup, but also to the grid preparation, as we observed quite dirty backgrounds with several empty grids. Therefore, it will be essential in the future to perform also a qualitative analysis, such as EDX or XPS, of the deposits found at the DNA extremities in order to confirm the nature of the deposit.

Even though the obtained results were not very conclusive, they look really promising. Further confirmation of the deposit composition will provide a strong direct proof of the DNA conductivity. It will also open a new strategy for sensing the DNA conductivity using bipolar electrochemistry by changing the ionic strength of the surrounding solution when the DNA strands have almost the same length. As a hot topic in the frame of nanotechnology, more experiments will be performed in order to improve the modification process in such a way to have cleaner and reproducible samples. Introduction of mismatches⁵⁴ or intercalators¹⁸ is another possibility to investigate the DNA conductivity. Finally other factors such as pH, temperature and the introduction of other compounds that might result in a DNA denaturation should be also considered, as they can strongly affect the CT along dsDNA.

References

1. *The Free Encyclopedia* <http://en.wikipedia.org/wiki/DNA> Accessed **05, 2013**.
2. Dahm, R., *Hum. Genet.* **2008**, *122* (6), 565-581.
3. Watson, J. D.; Crick, F. H. C., *Nature* **1953**, *171* (4356), 737-738.
4. Chargaff, E.; Lipshitz, R.; Green, C., *J. Biol. Chem.* **1952**, *195* (1), 155-160.
5. Lehn, J.-M.; Sanders, J., *Supramol. chem: concepts and perspectives*. Vch Weinheim: 1995; Vol. 154.
6. Zhang, Y.; Seeman, N. C., *J. Am. Chem. Soc.* **1994**, *116* (5), 1661-1669.
7. Zhang, C.; Su, M.; He, Y.; Zhao, X.; Fang, P.-a.; Ribbe, A. E.; Jiang, W.; Mao, C., *Proc Natl Acad Sci USA* **2008**, *105* (31), 10665-10669.
8. Braun, E.; Eichen, Y.; Sivan, U.; Ben-Yoseph, G., *Nature* **1998**, *391* (6669), 775-778.
9. Bhalla, V.; Bajpai, R. P.; Bharadwaj, L. M., *EMBO Rep.* **2003**, *4* (5), 442-445.
10. Liberski, A. R.; Delaney, J. T.; Liberska, A.; Perelaer, J.; Schwarz, M.; Schuler, T.; Moller, R.; Schubert, U. S., *RSC Advances* **2012**, *2* (6), 2308-2313.
11. Farjami, E.; Clima, L.; Gothelf, K.; Ferapontova, E. E., *Anal. Chem.* **2011**, *83* (5), 1594-1602.
12. Komor, A. C.; Barton, J. K., *Chem. Commun.* **2013**, *49* (35), 3617-3630.
13. Boal, A. K.; Genereux, J. C.; Sontz, P. A.; Gralnick, J. A.; Newman, D. K.; Barton, J. K., *Proc. Natl. Acad. Sci. USA* **2009**, *106* (36), 15237-15242.
14. Sontz, P. A.; Mui, T. P.; Fuss, J. O.; Tainer, J. A.; Barton, J. K., *Proc. Natl. Acad. Sci. USA* **2012**, *109* (6), 1856-1861.
15. Sontz, P. A.; Muren, N. B.; Barton, J. K., *Acc. Chem. Res.* **2012**, *45* (10), 1792-1800.
16. Eley, D. D.; Spivey, D. I., *Trans. Faraday Soc.* **1962**, *58*, 411-415.
17. Murphy, C.; Arkin, M.; Jenkins, Y.; Ghatlia, N.; Bossmann, S.; Turro, N.; Barton, J., *Science* **1993**, *262* (5136), 1025-1029.
18. Muren, N. B.; Olmon, E. D.; Barton, J. K., *Phys. Chem. Chem. Phys.* **2012**, *14* (40), 13754-13771.
19. Wan, C.; Fiebig, T.; Schiemann, O.; Barton, J. K.; Zewail, A. H., *Proc. Natl. Acad. Sci. USA* **2000**, *97* (26), 14052-14055.
20. Paleček, E.; Bartošík, M., *Chem. Rev.* **2012**, *112* (6), 3427-3481.
21. Genereux, J. C.; Barton, J. K., *Chem. Rev.* **2010**, *110* (3), 1642-1662.
22. Boon, E. M.; Barton, J. K., *Curr. Opin. Struct. Biol.* **2002**, *12* (3), 320-329.
23. Kanvah, S.; Joseph, J.; Schuster, G. B.; Barnett, R. N.; Cleveland, C. L.; Landman, U., *Acc. Chem. Res.* **2009**, *43* (2), 280-287.
24. Oliveira-Brett, A. M.; Piedade, J. A. P.; Silva, L. A.; Diculescu, V. C., *Anal. Biochem.* **2004**, *332* (2), 321-329.
25. Stempkowska, I.; Ligaj, M.; Jasnowska, J.; Langer, J.; Filipiak, M., *Bioelectrochemistry* **2007**, *70* (2), 488-494.
26. Wagenknecht, H.-A., *Nat. Prod. Rep.* **2006**, *23* (6), 973-1006.
27. Abi, A.; Ferapontova, E. E., *J. Am. Chem. Soc.* **2012**, *134* (35), 14499-14507.
28. Farjami, E.; Campos, R.; Ferapontova, E. E., *Langmuir* **2012**, *28* (46), 16218-16226.
29. Genereux, J. C.; Barton, J. K., *Nat Chem* **2009**, *1* (2), 106-107.

30. Genereux, J. C.; Wuerth, S. M.; Barton, J. K., *J. Am. Chem. Soc.* **2011**, *133* (11), 3863-3868.
31. Kelley, S. O.; Barton, J. K., *Science* **1999**, *283* (5400), 375-381.
32. Klotz, D.; Römer, R. A.; Turner, M. S., *Biophys. J.* **2005**, *89* (4), 2187-2198.
33. Liu, T.; Barton, J. K., *J. Am. Chem. Soc.* **2005**, *127* (29), 10160-10161.
34. Olmon, E. D.; Hill, M. G.; Barton, J. K., *Inorg. Chem.* **2011**, *50* (23), 12034-12044.
35. Pheeney, C. G.; Barton, J. K., *Langmuir* **2012**, *28* (17), 7063-7070.
36. Shao, F.; Augustyn, K.; Barton, J. K., *J. Am. Chem. Soc.* **2005**, *127* (49), 17445-17452.
37. Wan, C.; Fiebig, T.; Kelley, S. O.; Treadway, C. R.; Barton, J. K.; Zewail, A. H., *Proc. Natl. Acad. Sci. USA* **1999**, *96* (11), 6014-6019.
38. Wang, H.; Muren, N. B.; Ordinario, D.; Gorodetsky, A. A.; Barton, J. K.; Nuckolls, C., *Chem. Sci.* **2012**, *3* (1), 62-65.
39. Wohlgamuth, C. H.; McWilliams, M. A.; Slinker, J. D., *Anal. Chem.* **2013**.
40. Liu, S.; Clever, G. H.; Takezawa, Y.; Kaneko, M.; Tanaka, K.; Guo, X.; Shionoya, M., *Angew. Chem.* **2011**, *123* (38), 9048-9052.
41. Endres, R. G.; Cox, D. L.; Singh, R. R. P., *Reviews of Modern Physics* **2004**, *76* (1), 195-214.
42. Cohen, H.; Nogues, C.; Naaman, R.; Porath, D., *Proc. Natl. Acad. Sci. U. S. A.* **2005**, *102* (33), 11589-11593.
43. Heim, T.; Deresmes, D.; Vuillaume, D., *J. Appl. Phys.* **2004**, *96* (5), 2927-2936.
44. Kratochvílová, I.; Král, K.; Bunčák, M.; Víšková, A.; Nešpůrek, S.; Kochalska, A.; Todorciuc, T.; Weiter, M.; Schneider, B., *Biophys. Chem.* **2008**, *138* (1-2), 3-10.
45. Shapir, E.; Cohen, H.; Calzolari, A.; Cavazzoni, C.; Ryndyk, D. A.; Cuniberti, G.; Kotlyar, A.; Di Felice, R.; Porath, D., *Nat. Mater.* **2008**, *7* (1), 68-74.
46. van Zalinge, H.; Schiffrin, D. J.; Bates, A. D.; Haiss, W.; Ulstrup, J.; Nichols, R. J., *ChemPhysChem* **2006**, *7* (1), 94-98.
47. van Zalinge, H.; Schiffrin, D. J.; Bates, A. D.; Starikov, E. B.; Wenzel, W.; Nichols, R. J., *Angew. Chem. Int. Ed.* **2006**, *45* (33), 5499-5502.
48. Xu; Zhang; Li; Tao, *Nano Lett.* **2004**, *4* (6), 1105-1108.
49. Guo, X.; Gorodetsky, A. A.; Hone, J.; Barton, J. K.; Nuckolls, C., *Nat Nano* **2008**, *3* (3), 163-167.
50. Porath, D.; Bezryadin, A.; de Vries, S.; Dekker, C., *Nature* **2000**, *403* (6770), 635-638.
51. Righetti, P. G.; Gelfi, C.; D'Acunzio, M. R., *Electrophoresis* **2002**, *23* (10), 1361-1374.
52. Stoeckenius, W., *J. Biophys. Biochem. Cytol.* **1961**, *11* (2), 297-310.
53. Hayat, M. A., *Principles and techniques of electron microscopy: biological applications*. Cambridge University Press: **2000**, 342.
54. Wohlgamuth, C. H.; McWilliams, M. A.; Slinker, J. D., *Anal. Chem.* **2013**, *85* (3), 1462-1467.

Chapter 5

Conclusion and Perspectives

5.1. Conclusion

Electric fields were employed in the present thesis for studying the asymmetric reactivity along objects that are electrically conductive based on the principle of bipolar electrochemistry. The theoretical framework as well as the typical and also emerging applications of this method have been introduced in the first chapter.

The bulk synthesis of asymmetric particles is of great importance, and it was mainly presented in chapter two. Our experimental work started by investigating capillary-assisted bipolar electrodeposition which is based on the use of a conventional capillary electrophoresis instrument. This technique allows applying high electric fields up to 100 kV m^{-1} inside a 30 cm-long capillary as a typical length. Carbon microtubes could be modified asymmetrically by electrodepositing different metals at its one extremity. Silver and platinum metals were separately used for the electrodeposition process which led to carbon tube/metal hybrid structures.

The main disadvantage of this technology is the limited reaction volume which is conditioned by the dimensions of the capillary. Therefore, another approach based on the design of new bipolar cells that can provide comparable electric fields but allows working in much larger volumes was employed. Platinum/carbon microtube asymmetric particles were prepared using this technology.

With a setup that is analogous to the capillary electrophoresis but at a significantly larger scale in terms of capillary diameter, it was possible to modify millimeter-long carbon fibers with platinum or nickel at one end of the fibers.

Bipolar electrochemistry also allows the fine-tuning of the local orientation of the metal deposit during the nucleation and growing steps. The site of deposition on the resulting hybrids is directly determined by controlling the alignment of the objects in the electric field during the electrodeposition process. For this, the later setup was used for a proof-of-principle experiment in order to modify mechanically aligned carbon fibers with a copper deposit. Two different topologies (centered versus non-centered) have been obtained. By carefully choosing the experimental conditions in a bulk bipolar electrochemical cell, the site-selective copper deposition on carbon microtubes was also demonstrated. In this case, the alignment of the carbon tubes was controlled electrically by applying two successive potential steps (first one was below, and the second above the potential threshold value for copper electrodeposition) and by adjusting the viscosity of the surrounding medium. Three different topologies of copper clusters with respect to the main axis of the modified object were produced respectively: (1) a fully centered topology, (2) a fully non-centered topology, and (3) a combination of centered and non-centered modifications.

Electrodeposition using the bipolar setup is not limited to metals by direct electron transfer from electroactive precursors. The deposit can also be triggered indirectly at the reactive pole of the BPe by reducing species that can further react locally with another soluble precursor. This process which is called indirect bipolar electrochemistry¹ was adapted for the selective deposition of a functional inorganic layer on graphite rods. The successful deposition of water-insoluble Prussian Blue and related iron compounds resulting in formation of Janus objects that are able to promote chemical light emission at its modified part.

Electrocrystallization of ionic compounds on carbon substrates was demonstrated for the first time to be possible using bipolar electrochemistry. Ionic platinum and gold single crystals were electrogenerated on various carbon substrates. The phenomenon was not fully understood and need therefore to be further investigated.

The potential gradient alongside the BPe during the electrodeposition is expected to dominate the generation of several morphologies of metal deposits on a single substrate. Different copper morphologies were observed when this metal was electrodeposited on relatively long carbon fibers (0.5 – 1.0 cm) under high electric fields, and the process is still under study.

Bipolar electrochemical bulk cells displayed a relatively high convection rate between its compartments due to the porosity of separator membranes as well as the way these membranes are fixed to the core of the cells. In order to overcome this issue, a new technology has been developed by introducing an independent reaction compartment into the cell. One advantage among others of the new design is that the mass-transfer becomes controlled by electromigration. In this case, the electrodeposition of metals from negatively charged ions leads to an attractive microstructuration of spherical bipolar surfaces with metal rings. The cell has been used for example to generate platinum rings on glassy carbon microbeads.

Chapter three discussed the asymmetry of (micro)objects that can lead to their controlled motion. Bipolar electrochemistry was adapted for generating microswimmers according to two strategies. The first one includes the use as swimmers of the asymmetric particles that have been prepared by bipolar electrodeposition of metals on carbon substrates. In this context, carbon fiber/nickel hybrids could be driven in a two-dimensional space by using external magnetic fields whereas carbon tubes/platinum objects could be propelled in two different modes (translation versus rotation) by the generation of oxygen bubbles upon the presence of hydrogen peroxide solution (chemical fuelling). The latter approach relies on the direct symmetry break on isotropic particles that can be provoked by the applied fields leading to the controlled motion of the BPes. Using this principle, the accumulation of bubbles under a graphite bead led to its levitation inside a vertical capillary which was coupled to electrochemiluminescence at the anodic pole.

Finally, bipolar electrochemistry was extended to biological materials. DNA conductivity and charge transport, which is of great importance in nanotechnology, was discussed in chapter four. Different metals and counter reactions have been employed for DNA mediated metal deposition at one extremity of dsDNA. Promising results were obtained for copper and nickel deposits attached to the end of long DNA samples; however, further experiments and analysis are still required in order to definitely conclude on using a biopolymer as a BPe.

5.2. Perspectives

In the frame of materials science, a wide variety of possibilities can be considered for adapting bipolar electrochemistry. The size of the modified objects and the combination of several materials (nature or composition) are very important in modern technologies as well as the yields of production can be further developed. In the case of electrocrystallization discussed in section 2.5.5., studying the effect of salt concentration, time of deposition and the beneficial addition of positively charged counter ions, which is necessary for the crystal formation, may clarify the optimum conditions for the generation of single crystals. The process is very appealing since the electrocrystallization of other materials such as organic, inorganic and biological compounds (which are possible to crystallize with classical electrochemistry), can be achieved in principle with bipolar electrochemistry. The structure of different metal deposits and the potential of certain morphologies, which is especially important for industrial applications, can be simply provided on a single substrate by bipolar electrochemistry. This aspect was highlighted in section 2.5.6. where several copper morphologies grew on a carbon fiber. However, it requires further investigation on the influence of the pH, potential, and concentration effect in order to identify the parameters that are controlling this phenomenon. In a similar context, it could also be possible to generate metals library on a single object by the electrodeposition from a mixture of precursor salts and based on the difference in the standard reduction potentials of the metals.

The successful control of the deposit topology (section 2.5.3.) can be developed further for “bipolar electrochemical writing”. Unlike other techniques such as lithography, bipolar electrochemistry is a cheap and simple method that might be useful for the formation of 3D structure shapes. This can be obtained by adjusting the design of the reactor, the number and position of the feeder electrodes and the orientation of the applied electric fields as depicted in Figure 5.1. By switching the applied potential between the feeder electrodes 1 to 2 and vice versa, it should be possible to get a one-dimensional zigzag shape of the deposit on the BPe (Fig. 5.1a); the orientation of the substrate should be controlled in this case. If we introduce more feeder electrodes positioned with an adequate angle with respect to the first electrodes, a two-dimensional (Fig. 5.1b) or even three-dimensional zigzag shape may be potentially generated.

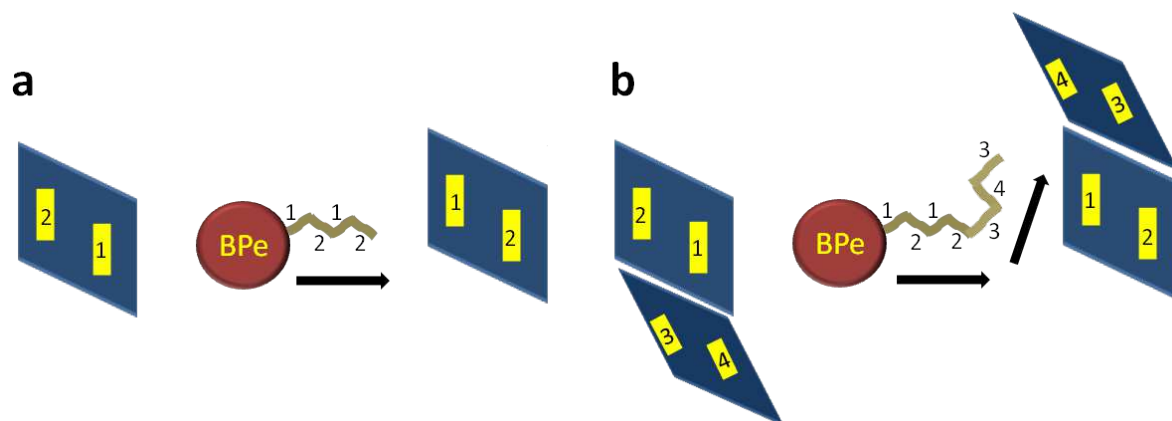


Figure 5.1 Schematic illustration of the fabrication of zigzag deposits in a one (a), and two- (b) dimensional shape using bipolar electrodeposition. The arrow refers to the deposit growth direction.

Different promising perspectives can also be imagined for the self-propelled objects. The speed of the motors is one important factor that can be enhanced, for example, by depositing porous platinum by using surfactants during the experiment. Pt deposition at the opposite ends of the BPe is also possible by inverting the direction of the applied potential and should double the theoretical speed of the resulting swimmers. The light emitting motors are very interesting as their trajectory can be tracked, for instance, in microfluidic devices. In this frame, the electrodeposition of Prussian blue (section 2.5.4.) on porous microbeads, can improve the deposit thickness and allow light-emitting JP to move for a suitable time before consuming the entire deposit layer. The porous structure of the swimmers can be loaded with other materials that can be released upon changes, e.g., in pH or temperature. Insulating materials can also be used for preparing microswimmers by bipolar electrodeposition after coating with a conductive layer. Figure 5.2 shows SEM image of a silica micro-spiral (on the right) and illustrates the strategy that enables fabrication of an original light-emitting swimmer. After gold sputtering on the top of the dispersed spirals, the half-coated objects can be submitted to the electric field for the bipolar electrodeposition of platinum at its extremity. The gold layer of these modified spirals can be further functionalized with a fluorophore. The motion of the blinking swimmers in a hydrogen peroxide solution could be followed under a fluorescence microscope. Employing the motors described in section 3.3. for studying *in situ* depollution of toxic metals by electrodeposition at the cathodic pole of the motor during its motion looks also promising. A very interesting aspect will be the fabrication of micro- and

nanoswimmers that are biocompatible for *in vivo* applications such as drug delivery. In this case, higher electric fields will be needed for preparing such small swimmers.

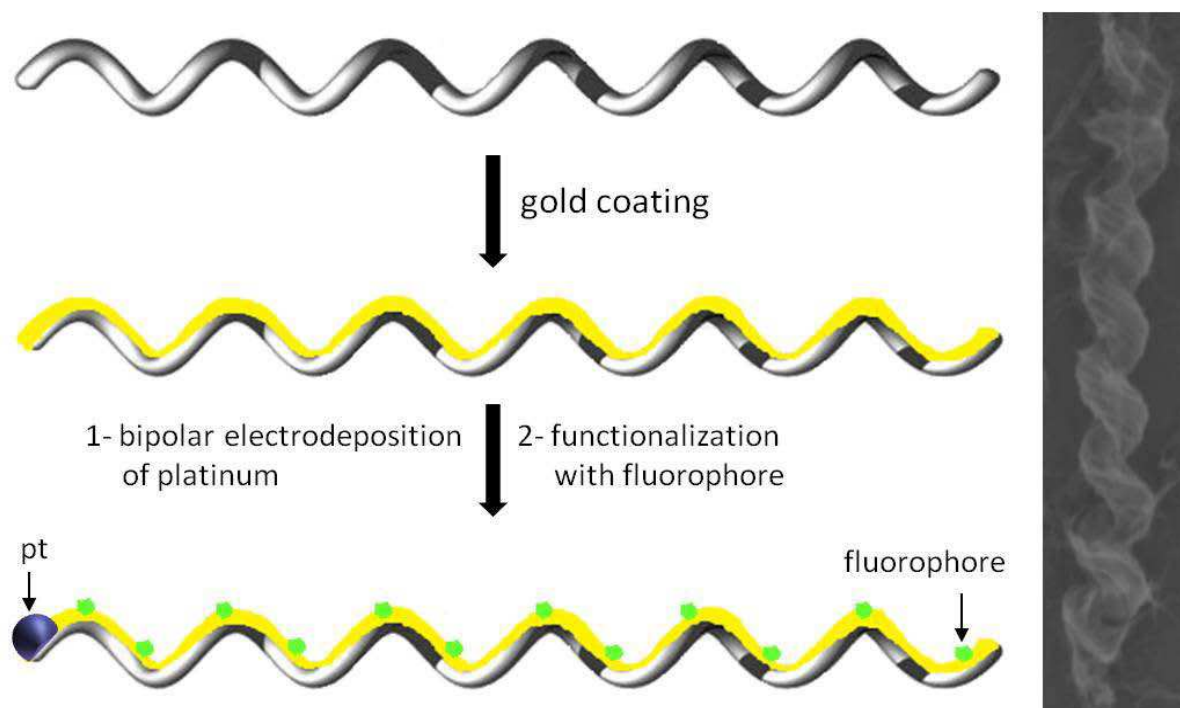


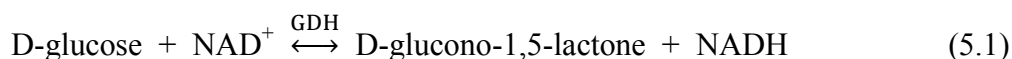
Figure 5.2 Illustration of the stepwise preparation of light-emitting swimmers using a silica spiral. The right inset SEM image is for a 18 μm -long silica spiral.

The application of bipolar electrochemistry for studying biological compounds such as DNA as discussed in section 4.2., opens a wide perspectives for employing this technique to investigate these important classes of molecules. Concerning DNA, one strategy to improve the size of the deposit is to increase the value of the applied electric field in capillary electrophoresis. The typical length of the capillary is 30 cm; however, some modification can be done to the setup in order to reach to a length of ~ 20 cm which will improve the potential limit up to ~ 150 kV. The effect of other parameters such as the pH and temperature has also to be considered. The presence of mismatch might help as well to investigate the DNA conductivity, in addition to a qualitative analysis which is very important for the confirmation of the nature of the deposit.

The reactivity of other biomolecules such as enzymes (proteins necessary to catalyze biochemical reactions) is very interesting to explore under the effect of electric fields. The substrate usually binds to the active site of the enzyme where the reaction can be catalyzed.² Enzymes can also contain sites that bind selectively to coenzymes, which are needed for

catalysis by providing an greater enzyme/substrate binding.² The coenzyme can also be considered as a secondary substrate since its chemical structure changes during the enzymatic reaction. Figure 5.3b shows a schematic representation of a reaction that is catalyzed upon an enzymatic recognition event. The activity of some enzymes was monitored and found to be altered under the influence of electric fields.³ This behavior was employed in order to develop biosensors such as a glucose sensor.⁴ The electric potential can induce a variation in the enzyme structure and modulate the enzyme activity due to electrostatic effects.³

The first enzymatic system that we chose to study was based on the oxidation of glucose by nicotinamide adenine dinucleotide (NAD⁺), coenzyme, that is catalyzed by glucose dehydrogenase (GDH) (eq. 5.1).⁵ This reaction is very important and usually used to determine glucose concentration in serum samples.⁶



The reduction of NAD⁺ into NADH can be followed by a spectrophotometer as both forms strongly absorb UV light at 259 nm and 339 nm, respectively. Therefore, the activity of GDH can be estimated indirectly by measuring the absorbance (Abs) of NAD⁺/NADH in the reaction mixture. Preliminary experiments were done in order to study this reaction. Figure 5.3a shows the experimental absorption spectrum recorded during 160 min for a solution containing 0.15 mM NAD⁺, 5 mM glucose and 22.5 U of GDH in phosphate buffer (PB) pH=7.4. The decrease in NAD⁺ Abs during the reaction time was correlated to an increase in the Abs of NADH. The application of electric fields on this system in a bipolar setup can be investigated which might influence the thermodynamic of substrate/enzyme complex formation. The rate of the reaction can then be easily detected by following the changes in the NDA⁺/NADH spectrum.

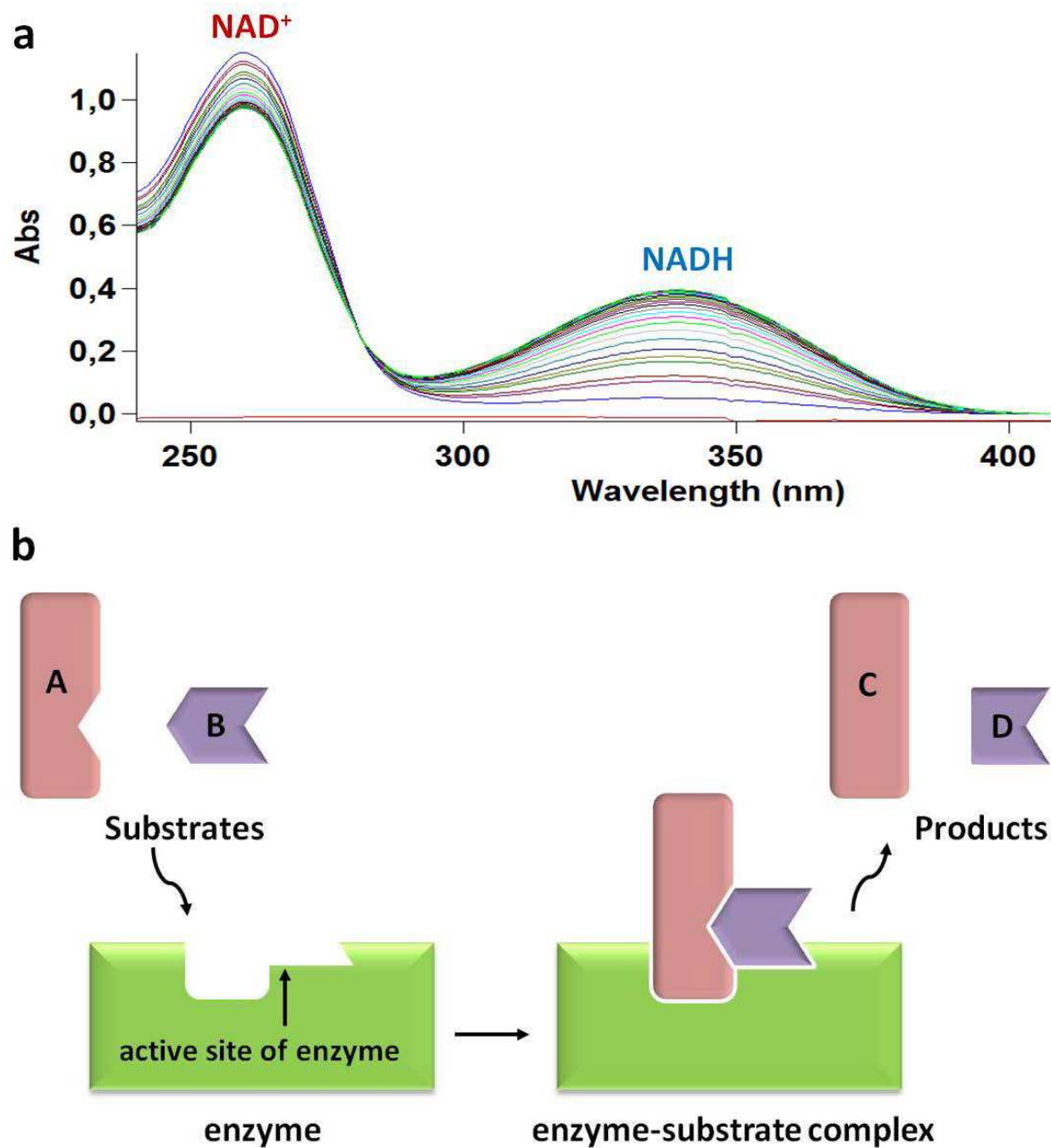


Figure 5.3 Enzymatic system. a) Electronic absorption spectrum of NAD⁺ and NADH in the presence of glucose and GDH. b) Schematic representation of a catalytic enzyme reaction.

References

1. Loget, G.; Roche, J.; Gianessi, E.; Bouffier, L.; Kuhn, A., *J. Am. Chem. Soc.* **2012**, *134* (49), 20033-20036.
2. *Encyclopedia*, <http://en.wikipedia.org/wiki/Enzyme> Accessed **09, 2013**.
3. Chao, C.-H.; Li, K.-L.; Wu, C.-S.; Lee, C.-C.; Chiang, H.-P.; Yang, Y.-S.; Pan, T.-M.; Ko, F.-H., *Int. J. Electrochem. Sci* **2012**, *7*, 5100-5114.
4. Tseng, T.-F.; Yang, Y.-L.; Lin, Y.-J.; Lou, S.-L., *Sensors* **2010**, *10* (7), 6347-6360.
5. Wong, C.; Drueckhammer, D. G.; Sweers, H. M., *J. Am. Chem. Soc.* **1985**, *107* (13), 4028-4031.
6. Bondar, R. J. L.; Mead, D. C., *Clinical Chemistry* **1974**, *20* (5), 586-590.

Appendix

1. Preparation of Ethyl Cellulose Gel, and Recovery of the Modified Carbon Beads

Ethyl cellulose dissolved in absolute ethanol (200 g.L^{-1}) was sonicated for at least 1 hour until a homogeneous gel was obtained. Previously washed glassy carbon beads were mixed with the gel and submitted to the bipolar electrodeposition. At the end of the experiment, the gel containing the modified beads was dissolved in 50 mL of absolute ethanol under stirring. The resulting solution was then centrifuged at 3000 rpm for 2 min. The supernatant was removed and this washing process was repeated 3 times. Finally, the modified beads were kept in a small volume of ethanol for conservation.

2. The Electrochemical Measurement of H_2O_2 and luminol in NaOH Solution, Combined with a Simultaneous Monitoring of the ECL Intensity

Cyclic voltammograms were recorded on a μ -Autolab potentiostat. A glassy carbon electrode was used as the working electrode and a platinum wire was the counter electrode. To generate ECL, the potential of the working electrode was swept between 0 to -1.5 and $+1.0$ V (vs. a saturated Ag/AgCl reference electrode) at a scan rate of 0.1 V/s . ECL intensity was recorded using a Hamamatsu photomultiplier tube R5070 with a Hamamatsu C9525 high voltage power supply. The PMT detector was placed a few millimeters in front of the working electrode and the output signal was amplified by a Keithley 6485 Picoammeter before acquisition via the second input channel of the μ -Autolab.

3. Fabrication of the PDMS Bipolar Electrochemical Cell

For the PDMS cell, a kit containing a curing agent and the pre-polymer (RTV-615, Momentive Performance Materials) was used. The two components were perfectly mixed with a mass ratio of 1:9, respectively, and then centrifuged in order to exclude air bubbles. The mold consisted of a rubber part that was usually cut with the desired shape for the final cell, and which was put into a flexible container (Figure A.1). The PDMS mixture was poured slowly into the mold to prevent air bubbles formation, and then put in an oven for several hours at 70 °C. After removing the mold parts, the PDMS cell can be recovered and used.

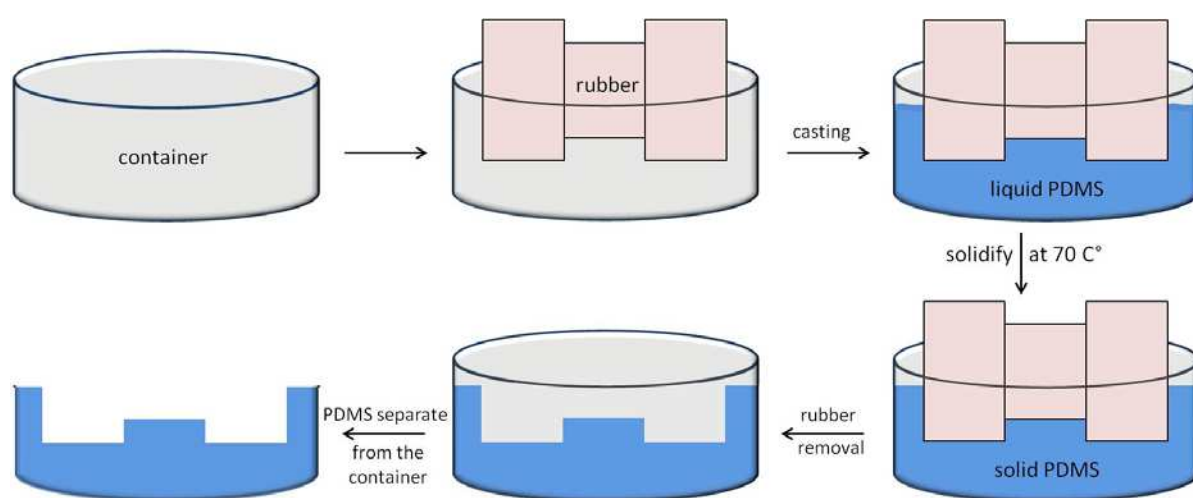


Figure A.1 Schematic illustration of the molding steps of PDMS.

4. Collaborations

The co-workers contributed in different parts of the thesis are presented in following:

Pr. Alexander Kuhn contributed to all the parts of this thesis as the principle supervisor.

Dr. Laurent Bouffier contributed as the co-supervisor to all the parts of this thesis.

Pr. Jumras Limtrakul and Dr. Chompunuch Warakulwit from Kasetsart University (Thailand) synthesized and provided the carbon microtubes used in section 2.4.2. and 2.5.2., together with Chawanwit Kumsapaya who synthesized the sample used in section 2.5.3.2. and she also provided the pictures in Figure 2.10 as a courtesy.

Julie Gillion modified the carbon fibers in Fig. 2.20b, c and Fig. 2.41. She also recorded the movies from which the pictures of Fig. 3.5b and d were extracted.

Dr. Christine Labrugère from ICMCB (Bordeaux1 University) recorded the XPS spectra presented in Figure 2.39b and c.

Dr. Brice Kauffmann (IECB, Bordeaux1 University) recorded the X-ray diffraction patterns in Figure 2.40.

Dr. Jérôme Roche contributed to the design of the bipolar cell presented in Figure 2.42, he also performed the modification of the GC beads presented in Figure 2.44.

Dr. Gabriel Loget contributed to section 3.2.2.

Dr. Laurent Bouffier, Dr. Dodzi Zigah, Catherine Adam and Milica Sentic experimentally contributed to the work presented in section 3.3.

The contribution from all collaborators is gratefully acknowledged.

5. List of Publications That Came out of This Thesis

- 1 – Fattah, Z.; Loget, G.; Lapeyre, V.; Garrigue, P.; Warakulwit, C.; Limtrakul, J.; Bouffier, L.; Kuhn, A. Straightforward single-step generation of microswimmers by bipolar electrochemistry *Electrochim. Acta* **2011**, *56* (28), 10562.
- 2 – Fattah, Z.; Garrigue, P.; Lapeyre, V.; Kuhn, A.; Bouffier, L. Controlled Orientation of Asymmetric Copper Deposits on Carbon Microobjects by Bipolar Electrochemistry *J. Phys. Chem. C* **2012**, *116* (41), 22021.
- 3 – Fattah, Z.; Garrigue, P.; Goudeau, B.; Lapeyre, V.; Kuhn, A.; Bouffier, L. Capillary electrophoresis as a production tool for asymmetric microhybrids *Electrophoresis* **2013**, *34* (14), 1985.
- 4 – Fattah, Z.; Roche, J.; Garrigue, P.; Zigah, D.; Bouffier, L.; Kuhn, A. Chemiluminescence from Asymmetric Inorganic Surface Layers Generated by Bipolar Electrochemistry *ChemPhysChem* **2013**, *14* (10), 2089.
- 5 – Roche, J.; Loget, G.; Zigah, D.; Fattah, Z.; Goudeau, B.; Bouffier, L.; Arbault, S.; Kuhn, A. Template-free generation of metal rings on microobjects *in preparation* **2013**.
- 6 – Bouffier, L.; Zigah, D.; Adam, C.; Sentic, M.; Fattah, Z.; Manojlovic, D.; Kuhn, A.; Sojic, N. Lighting Up Redox Propulsion with Luminol Electrogenerated Chemiluminescence *ChemElectroChem* **2014**, in press.

Résumé

L'électrochimie bipolaire se produit lorsqu'un substrat conducteur isolé qui n'a pas de connexion directe avec une source de tension est exposé à un champ électrique. Par conséquent, elle peut être considérée comme une « technique sans fil ». La polarisation du substrat par rapport au milieu environnant génère une différence de potentiel entre ses deux extrémités qui peuvent subir des réactions de réduction et d'oxydation électrochimiques localisées et ainsi rompre la symétrie de la surface du substrat. Le concept n'est pas nouveau, cependant, il a récemment été identifié comme une méthode nouvelle et facile à mettre en œuvre pour différentes applications. L'objectif de cette thèse est de développer davantage ce concept d'électrochimie bipolaire et ses applications notamment pour la science des matériaux et les systèmes biologiques.

Une introduction à l'électrochimie bipolaire, ses principes et les applications historiques et récentes de la technique dans différents domaines comme l'électronique, l'électroanalyse et les procédés d'électrodéposition sont rapportés dans le premier chapitre. Dans les chapitres suivants (2, 3 et 4), la partie expérimentale et les résultats obtenus de la thèse sont présentés.

L'électrochimie bipolaire a été adaptée pour la préparation en volume (3D) de particules asymétriques, également appelées particules « Janus », qui sont d'une grande importance dans des domaines variés, et nécessitent généralement l'utilisation d'interfaces (2D) pour leur processus de fabrication. Des substrats conducteurs de différentes nature, taille et forme ont été modifiés avec divers matériaux tels que des métaux, des composés ioniques et inorganiques en utilisant cette approche. Les objets modifiés ont été étudiés par microscopie optique et électronique à balayage en plus de l'utilisation d'autres techniques qualitatives pour caractériser les dépôts. Des métaux comme l'argent et le platine ont été utilisés séparément pour le processus de dépôt électrolytique bipolaire sur des microtubes de carbone placés dans un capillaire, ce qui a conduit à des structures hybrides tube de carbone/métal. Cette technique est basée sur l'utilisation d'une électrophorèse capillaire, afin d'appliquer des champs électriques élevés jusqu'à $\sim 100 \text{ kV / m}$ dans un capillaire qui mesure typiquement une trentaine de centimètres. Le volume de réaction est limité dans la configuration d'électrophorèse capillaire, ce qui rend le processus insuffisant pour produire des quantités

importantes de particules asymétriques afin d'envisager des applications industrielles. Par conséquent, une nouvelle cellule électrochimique bipolaire a été adaptée pour la préparation dans le volume de ces particules.

La cellule est constituée d'un seul bloc qui a été séparé par deux membranes pour isoler un compartiment de réaction central dans lequel est disposée la suspension de substrat, et deux compartiments extérieurs, dans lesquels les électrodes sources connectées à une alimentation électrique. Les séparateurs sont faits soit en verre fritté ou en polymère afin de contrôler la perméabilité et la stabilité mécanique. Les substrats conducteurs sont généralement placés dans le compartiment de réaction, et la modification est effectuée en appliquant la tension entre les électrodes d'alimentation en présence d'un sel métallique. Des particules asymétriques de type Platine/microtubes de carbone ont été préparées en utilisant cette technologie. Avec une configuration analogue à l'électrophorèse capillaire, mais avec un capillaire de grand diamètre, il est possible de modifier des fibres de carbone de longueur millimétrique avec du platine ou du nickel, à une extrémité de ces fibres.

En outre, un réglage fin de la topologie du dépôt peut être obtenu sur des substrats de carbone à différentes échelles de taille. Le site de dépôt sur les matériaux hybrides générés est directement déterminé par le contrôle de l'alignement des objets dans le champ électrique durant le processus d'électrodéposition. Pour cela, la configuration précédente a été utilisée pour une expérience de validation de principe en vue de modifier avec un dépôt de cuivre des fibres de carbone alignées mécaniquement. Deux topologies différentes (centrée et non-centrée) ont été obtenus. En choisissant soigneusement les conditions expérimentales dans une cellule électrochimique bipolaire, la localisation sélective d'un dépôt de cuivre a également été démontrée sur des microtubes de carbone. Dans ce cas, l'alignement des tubes en carbone est contrôlé par l'application du champ électrique en deux étapes successives (valeur du premier potentiel en dessous, puis second potentiel supérieur à la valeur du seuil permettant l'électrodéposition du cuivre) et en ajustant la viscosité du milieu environnant. Trois types de d'aggrégats de cuivre ont été produits respectivement avec des topologies différentes par rapport à l'axe principal de l'objet modifié : (1) une topologie complètement centrée, (2) une topologie entièrement non-centrée, et (3) une combinaison des deux modifications précédentes. La sélectivité de site du dépôt métallique est importante pour certaines applications comme des systèmes électroniques dans lesquels l'électrochimie classique n'est pas appropriée, et aussi pour le contrôle du mode de mouvement d'objets autopropulsés.

Le dépôt électrolytique bipolaire n'est pas limité au transfert d'électrons directement à partir de précurseurs électroactifs tels que les sels métalliques. La déposition peut également être déclenchée indirectement au pôle réactif de l'électrode bipolaire en réduisant des espèces qui peuvent ensuite réagir localement avec un autre précurseur non électroactif. Ce processus qui est appelé électrochimie bipolaire indirecte a été utilisé pour le dépôt sélectif d'une couche inorganique fonctionnelle sur des tiges en graphite. Le dépôt de bleu de Prusse insoluble dans l'eau ainsi que d'autres composés relatifs à base de fer a abouti à la formation d'objets Janus qui sont capables de promouvoir l'émission de lumière par chimiluminescence.

L'électrocristallisation de composés ioniques sur des substrats en carbone a été démontrée pour la première fois par électrochimie bipolaire. Des monocristaux de sels de platine et d'or ont été électrogénérés sur des fibres de carbone et des barres de graphite. Différentes morphologies et tailles de cristaux ont été observées sur les substrats et ont été caractérisées en utilisant plusieurs techniques, notamment des analyses dispersives en énergie X (EDX), des mesures de spectrométrie photoélectronique X (XPS) et la diffraction des rayons X. Le mécanisme de formation des cristaux n'est pas encore complètement élucidé et doit être étudié davantage.

Le gradient de potentiel le long de l'électrode bipolaire établi durant l'électrodéposition permet la génération de différentes morphologies de dépôts métalliques sur un substrat isolé. Les morphologies adoptées par le cuivre sous l'influence de champs électriques élevés ont été observées lorsque ce métal est électrodéposé sur des fibres au carbone relativement longues (0,5 à 1,0 cm). Une investigation plus poussée s'avère nécessaire pour mieux comprendre le processus.

Un développement technologique de la cellule d'électrochimie bipolaire a été réalisé grâce à l'introduction d'un compartiment de réaction amovible, qui permet de limiter une convection trop importante entre les compartiments. Grâce à cette avancée, quand un précurseur métallique anionique est engagé dans des conditions de faible force ionique, le transfert de masse est dominé par la migration durant l'électrodéposition. Cela permet de générer un dépôt métallique en forme d'anneau sur la surface d'une électrode bipolaire sphérique au lieu de former une particule Janus classique. Ce mécanisme nous a permis d'utiliser la technologie bipolaire comme un processus simple pour micro-structurer des objets conducteurs qui ont potentiellement une large applicabilité dans des domaines variés.

La structure asymétrique des particules qui est la clé pour générer des micro-nageurs autonomes est discutée dans le chapitre 3. Dans ce contexte, l'électrochimie bipolaire s'est avérée être très utile pour induire le mouvement des particules selon deux stratégies. La première correspond à l'utilisation en tant que nageurs de particules asymétriques qui ont été préparées par électrodéposition bipolaire de métaux sur des substrats en carbone. En d'autres termes, l'électrochimie bipolaire joue ici un rôle indirect comme outil de fabrication. Dans ce contexte, des hybrides fibres de carbone / nickel peuvent être déplacés dans un espace à deux dimensions en utilisant un champ magnétique externe ; tandis que les hybrides tubes de carbone / platine sont propulsés selon deux modes différents (translation ou rotation, selon la topologie du dépôt de platine) par la génération de bulles d'oxygène en présence de peroxyde d'hydrogène (carburant chimique).

La seconde stratégie repose sur la rupture directe de symétrie au sein de particules isotropes qui peut être provoquée par le champ électrique appliqué, menant au mouvement contrôlé de l'objet bipolaire. Selon ce principe, l'accumulation de bulles sous une bille en graphite conduit à sa lévitation dans un capillaire vertical. Cette mise en mouvement a été couplée à une réaction d'électrochimiluminescence au pôle anodique. Ce type de nageurs auto-électroluminescent est très intéressant, car on peut facilement suivre leur trajectoire visuellement.

L'électrochimie bipolaire a également été employée pour étudier des systèmes biologiques. La conductivité et le transport de charge dans l'ADN, qui est une question fondamentale dans de nombreuses applications ont été brièvement abordés dans le chapitre 4, sur la base de travaux décrits précédemment dans ce domaine. L'électrophorèse capillaire a été principalement utilisée pour étudier les propriétés électriques de l'ADN. Différents précurseurs métalliques et contre-réactions ont été utilisés pour le dépôt de métal médié par l'ADN à une extrémité du double brin. Des résultats prometteurs ont été obtenus pour les dépôts de cuivre et de nickel à l'extrémité d'échantillons d'ADN longs, cependant d'autres expériences et des analyses restent encore nécessaires afin de conclure définitivement sur l'utilisation d'un biopolymère comme électrode bipolaire.

Ainsi, l'électrochimie bipolaire représente une approche très attractive et polyvalente pour étudier différents systèmes. Un résumé détaillé et une conclusion de ce qui a été rapporté dans cette thèse, en plus de différentes perspectives possibles dans les domaines de la science des matériaux, des micro-nageurs et les systèmes biologiques ont été inclus dans le dernier chapitre de ce manuscrit.

